

UNIVERSITY
OF OSLO

Jonas Rønning

Topological Defects and Flows in BECs and Active Matter

Thesis submitted for the degree of Philosophiae Doctor

Department of Physics
Faculty of Mathematics and Natural Sciences

The Njord Center



2023

© **Jonas Rønning, 2023**

*Series of dissertations submitted to the
Faculty of Mathematics and Natural Sciences, University of Oslo
No. 2642*

ISSN 1501-7710

All rights reserved. No part of this publication may be
reproduced or transmitted, in any form or by any means, without permission.

Cover: UiO.
Print production: Graphic center, University of Oslo.

Preface

This thesis is submitted in partial fulfillment of the requirements for the degree of *Philosophiae Doctor* at the University of Oslo. The research presented here was conducted at the University of Oslo, under the supervision of Professor Luiza Angheluta.

The thesis is a collection of five papers, presented in chronological order of writing. The common theme to them is the dynamics and/or nucleation of topological defects in non-linear fields. The thesis includes an introduction to topological defects in superfluid Bose-Einstein condensates and active liquid crystals. This is followed by a discussion of the individual research papers and the connection between them. In addition to the five attached papers, I have coauthored two additional papers.

Acknowledgements

First and foremost, I would like to thank my supervisor Professor Luiza Angheluta for her great guidance and discussions during the work on this project. Luiza has been my supervisor since my master's project and her great knowledge and infectious enthusiasm towards physics have had a great influence on shaping this project and my perspective on physics. I have truly enjoyed working with her.

I would also like to thank Vidar Skogvoll, Harish P. Jain, Richard D. Jun-Geet Ho, M. Cristina Marchetti, Amin Doostmohammadi, Marco Salvalaglio, Jorge Viñals, Kristian S. Olsen, Emily Q. Z. Moen, Mark J. Bowick, Julian Renaud and Benjamin H. Andersen for great collaboration and interesting discussions. I have benefited greatly from their insights.

I want to acknowledge all my wonderful colleagues at Njord and PoreLab for providing a great work environment.

Last, but not least I would like to thank my friends and family for their great support.

• **Jonas Rønning**
Oslo, August 2023

List of publications

During my PhD I have been involved in seven submitted papers. Five of these are the basis for this thesis. They are the following:

- I Rønning, J., Marchetti, C. M., Bowick, M. J., and Angheluta, L. “Flow around topological defects in active nematic films”. In: *Proceedings of the Royal Society A*. Vol. 478, no. 2257 (2022), p. 20210879. DOI: 10.1098/rspa.2021.0879. Reference: [1]
- II Rønning, J., Marchetti, C. M., and Angheluta, L. “Defect self-propulsion in active nematic films with spatially varying activity”. In: *Royal Society Open Science*. Vol. 10, no. 2 (2023), p. 221229. DOI: 10.1098/rsos.221229. Reference: [2]
- III Rønning, J., and Angheluta, L. “Precursory patterns to vortex nucleation in stirred Bose-Einstein condensates”. In *Physical Review Research*. Vol. 5, no. 2 (2023), p. 023108. DOI: 10.1103/PhysRevResearch.5.023108. Reference: [3]
- IV Skogvoll, V., Rønning, J., Salvalaglio, M. and Angheluta, L. “A unified field theory of topological defects and non-linear local excitations”. In *npj Computational Materials*. Vol. 9, no. 122 (2023) DOI: 10.1038/s41524-023-01077-6. Reference: [4]
- V Rønning, J., Renaud, J., Doostmohammadi, A. and Angheluta, L. “Spontaneous flows and dynamics of full-integer topological defects in polar active matter”. To appear in *Soft Matter*. DOI: 10.1039/D3SM00316G Reference: [5]

These are attached at the end of the thesis. In addition to the five listed above I have co-authored two articles that are not included here. They are:

1. Moen, E. Q. Z., Olsen, K. S., Rønning, J. and Angheluta, L. “Trapping of active Brownian and run-and-tumble particles: A first-passage time approach”. In: *Physical Review Research*. Vol. 4, no. 4 (2022), p. 043012. DOI: 10.1103/PhysRevResearch.4.043012 Reference: [6]
2. Andersen, B. H., Renaud, J., Rønning, J., Angheluta, L. and Doostmohammadi, A. “Symmetry-restoring crossover from defect-free to defect-laden turbulence in polar active matter”. In *Physical Review Fluids*. Vol. 8, no. 6 (2023), p. 063101. DOI: 10.1103/PhysRevFluids.8.063101 Reference: [7]

Abstract

We study the nucleation and dynamics of topological defects in two-dimensional superfluid Bose-Einstein condensates and active liquid crystals. Using the property that these are emergent states of matter with broken rotational symmetry, we formulate a generic mathematical framework that we use to describe the properties of the corresponding topological defects. The active liquid crystals consist of micro-organisms that have an intrinsic activity which is injecting energy into the system. When the intrinsic energy production is large enough, it will result in the spontaneous creation of topological defects. These defects are localized sources of long-range elastic distortions which generate large-scale flows. We are able to solve the flow equations for isolated defects in the limit of point-like defects with an idealized far-field structure that is subject to both friction and viscous dissipation. The induced flow feeds back into the evolution equation for the order parameter of the liquid crystal and has effects on the motion of the defects by making them self-propelled and by mediating effective interactions between them. In contrast, the Bose-Einstein condensate is a passive system where energy is injected by externally applied potentials. One way to create defects is by stirring the condensate with a moving potential. Quantum vortices are then nucleated in pairs and shed from the stirring potential. We show how the defect nucleation and motion are determined by the evolution of the superfluid wave function. In this thesis, we demonstrate that even though the energy is injected and transported differently in these two systems, there are similarities in the fundamental mechanisms for the nucleation of topological defects and in the correspondence between defect kinematics and the evolution of the order parameter.

Sammendrag

I denne avhandlingen studerer vi nukleasjonen og dynamikken til topologiske defekter i to dimensjonale Bose-Einstein kondensater og aktivt flytende krystaller. Disse systemene er resultatet av det samme symmetribrudet, noe vi utnytter til å beskrive dem ved hjelp av det samme matematiske rammeverket, og bruker dette til å studere systemenes topologiske defekter. Den aktive flytende krystallen er bygget opp av mikroorganismer som har en iboende aktivitet som tilfører energi til systemet. Om den iboende energi-injeksjonen er sterk nok vil man få spontan dannelse av topologiske defekter. Disse defektene er lokaliserte kilder til langt rekende elastiske deformasjoner som stresser materialet og genererer strømninger. Vi løser strømningsligningene for isolerte defekter, under antagelsen om at defektene er punktlignende med idealiserte fjernfelt. Vi inkluderer både friksjon og viskøs dissipasjon. De induerte strømningene mates inn i likningene som beskriver utviklingen til den flytende krystallens ordensparameter, og påvirker dermed hvordan defektene beveger seg ved å gjøre dem selvdrevne og formidle interaksjoner mellom dem. I kontrast er Bose-Einstein kondensatet et passivt system der vi må tilføre energi eksternt ved å røre med et tidsavhengig potensiale. Dette resulterer i at kvantifiserte virvler blir produsert i par og slippes fra potensialet. Vi viser hvordan nukleasjonen og bevegelsen til defektene er knyttet til utviklingen av den superflytende bølgefunksjonen. I denne avhandlingen demonstrerer vi at selv om energien er tilført og transportert forskjellig i disse to systemene så er det likheter i de fundamentale mekanismene for defekt nukleasjon og i korrespondansen mellom defektkinematikken og utviklingen av ordensparameteren.

Contents

Preface	iii
List of publications	v
Abstract	vii
Sammendrag	ix
Contents	xi
List of Figures	xiii
1 Introduction	1
1.1 Structure of the thesis	3
1.2 Notation	3
2 Preliminaries	5
2.1 Symmetry, order and order parameters	5
2.2 Equilibrium statistical mechanics and mean-field theory . .	7
2.3 Hydrodynamics of a simple fluid	10
2.4 Complex integration	16
3 Bose-Einstein Condensates and Topological Defects	21
3.1 Bose-Einstein condensation and the Gross-Pitaevskii equation	21
3.2 Ground state and linear modes	23
3.3 Hydrodynamic description and superfluidity	27
3.4 Topological defects	30
3.5 Vortex tracking	36
4 Hydrodynamics for Active Fluids	41
4.1 Introduction to active fluids	41
4.2 Nematic active matter	42
4.3 Polar active matter	53
5 Numerical Methods	59
5.1 Finite elements	59
5.2 Pseudospectral methods and exponential time differentiation	62
6 Papers: Summary and Outlook	65
6.1 Paper I	65

Contents

6.2	Paper II	66
6.3	Paper III	67
6.4	Paper IV	68
6.5	Paper V	70
7	Conclusion	73
	Bibliography	77
	Papers	86
I	Flow around topological defects in active nematic films	
II	Defect self-propulsion in active nematic films with spatially varying activity	
III	Precursory patterns to vortex nucleation in stirred Bose-Einstein condensates	
IV	A unified field theory of topological defects and non-linear local excitations	
V	Spontaneous flows and dynamics of full-integer topological defects in polar active matter	
	Appendices	
A	Supplementary information for Paper (IV)	
B	Supplementary information for Paper (V)	

List of Figures

2.1	Isotropic and crystal phase	6
2.2	Double well	11
2.3	Hele-Shaw cell	15
2.4	Complex Integration	17
2.5	Keyhole contour	19
3.1	Thomas-Fermi ground state	25
3.2	The Bogoliubov spectrum	26
3.3	Energy Spectrum	29
3.4	Closed curves on \mathcal{S}_2 and \mathcal{P}_2	32
3.5	Vortex core	35
4.1	Nematic order	43
4.2	Force dipole	45
4.3	Growth factor	49
4.4	Nematic defects	50
4.5	Polar order	54
4.6	Polar defects	56
5.1	Mesh of triangular elements	60

Chapter 1

Introduction

The natural world is separated into many length scales where the interactions on the small scales determine the behavior on the larger scales. New phenomena emerge on the large scale due to the interaction of many microscopic constituents on a smaller scale. For example, ocean waves are macroscopic patterns emerging when a macroscopic number of air and water molecules interact with each other but will have no meaning in systems consisting of only a few molecules [8]. It is, in principle, possible to derive all laws of science from the interactions on the smallest length scales, which to the current date are the fundamental particles that are described by the standard model of particle physics.

In practice, however, this is an impossibly hard problem, and in fact, it is not even needed. Biologists do not use the standard model of particle physics to explain moose-three scattering. At each new level of complexity, new laws, concepts, and generalizations are required to describe the system [8]. In condensed matter physics, we often want to bridge the description on the microscopic scale with the observed dynamics on the macroscopic scale. This is a formidable task. Luckily, not all details of the interactions between the microscopic constituents are important when looking at the collective properties of a system consisting of a large number of them [9]. Because of this, one can construct simplified models that include the most relevant information that survives the coarse-graining while ignoring the small-scale details. In some cases, we rely on the underlying broken symmetries and conservation laws to describe the emergent behavior on the macroscopic scale [9, 10].

Symmetries are fundamental properties that govern macroscopic behaviors and provide a key to connecting systems that have different microscopic units. In other words, the shared symmetries allow us to use the same framework to study two systems that at first glance seem to be unrelated, like active matter and Bose-Einstein condensates (BEC). Active matter is a term that refers to systems that are built up of many self-driven units, e.g. bacteria or migrating cells. Bose-Einstein condensate is a quantum state formed in ultra-cold Bose gasses. Even though one bacteria and one boson are quite different, the broken symmetries in the active nematic and the Bose-Einstein condensate are the same so the macroscopic systems can be described in a similar way. That we can use a shared macroscopic description to study systems that have different microscopic descriptions is something we are going to explore in this thesis.

Ordered systems will in general not be perfectly homogeneous but will contain defects that are sources of distortions, stresses, and flows. Order goes

1. Introduction

hand in hand with symmetry and topology, which is why the defects that locally tear the order are known as topological defects. These are defects in the system's order that are protected by topological constraints [9, 11]. Even though the defects are localized on small scales they induce global effects. Some examples of topological defects are dislocations in crystals [12–14], disclinations in liquid crystals [15, 16] and cosmic strings [17]. These defects and interactions between them are important for many of the properties we see in condensed matter. In Bose-Einstein condensates the defects are driving a chaotic state known as quantum turbulence [18], and contribute to the persistence of large-scale currents [19]. Topological defects also play a prominent role in many biological processes like the Hydra morphogenesis [20], where during the regeneration of a hydra topological defects are acting as organization centers for the development of body parts like the hydra's foot and mouth.

Topological defects are the fingerprints of an ordered state, and in general, emerge in systems where the ground state is degenerate [21]. A way of making them is by rapidly cooling down a system from a disordered state. In such a process there will be formed patches of ordered domains with defects emerging between the domains due to incompatibility in the local ordering. The formation of defects during the cooling and relaxation to an equilibrium of a high-temperature disordered state is well studied [22]. The nucleation mechanisms we have focused on in this thesis are instead that of non-equilibrium-driven states, where there is a lot of research activity to better understand fundamental mechanisms [23, 24]. The driving mechanisms of the active liquid crystal and the Bose-Einstein condensate differ. In the active system, the energy injection happens at the single particle scale where the self-driven active particles consume energy from the environment, e.g. by eating, and turning it into mechanical energy. If the intrinsic activity of the particles is large enough the system spontaneously creates topological defects [24, 25]. In the Bose-Einstein condensate, the driving mechanism is external and happens on a scale that is larger than that of the single particle. This could be done either by stirring the condensate or by rotating it [26–29].

Once the defects are formed, they will move around in the systems and interact with each other. In both systems, defect motion is determined by the evolution of the ordered system. In active fluids, due to intrinsic activity, any distortion in the order will induce spontaneous flows. This flow makes the defects self-propelled and mediates interactions between them. We have explored different hydrodynamic dissipative effects like friction with the substrate and viscosity, and studied how they impact self-propulsion and spontaneous flow profiles around the defects. By using an idealized minimal model for the defects' structure, we are able to get insight into the mechanism behind the effects observed in numerical and experimental works.

In this thesis, we put forward a unified mathematical framework to study the defect dynamics and nucleation processes in Bose-Einstein condensates and active liquid crystals, taking advantage of their similar rotational symmetries.

There are unanswered questions about the defect nucleation and kinematics in both these systems. That we are able to describe the systems using the same frameworks illustrates that these problems are not isolated and that we can get insight into the systems by taking advantage of the knowledge that has been developed in both fields. The formalism that we present was developed for tracking defects, and we show that we can use it to extract additional information about the nucleation process. Since the broken rotational symmetry that is shared by these systems is common in physics the themes that are discussed here are not restricted to these two systems.

1.1 Structure of the thesis

The thesis is article-based and is divided into two parts. The first part, referred to as the main text, is a theoretical introduction to the framework we are using in the articles. This is meant as a companion for the articles in which the reader can find additional information if they want some additional explanations of a concept. The second part is the attached papers. The structure of the main text is as follows:

Chapter 2 is a theoretical prelude, where we introduce some important concepts that are used throughout the thesis. We start by introducing the concept of symmetries and order parameters before we have a brief introduction to equilibrium statistical mechanics. This is followed by a discussion of hydrodynamics and the chapter ends with an introduction to complex analysis. Chapter 3 introduces the Gross-Pitaevskii theory for Bose-Einstein condensates of weakly interacting Bose gasses. We start by motivating the Gross-Pitaevskii equation from the second-quantized many-body Hamiltonian of a weakly interacting Bose gas and discuss some properties of this equation. Then we use this system to introduce the concept of topological defects which we give a general treatment before looking at some model-dependent properties like the far-field energy. In Chapter 4 we introduce the two models for active matter that we have used in this thesis, namely the active nematic and an active polar model. We here take advantage of the fact that the defects in the Bose-Einstein condensate are very similar to the ones in the active matter models which makes this discussion brief. In Chapter 5 we discuss the numerical methods we have used. We then summarise the papers and give possible outlooks in Chapter 6 before we conclude in Chapter 7.

1.2 Notation

The notation used in the papers varies. In the main text, we will stick to the following standard convention. Vectors like \mathbf{v} are given in bold font and the corresponding length is given as v . We have two exceptions to this notation; In Chapter 4 we introduce a complex field u , therefore to distinguish the complex field from the length of the vector we will in this chapter use $|u|$ for the latter,

1. Introduction

and in Chapter 3 we introduce the vector field $\vec{\Psi}$ which has been given the arrow notation to easier distinguish it from all the other ψ fields in the chapter.

The i 'th Cartesian component of the vector field \mathbf{v} is written as v_i , and repeated indices are summed over. The dot product is therefore written as $\mathbf{v} \cdot \mathbf{u} = v_i u_i$. The partial derivative with respect to the i 'th Cartesian coordinate is written as $\partial_i = \frac{\partial}{\partial x_i}$ and the partial derivative with respect to time is written ∂_t . We are going to use the convention that differential operators are only acting on the symbol to their immediate right. We therefore have that $\partial_i f \partial_j g = (\partial_i f)(\partial_j g)$. Also, note that ∂ will also be used to denote the boundary of a domain D as ∂D . From the context, the distinction should be clear.

For tensors of rank 2 or higher, we do not have any special notation. These will mostly be written as Greek letters like σ and Ω or as capital letters like E and Q . The dot product will mean contraction over the last index so $(\nabla \cdot Q)_i = \partial_j Q_{ij}$. Two rank 2 tensors written next to each other denote a standard matrix multiplication given in index notation as $(QE)_{ij} = Q_{ik} E_{kj}$.

The imaginary unit is written as i . The distinction with the i 'th Cartesian component should be clear from the context. For coordinates in the complex plane, we use $z = x + iy$ and its complex conjugate $\bar{z} = x - iy$ with the derivatives given as $2\partial_z = \partial_x - i\partial_y$. Complex fields will either appear as Greek letters like ψ or as a complex velocity $u = u_x + iu_y$. For complex conjugates, we use the bar notation \bar{z} for fields denoted by Latin letters and a star ψ^* for the ones denoted with Greek. This is to easier distinguish the complex conjugate of the complex field ψ^* from the Fourier transform $\tilde{\psi}$ and the quantum operator $\hat{\psi}$.

For labeling individual defects in a set of N we will use Greek letters. The charge of the vortex labeled α is, therefore, q_α . For vector quantities, like the defect velocity \mathbf{v}^α , the label is written as an exponent to avoid confusion with the Cartesian components. To label quantities related to microscopic particles, we will use Greek letters in a parenthesis. The director of the particle labeled α in an active nematic is therefore written as $\tilde{\mathbf{n}}^{(\alpha)}$. Here the tilde is used to distinguish microscopic from macroscopic quantities. We do not use the Einstein summation convention for these indices. Note that we also use α as the activity parameter in Chapter 4.

In Chapter 3 we are going to encounter some quantum operators. We have given these small hats $\hat{\psi}$. The Fourier transform of the function f is written as $\mathcal{F}[f]$ with the inverse $\mathcal{F}^{-1}[\tilde{f}]$. We use the following convention

$$\tilde{f}(\mathbf{k}) = \mathcal{F}[f](\mathbf{k}) = \int d\mathbf{r} f(\mathbf{r}) e^{-i\mathbf{k} \cdot \mathbf{r}}, \quad (1.1)$$

$$f(\mathbf{r}) = \mathcal{F}^{-1}[\tilde{f}](\mathbf{r}) = \frac{1}{(2\pi)^d} \int d\mathbf{k} \tilde{f}(\mathbf{k}) e^{i\mathbf{k} \cdot \mathbf{r}}. \quad (1.2)$$

Here, d is the dimension, which is mostly going to be $d = 2$.

Chapter 2

Preliminaries

This chapter will give a short overview of some concepts that are used throughout the thesis. We start with a short discussion about what is meant by symmetry, ordered system, and order parameters. This is followed by an introduction to statistical mechanics and mean field theory before we discuss hydrodynamic models and give the example of a simple fluid. The last part of this chapter is a short introduction to complex analysis.

2.1 Symmetry, order and order parameters

Symmetry We say that a system has a symmetry if it stays the same (i.e. is invariant) after some transformation. E.g a system with rotational symmetry looks the same after you rotate it. Symmetries can be either continuous or discrete. The difference can be illustrated by a circle and a square. The circle has a continuous rotational symmetry since it can be rotated by any angle and it will still look the same, while the square has a discrete symmetry since it is only invariant to rotations that are a multiple of $\pi/2$. We can say that the circle is more symmetric than the square since it is invariant under more transformations.

Symmetries are very important in condensed matter physics because they have consequences for the physical properties of the system, and it is often, but not always, the thing that distinguishes different phases [11]. This is the case when a liquid freezes to a crystalline solid, as illustrated in Fig. 2.1. The fluid phase where the particles are randomly placed is shown in Fig. 2.1 a) and Fig. 2.1 b) shows a solid crystal where the particles are situated on a triangular lattice defined by the lattice vectors \mathbf{a} and \mathbf{b} which are of equal length. The fluid has here more symmetries than the solid. This might be hard to see from the figure since the solid has clear symmetries to translations by multiples of the lattice vectors and it is invariant to rotations of $\pi/3$. The fluid however has continuous rotational and translational symmetries, because wherever we are in the fluid it will look the same. These symmetries do not show up in the microstate in Fig. 2.1a), but in the macroscopic state that is the result of averaging over many microstates that are prepared similarly. This averaging process is known as an ensemble average [11, 30], and is going to be discussed further in the next section. Since the particles in the fluid are randomly placed the average number density $\langle n \rangle = n_0$ will be a constant of space, and is therefore symmetric to all rotations and translations. If we take the ensemble-averaged number density of the crystal it is more probable that the particles are on the lattice sites so this structure will show up also after averaging [11].

2. Preliminaries

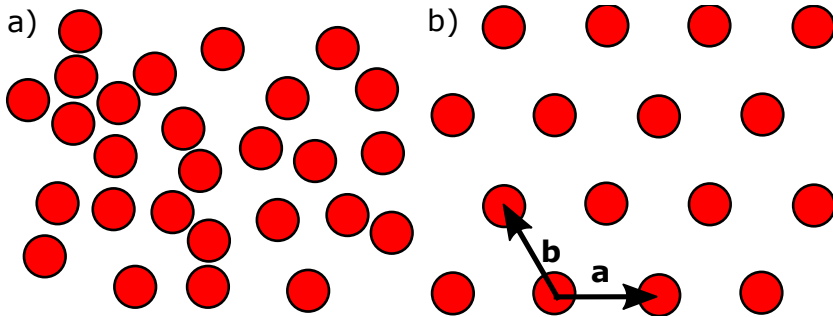


Figure 2.1: a) the position of particles in a two-dimensional isotropic liquid is random. b) after freezing the particles are ordered on a lattice characterized by the lattice vectors \mathbf{a} and \mathbf{b} .

As discussed above a symmetry leaves the system invariant under some transformation. These transformations belong to some group \mathcal{G} [9]. A group \mathcal{G} is a set with a multiplication operator \cdot that satisfies [31]

1. The group is closed under multiplication. Meaning that for $g, h \in \mathcal{G}$ implies $g \cdot h \in \mathcal{G}$.
2. Associativity of multiplication so that for $g, h, k \in \mathcal{G}$ we have $(g \cdot h) \cdot k = g \cdot (h \cdot k)$.
3. There exists an identity element $e \in \mathcal{G}$ which has the property that for any $g \in \mathcal{G}$ we have $e \cdot g = g \cdot e = g$.
4. For all $g \in \mathcal{G}$ there exists an inverse $g^{-1} \in \mathcal{G}$ so that $g^{-1} \cdot g = g \cdot g^{-1} = e$.

Note that in general the multiplication operator is not required to commute, so the relation $g \cdot h = h \cdot g$ is therefore not guaranteed to hold. One example of a group is the integers \mathbb{Z} under addition $+$. Here the inverse of g is $-g$ and the identity is 0. Another example is the set of real numbers excluding zero, $\mathbb{R}/0$, under multiplication. In this group, the inverse of g is $1/g$ and the identity is 1. The first example here is a discrete group, while the second is a continuous group.

We mentioned that the transformations that leave the system invariant can be described by a group. For example, the fluid mentioned above has rotational, reflection, and translational symmetries. In n dimensions this corresponds to the $O(n)$ group which includes both continuous rotation and reflection, and the translation group \mathcal{T} . The product of these is known as the Euclidean group [9]. After the transition to the crystal phase, these symmetries are broken and replaced by discrete symmetries represented by discrete groups.

In this thesis, we have mostly been concerned with systems that have a broken $O(n)$ symmetry. The representation of this group is real matrices with determinant ± 1 and the multiplication operator is standard matrix multiplications[31]. A subgroup of $O(n)$ is $SO(n)$ which describes rotations and is represented by matrices with determinant 1. In two dimensions, $SO(2)$, this group is isomorphic to the group $U(1)$ which is represented by all complex numbers of length 1.

Order parameter When the liquid freezes and becomes a crystal its continuous rotational and translational symmetries are broken, and the result is a new phase with discrete symmetries. The particles have gone from being anywhere in space with equal probability, to being in the positions of the lattice sites. To characterize this new ordered phase, we can introduce an order parameter. This is a parameter that is constructed in such a way that it is zero in the disordered phase and non-zero in the ordered phase. During the fluid-solid phase transition illustrated in Fig. 2.1 the order parameter is the average number density subtracted from the number density of the fluid, i.e. $\langle \delta n(\mathbf{r}) \rangle = \langle n(\mathbf{r}) \rangle - n_0 = \sum_{\mathbf{G}} n_{\mathbf{G}} e^{i\mathbf{G}\cdot\mathbf{r}}$ [9]. We have here written it in terms of its Fourier series with \mathbf{G} being the reciprocal lattice vectors to highlight the spatial dependence. Since $\langle \delta n(\mathbf{r}) \rangle$ is real the Fourier coefficients have to fulfill $n_{\mathbf{G}}^* = n_{-\mathbf{G}}$. The Fourier representation also makes the translational symmetry of the crystal clear because the dot product of a lattice vector \mathbf{T} with a reciprocal lattice vector \mathbf{G} is $\mathbf{T}\cdot\mathbf{G} = 2\pi N$ with N being an integer. The system is therefore invariant under uniform translation with a lattice vector $\mathbf{r} \rightarrow \mathbf{r} + \mathbf{T}$.

In the above example, the order parameter was a real scalar field. A phase transition where the order parameter is instead a vector is the transition from a paramagnetic to a ferromagnetic phase. In the paramagnetic phase all the magnetic moments are randomly oriented and the average magnetic moment $\langle \mathbf{m} \rangle$ vanishes. The ferromagnetic phase emerges when the magnetic moments start to align and point out a direction, giving a non-zero averaged moment. Since one direction is pointed out the system has now lost its rotational symmetry, i.e. the $O(n)$ symmetry has been broken.

2.2 Equilibrium statistical mechanics and mean-field theory

Many systems in nature are impossible to study by directly considering the dynamics of their microscopic constituents [11, 30]. It is for example impossible to know the position and momentum of all air molecules in a balloon. Intuitively it is also not very important, we do not observe that the balloon behaves strikingly differently just because one of the molecules is shifted a micrometer to the left. What is more important for the balloon is the volume of air inside it, the temperature of the air, and its pressure. This is an example of a thermodynamic or macroscopic description, while the position and momentum of the air molecules are examples of a microscopic description. Other examples

2. Preliminaries

of macroscopic quantities are the tension in the balloon and the mean magnetization in a ferromagnet. There are a lot of interesting phenomena that only emerge in a macroscopic system like waves in a fluid, phonons in a solid, and the crystallization of water when it freezes. Such phenomena do not show in the dynamics of single particles, but emerge when many of them are interacting.

Statistical mechanics is the field of physics that bridges these scales and tries to describe the macroscopic system that emerges from the dynamics of its microscopic constituents. In order to do so one does not try to describe the system in detail, but instead describes the average behavior of many systems that are prepared in a similar way [11, 30]. Such a collection of similar systems is known as an ensemble. Three very important ensembles in statistical mechanics are the microcanonical-, the canonical-, and the grand canonical ensemble. In this section, we will limit our discussion to the canonical ensemble and discuss how we can use its probability density to find thermodynamic quantities. The canonical ensemble consists of systems that are in thermal equilibrium with a heat bath of temperature T and can exchange energy with this bath [11, 30]. The probability of one microstate $\tilde{\mu}$ at a given temperature T is for such a system given as [32]

$$\mathcal{P}(\tilde{\mu}) = Z^{-1} e^{-\beta \tilde{H}(\tilde{\mu})}, \quad (2.1)$$

Where $\beta = 1/(k_B T)$ is the Boltzmann constant and $\tilde{H}(\tilde{\mu})$ is the energy of the microstate. The partition function Z^{-1} comes into the theory as a normalization constant.

This normalization constant turns out to be the most important quantity in equilibrium statistical mechanics because if we know it, we will be able to calculate thermodynamic quantities like the free energy, entropy, and pressure [9, 11, 30]. Since the probability is normalized the partition function can be found by summing over all the possible microstates. It is therefore given as

$$Z = \text{Tr}(e^{-\beta \tilde{H}(\tilde{\mu})}) = \sum_{\tilde{\mu}} e^{-\beta \tilde{H}(\tilde{\mu})}, \quad (2.2)$$

with the sum being over all microstates. This can usually not be solved, except for some idealized systems. From eq. (2.1) we can find the average energy of the system, i.e the internal energy U , by calculating the expectation value

$$U = \langle E \rangle = \sum_{\tilde{\mu}} \tilde{H}(\tilde{\mu}) e^{-\beta \tilde{H}(\tilde{\mu})} Z^{-1} = -\partial_{\beta} \ln Z. \quad (2.3)$$

Another macroscopic quantity that is useful to describe a macroscopic system is the entropy S . The entropy of a system of N equally likely microstates is $-k_B \ln(1/N)$. Noticing that $\mathcal{P} = 1/N$ is the probability of one microstate we can write the entropy as $S = -k_B \langle \ln(\mathcal{P}) \rangle$. This expression can be generalized to systems where the microstates have different probabilities and we get [11]

$$S = -k_B \langle \ln(\mathcal{P}) \rangle = -k_B \sum_{\tilde{\mu}} \mathcal{P}(\tilde{\mu}) \ln(\mathcal{P}(\tilde{\mu})). \quad (2.4)$$

Using the probability density from eq. (2.1) it follows that the entropy of the system is

$$S = \frac{U}{T} + k_B \ln(Z). \quad (2.5)$$

Since we know the internal energy and the entropy we can find the Helmholtz free energy from the thermodynamic relation [11, 30]

$$F = U - TS = -k_B T \ln Z. \quad (2.6)$$

As demonstrated the partition function Z provides the information needed to derive the equilibrium thermodynamics of the system.

2.2.1 Fields

Some of the fluctuations of a system happen on the mesoscale, which is small compared to the macroscale, but large compared to the microscale. When working with these types of properties it is useful to construct a field. We can construct a field by coarse-graining [9, 32], meaning that instead of working with the microscopic variables, like the momentum or spin of individual particles, we divide the system up in boxes and average a function of them, the microscopic order parameter $\tilde{\phi}$, over the box. The tilde is used to distinguish the microscopic order parameter, which is a function of the microscopic variables, from the coarse-grained order parameter ϕ which is averaged. We assume that the number of particles in each box is so large that ϕ can be treated as a continuous field. When doing this mapping from the microscopic description to the field description the partition function is mapped to [32]

$$Z = \int \mathcal{D}\phi(\mathbf{r}) e^{-\beta H[\phi(\mathbf{r})]}, \quad (2.7)$$

with the mesoscopic Hamiltonian H . The symbol $\mathcal{D}\phi(\mathbf{r})$ denotes a path integral over all possible functions ϕ .

Finding a precise form of the mesoscopic Hamiltonian is in general quite hard, and in addition, it does not simplify the partition function. It is therefore desirable to construct an effective Hamiltonian. We construct the effective Hamiltonian with a series expansion in ϕ and its gradients by writing all terms that satisfy the microscopic and spatial symmetries and then truncating the expansion at a given order. A much-used effective Hamiltonian is the ϕ^4 Hamiltonian, where we truncate the expansion to the fourth order and keep up to the second order in gradients

$$H[\phi] = \int d\mathbf{r} [r\phi^2 + g\phi^4] + \int d\mathbf{r} k |\nabla\phi|^2. \quad (2.8)$$

When truncating the expansion at the fourth order the coefficient g has to be positive to ensure that the energy is bounded from below.

2. Preliminaries

Mean-field theory The simplest estimate for the partition function is to only include the most probable value of the order parameter. This is what is known as the mean-field theory, and it is often the first approach one uses to describe phase transitions [9, 32]. The Gross-Pitaevskii theory described in the next chapter is an example of a mean-field theory and we are going to use the mean-field free energy when discussing a hydrodynamic model for the active matter in Chapter 4. In this approximation, the free energy and the Hamiltonian become the same and we therefore have [9]

$$F[\phi] = \int d\mathbf{x} [r\phi^2 + g\phi^4] + \int d\mathbf{x} k |\nabla\phi|^2. \quad (2.9)$$

The state ϕ will be the one that minimizes the free energy [9]. The interaction term punishes spatial variations, making the ground state homogeneous. The lowest energy state is thus the constant ϕ that minimizes the free energy density

$$f[\phi] = r\phi^2 + g\phi^4, \quad (2.10)$$

which is found to be

$$\phi = \begin{cases} 0, & r > 0, \\ \pm\sqrt{-r/(2g)}, & r < 0. \end{cases} \quad (2.11)$$

The free energy provides a continuous phase transition at $r = 0$ where the order parameter ϕ obtains a non-zero value. The profile of $f[\phi]$ is plotted in Fig. 2.2 for r below and above the critical value, showing the change in the location of the minima. One often assumes that r is linearly dependent on the temperature and changes sign for $T = T_c$ [9]. The order parameter close to the order/disorder phase transition then goes as $\phi \sim (T - T_c)^{1/2}$. It turns out that the critical exponent that is found using the mean field approximation is exact in 4 or more spatial dimensions. For lower dimensions the neglected fluctuations are important and give corrections to this [9]. These corrections can be found by for example renormalization.

2.3 Hydrodynamics of a simple fluid

Hydrodynamic model for an isotropic fluid In the above section, we had a brief introduction to equilibrium statistical mechanics and thermodynamics. Most of the work in this thesis is done out of equilibrium either by driving the system with an external potential or because the system is active. Systems that are out of equilibrium, but where each point in space is close to thermodynamic equilibrium can be described by hydrodynamical models [9]. These are models that aim at describing the low-frequency, long-wavelength modes in a system. By long wavelength and low frequency, we refer to modes that have a wavelength that is much bigger than the mean free path for particles λ and are slow compared to the characteristic time of particle collisions τ . Because of this every cycle of the modes contains a large number of single-particle interactions on the microscale, ensuring that locally the system is close to thermodynamic equilibrium and

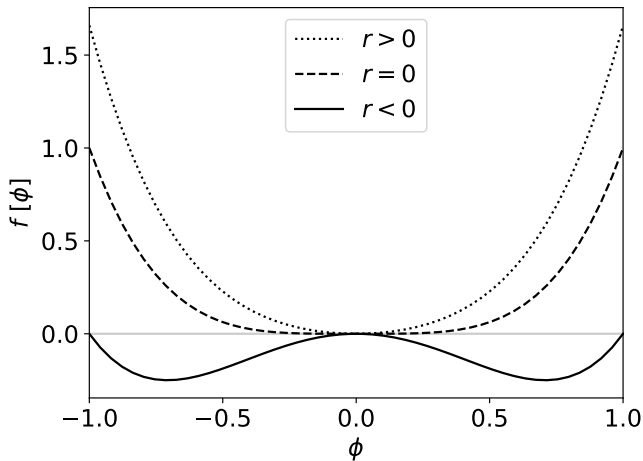


Figure 2.2: Plot of the free energy density $f[\phi]$ for $r < 0$ (solid), $r = 0$ (dashed) and $r > 0$ (dotted). The minimum of the free energy is displaced from $\phi = 0$ to two degenerate minima at $\phi \pm \sqrt{-r/2g}$ when r changes sign. We have set $g = 1$

that we can treat the modes as perturbations to the equilibrium [9]. We are here going to introduce the main ideas behind these types of models through the practical example of a simple isotropic fluid following the discussions in [9, 10].

It is typically few variables that support these low-frequency large wavenumber disturbances because most disturbances will have frequencies proportional to τ^{-1} . The variables that are guaranteed to have the desired properties are conserved densities and broken-symmetry elastic variables. For the isotropic fluid, there is no broken symmetry variable. However, there are five conserved quantities. These are mass, momentum (in 3 dimensions), and energy. The conservation laws for the conserved densities are respectively [9, 10]

$$\partial_t \rho + \nabla \cdot \mathbf{g} = 0, \quad (2.12)$$

$$\partial_t \mathbf{g} + \nabla \cdot \pi = 0, \quad (2.13)$$

$$\partial_t \epsilon + \nabla \cdot \mathbf{j}^\epsilon = 0, \quad (2.14)$$

with the densities being the mass density ρ , momentum density \mathbf{g} and the energy density ϵ . Note that the momentum density \mathbf{g} acts as a current for the mass density ρ . The other currents are the momentum current tensor π and the energy current \mathbf{j}^ϵ . If we Fourier transform these conservation equations in time and space it hints that the frequencies ω will go to zero with the wavenumber q , which means that the long wavelength modes are slow [9, 11].

2. Preliminaries

Having the currents our next step is to relate them to their conjugate thermodynamic fields. We do this by using the following thermodynamic identity for the simple fluid [9, 10]

$$Tds = d\epsilon - \mu d\rho - \mathbf{v} \cdot d\mathbf{g}. \quad (2.15)$$

In this section μ is the chemical potential per unit mass. From this, we can identify the thermodynamic fields as temperature T , chemical potential per unit mass μ , and velocity \mathbf{v} . Taking the time derivative of this identity and using the conservation laws given in eq. (2.12 - 2.14) we get

$$T\partial_t s = -\nabla \cdot \mathbf{j}^\epsilon + \mu \nabla \cdot \mathbf{g} + v_i \partial_j \pi_{ij}, \quad (2.16)$$

and the spatial derivative is

$$T\mathbf{v} \cdot \nabla s = \mathbf{v} \cdot \nabla \epsilon - \mu \mathbf{v} \cdot \nabla \rho - v_i v_j \partial_i g_j. \quad (2.17)$$

Adding these two equations and using the product rule for differentiating we find the relation

$$T [\partial_t s + \nabla \cdot (\mathbf{v}s + T^{-1}\mathbf{Q})] = -\mathbf{Q} \cdot T^{-1} \nabla T - (\mathbf{g} - \rho \mathbf{v}) \cdot \nabla \mu - (\pi_{ij} - p\delta_{ij} - v_j g_i) \nabla_j v_i. \quad (2.18)$$

This is the entropy production equation with the term in the bracket on the left-hand side being the change of the entropy density, s , where the entropy current is given as $\mathbf{v}s + T^{-1}\mathbf{Q}$. We have used that the pressure is $p = \mu\rho + Ts + \mathbf{g} \cdot \mathbf{v} - \epsilon$ and identified the heat current as $\mathbf{Q} = \mathbf{j}^\epsilon - \mu(\mathbf{g} - \rho\mathbf{v}) - \mathbf{v}\epsilon + (\mathbf{v} \cdot \mathbf{g})\mathbf{v} - \mathbf{v} \cdot \pi^T$ [9]. Integrating eq. (2.18) over a large volume and removing the surface terms we get

$$T \frac{dS}{dt} = \int dr (-\mathbf{Q} \cdot T^{-1} \nabla T - (\mathbf{g} - \rho \mathbf{v}) \cdot \nabla \mu - (\pi_{ij} - p\delta_{ij} - v_j g_i) \nabla_j v_i), \quad (2.19)$$

with S being the total entropy.

We can now find the reversible relations between the currents and fields by noting that for reversible processes the entropy is constant. This means that the integrand on the right-hand side has to vanish, which gives the equations

$$\mathbf{g} = \rho \mathbf{v}, \quad (2.20)$$

$$\pi_{ij} = p\delta_{ij} + \rho v_i v_j, \quad (2.21)$$

$$\mathbf{j}^\epsilon = (\epsilon + p)\mathbf{v}. \quad (2.22)$$

Inserting the first two of these into the conservation equations of density and momentum, eq. (2.12) and (2.13), we get after some work the following relations

$$\partial_t \rho + \nabla(\rho \mathbf{v}) = 0, \quad (2.23)$$

$$\partial_t \mathbf{v} + (\mathbf{v} \cdot \nabla)\mathbf{v} = -\frac{1}{\rho} \nabla p. \quad (2.24)$$

This is the mass conservation equation and the Euler equation for an ideal/dissipationless fluid [33].

We now want to find how this is modified when we include the dissipative modes. These are the irreversible modes that we can find by considering relations between fields and currents that transform with the opposite sign [9]. We start by rewriting eq. (2.19) to

$$T \frac{dS}{dt} = \int d\mathbf{r} \left(-\mathbf{Q} \cdot T^{-1} \nabla T + \sigma'_{ji} \nabla_j v_i \right), \quad (2.25)$$

Here σ' is the dissipationless part of the momentum current tensor. We have here used that the momentum is given as $\mathbf{g} = \rho \mathbf{v}$ also when we include dissipation [9]. As discussed above the dissipative relations will be between the currents and the fields which transform with opposite signs under time reversal. Here \mathbf{Q} and \mathbf{v} change sign under time reversal while σ and T do not. There will therefore be a coupling between \mathbf{Q} and T , and one between σ' and \mathbf{v} . To find how these relations look we have to argue based on the physics and symmetry of the system.

A constant temperature cannot be the source for a heat current so \mathbf{Q} has to be proportional to the gradient of T [9]. Since the fluid is isotropic the relation takes the form

$$\mathbf{Q} = -\kappa \nabla T, \quad (2.26)$$

with κ being positive to ensure that currents flow from hot to cold regions and that this term in the entropy production is positive. Similarly, the stress tensor σ' is invariant to translations and is, to first order, proportional to the gradient of the velocity [9, 33]. In addition, when the fluid is in uniform rotation there should be no internal friction in it so the stress has to vanish. These constraints, in addition to the fluid being isotropic, means that the dissipative part of the stress tensor has to have the form

$$\sigma'_{ij} = \eta (\partial_i v_j + \partial_j v_i - \frac{2}{3} \delta_{ij} \nabla \cdot \mathbf{v}) + \zeta \delta_{ij} \nabla \cdot \mathbf{v}, \quad (2.27)$$

with the constants η and ζ being the shear and bulk viscosity respectively [33].

Navier-Stokes We can now write down the equations of motion for the fluid. To make them easier to work with we are going to simplify them by assuming that the fluid is incompressible, i.e. ρ is constant. The equations for mass and momentum conservation then become

$$\nabla \cdot \mathbf{v} = 0, \quad (2.28)$$

$$\rho \partial_t \mathbf{v} + \rho (\mathbf{v} \cdot \nabla) \mathbf{v} = -\nabla p + \eta \nabla^2 \mathbf{v}. \quad (2.29)$$

This is the incompressible Navier-Stokes equation [33]. Flows described by these equations are fully characterized by the geometry of the system and one

2. Preliminaries

dimensionless number known as the Reynolds number. The Reynolds number $\text{Re} = UL/\nu$ gives the ratio between the advective part and the viscous part of the equation. Here U is a typical velocity, L is a typical length, and $\nu = \eta/\rho$ is the kinematic viscosity. If the Reynolds number is low it is the dissipation that dominates the dynamics. Disturbances in the flow are then quickly removed by the dissipation and the fluid can be described by the Stokes equation

$$\eta\nabla^2\mathbf{v} = \nabla p. \quad (2.30)$$

This equation is relevant when discussing flows in biological active matter since it often occurs at low Reynolds number [34]. In the other limit when the flow has a high Reynolds number the inertial part of the Navier-Stokes equation dominates and the system is said to be turbulent.

The Navier-Stokes equation is going to turn up in both the systems we are considering in this thesis. For the active fluids that we discuss in Chapter 4 we couple the Navier-Stokes equation with an evolution equation for the order parameter. Here the flow field advects and rotates the order parameter, while the order parameter is a source of stress and in that way influences the flow. For the Bose-Einstein condensate discussed in Chapter 3 we will show that in some limits, we can map the equation for the complex order parameter ψ into the Navier-Stokes equation, and identify that the viscosity is due to interactions with a thermal cloud.

General hydrodynamics In systems with broken symmetry, one will also get modes that are related to the broken symmetry. These are the so-called Goldstone modes, which are related to the Goldstone theorem that states that when a continuous symmetry is broken the low wavenumber excitations in the symmetry direction should have long periods [11]. When we know the broken symmetries and the conservation laws we can find the hydrodynamic description by using the following recipe. First, we identify conserved densities and broken symmetry variables and their related currents. When this is done we write out the thermodynamics of the system and identify the conjugated fields related to the currents. The last step is then to find the constituent relations. This is the relationship between the currents and the thermodynamic fields, which can be either reversible or irreversible [9]. The reversible relations are between fields and currents that transform with the same sign under time reversion. These modes are non-decaying and responsible for the propagating modes. One can often obtain these relations from invariance arguments [9]. The irreversible relations are between fields and currents that transform with the opposite sign. These are the dissipative modes.

Reduction to two dimensions We are for the most part interested in two-dimensional systems. We can motivate effective two-dimensional flow equations by considering the flow in a Hele-Saw cell as depicted in Fig. 2.3. The cell

consists of two plates that are parallel with a gap of $2h$ between them. We assume that the gap is much smaller than the sides of the cell, and we also assume that the Reynolds number is low so that we can describe the system as a Stokes flow

$$\nabla \cdot \mathbf{v} = 0, \quad (2.31)$$

$$\nabla p - \eta \nabla^2 \mathbf{v} = \mathbf{f}(\mathbf{r}). \quad (2.32)$$

Here \mathbf{f} is a driving force. The center of the cell is set at $z = 0$ so that the boundaries are at $z = \pm h$, the center is thus the xy -plane. We first consider the incompressibility condition and take the variations in the z direction to happen on the scale h while variations in the xy -plane happen on a scale L which we assume to be much larger. Doing a scaling analysis we then get

$$\nabla_{\parallel} \cdot \mathbf{v}_{\parallel} + \partial_z v_z \sim \frac{v_{\parallel}}{L} + \frac{v_z}{h} = 0 \implies v_z \sim v_{\parallel} \frac{h}{L}, \quad (2.33)$$

whereby \mathbf{v}_{\parallel} we refer to the velocity vector that is parallel to the plates and $\nabla_{\parallel} = \partial_x \mathbf{e}_x + \partial_y \mathbf{e}_y$ is the differential operator in this plane. Using the assumption $L \gg h$ we neglect v_z . It then follows from eq. (2.32) that the pressure gradient and the driving force are balancing in the z direction.

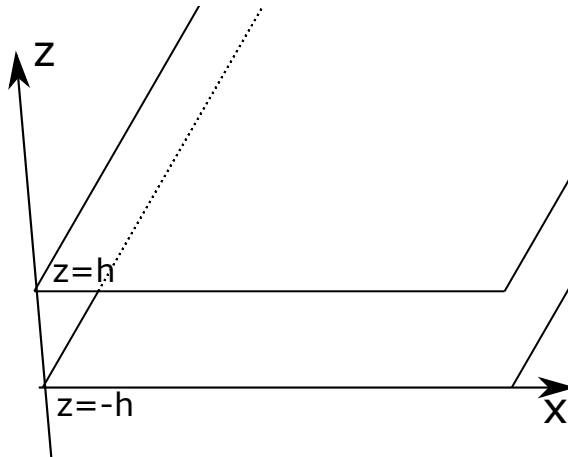


Figure 2.3: Sketch of the Hele-Shaw cell. The cell consists of two parallel plates with a distance $2h$ between them. We consider a flow in such a system in the limit that the plates are infinite in size.

Another consequence of L being so large compared to h is that we can approximate the flow as being a Poiseuille flow of the form [35]

$$\mathbf{v}_{\parallel}(\mathbf{r}) \approx \frac{3}{2h^2} \mathbf{u}(x, y)(h^2 - z^2), \quad (2.34)$$

2. Preliminaries

where \mathbf{u} is the flow after averaging out the z direction. Inserting this into the Stokes equation for the velocity parallel to the plate we find

$$\nabla_{\parallel} p - \eta \frac{3}{2h^2} (h^2 - z^2) \nabla_{\parallel}^2 \mathbf{u}(x, y) - \eta \frac{3}{h^2} \mathbf{u}(x, y) = \mathbf{f}_{\parallel}(\mathbf{r}). \quad (2.35)$$

We now integrate out the z dependence from $-h$ to h so that the equation becomes [35]

$$\Gamma \mathbf{u}(x, y) - \eta \nabla_{\parallel}^2 \mathbf{u}(x, y) = -\nabla_{\parallel} p + \mathbf{F}, \quad (2.36)$$

where $\Gamma = 3\eta/h^2$ is an effective friction coefficient and \mathbf{F} is the effective two-dimensional force. We will for the most part in this thesis be in two dimensions so we will not carry the notation ∇_{\parallel} any further. Here we did the reduction of dimensionality using a Hele-Shaw cell. Notice that we can arrive at eq. (2.36) as long as the flow in the xy -plane can be written as

$$\mathbf{v}_{\parallel}(\mathbf{r}) = u(x, y)Z(z), \quad (2.37)$$

with $Z(z)$ being non-linear in z . The above discussion is thus relevant for more systems than the one we discuss here.

2.4 Complex integration

When solving the flow equations around the topological defects in the active matter with nematic and polar symmetries in Paper (I) and (V) we make use of the fact that we can map the two-dimensional integral into an integral in the complex plane and write the integrals on the form

$$I(\mathbf{r}) = \int_0^{\infty} dr' G(r') \oint_C d\hat{z} f(\hat{z}, r', \mathbf{r}). \quad (2.38)$$

Here C is the unit circle in the complex plane, and \mathbf{r} is the position in space that we evaluate the integral. The integration variables are written in terms of complex polar variables $z' = r'\hat{z}$ with $\hat{z} = e^{i\theta'}$. In this section, we introduce and motivate the integration techniques that we employ to solve the path integral over the complex variable \hat{z} . We are not going to do any rigorous proofs.

Residual integration Given a function $f(z)$ of the complex variable z we want to find the path integral over the curve C in the complex plane. I.e. we want to evaluate

$$\oint_C dz f(z). \quad (2.39)$$

If the function $f(z)$ is analytical in the space bounded by the curve C the integral vanishes due to Cauchy's integral theorem [36]. Suppose now that $f(z)$ has a singularity at the point $z = z_0$ inside of the contour C . We are going to assume C to be a circle of radius R . If C is not a circle to start with we can map the

integral to an integral over the curve C_1 which is a circle, i.e. we want to show that

$$\oint_C dz f(z) = \oint_{C_1} dz f(z), \quad (2.40)$$

for the paths C and C_1 shown in Fig. 2.4 a). To do this, we consider the integral over the edge of the two domains D_1 and D_2 which are drawn in Fig. 2.4 b). Note that C_1 has here been reversed. Since there is no singularity inside either of the domains we have that

$$\oint_{\partial D_1} dz f(z) + \oint_{\partial D_2} dz f(z) = 0. \quad (2.41)$$

Since we integrate both ways on the lines l_1 and l_2 the integral over them cancels. The above expression reduces to

$$\oint_C dz f(z) - \oint_{C_1} dz f(z) = 0. \quad (2.42)$$

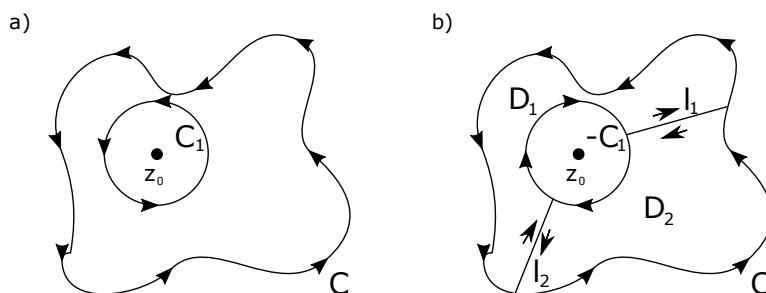


Figure 2.4: When integrating a function $f(z)$ on a curve C that encircles a point z_0 where f is singular we can map this to the integral on the circle C_1 containing z_0 . a) shows a general surface C and the circle C_1 , while in b) we show the construction of two domains D_1 and D_2 . Since the two domains do not contain any singularity the integral over their boundaries vanishes. When we add these two integrals we integrate back and forth on the lines l_1 and l_2 so those disappear. This shows that the integral over C and C_1 is equal.

Now consider the integral over the circle C_1 . Because of the singularity at z_0 , we can not use Cauchy's theorem, so we need another trick to perform this integration. We can start by finding the Laurent series of f around the point z_0

$$f(z) = \sum_{n=0}^{\infty} a_n (z - z_0)^n + \sum_{m=1}^{\infty} \frac{b_m}{(z - z_0)^m}. \quad (2.43)$$

Inserting this into the integral we find

$$\oint_{C_1} dz f(z) = \oint_{C_1} dz \left(\sum_{k=0}^{\infty} a_k (z - z_0)^k + \sum_{m=1}^{\infty} \frac{b_m}{(z - z_0)^m} \right). \quad (2.44)$$

2. Preliminaries

The integral over the first sum vanishes because this is analytic in the entire domain. Changing variables to $w = z - z_0$ and then using that R is constant on C_1 we have $dw = d(Re^{i\theta}) = Re^{i\theta}id\theta$, so that we can write the integral as

$$\oint_{C_1} dz f(z) = \sum_{m=1}^{\infty} ib_m R^{1-m} \int_0^{2\pi} d\theta e^{i\theta(1-m)}. \quad (2.45)$$

The integral over the angle θ vanishes unless $m = 1$. We then get

$$\oint_{C_1} dz f(z) = 2\pi ib_1, \quad (2.46)$$

so the problem is reduced to finding the coefficient b_1 which is known as the residue of $f(z)$ at the point z_0 [36].

In some cases, we do not need to find the whole series to do this. Suppose we can write the function as $f(z) = h(z)/g(z)$ with both $g(z)$ and $h(z)$ being analytic in the interior of C and let $g(z)$ have an n 'th order zero at $z = z_0$ and $h(z_0) \neq 0$. That $g(z)$ has an n 'th order zero means that $g(z_0) = \partial_z g(z)|_{z=z_0} = \dots = \partial_z^{n-1} g(z)|_{z=z_0} = 0$. This means that the first n terms, including the constant, of the Taylor series of $g(z)$ around z_0 vanishes so that we have $g = (z - z_0)^n [g_n + g_{n+1}(z - z_0)^1 \dots] = (z - z_0)^n G(z)$, where $G(z)$ does not have a zero at z_0 . We can now write f as

$$f(z) = \frac{1}{(z - z_0)^n} \frac{h(z)}{G(z)} = \frac{b_n}{(z - z_0)^n} + \frac{b_{n-1}}{(z - z_0)^{n-1}} + \dots + \frac{b_1}{(z - z_0)} + a_0 + \dots \quad (2.47)$$

Here we have used that since $h(z)$ is analytic and non-singular in the domain and $G(z)$ does not have any zeros at z_0 , we have that the fraction $h(z)/G(z)$ does not have any singularities in the domain and can be expanded as a Taylor series (no negative exponent). Since the biggest negative exponent in the Laurent series is $-n$ we have

$$f(z)(z - z_0)^n = b_n + b_{n-1}(z - z_0) + \dots + b_1(z - z_0)^{n-1} + a_0(z - z_0)^n + \dots \quad (2.48)$$

Now we take the derivative of this $n - 1$ times to find

$$\partial_z^{n-1} [f(z)(z - z_0)^n] = (n-1)!b_1 + n!a_0(z - z_0) + \frac{(n+1)!}{2}a_1(z - z_0)^2 + \dots \quad (2.49)$$

If we evaluate this at z_0 , we get the residual b_1 as

$$b_1 = \text{Res}_{z=z_0} f(z) = \frac{1}{(n-1)!} \lim_{z \rightarrow z_0} \partial_z^{n-1} [f(z)(z - z_0)^n], \quad (2.50)$$

which we can put into eq (2.46) to get an expression for the integral. In some cases, the function f has more than one pole inside the contour C . It is then straightforward to generalize this discussion and show that the integral becomes

$$\oint_c dz f(z) = 2\pi i \sum_{i=0}^k \text{Res}_{z=z_i} f(z), \quad (2.51)$$

where z_0, \dots, z_k are the zeros of f encapsulated by the contour. This is known as the residue theorem [36].

Branch cuts Some complex functions are multi-valued. Let us consider the function $f(z) = \sqrt{z}$. Using the polar representation we can write $z = |z|e^{i\theta}$ and the function takes the form $f(|z|, \theta) = \sqrt{|z|}e^{i\theta/2}$. Notice that $\theta = 0$ and $\theta = 2\pi$ is the same point in space, but inserted into f gives $f(|z|, 0) = \sqrt{|z|}$ and $f(|z|, 2\pi) = -\sqrt{|z|}$. Therefore if we follow any path that encircles $z = 0$, which is a branch point, we find that the value of the function will differ depending on how many times the path circles the origin [37]. Since a function should not have more than one value at each point we need to define a branch cut where we specify what the value of the function is in order to make it uniquely defined. This is similar to how we define the square root of a positive real number to be positive. The placement of the branch cut is arbitrary as long as it extends from a branch point. For the above example, we can set $f(z)$ positive on the real axis. Another typical example of a multi-valued function is the complex logarithm $\ln(z)$.

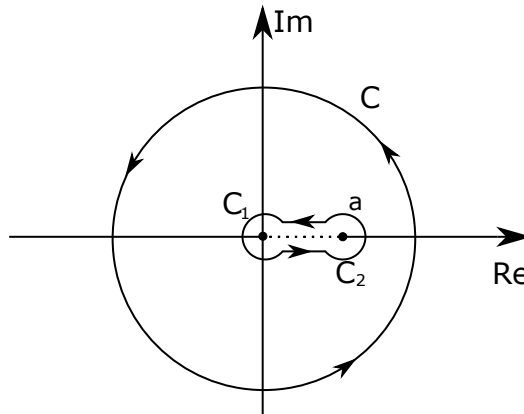


Figure 2.5: Sketch of the contour C and the keyhole contour around the branch cut (dashed line). We map the integral around C in eq. (2.52) to an integral around the keyhole, which consists of two circles C_1 and C_2 centered at the branch points $z = 0$ and a , and the line connecting the circles being ϵ above and below the branch cut.

Here we are going to show a method for solving some integrals that contain a branch cut. Consider the complex function

$$f(z) = \frac{1}{\sqrt{z}\sqrt{z-a}}. \tag{2.52}$$

This function has two branch points at $z = 0$ and $z = a$ which we have assumed to be real. We can therefore make it single-valued by taking a branch cut from 0 to a [37]. Suppose now that we want to consider the integral over a contour C

2. Preliminaries

that encapsulates the branch points as shown in Fig. 2.5. To solve the integral

$$\oint_C dz f(z) \quad (2.53)$$

we use Cauchy's theorem to map it into an integral over the contour made up of the two circles C_1 and C_2 and the lines connecting them. The circles have radius ϵ and the lines are ϵ above and below the branch cut. We can now decompose the integral into

$$\oint_C f(z) = \int_{C_1} dz f(z) - \int_{C_2} dz f(z) + \int_{-i\epsilon}^{a-i\epsilon} dz f(z) + \int_{a+i\epsilon}^{i\epsilon} dz f(z). \quad (2.54)$$

In the limit of $\epsilon \rightarrow 0$ the integrals over the circles C_1 and C_2 vanish. We can show this by considering the one centered at a and changing the variable to $z' = z - a$. The integration variable, z' is on the circle C_2 and can therefore be written as $z' = \epsilon e^{i\theta}$. The integral over the circle C_2 in the limit that its radius ϵ goes to zero is then

$$\lim_{\epsilon \rightarrow 0} \oint_{C_2} dz' \frac{1}{\sqrt{z'}\sqrt{z'+a}} = \lim_{\epsilon \rightarrow 0} \int_0^{2\pi} d\theta \frac{\epsilon i e^{i\theta}}{\sqrt{\epsilon e^{i\theta}}\sqrt{a}} \sim \lim_{\epsilon \rightarrow 0} \sqrt{\epsilon} = 0, \quad (2.55)$$

and similarly for the integral over C_1 . Using now that $f(z)$ is positive above the branch cut and negative below, we can write the integral as

$$\oint_C dz f(z) = -2 \int_0^a \frac{dx}{\sqrt{x}\sqrt{x-a}}, \quad (2.56)$$

which we can solve. In Paper (I) and (V) we do a similar construction to solve the complex part of integrals that have the form shown in eq. 2.38.

Chapter 3

Bose-Einstein Condensates and Topological Defects

In this chapter, we are going to introduce the Bose-Einstein Condensate (BEC) and discuss some of its properties. The condensation of particles following Bose-Einstein statistics is due to the quantum properties of the gas [11]. At low temperatures, the BEC can be described by a semi-classical mean-field approach. We start our discussion by motivating the Gross-Pitaevskii equation as the conservative dynamics of a grand canonical Hamiltonian. We then discuss the BEC's ground state and linear excitations. After this, we introduce the concept of topological defects in BECs before we make a brief generalization of their properties focusing on BEC and nematic liquid crystals. After introducing the topological defects, we will discuss a scheme for tracking their position and use this to derive their kinematics. The chapter then ends with a discussion of vortex kinematics.

3.1 Bose-Einstein condensation and the Gross-Pitaevskii equation

Bose-Einstein condensates form in gasses of particles obeying Bose-Einstein statistics when they are cooled below a critical temperature T_c [11]. This phase is characterized by having a macroscopic occupation of the ground state N_0 , meaning that the fraction of particles in the ground state N_0/N stays finite in the thermodynamic limit $N \rightarrow \infty$. The Bose gas can in the second quantization be described by a grand canonical Hamiltonian given by [38–40]

$$\hat{K} = \hat{H} - \mu\hat{N} = \int d\mathbf{r} \left[\frac{\hbar^2}{2m} \nabla\hat{\Psi}^\dagger(\mathbf{r}) \cdot \nabla\hat{\Psi}(\mathbf{r}) + \mathcal{U}(\mathbf{r})\hat{\Psi}^\dagger(\mathbf{r})\hat{\Psi}(\mathbf{r}) - \mu\hat{\Psi}^\dagger(\mathbf{r})\hat{\Psi}(\mathbf{r}) \right] \quad (3.1)$$
$$+ \frac{1}{2} \int d\mathbf{r} \int d\mathbf{r}' \hat{\Psi}^\dagger(\mathbf{r})\hat{\Psi}^\dagger(\mathbf{r}')v(\mathbf{r} - \mathbf{r}')\hat{\Psi}(\mathbf{r})\hat{\Psi}(\mathbf{r}'),$$

where $\hat{\Psi}(\mathbf{r}), \hat{\Psi}^\dagger(\mathbf{r})$ are the bosonic field operators, μ is the chemical potential, m is the particle mass, $v(\mathbf{r} - \mathbf{r}')$ is the two-body interatomic potential and $\mathcal{U}(\mathbf{r})$ is an external potential, e.g., a harmonic trap. The field operator can be decomposed into $\hat{\Psi} = \hat{\psi} + \hat{\phi}$, with $\hat{\psi}$ and $\hat{\phi}$ being the operators for the ground state and excited states respectively.

Below the critical temperature for condensation the occupation of the ground state has become macroscopic $\langle \hat{\psi}\hat{\psi}^\dagger \rangle = N_0 \gg 1$ making it much larger than the

3. Bose-Einstein Condensates and Topological Defects

commutator $[\hat{\psi}, \hat{\psi}^\dagger] = 1$. Because of this, the mistake we make by ignoring the commutation relation is negligible and we can replace the quantum field with a complex field ψ . This approximation where we treat the ground state as a classical field is known as the Bogoliubov prescription [38]. If we in addition neglect all the excited states, the Hamiltonian becomes

$$K = \int d\mathbf{r} \left[\frac{\hbar^2}{2m} \nabla\psi^* \cdot \nabla\psi + (\mathcal{U} - \mu)|\psi|^2 + \frac{g}{2}|\psi|^4 \right]. \quad (3.2)$$

We have here assumed that the gas is dilute so that the two-body interaction potential is well described by a delta function $v(\mathbf{r} - \mathbf{r}') = g\delta(\mathbf{r} - \mathbf{r}')$, with g being the interaction strength. The BEC at zero temperature satisfies conservative dynamics and we can find the evolution equation of the macroscopic wave function as [39]

$$i\hbar\partial_t\psi = \frac{\delta K}{\delta\psi^*} = \left[-\frac{\hbar^2}{2m}\nabla^2 + \mathcal{U} - \mu + g|\psi|^2 \right] \psi. \quad (3.3)$$

This is known as the Gross-Pitaevskii equation (GPE). Note that the complex wave function $\psi = |\psi|e^{i\phi}$ has in the ground state a coherent phase and therefore breaks the rotational symmetry of the isotropic gas. The broken symmetry is here an $U(1)$ symmetry which is isomorphic to $SO(2)$ as discussed in Chapter 2.

The damped GPE As discussed above, one gets the GPE by neglecting the excited states making it a zero-temperature approximation. At any finite temperature, there will be some occupation in the excited states and hence interactions between the condensate and the thermal cloud. One can take these interactions into account by treating the atoms above an energy cutoff ϵ as a thermal reservoir which we will refer to as the thermal cloud or the normal gas. This leads to the Stochastic projected GPE [41, 42], or the Stochastic GPE [42–44] depending on which assumptions are made for the condensate and the thermal cloud. Both approaches lead to the dissipation of energy from the condensate into the normal gas, and when neglecting the noise, both reduces to the damped GPE (dGPE)

$$i\hbar\partial_t\psi = (1 - i\gamma) \left[-\frac{\hbar^2}{2m}\nabla^2 + \mathcal{U} - \mu + g|\psi|^2 \right] \psi. \quad (3.4)$$

The parameter $\gamma \geq 0$ is a function of temperature, chemical potential and the energy of the thermal cloud [45]. It is typically very small $\gamma \ll 1$. The addition of the damping parameter γ causes energy to dissipate from the system. We can see this by taking the time derivative of the Hamiltonian and using the dGPE [46, 47]

$$\partial_t K = \int d\mathbf{r} \left(\frac{\delta K}{\delta\psi} \partial_t\psi + \frac{\delta K}{\delta\psi^*} \partial_t\psi^* + \frac{\delta K}{\delta\mathcal{U}} \partial_t\mathcal{U} \right)$$

$$\begin{aligned}
 &= \int d\mathbf{r} \left(\frac{\delta K}{\delta\psi} \frac{1 - i\gamma}{i\hbar} \frac{\delta K}{\delta\psi^*} + \frac{\delta K}{\delta\psi^*} \frac{1 + i\gamma}{i\hbar} \frac{\delta K}{\delta\psi} + \frac{\delta K}{\delta\mathcal{U}} \partial_t \mathcal{U} \right) \\
 &= -\frac{2\gamma}{\hbar} \int d\mathbf{r} \left| \frac{\delta K}{\delta\psi^*} \right| + \int d^d |\psi|^2 \partial_t \mathcal{U}.
 \end{aligned} \tag{3.5}$$

The first term is negative and will dissipate energy out of the condensate, while the second term makes it possible to inject energy into the condensate by making the potential time-dependent. This is utilized in Paper (III) where we use a repulsive Gaussian stirring potential to study the nucleation of defects. The repulsive potential reduces the condensate density, $|\psi|^2$, under it. When it moves, above a critical velocity (see Section 3.2), it pushes a compressible wave in front of itself while leaving a diluted wake behind [46, 48]. The density $|\psi|^2$ is, therefore, a bit higher in front of the potential where the time derivative of the potential is positive and lower behind where the derivative is negative. Stirring the condensate thus leads to additional energy being added. We use this to make topological excitations in the condensate.

Dimensionless units To make the analysis of the dGPE more convenient, we will introduce dimensionless units to ease the notation [46, 47]. We, therefore, set the unit for energy to the chemical potential μ , and the unit for velocity is set to $c = \sqrt{\mu/m}$, which we will see is the speed of the long wavelength linear excitations [39]. We measure lengths in units of the healing length $\xi = \hbar/\sqrt{m\mu}$. Having a unit for length and velocity, we get that the unit of time has to be $\tau = \xi/c$. In these units, the equation reads

$$i\partial_t \psi = (1 - i\gamma) \left[-\frac{1}{2} \nabla^2 + \mathcal{U} - 1 + \frac{g}{\mu} |\psi|^2 \right] \psi. \tag{3.6}$$

We further simplify this by rescaling the wave function to $\psi \rightarrow \sqrt{\frac{g}{\mu}} \psi$, and thus obtain a dimensionless equation with the thermal dissipation γ being the only tunable parameter

$$i\partial_t \psi = (1 - i\gamma) \left[-\frac{1}{2} \nabla^2 + \mathcal{U} - 1 + |\psi|^2 \right] \psi. \tag{3.7}$$

The Hamiltonian in these units becomes

$$K = \int d\mathbf{r} \left[\frac{1}{2} \nabla\psi^* \cdot \nabla\psi + (\mathcal{U} - 1)|\psi|^2 + \frac{1}{2} |\psi|^4 \right]. \tag{3.8}$$

3.2 Ground state and linear modes

We are now going to look for the ground state of the system which we can find by minimizing the Hamiltonian. To find this state, we first rewrite the grand

3. Bose-Einstein Condensates and Topological Defects

canonical Hamiltonian eq. (3.2) to

$$K = \int d\mathbf{r} \left[\frac{\hbar^2}{2m} \nabla\psi^* \cdot \nabla\psi + \frac{\mu^2}{2g} \left[\frac{g}{\mu} |\psi|^2 + \left(\frac{1}{\mu} \mathcal{U} - 1 \right) \right]^2 \right], \quad (3.9)$$

by completing the square and ignoring a constant in the energy. We have assumed that \mathcal{U} does not vary in time. We now assume that the ground state is varying slowly in space so that we can ignore the gradient term. The Hamiltonian is now lowest when the integrand

$$\frac{\mu^2}{2g} \left[\frac{g}{\mu} |\psi|^2 + \left(\frac{1}{\mu} \mathcal{U} - 1 \right) \right]^2 \quad (3.10)$$

is as small as possible. If $\mathcal{U} > \mu$ both terms in the bracket are positive so the minimum is when $|\psi|^2 = 0$, while if $\mathcal{U} < \mu$ we get that the minimum is

$$\rho_{TF} = |\psi_{TF}|^2 = \frac{\mu - \mathcal{U}}{g}, \quad (3.11)$$

since this makes the integrand zero. This is the Thomas-Fermi ground state [39, 49]. In Fig. 3.1, we have plotted it against a numerical estimate for the ground state of a BEC in a harmonic trap.

This approximation is decent in the bulk but breaks down at the edges of the condensate where the neglected gradients become large. We can see this by inserting the harmonic potential $\mathcal{U} \sim r^2$ into eq. (3.11). It becomes

$$\psi_{TF} = \sqrt{\frac{\mu}{g}} \sqrt{1 - \frac{r^2}{R_{TF}^2}}, \quad (3.12)$$

where R_{TF} , known as the Thomas-Fermi radius, is the radius where the ground state vanishes. The squared gradient of this wave function is

$$|\nabla\psi_{TF}|^2 = \frac{\mu}{g} \frac{r^2}{R_{TF}^4 - R_{TF}^2 r^2}. \quad (3.13)$$

This diverges in the limit $r \rightarrow R_{TF}$, breaking the assumption that the gradient term in the Hamiltonian eq. (3.9) is small. We also see from eq. (3.13) that the approximation holds better in the bulk when the Thomas-Fermi radius is large. Noticing that if we change the time in the GPE to imaginary time $t \rightarrow i\tau$ the equation becomes dissipative. We can therefore use the Thomas-Fermi ground state as a starting point for numerical simulations and find a lower energy state by evolving the GPE in imaginary time.

Linear excitations We now set $\mathcal{U} = 0$ and consider linear excitations to the ground state. We start by writing the wave function as [39, 47]

$$\psi = \psi_0 + \delta\psi, \quad (3.14)$$

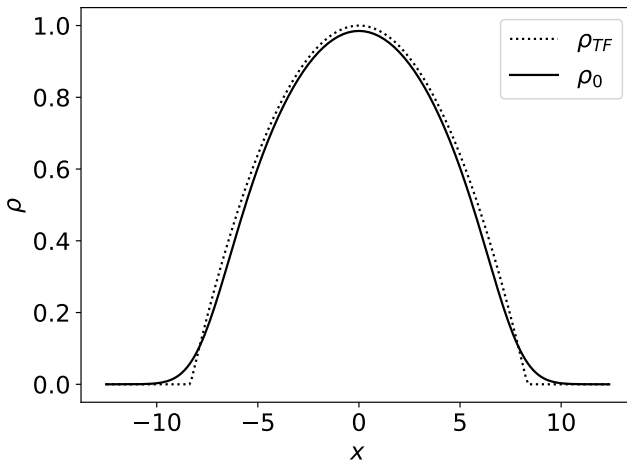


Figure 3.1: Plot of the density of the Thomas-Fermi ground state ρ_{TF} (dotted line) against that of a numerically obtained ground state ρ_0 (solid line) for a harmonic potential $\mathcal{U} \sim r^2$. ρ_0 is found by evolving the GPE in imaginary time as described in the text.

with $\psi_0 = 1$ being the homogeneous ground state in dimensionless units and $\delta\psi$ are linear excitations to this state. Putting this into the dimensionless dGPE we can find a linear equation for the excitations as

$$\partial_t \delta\psi = (i + \gamma) \left[-\frac{1}{2} \nabla^2 \delta\psi + (\mathcal{U} + 1) \delta\psi + \delta\psi^* \right]. \quad (3.15)$$

Writing the perturbation as plane waves, $\delta\psi = u(r)e^{-i\omega t} + v(r)e^{i\omega^* t}$, doing a Fourier transform in space and using that $e^{i\omega^* t}$ and $e^{-i\omega t}$ are linearly independent we get the following system of equations

$$\begin{bmatrix} \omega - (1 - i\gamma)[\frac{1}{2}k^2 + 1] & -(1 - i\gamma) \\ -(1 + i\gamma) & -\omega - (1 + i\gamma)[\frac{1}{2}k^2 + 1] \end{bmatrix} \begin{bmatrix} \tilde{u}(k) \\ \tilde{v}(k) \end{bmatrix} = 0. \quad (3.16)$$

We are interested in those frequencies that have non-trivial solutions. Therefore we look for the frequencies where the determinant of this matrix vanishes. This results in the following dispersion relation

$$\omega = -i\gamma \left(1 + \frac{1}{2}k^2 \right) + \sqrt{\frac{1}{2}k^2 \left(2 + \frac{1}{2}k^2 \right) - \gamma^2}. \quad (3.17)$$

The first term is an exponential damping due to the dissipative factor γ . Notice that it increases quadratically with wavenumber so that small wavelength

3. Bose-Einstein Condensates and Topological Defects

perturbations are damped faster. The real part of the dispersion relation is giving the frequency of the oscillations and can be used to find the velocity of the waves. In the zero temperature limit $\gamma = 0$ the imaginary part of the dispersion relation vanishes and we get

$$\omega(k) = k\sqrt{1 + \frac{1}{4}k^2}, \quad (3.18)$$

which is plotted as the solid line in Fig. 3.2. This is called the Bogoliubov Spectrum [39].

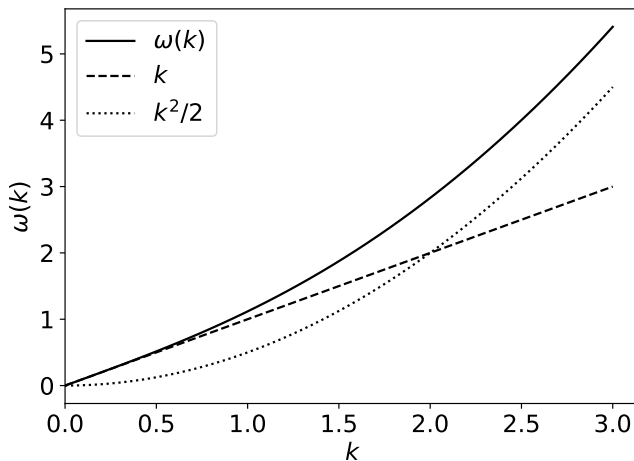


Figure 3.2: Figure of the dispersion relation (solid line) given in eq. (3.18). The dashed line is the phonon dispersion $\omega = k$ (in dimensionless units) and is due to the interaction term in the Hamiltonian eq. (3.2). The dotted line is the spectrum of a free particle $\omega = k^2/2$.

By squaring and inserting back the units we can get a better understanding of where the terms come from

$$(\hbar\omega)^2 = 2g\rho_0 \frac{\hbar^2 k^2}{2m} + \left(\frac{\hbar^2 k^2}{2m} \right)^2. \quad (3.19)$$

The first term is due to the interaction term in the Hamiltonian eq. (3.2), and in the next section we are going to show that it is this term that makes the BEC a superfluid. For small k it is this term that is dominant and the dispersion relation becomes $\omega = ck$, which is the dispersion relation of acoustic phonons. We see that the speed of the excitations is $c = \sqrt{\mu/m}$, which is what we used as the unit for velocity when introducing the dimensionless units. In the other limit of large k , the spectrum becomes that of a free particle $\hbar\omega = \hbar^2 k^2/2m$. The small/large k asymptotes are shown as the dashed/dotted line in Fig. 3.2.

3.3 Hydrodynamic description and superfluidity

In this section, we want to use the dGPE to map the hydrodynamic description of the condensate into the Navier-Stokes equation eq. (2.29) and introduce the quantum pressure discussed in Paper (IV). To do this, we will use the Madelung transform $\psi = \sqrt{\rho}e^{i\phi}$ [39, 42], with $\rho = |\psi|^2$ being the condensate density and ϕ being the argument of the wave function. At zero temperature, $\gamma = 0$, the condensate density is a conserved quantity that satisfies the conservation equation [39]

$$\partial_t \rho + \nabla \cdot \mathbf{J} = 0. \quad (3.20)$$

Using the GPE to find an expression for $\partial_t \rho$, we get that the conserved current density is

$$\mathbf{J} = \text{Im}(\psi^* \nabla \psi) = \rho \nabla \phi = \rho \mathbf{v}, \quad (3.21)$$

where we have identified the superfluid velocity as $\mathbf{v} = \nabla \phi$. That the velocity field can be written as the gradient of a scalar field is something we will discuss more in the next section. If we now insert the Madelung transformation into the dGPE, multiply with ψ^* , and use that the real and the imaginary part are independent, we get the equations

$$\partial_t \rho + \nabla \cdot (\rho \mathbf{v}) = 2\gamma \rho (1 - \mathcal{U}_{eff}), \quad (3.22)$$

$$\partial_t \phi = 1 - \mathcal{U}_{eff} + \rho + \frac{\gamma}{2\rho} \nabla \cdot (\rho \mathbf{v}). \quad (3.23)$$

Notice that eq. (3.22) shows that the consequence of having non-zero γ is that the particle number is not conserved. The source term on the right-hand side drives the system towards particle number equilibrium with the thermal cloud [42, 47], which is reached when $\mathcal{U}_{eff} = 1$ or $\mathcal{U}_{eff} = \mu$ in real units. The effective potential is

$$\mathcal{U}_{eff} = \frac{v^2}{2} + \mathcal{U} + \rho - \frac{1}{2} \frac{\nabla^2 \sqrt{\rho}}{\sqrt{\rho}}, \quad (3.24)$$

with the last part being the quantum pressure. This pressure is usually small unless ρ changes rapidly [42]. We use the quantum pressure in Paper (IV) to visualize the non-linear excitations that are created during an annihilation event.

Taking now the gradient of eq. (3.23), we get

$$\partial_t \mathbf{v} = -\nabla \frac{v^2}{2} - \nabla(\mathcal{U} + \rho) + \frac{1}{2} \nabla \frac{\nabla^2 \sqrt{\rho}}{\sqrt{\rho}} + \frac{\gamma}{2\rho} \nabla \nabla \cdot (\rho \mathbf{v}). \quad (3.25)$$

Assuming there are no phase singularities so that we can neglect terms that include the curl of the velocity and that the condensate is slowly varying, we arrive at [42, 46]

$$\partial_t \mathbf{v} - \mathbf{v} \cdot \nabla \mathbf{v} = -\nabla(\mathcal{U} + \rho) + \frac{\gamma}{2} \nabla^2 \mathbf{v}. \quad (3.26)$$

This is the Navier-Stokes equation with the pressure $(\mathcal{U} + \rho)$ and the viscosity $\nu = \gamma/2$. In the zero temperature limit $\gamma = 0$ this reduces to the Euler equation

3. Bose-Einstein Condensates and Topological Defects

for an ideal fluid [39]. The related Hamiltonian can be found by inserting the Madelung transformation into eq. (3.8)

$$K = \int d\mathbf{x} \left[\frac{1}{2} \rho v^2 + \frac{1}{8} \frac{|\nabla \rho|^2}{\rho} + \mathcal{U} \rho + (\rho^2 - 1)^2 \right]. \quad (3.27)$$

Note that here, \mathcal{U} is not restricted to be stationary and so including it in the quadratic term as we did in eq. (3.9) would lead to an additional $-U^2$ term that we cannot remove. The first term in the Hamiltonian is the kinetic energy, the second gives the energy due to density distortions, the third is the energy due to the external potential and the last term is balancing the interaction and chemical potential [46, 47].

Superfluidity That the hydrodynamic equations reduce to the Euler equation for ideal fluids in the limit when the velocity is curl-free and the density is slowly varying hints at another property of the weakly interacting BEC, namely, its ability to sustain frictionless flows at zero temperature. This ability is due to the interaction term in the Hamiltonian, and we will show here that a BEC consisting of non-interacting free particles will not experience any superfluidity. We start by assuming that the BEC is at zero temperature, $\gamma = 0$, and flowing in a tube at velocity \mathbf{v} . If there is friction between the condensate and the walls, this will induce energy into the BEC, but since this is a quantum fluid the energy has to be induced in the form of elementary excitations [40, 50]. In the system that is moving with the liquid, the excitation has an energy $\epsilon(\mathbf{P})$ and momentum p , so that the energy and momentum of the fluid become $E = \epsilon(p) + E_0$ and $\mathbf{P} = \mathbf{p}$ in this reference frame. We now transform to the frame that is stationary with respect to the tube. The energy and momentum in the new frame is

$$E' = E + \mathbf{P} \cdot \mathbf{v} + \frac{1}{2} M v^2, \quad (3.28)$$

$$\mathbf{P}' = \mathbf{p} + M \mathbf{v}, \quad (3.29)$$

with M being the mass of the condensate. We have here used the transformation laws for a fluid, where the first follows from the kinetic term in the Hamiltonian eq. (3.27) and the second is trivial. The energy of the excitation in the frame where the tube is stationary is then

$$\epsilon(p) + \mathbf{p} \cdot \mathbf{v}. \quad (3.30)$$

In order for the creation of excitations to be spontaneous the energy has to be lowered after its creation. We, therefore, get the requirement

$$\epsilon(p) + \mathbf{p} \cdot \mathbf{v} < 0. \quad (3.31)$$

This means that the lowest velocity that can spontaneously create excitations is given as

$$v_c = \min_p \frac{\epsilon(p)}{p}. \quad (3.32)$$

This is the Landau critical velocity [40, 47, 50]. From eq. (3.19) we find that we can write the energy spectrum of the excitations as

$$\epsilon(p) = \frac{p}{\sqrt{2m}} \sqrt{\frac{p^2}{2m} + 2g\rho_0} \quad (3.33)$$

in physical units.

In Fig. 3.3 we have plotted $\epsilon(p)/p$ setting $2m = \rho_0 = 1$ for different values of g . Using this energy spectrum, we see that ϵ/p has a minimum at $p = 0$ so that the critical velocity becomes

$$v_c = c. \quad (3.34)$$

Here $c = \sqrt{\mu/m}$ is the velocity we used to make the dGPE, eq. (3.7), dimensionless, and we saw in the previous section that it is the velocity of the long wavelength excitation. If we ignore the interaction and instead use the dispersion relation for free particles $\hbar\omega = \hbar^2 k^2 / 2m$, we get $v_c = 0$, which can also be seen from Fig. 3.3. The ideal Bose gas is thus not a superfluid [50].

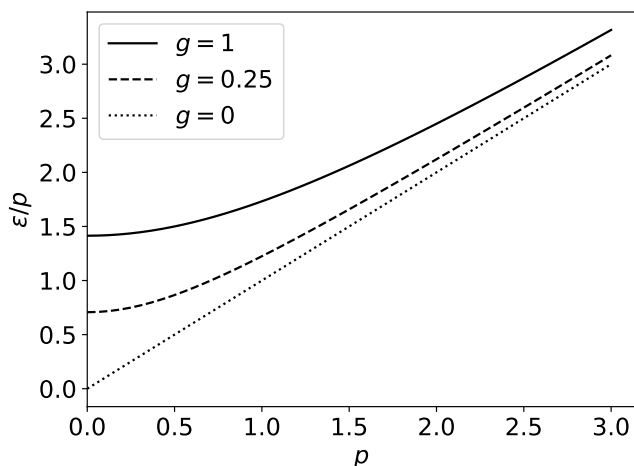


Figure 3.3: Plot of ϵ/p for different values of the interaction strength g . The minimum at $p = 0$ decreases with g and for non-interacting particles, $g = 0$, the minimum goes to zero, meaning that the ideal BEC is not a superfluid. We have fixed the parameters to $2m = \rho_h = 1$. Figure inspiration from [47].

This critical velocity holds well also for condensates that are stirred by a weak Gaussian potential [47, 48, 51, 52]. That is a potential of the form

$$\mathcal{U}_s = g_s e^{-(\mathbf{r}-\mathbf{r}_s)^2/d_s^2}. \quad (3.35)$$

If the potential strength g_s is not too large, the potential will only be able to create perturbations in the form of phonons. However, if g_s and d_s are large enough, it will also be able to excite topological defects in the form of quantized vortices into the condensate. Since the vortices are non-linear excitations, it is hard to find an analytical expression for the critical velocity for vortex formation. It can be done in the limit of solid/impenetrable obstacles [53–55], but for penetrable obstacles like the Gaussian it has to be measured experimentally or numerically [23, 56]. In Paper (III) we study numerically the onset of nucleation close to the critical point, with a focus on how the phase slip forms and develops a core.

3.4 Topological defects

We are now going to consider the topological defects in a BEC, which take the form of quantized vortices. From the hydrodynamic description, we saw that the superfluid velocity is the gradient of the phase $\mathbf{v} = \nabla\phi$. This has the consequence that the vorticity $\omega = \nabla^\perp \cdot v$, with $\nabla^\perp = (\partial_y, -\partial_x)$ is the rotated gradient, has to vanish unless the phase is singular. These singular points are the topological defects of the condensate. If we consider an integral of the phase around a closed curve C , the integral has to be an integer multiple of 2π due to the wavefunction being single-valued. We can then define the topological charge q as [9, 39, 40, 46, 47]

$$\int_C d\phi = \int_C d\mathbf{l} \cdot \nabla\phi = 2\pi q. \quad (3.36)$$

Moreover, as long as ϕ is smooth, we can deform C continuously without changing the integral because it can only take discrete values. In the same way, we can not change the result by applying continuous deformations on the phase θ . It can only change discontinuously as we move the curve through the phase singularity. Imagine now that we shrink the contour to a point without moving it through any discontinuities in the phase. For eq. (3.36) to hold when C is shrunk to a point, the gradient has to become infinitely large, meaning that this point is a phase singularity [21]. If there is more than one singularity inside the curve, we continuously deform the curve into smaller curves, C_i , containing one singularity each. The integral then becomes

$$\int_C d\mathbf{l} \cdot \nabla\phi = \sum_i \int_{C_i} d\mathbf{l} \cdot \nabla\phi = 2\pi \sum_i q_i, \quad (3.37)$$

meaning that the topological charge is additive. The sum is here over all defects contained in C . Eq. (3.36) is a topological constraint on the singularity, which is why we call it a topological defect. This constraint also implies that the defects of the lowest charge are stable because there is no way for them to gradually decrease in strength. They can only be removed by migrating out of the condensate or by annihilation with an oppositely charged defect.

3.4.1 Minimal manifold and homotopy theory

For a two-dimensional BEC, the topological defects are points-like [9, 21], because we can continuously deform the loop into a point. In three dimensions the vortex is line-like, which can be seen from a similar argument. Consider a point defect in the condensate. If we now put a loop C around the vortex and assume that the integral of the phase around the loop is $2\pi q$ with q non-zero. It is now fairly easy to deform the loop to a point that does not contain the singularity by deforming out of the plane. The integral over the loop is then zero since it is over a point that is not singular. Since the integral can only change value discretely when the line goes through a singularity, it means that it also had to start out as zero. This is a contradiction, which implies that there is no point defect for a complex order parameter in three-dimensional space. If we instead start out with a line defect centered in the loop, then there is no way to continuously deform the path C so that it does not contain the singularity, without passing through the line.

We want to discuss what types of defects are stable for a general order parameter, and start by introducing an order parameter space \mathcal{M} which is the ground state manifold of the order parameter [9, 21]. By ground state manifold we mean the space of parameters that leaves the equilibrium energy invariant, which for vector order parameters will be the angles. For a two-dimensional vector order parameter \mathcal{M} is then the unit circle \mathcal{S}_1 , while for a three-dimensional order parameter, it is the unit sphere \mathcal{S}_2 . In general a n dimensional vector order parameter \mathcal{M} is the n dimensional unit sphere \mathcal{S}_{n-1} , provided that the order parameter has the symmetries of a normal vector. For a vector order parameter with the minimal manifold being the unit sphere, \mathcal{S}_{n-1} , the dimension of the defect core will be set by the dimension of the order parameter n , and the dimension of the space d . For the condensate $n = 2$ since the wave function can be mapped to a two-dimensional vector order parameter.

From the dimension of the space d and the dimension of the defect core d_c one can define the codimension $d' = d - d_c$ [9, 21]. When the minimal manifold is \mathcal{S}_{n-1} the defect is stable if $d' = n$. From this, we see that in two dimensions, $d = 2$, with a two-dimensional order parameter, $n = 2$, $d_c = 0$ should be stable and the defect is thus point-like. In three dimensions $d_c = 1$ should be stable, corresponding to a line-like defect. The line defect has to either form a loop or extend to the edges of the system in order for the defect to be topologically protected by eq. (3.36). We also see that if we have a three-dimensional vector order parameter in three dimensions, then the topological defects would be point-like with core dimension $d_c = 0$. The codimension of the defects is a fast way of determining its stability, but it does not always work if the minimal manifold of the order parameter is not \mathcal{S}_{n-1} . An example of this is the existence of line defects, $d' = 2$, in three-dimensional nematics, where the order parameter is the director field with $n = 3$. The reason for this is that the order parameter of the nematic is headless vectors, meaning

3. Bose-Einstein Condensates and Topological Defects

that they are symmetric to rotations of π instead of 2π . The minimal manifold is therefore not \mathcal{S}_2 , but \mathcal{P}_2 which is the sphere with antipodal points identified [9].

To get insight into why the defects are stable, consider a map from coordinate space to the order parameter space. In three dimensions this could just be the angles of the order parameter, ϕ and θ , evaluated at some position in space. In order for the defect to be topologically protected the map from a line or surface in the d dimensional coordinate space to the $n - 1$ dimensional order parameter space (minimal manifold) has to be impossible to shrink down to a point by doing continuous deformations. If we use the angles ϕ and θ to map a curve in coordinate space to the order parameter space, it will map to a closed curve. Why an order parameter with the minimal manifold \mathcal{S}_2 has no stable line defects in three dimensions can then be seen from Fig. 3.4 a). Any closed curve on the two-sphere can be "rolled" off to one of the poles and shrunk to a point. The point represents a homogeneous order parameter in real space. A point defect in this order parameter is stable since if one puts a closed surface around the defect, then the angle of the order parameter on the surface will map out the entire two-sphere. It is not possible to shrink the surface covering the two-sphere down to a point by continuously deforming it.

The line defects in the three-dimensional nematic are stable because antipodal points on \mathcal{P}_2 are identified, which allows us to make closed curves on the surface that it is not possible to remove continuously. These are the curves that start at one pole and end on the other as shown in Fig. 3.4 b). These curves are the maps from paths that encircle the $1/2$ defects. Interestingly in the three-dimensional nematic, only the $1/2$ defect is stable [9]. This is because the integer defects can be deformed to a point and all half-integer defects, i.e. the ones that circle multiple times around the \mathcal{P}_2 , can be deformed continuously to the $1/2$ defect.

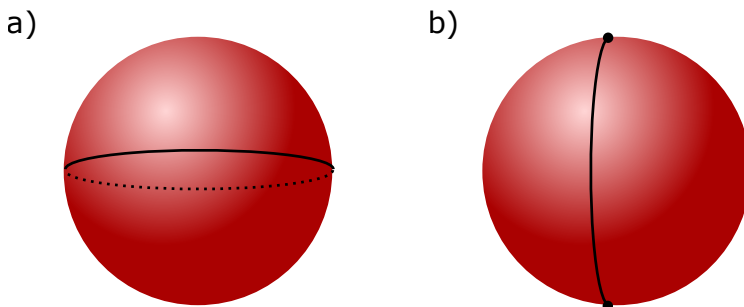


Figure 3.4: a) shows a closed curve on \mathcal{S}_2 . This curve can be continuously deformed to a point and is therefore not a defect. b) shows a closed curve \mathcal{P}_2 which we are not able to deform into one point since the endpoints are identified.

Homotopy theory Above we discussed that when we map a closed loop or surface around a topological defect in coordinate space to the minimal manifold, it results in a closed loop or surface that is impossible to remove by continuous deformations. This allows us to use homotopy theory to classify and identify topological defects [9, 11, 21, 57]. Two curves f_1 and f_2 are homotopic if we can continuously deform them into each other. The loop shown in Fig. 3.4 a) is therefore homotopic with a point placed anywhere on the sphere, corresponding to a state where all the vectors in real space are parallel. For the two-dimensional Bose-Einstein condensate, all curves in real space that do not circle a vortex will map to a curve on the minimal manifold that is homotopic to a state where the wave function is a constant.

Topological defects can be classified by the homotopy class of the surface that it maps out in the minimal manifold. For example, the homotopy class of point defects in the two-dimensional BEC is indexed by the winding number, because this gives how many times the curve wraps \mathcal{S}_1 [9]. If the order parameter has the minimal manifold \mathcal{S}_2 all maps from closed loops will be homotopic since they can be deformed to a point. If we instead put a closed surface around the defect, we find that the homotopy classes are indexed by how many times the map covers \mathcal{S}_2 . The nice thing about the homotopy classes is that they give a straightforward way of adding defects. Consider two defects in the two-dimensional condensate with winding numbers $+2$ and -1 . In order parameter space this corresponds to one curve that loops around \mathcal{S}_1 two times counterclockwise and one curve that loops around once clockwise. Deforming these paths into each other, we find that this is the same as looping around once counterclockwise, i.e. a $+1$ defect.

So the paths of the homotopy classes have an operator, the combination of curves in the above example, that acts on two elements and returns a curve of a different homotopy class. It turns out that the set of homotopy classes is a group [9]. Moreover, the group associated with the loops around \mathcal{S}_1 is simply the signed integers \mathbb{Z} with normal addition, so to combine defects in this order parameter, we just add the winding numbers. This is the main advantage of homotopy theory, we get a group structure that tells us how defects are combined [9, 57]. We can now define the first homotopy group of the minimal manifold \mathcal{M} , which we write as $\pi_1(\mathcal{M})$, as the group associated with closed curves in \mathcal{M} . For a three-dimensional vector order parameter all loops are equal so we have $\pi_1(\mathcal{S}_2) = 0$, i.e. the group only consists of one element, the identity. The m 'th homotopy group of the manifold \mathcal{M} , $\pi_m(\mathcal{M})$, is the group associated with the closed m dimensional surface in \mathcal{M} . If \mathcal{M} is the two-sphere then $\pi_2(\mathcal{S}_2) = \mathbb{Z}$, and in general for the i spheres we have that

$$\pi_i(\mathcal{S}_i) = \mathbb{Z}, \quad (3.38)$$

$$\pi_j(\mathcal{S}_i) = 0, \quad i < j. \quad (3.39)$$

This is why the stable defects in such systems are those where $d' = n$. Since the only stable line defect in the three-dimensional nematic is the $1/2$ it follows

3. Bose-Einstein Condensates and Topological Defects

that the first homotopy group is the integers modulo 2, $\pi_1(\mathcal{P}_2) = \mathbb{Z}_2$ [9]. For two-dimensional nematics, the minimal manifold is the unit circle with opposite points identified, \mathcal{P}_1 . Here all loops with half-integer winding numbers are stable and the first homotopy group is \mathbb{Z} [9]. We are going to come back to these defects in the next chapter.

3.4.2 Core structure and far-field energy

As we have seen, the vortices are singularities in the phase. To avoid divergences in the energy the superfluid density ρ has to go to zero at the defect's position. The region where the defect goes from the far-field value, which for a homogeneous condensate in dimensionless units is $\rho = 1$, to zero at the singularity is called the core of the defect. Having zero density is energetically unfavorable so the core region will not extend far into the condensate. From the Hamiltonian eq. (3.9), the energy penalty of a core with radius ℓ_c is in two dimensions proportional to $\mu^2 \ell_c^2 / (2g)$, which has to be balanced by the kinetic term which for a linear increase in $|\psi|$ from 0 to the far-field value given by the Thomas-Fermi ground state is proportional to $\mu \hbar^2 / (2mg)$. This should balance so the core size is roughly $\ell_c \sim \hbar / \sqrt{\mu m}$, i.e., it is of the size with the healing length.

The core structure of the defects is given by the Gross-Pitaevskii equation. Consider a stationary vortex of charge q centered at the origin in an otherwise unperturbed condensate in two dimensions. The stationary GPE is

$$\left[-\frac{1}{2} \nabla^2 - 1 + |\psi|^2 \right] \psi = 0. \quad (3.40)$$

To solve this, we will assume that the vortex is radially symmetric and use the ansatz $\psi_0(r, \theta) = \chi(\mathbf{r}) e^{iq\theta}$ [21, 39]. Writing the stationary GPE in polar coordinates, we find

$$-\frac{1}{2} \left(\partial_r^2 + \frac{1}{r} \partial_r + \frac{1}{r^2} \partial_\theta^2 \right) [\chi(\mathbf{r}) e^{iq\theta}] - \chi(\mathbf{r}) e^{iq\theta} + \chi^3(\mathbf{r}) e^{iq\theta} = 0. \quad (3.41)$$

This we can rewrite to

$$r^2 \partial_r^2 \chi(r) + r \partial_r \chi(r) - q^2 \chi(r) = 2r \chi(r) (\chi^2(r) - 1), \quad (3.42)$$

with the boundary conditions $\chi(0) = 0$ and $\lim_{r \rightarrow \infty} \chi(r) = 1$. This equation is not analytically solvable, but close to the singularity we can neglect the right-hand side. The resulting equation is

$$r^2 \partial_r^2 \chi(r) + r \partial_r \chi(r) - q^2 \chi(r) = 0. \quad (3.43)$$

This is the Euler-Cauchy equation [36]. Using the boundary condition, $\chi(0) = 0$, we find that it has the solution $\chi(r) = \Lambda r^{|q|}$, where Λ is a constant that can be determined numerically. In Ref. [42] they found that the constant for $|q| = 1$ is

$\Lambda^2 \approx 0.68$.

We can find an approximation of the core structure of the form [21, 58]

$$\chi_0^2(r) = \frac{A(r)}{B(r)} = \frac{a_0 + a_1 r + a_2 r^2}{1 + b_1 r + b_2 r^2}, \quad (3.44)$$

by matching the asymptotes (i) $\chi^2(r \rightarrow 0) = \Lambda^2 r^2$ and (ii) $\chi^2(r \rightarrow \infty) = 1$. We find that the core is approximately given as

$$\chi_0^2(r) = \frac{\Lambda^2 r^2}{1 + \Lambda^2 r^2}, \quad (3.45)$$

which has the correct asymptotic behavior. This can be seen in Fig. 3.5 where we have plotted this approximation against the profile from a numerical simulation.

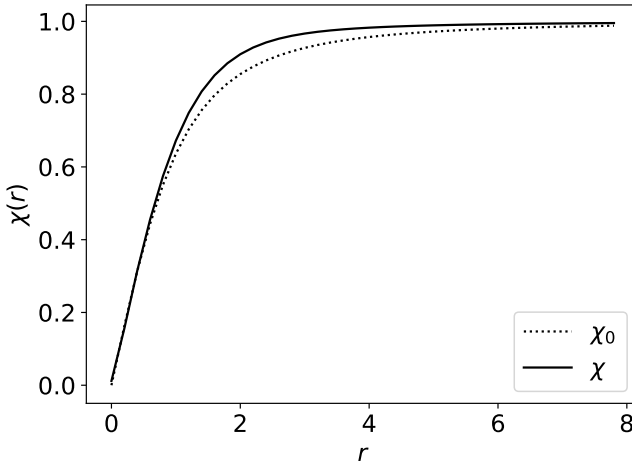


Figure 3.5: Plot of the analytical estimate of the core function $\chi_0(r)$ (dotted) obtained by matching the asymptotes against the vortex profile $\chi(r)$ (solid) taken from numerical simulations.

Far-field energy From the discussion in sec. 3.4.1, we saw that we could combine two vortices of charge +1 into one vortex of charge +2, and in a similar way, a charge +2 vortex can split up into two defects of charge +1. We now want to consider the energy of these vortices to see whether it is favorable to have one vortex of higher charge or many single-charged ones. We start by considering the far-field energy around a vortex of charge q in an otherwise homogeneous condensate. Subtracting the ground-state energy we find that it is

$$K - K_0 = \int d\mathbf{r} \frac{1}{2} \nabla \psi^* \cdot \nabla \psi, \quad (3.46)$$

3. Bose-Einstein Condensates and Topological Defects

in dimensionless units. Inserting that outside of the defect core the wave function is $\psi = e^{i\phi}$ the energy becomes

$$K - K_0 = \frac{1}{2} \int d\mathbf{r} \nabla e^{-i\phi} \cdot \nabla e^{i\phi} = \frac{1}{2} \int d\mathbf{r} (\nabla\phi)^2. \quad (3.47)$$

To evaluate this integral, we need to get an expression for the angle ϕ . Such an expression can be found from eq. (3.36) by taking the domain C to be a circle of radius r centered at the defect position. Assuming that the defect is the only perturbation in an otherwise unperturbed condensate, we then find

$$\nabla\phi(r, \theta) = \frac{q}{r} \hat{\theta}. \quad (3.48)$$

Here, $\hat{\theta}$ is the azimuthal unit vector. Inserting eq. (3.48) into eq. (3.47) and changing to polar coordinates, we get

$$K - K_0 = \pi \int_{R_c}^R dr \frac{q^2}{r} = q^2 \pi \ln \left(\frac{R}{R_c} \right), \quad (3.49)$$

where R is the system size and $R_c \sim \xi$ is the radius of the core [21, 46]. Notice that this energy is proportional to the square of the vortex charge q^2 . This is also the case if we include the core contribution to the energy [21], and consequently, only the single charge defects are stable while defects of higher charge tend to split up into vortices of unit charge. In the next section, we are going to show that these smaller vortices of the same charge repel each other.

3.5 Vortex tracking

We are now going to discuss a method for tracking topological defects that is due to Halperin [59] and Mazenko [60, 61]. There are multiple ways of motivating this method. The approach used by Halperin [59] was to identify the defects as zeros in the wave function and map them with a delta function. Mazenko later extended this approach and found an expression for the velocity of the defects, which can then be used to derive the kinematic equations of the vortices [60, 61]. We are here going to show how Halperin and Mazenko motivated this formalism, and how we can use it to derive the kinematic equations of the vortices. In Paper (IV) an alternative approach is given which also works for defects of higher charge in addition to a generalization to arbitrary dimensions. We start out the motivation by writing the order parameter as a vector-field $\vec{\Psi} = (\psi_1, \psi_2)$, with the components ψ_1 and ψ_2 being the real and imaginary part of ψ respectively. Here we show the method in two dimensions, but it is possible to extend it to arbitrary dimensions.

3.5.1 Motivation and defect kinematics

We start by noting that the number density of topological defects, $n = \sum_{\alpha} \delta(\mathbf{r} - \mathbf{r}^{\alpha}(t))$, can be written as

$$\sum_{\alpha} \delta(\mathbf{r} - \mathbf{r}^{\alpha}(t)) = |D| \delta(\vec{\Psi}), \quad (3.50)$$

where we have changed the variables from position space $\{\mathbf{r}\}$ to the order parameter space by using the transformation law for delta functions. Here \mathbf{r}^{α} is the position of the defect labeled α and D is the determinant of the Jacobian for the transformation from the variables (ψ_1, ψ_2) to (x, y) given by

$$D = \begin{vmatrix} \partial_x \psi_1 & \partial_x \psi_2 \\ \partial_y \psi_1 & \partial_y \psi_2 \end{vmatrix} = \partial_x \psi_1 \partial_y \psi_2 - \partial_y \psi_1 \partial_x \psi_2 = \epsilon_{ij} \partial_i \psi_1 \partial_j \psi_2. \quad (3.51)$$

Inserting the linear core approximation, it is straightforward to show that for vortices of charge ± 1 , D will have the same sign as the topological charge. We can therefore replace the number density with the vortex charge density, $\rho_v = \sum_{\alpha} q_{\alpha} \delta(\mathbf{r} - \mathbf{r}^{\alpha}(t))$ and find

$$\rho_c = \sum_{\alpha} q_{\alpha} \delta(\mathbf{r} - \mathbf{r}^{\alpha}(t)) = D \delta(\vec{\Psi}). \quad (3.52)$$

The topological charge is a conserved quantity so the singular topological charge density satisfies the equation

$$\partial_t \rho_c = -\nabla \cdot \mathbf{j}^c. \quad (3.53)$$

We can also derive a conservation equation for the D field by taking the time derivative

$$\partial_t D = -\nabla \cdot \mathbf{j}^D, \quad (3.54)$$

with $j_i^D = -\epsilon_{ij} \epsilon_{mn} (\partial_t \psi_m) (\partial_j \psi_n)$. Multiplying eq. (3.54) with $\delta^2(\vec{\Psi})$ and using the product rule we find

$$\partial_t \rho_v - D \partial_t \delta^2(\vec{\Psi}) = -\partial_i (j_i^D \delta^2(\vec{\Psi})) + j_i^D \partial_i \delta^2(\vec{\Psi}), \quad (3.55)$$

where we have used eq. (3.52) to identify ρ_c . We now consider the last term on the right-hand side. Notice that we can rewrite this to

$$\begin{aligned} j_i^D \partial_i \delta^2(\vec{\Psi}) &= \epsilon_{ij} \epsilon_{kl} \partial_j \Psi_k \partial_t \Psi_l \partial_i \Psi_m \frac{d}{d\Psi_m} \delta^2(\vec{\Psi}) \\ &= \epsilon_{kl} (\epsilon_{ij} \partial_i \Psi_m \partial_j \Psi_k) \partial_t \Psi_l \frac{d}{d\Psi_m} \delta^2(\vec{\Psi}) \\ &= -D \partial_t \delta^2(\vec{\Psi}), \end{aligned} \quad (3.56)$$

where in the last step we have used that the tensor ϵ_{ij} is anti-symmetric to remove vanishing terms. Putting this result into eq. (3.55), we get

$$\partial_t \rho_v = -\partial_i (j_i^D \delta^2(\vec{\Psi})), \quad (3.57)$$

3. Bose-Einstein Condensates and Topological Defects

and identify the singular defect density current as

$$\mathbf{j}^c = \mathbf{j}_i^D \delta^2(\vec{\Psi}) = \sum_{\alpha} q_{\alpha} \frac{\mathbf{j}^{(D)}(\mathbf{r}^{\alpha})}{D(\mathbf{r}^{\alpha})} \delta^2(\mathbf{r} - \mathbf{r}^{\alpha}), \quad (3.58)$$

where we have used the transformation law for delta functions and used that q_{α} has the same sign as D . An alternative expression for this current is

$$\mathbf{j}^c = \sum_{\alpha} q_{\alpha} \mathbf{v}^{\alpha} \delta(\mathbf{r} - \mathbf{r}^{\alpha}(t)), \quad (3.59)$$

which follows from eq. (3.52). We can now identify the defect velocity as

$$\mathbf{v}^{\alpha} = \frac{\mathbf{j}^D}{D} \Big|_{\mathbf{r}^{\alpha}}. \quad (3.60)$$

Writing now the D field and its current in complex form,

$$D = \frac{\epsilon_{ij}}{2i} \partial_i \psi^* \partial_j \psi, \quad (3.61)$$

$$j_i^D = \epsilon_{ij} \text{Im}(\partial_t \psi \partial_j \psi^*), \quad (3.62)$$

we can use eq. (3.60) and the dGPE eq. (3.7) to derive an expression for the vortex kinematics.

Kinematics in the frozen core approximation We now going to use eq. (3.60) to derive a phenomenological model for the motion of N interacting defects, and we start by assuming that we have an ideal vortex at position \mathbf{r}^{α} . We assume that the wave function has the form $\psi = \psi_0 e^{i\delta\phi + \delta\lambda}$, with ψ_0 being the ideal quasi-static vortex solution, $\delta\phi$ being perturbations in the phase and $\delta\lambda$ being perturbations in the density. The effect of a finite velocity on the wave function is important for dissipative models and leads to logarithmic corrections to the velocity we discuss below [21, 62]. These effects are commonly ignored in order to make phenomenological models that capture the qualitative behavior of the defects [63]. Inserting the ansatz into the dGPE eq. (3.7) to get an expression for the time derivative, we find

$$\partial_t \psi(\mathbf{r}^{\alpha}) = (i + \gamma) \nabla \psi_0 \cdot \nabla (i\delta\phi + \delta\lambda) e^{i\delta\phi + \delta\lambda} \Big|_{\mathbf{r}^{\alpha}}, \quad (3.63)$$

where we have used that $\psi_0(\mathbf{r}^{\alpha}) = \nabla^2 \psi_0 \Big|_{\mathbf{r}^{\alpha}} = 0$. Inserting this into eq. (3.60) and using the relation $i\partial_k \psi_0 = q\epsilon_{ki} \partial_l \psi_0$ [46], we find that the velocity of the defect is given as

$$v_i^{\alpha} = (\partial_i \delta\phi - \gamma \partial_i \delta\lambda + \gamma q \epsilon_{ij} \partial_j \delta\phi + q \epsilon_{ij} \partial_j \delta\lambda) \Big|_{\mathbf{r}=\mathbf{r}^{\alpha}}. \quad (3.64)$$

This derivation was done by Mazenko in Ref. [64] and it shows that the method reproduces a known result for complex Ginsburg-Landau equations [65].

If we neglect core deformation and assume that the vortices are well separated the velocity is only determined by the phase perturbations and becomes

$$\mathbf{v}^\alpha = (\nabla\delta\phi + \gamma q_\alpha \nabla^\perp \delta\phi)_{\mathbf{r}=\mathbf{r}^\alpha}. \quad (3.65)$$

The velocity is in this limit due to the superfluid velocity $\mathbf{v} = \nabla\phi$ induced by other defects or other sources of perturbations in the condensate. Assuming that the perturbations are dominated by the presence of the other vortices we write the wave function close to the defect labeled α as

$$\psi = \chi(|\mathbf{r} - \mathbf{r}^\alpha|) e^{iq_\alpha \theta_\alpha} e^{i \sum_{\beta \neq \alpha}^N q_\beta \theta_\beta}. \quad (3.66)$$

Here, θ_β is the polar angle centered at the defect labeled β , and $\chi(|\mathbf{r} - \mathbf{r}^\alpha|) e^{iq_\alpha \theta_\alpha}$ is the unperturbed wave function ψ_0 for the defect labeled α . The phase perturbation is thus $\delta\phi = \sum_{\beta \neq \alpha}^N q_\beta \arctan\left(\frac{y-y_\beta}{x-x_\beta}\right)$. Inserting this into eq. (3.65) and evaluating the expression at the position of defect α , we find

$$\mathbf{v}^\alpha = - \sum_{\beta \neq \alpha} q_\beta \frac{(\mathbf{r}^\alpha - \mathbf{r}^\beta)^\perp}{|\mathbf{r}^\alpha - \mathbf{r}^\beta|^2} + \gamma \sum_{\beta \neq \alpha} q_\alpha q_\beta \frac{\mathbf{r}^\alpha - \mathbf{r}^\beta}{|\mathbf{r}^\alpha - \mathbf{r}^\beta|^2}. \quad (3.67)$$

From this equation, we see that the dissipative term makes oppositely charged vortices attract and like signed vortices repel. Eq. (3.67) is frequently used in the literature to study, among other things, the inverse energy cascade in quantum turbulence [66] and expanding vortex clusters [63].

In the $\gamma = 0$ limit eq. (3.67) is the same as the Hamiltonian point vortex model for a classical fluid [46, 66, 67]. In this limit, the equation of motion can be written as

$$\dot{x}_\alpha = \frac{1}{2\pi q_\alpha} \frac{\partial H}{\partial y_\alpha}, \quad \dot{y}_\alpha = -\frac{1}{2\pi q_\alpha} \frac{\partial H}{\partial x_\alpha}, \quad (3.68)$$

i.e as Hamiltonian dynamics with x_α and y_α being the conjugate variables. The Hamiltonian H of the system is

$$H = -\pi \sum_{\alpha \neq \beta} q_\alpha q_\beta \ln(|\mathbf{r}^\alpha - \mathbf{r}^\beta|). \quad (3.69)$$

To model the effects of boundaries and confining potentials on the system one places image vortices outside the domain to get the boundary conditions right.

Above we have introduced the D field and showed that the vortex density can be written as $\rho_v = D\delta^{(2)}(\tilde{\Psi})$. We used this to derive the point defect dynamics. One of the major themes in Paper (III) and (IV) is that the D field without the delta function gives valuable information about the vortices and their interactions. In addition, this approach can be generalized to any system with a broken $O(n)$ symmetry as discussed in Paper (IV). We also use this approach to derive a point defect description of the defects in an active system with a vector order

3. Bose-Einstein Condensates and Topological Defects

parameter in Paper (V). In Ref. [7] we use the D field to estimate the onset of defect turbulence in an active system with a polar order parameter and manage to show that this will be asymmetric in the flow alignment parameter (discussed in the next chapter).

Chapter 4

Hydrodynamics for Active Fluids

In this chapter, we are going to discuss two hydrodynamic models for active matter. We will see that there are many similarities between these systems and the Bose-Einstein condensate we discussed in the previous section. This chapter starts with an introduction to active fluids, which is followed by a discussion on active nematics, and then a model for an active polar system.

4.1 Introduction to active fluids

Active matter is an umbrella term for non-equilibrium systems where the smallest constituents, referred to as active particles, are consuming energy from the environment and turning it into mechanical stresses and energies [34, 68]. It is the energy injection on the single particle scale that drives the system out of equilibrium. This is in contrast to a passive system, like the Bose-Einstein condensate which was discussed in the previous chapter, where the system is driven out of equilibrium by an external force. An example of an external forcing is the stirring potential that we use in Paper (III).

Active matter includes both biological systems like micro-swimmers, flocks of birds, and mixtures of cytoskeletal filaments and motor proteins [34, 68–71], and non-living matter like vibrated granular rods, Janus particles, and robots [72–74]. The interaction between the active particles, either direct or mediated through a medium, gives rise to self-sustained flows and pattern formations [25, 34, 68]. These interactions result in fascinating collective dynamics, for example, schools of fish exhibit a polar order that can change direction abruptly and form vortices in response to predators [34, 75]. Since active particles can exist on very different scales, have different symmetries, and be submerged in a wide range of environments, there exist many models to describe their collective motion.

A classical model for studying flocking behavior is the Vicsek model [76]. This is an agent-based model where the active particles are subject to an alignment interaction with their neighbors. In two dimensions this is similar to the XY-model for magnetic systems, but instead of the spins sitting on a lattice, they are moving with a constant speed in the direction of their polarity. Something that was surprising with the Vicsek model is that the system can exhibit long-range order even in the presence of noise to the direction of the particles [76, 77]. This was surprising because the XY-model does not have long-ranged order at finite temperatures due to the Mermin-Wagner theorem [9, 78]. Using a hydrodynamic model for self-propelled polar particles, known as the Toner-Tu model, Toner and Tu showed rigorously that such systems can form a broken symmetry system

4. Hydrodynamics for Active Fluids

even in two dimensions [77, 79]. Interestingly, since the "microscopic" particles in the Toner-Tu model are birds or other flocking animals, the continuum equations describing the system have terms that are typically not encountered in the standard passive systems [79]. The Toner-Tu model is described by the following continuum equations

$$\partial_t \rho + \nabla \cdot (\rho \mathbf{v}) = 0 \quad (4.1)$$

$$\begin{aligned} \partial_t \mathbf{v} + \lambda_1 (\mathbf{v} \cdot \nabla) \mathbf{v} + \lambda_2 (\nabla \cdot \mathbf{v}) \mathbf{v} + \lambda_3 \nabla v^2 = (a - bv^2) \mathbf{v} - \nabla P \quad (4.2) \\ + D_L \nabla (\nabla \cdot \mathbf{v}) + D_1 \nabla^2 \mathbf{v} + D_2 (\mathbf{v} \cdot \nabla)^2 \mathbf{v} + \mathbf{f}. \end{aligned}$$

Here ρ is the density satisfying the conservation law, while \mathbf{v} is the velocity, P is the pressure, and \mathbf{f} is a noise term. The λ terms on the left-hand side of eq. (4.2) are a modification to the convective derivative. For Galilean invariant dynamics, the parameters are fixed to $\lambda_1 = 1$ and $\lambda_2 = \lambda_3 = 0$ corresponding to the material derivative on the right-hand side of the equation. On the right-hand side, the terms containing a and b give a non-zero velocity in the ordered phase, similar to the r and g of the ϕ^4 Hamiltonian eq. (2.8). The D 's are viscosities due to the mutual interactions. They cause velocity fluctuations to diffuse into the fluid.

In dry systems, the interaction between the active particles and the surrounding fluid is neglected, which breaks the Galilean invariance. The Vicsek (discrete) model and Toner-Tu (continuum) model are canonical toy models of dry active matter with polar order [34]. Other models, like the ones we are going to discuss in the following sections, include the interaction between the active particles and the surrounding fluid. These are classified as wet.

In addition to the distinction between wet and dry active matter one also classifies the matter based on the symmetries. Here we will only consider polar and nematic symmetries. The Toner-Tu model has polar symmetry, meaning that the particles have a preferred direction, and (when $a > 0$) the particles tend to point in the same direction. In the nematic system, the particles are parallel but do not on average point out a preferred direction. These systems will be discussed in more depth in the next section.

4.2 Nematic active matter

4.2.1 Hydrodynamic model for active nematic

Many active particles have an elongated shape and on large scales exhibit nematic order [34, 68]. The nematic order forms in systems consisting of many rod-like particles that have broken the isotropic phase by aligning [9], as depicted in Fig. 4.1. This phase can be found in systems where the particles are head-tail symmetric like in Fig. 4.1 or in systems where the rods have a polarity, but their heads are randomly oriented so that on average they do not point out a specific direction. Microscopically we can assign the vector $\tilde{\mathbf{n}}^{(\alpha)}$ to the rod labeled α to describe the direction the rod is pointing. Since the rods are head-tail symmetric

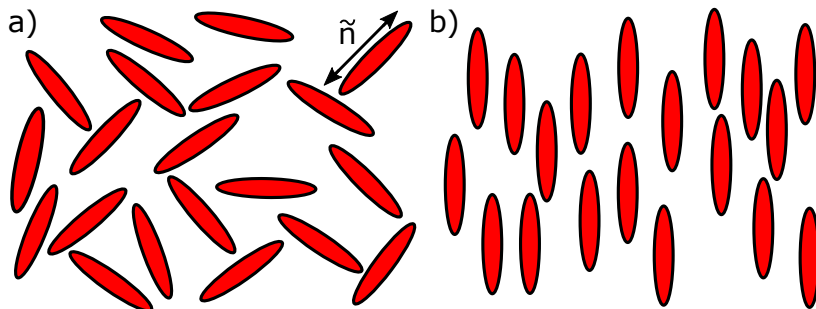


Figure 4.1: Rod-like particles forming an isotropic phase a) where the rods are randomly oriented and a nematic phase b) where the rods are aligned. The π symmetric microscopic director $\tilde{\mathbf{n}}$ of one of the rods is shown in the top right of a).

the theory should be invariant under the transformation $\tilde{\mathbf{n}}^{(\alpha)} \rightarrow -\tilde{\mathbf{n}}^{(\alpha)}$. A way of representing this is by defining the Q tensor order parameter which is defined in such a way that it is invariant to $\tilde{\mathbf{n}}^{(\alpha)} \rightarrow -\tilde{\mathbf{n}}^{(\alpha)}$. In two dimensions the tensor order parameter takes the form [9]

$$\tilde{Q}_{ij} = \frac{V}{N} \sum_n (\tilde{n}_i^{(\alpha)} \tilde{n}_j^{(\alpha)} - \frac{1}{2} \delta_{ij}) \delta(\mathbf{r} - \mathbf{r}^{(\alpha)}), \quad (4.3)$$

with V and N being the system's volume and the number of nematic particles. This is a symmetric and traceless tensor, therefore it has only two degrees of freedom, namely Q_{xx} and Q_{xy} . After coarse-graining, this order parameter becomes

$$Q_{ij} = S(n_i n_j - \frac{1}{2} \delta_{ij}). \quad (4.4)$$

Here \mathbf{n} is the coarse-grained nematic director field which is continuous and varies smoothly on length scales that are long compared to the interparticle distance. It is still a unit vector that describes the direction of alignment, while the parameter S gives the magnitude of the order. S is non-zero in the nematic phase, while in the limit of an isotropic fluid, it tends towards zero.

Having the coarse-grained order parameter, one can construct the Landau-de Gennes free energy. Since the free energy has to be symmetric under rotations and translations it has to be constructed using traces of Q^p , where p is a positive integer [9]. We truncate the expansion to the fourth order and include an interaction term so that the free energy takes the form

$$F = \int d\mathbf{r} \left[K |\nabla Q|^2 - \frac{g}{2} \text{Tr}(Q^2) + \frac{1}{4} \text{Tr}(Q^2)^2 \right]. \quad (4.5)$$

The term $\text{Tr}(Q^3)$ is also allowed by the symmetries, but due to the Q being a symmetric and traceless tensor, this term will always be zero in two dimen-

4. Hydrodynamics for Active Fluids

sions. In a three-dimensional model, it has to be included. The first term is the elastic free energy, where we have assumed a single elastic constant K so that the penalty for all distortions is treated equally. In general, this might not be the case. The negative sign in front of the $\text{Tr}(Q^2)$ term is chosen so that g is positive in the nematic state. Also, notice that we have scaled the equation so that the constant in front of the $\text{Tr}(Q^2)^2$ term is set to $1/4$.

From this free energy, we can find the homogeneous equilibrium state. In this case, we can write the free energy in terms of S

$$F = \int d\mathbf{r} \left[-\frac{g}{8} S^2 + \frac{1}{64} S^4 \right]. \quad (4.6)$$

This is the same as the double well potential that is shown in Fig. (2.2). Minimizing this with respect to S we find that the equilibrium state fulfills

$$S_0 = 2\sqrt{g}. \quad (4.7)$$

Note that contrary to the order parameter in eq. (2.8) S_0 has to be positive.

Knowing the equilibrium state is convenient, but an active nematic is intrinsically an out-of-equilibrium system so we need a hydrodynamic model to describe the dynamics. The evolution of the Q -tensor can be described by the Edward-Beris equation for a nematic liquid crystal submerged in a fluid [34, 80, 81]

$$\partial_t Q + \mathbf{u} \cdot \nabla Q + \Omega Q - Q \Omega = \lambda E Q - \gamma^{-1} H. \quad (4.8)$$

Here \mathbf{u} is the velocity of the flow field of the surrounding fluid. The term on the left-hand side is the corotational derivative which in addition to including the change in the order parameter due to advection also includes the effect of vorticity $2\Omega_{ij} = \partial_i u_j - \partial_j u_i$, which is to rotate the rods. This derivative has the property that it is both Galilean invariant and invariant to solid body rotations. On the right-hand side, we find first the flow alignment term λE , with the strain rate given as $2E = \partial_i u_j + \partial_j u_i$. This term gives the tendency for the rod-like particles to align with the shear, which is the same effect that is responsible for timber tending to point in the direction of the flow when moving down a river. The last term is a minimization of the free energy given through the molecular field

$$H_{ij} = \frac{\delta F}{\delta Q_{ij}}, \quad (4.9)$$

and the rotational diffusivity γ which sets the relaxation time.

To fully describe the dynamics of the active nematics one needs in addition to eq. (4.8), a model for the flow field. We will here assume that the flow has a low Reynolds number and is given as a quasi-two-dimensional incompressible Stokes flow satisfying the equations

$$(\Gamma - \eta \nabla^2) \mathbf{u} = -\nabla P + \nabla \cdot \sigma^a(Q) + \nabla \cdot \sigma^p \quad (4.10)$$

$$\nabla \cdot \mathbf{u} = 0. \quad (4.11)$$

Here eq. (4.10) is the Stokes equation that we discussed in sec. 2.3 with the viscosity η and friction with the substrate Γ . The nematic order parameter affects the flow through the active, $\sigma^a(Q)$, and the passive, σ^p , stress. We will assume that the active stress is dominant, and neglect the passive stress.

The active stress The only term in the set of coupled equations (4.8)-(4.11) that is not present for a passive nematic liquid crystal is the active stress $\sigma^a(Q)$. This stress is due to the microscopic constituents being self-propelled. The form of σ^a can be motivated from the dynamics of the single particles using Newton's third law, which states that the forces the active particle exerts on the fluid and the forces from the fluid acting on the active particle have to vanish upon integration [82]. The simplest model that captures this is to consider the rod-like particles as force dipoles, i.e the rod labeled α aligned parallel to the vector $\tilde{\mathbf{n}}^{(\alpha)}$ has a point force, $\tilde{\mathbf{f}}^{(\alpha)} = f\tilde{\mathbf{n}}^{(\alpha)}$, at each end that is equal in magnitude and oppositely directed. The forces on one rod are shown in Fig. 4.2. The distance from the center to the forces is a . The forces related to the rod labeled α can be written as $\tilde{\mathbf{F}}^{(\alpha)}(\mathbf{r}) = f\tilde{\mathbf{n}}^{(\alpha)}[\delta(\mathbf{r} - \mathbf{r}^{(\alpha)} + a\tilde{\mathbf{n}}^{(\alpha)}) - \delta(\mathbf{r} - \mathbf{r}^{(\alpha)} - a\tilde{\mathbf{n}}^{(\alpha)})]$. Summing

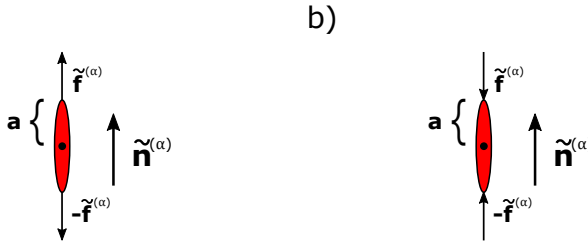


Figure 4.2: Sketch of the force dipole related to one active rod for a) an extensile and b) a contractile system. The forces $\tilde{\mathbf{f}}^{(\alpha)} = f\tilde{\mathbf{n}}^{(\alpha)}$ and $-\tilde{\mathbf{f}}^{(\alpha)}$ are equal in size and oppositely directed at the distance a from the centre of the rod. The director $\tilde{\mathbf{n}}^{(\alpha)}$ is also shown. Here we have given the director a unique direction in order to give the force in terms of it.

this over all the rods gives the force [82]

$$\tilde{\mathbf{F}}^a(\mathbf{r}) = \sum_{\alpha} f\tilde{\mathbf{n}}^{(\alpha)}[\delta(\mathbf{r} - \mathbf{r}^{(\alpha)} + a\tilde{\mathbf{n}}^{(\alpha)}) - \delta(\mathbf{r} - \mathbf{r}^{(\alpha)} - a\tilde{\mathbf{n}}^{(\alpha)})] = -\nabla \cdot \sigma^a, \quad (4.12)$$

which we have identified as the active force. Next, we use that the derivative of the delta function is given as $\partial_j \delta(\mathbf{r}) = \lim_{a_j \rightarrow 0} [\delta(\mathbf{r} + a_j \mathbf{e}_j) - \delta(\mathbf{r} - a_j \mathbf{e}_j)]/a_j$. This means that for small $|a|$ we can approximate the above force density as

$$(\nabla \cdot \sigma^a)_i = -af \partial_j \sum_{\alpha} \tilde{n}_i^{(\alpha)} \tilde{n}_j^{(\alpha)} \delta(\mathbf{r} - \mathbf{r}^{(\alpha)}). \quad (4.13)$$

4. Hydrodynamics for Active Fluids

After coarse-graining, we find that the active stress has this form

$$\sigma_{ij}^a = \alpha_0 \left(n_i n_j - \frac{1}{2} \delta_{ij} \right) = \alpha_0 Q_{ij}, \quad (4.14)$$

where we have added a constant that vanishes when acted on with the derivative. Notice that σ^a is proportional to the Q tensor with the proportionality constant α_0 . The sign of this constant is positive for contractile systems and negative for extensile systems. This expression for the active stress could also have been motivated by the fact that there is no symmetry or conservation law that rules it out for the self-propelled system [82]. Note that the activity α can be spatially varying. The active force in that case is

$$\mathbf{F}^a = \nabla \alpha(r) \cdot \mathbf{Q} + \alpha(r) \nabla \cdot \mathbf{Q}. \quad (4.15)$$

Complex representation In order to reuse some of the insight we got from the discussion of the Bose-Einstein condensate in the previous chapter we will map the Q tensor into a complex order parameter. We, therefore, note that the tensor can be written as

$$Q = \frac{S}{2} \begin{pmatrix} \cos(2\phi) & \sin(2\phi) \\ \sin(2\phi) & -\cos(2\phi) \end{pmatrix}, \quad (4.16)$$

where ϕ is the angle of the nematic director \mathbf{n} . We can therefore map it to the complex order parameter

$$\psi = Q_{xx} + iQ_{xy} = \frac{S}{2} e^{2i\phi}, \quad (4.17)$$

which changes eq. (4.8) so that it reads

$$\partial_t \psi + \mathbf{u} \cdot \nabla \psi = \lambda \partial_{\bar{z}} u + i\omega \psi + \nabla^2 \psi + (1 - |\psi|^2) \psi. \quad (4.18)$$

Similar to what we did to the dGPE, eq. (3.7), we have here chosen new units to make the equation dimensionless. The time is rescaled using the relaxation time $\tau = \gamma/g$ and the length is rescaled using the coherence length $\xi^2 = K/g$ [81]. It is this length that sets the size of the defect core in the system. In addition, the order parameter is rescaled as $\psi \rightarrow \sqrt{g} \psi$ so that it is normalized in equilibrium. The flow alignment is then rescaled to $\lambda \rightarrow \lambda/\sqrt{g}$. We have also introduced the complex derivative $\partial_{\bar{z}} = \frac{1}{2}(\partial_x + i\partial_y)$ and the complex velocity $u = u_x + iu_y$. Notice that this equation is very similar to the Gross-Pitaevskii equation, eq. (3.7), which we discussed in the previous chapter. This becomes even more apparent when we neglect the effect of the flow field

$$\partial_t \psi = \nabla^2 \psi + (1 - |\psi|^2) \psi. \quad (4.19)$$

Contrary to the GPE this equation is purely dissipative, which should not be a surprise since the equation without the flow field is just the relaxation of the Landau-de Gennes free energy eq. (4.5). In the stationary limit $\partial_t \psi = 0$ it

becomes the same as the stationary GPE, eq. (3.40).

We now introduce the rescaled units in the Stokes equation so that it reads

$$(1 - \zeta^2 \nabla^2) \mathbf{u} = -\nabla P + \mathbf{F}^a, \quad (4.20)$$

$$\nabla \cdot \mathbf{u} = 0. \quad (4.21)$$

We have now neglected the passive stress and defined the active force $\mathbf{F}^a = \nabla \cdot (\alpha Q)$. The constants here are the rescaled activity $\alpha = \alpha_0 \gamma / (\Gamma K)$ and $\zeta = \ell_d / \xi$ being the ratio between the hydrodynamic dissipation length $\ell_d = \sqrt{\eta / \Gamma}$ and the coherence length ξ . Taking the divergence of eq. (4.20) and using the incompressibility condition we get the following expression for the pressure

$$\nabla^2 P = \nabla \cdot \mathbf{F}^a. \quad (4.22)$$

Similarly we find the vorticity by applying the rotated divergence $-\nabla^\perp$ to eq. (4.20) so that it becomes

$$(1 - \zeta^2 \nabla^2) \omega = -\nabla^\perp \cdot \mathbf{F}^a. \quad (4.23)$$

We can solve for the velocity, pressure, and vorticity by using the Greens functions of eq. (4.20) and (4.22). The integrals we need to solve are

$$P(\mathbf{r}) = \frac{1}{2\pi} \int d\mathbf{r}' \ln(|\mathbf{r} - \mathbf{r}'|) \nabla' \cdot \mathbf{F}^a, \quad (4.24)$$

$$\mathbf{u}(\mathbf{r}) = \frac{1}{2\pi\zeta^2} \int d\mathbf{r}' K_0 \left(\frac{|\mathbf{r} - \mathbf{r}'|}{\zeta} \right) (\mathbf{F}^a(\mathbf{r}') - \nabla' P^a(\mathbf{r}')), \quad (4.25)$$

$$\omega(\mathbf{r}) = -\frac{1}{2\pi\zeta^2} \int d\mathbf{r}' K_0 \left(\frac{|\mathbf{r} - \mathbf{r}'|}{\zeta} \right) \nabla'^\perp \cdot \mathbf{F}^a(\mathbf{r}'). \quad (4.26)$$

These are the integrals we consider in Paper (I) and (II). In order to solve these it is convenient to change to complex variables and rewrite the integrals so they are of the form

$$I(\mathbf{r}) = \int_0^\infty dr' G(r') \oint_C d\hat{z} f(r', \hat{z}, \mathbf{r}), \quad (4.27)$$

where C here is the unit circle in the complex plane. The detailed expressions for G and f depend on the source of the active force. In the papers, we use ideal defects as the sources and use the techniques described in Section 2.4 to solve the integral over \hat{z} .

Instability due to the activity As mentioned, the active stress destabilizes the homogeneous nematic state. We can illustrate this by doing a linear stability analysis around the homogeneous state $\psi = 1$. We, therefore, write the complex order parameter as $\psi = 1 + \delta\psi$, with $|\delta\psi| \ll 1$ being linear perturbations. Note that the velocity u is first order in $\delta\psi$, which means that the advection term is second order and can be neglected. In addition, we also neglect the effects

4. Hydrodynamics for Active Fluids

of flow alignment and only consider perturbations in the phase $\delta\phi$ to make the discussion simple. The linearized equation for $\delta\psi$ and its conjugate is

$$\partial_t \delta\psi = i\omega + \nabla^2 \delta\psi - \delta\psi - \delta\psi^*, \quad (4.28)$$

$$\partial_t \delta\psi^* = -i\omega + \nabla^2 \delta\psi^* - \delta\psi - \delta\psi^*. \quad (4.29)$$

Subtracting these two equations gives

$$\partial_t(\delta\psi - \delta\psi^*) = 2i\omega + \nabla^2(\delta\psi - \delta\psi^*). \quad (4.30)$$

Note that we can write the perturbation as $\delta\psi = 2i\delta\phi$ so that this becomes

$$\partial_t \delta\phi = \frac{1}{2}\omega + \nabla^2 \delta\phi. \quad (4.31)$$

To close this we need to consider the vorticity ω . Using eq. (4.23) we see that it has the form

$$(1 - \zeta^2 \nabla^2)\omega = 2i\alpha(\partial_x^2 - \partial_y^2)\delta\phi. \quad (4.32)$$

The vorticity in Fourier space is therefore given as

$$\tilde{\omega}(\mathbf{k}) = -2\alpha \frac{k_x^2 - k_y^2}{1 + \zeta^2 k^2} \delta\tilde{\phi}(\mathbf{k}). \quad (4.33)$$

Fourier transforming eq. (4.31) and inserting the expression for the vorticity we find

$$\partial_t \delta\tilde{\phi}(\mathbf{k}, t) = - \left(\alpha \frac{\cos 2\theta_k}{1 + \zeta^2 k^2} + 1 \right) k^2 \delta\tilde{\phi}(\mathbf{k}, t), \quad (4.34)$$

where θ_k is the angle of the wave vector \mathbf{k} . Eq. (4.34) is a differential equation for each mode \mathbf{k} . It has the growth rate

$$g(k, \theta_k) = - \left(\alpha \frac{\cos 2\theta_k}{1 + \zeta^2 k^2} + 1 \right) k^2, \quad (4.35)$$

which is plotted in Fig. 4.3 for both $\alpha \cos(2\theta_k) = a(\theta_k) > 0$ and $a(\theta_k) < 0$. If the rate becomes positive, we have that the perturbations with those wave-vectors grow exponentially in time and are therefore unstable. This is only possible when

$$|\alpha| > 1 + \zeta^2 k^2, \quad (4.36)$$

showing that if the activity is large enough the homogeneous nematic phase becomes unstable to certain wave vectors. Note that this does not mean that the order parameter goes to zero, i.e. the system still has local nematic order.

A more rigorous stability analysis where they also allowed for variations in S was performed in Ref. [25] and gave the same result. Notice that the angle of the unstable modes depends on the sign of the activity. If $\alpha > 0$ we have instabilities when $\cos 2\theta_k < 0$ meaning that the most unstable mode is $\theta_k = \pi/2 \pm n\pi$ where n is some integer. Perturbations with these wave vectors are perpendicular

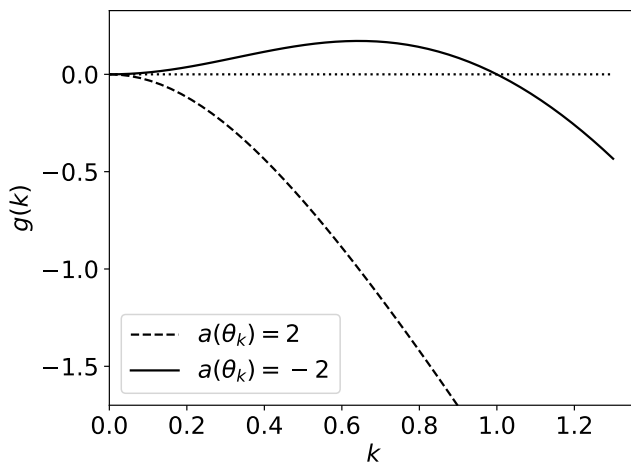


Figure 4.3: Plot of the growth rate $g(k, \theta_k)$ of the equation for the linear modes eq. (4.34) for fixed angles θ_k . When the growth factor is positive the perturbations grow exponentially making the equation unstable. We have set $\zeta = 1$ while $\alpha \cos(2\theta_k) = a(\theta_k) = 2$ for the dashed line and $a(\theta_k) = -2$ for the solid line.

to the director in the homogeneous state. For $\alpha < 0$ the first unstable mode is $\theta_k = 0 \pm n\pi$ corresponding to perturbations parallel to the director of the homogeneous state. The criterion discussed here is for linear instabilities. If the activity is high enough, it might be strong enough to spontaneously create topological defects in the nematic phase, leading up to a chaotic activity-driven flow state that is termed active turbulence [24, 83].

4.2.2 Nematic defects and their kinematics

The nematic defect One advantage of the complex representation $\psi = (Se^{2i\phi})/2$ in 2D is that it maps the nematic director into an order parameter space given by the unit disk (\mathcal{S}_1) where topological defects correspond to vortices, just like for the Bose-Einstein condensate. However, we do need to keep track of the winding number q since the nematic orientational field is π symmetric, and therefore half of the winding number of vortices. Also for this case, the Landau-de Gennes free energy is such that only the topological defects of the lowest absolute charge are energetically stable and higher-order defects tend to split up. The angle of the nematic director thus satisfies

$$\int_C d\phi = \int_C d\mathbf{l} \cdot \nabla\phi = 2\pi q, \quad (4.37)$$

4. Hydrodynamics for Active Fluids

so that the argument of the nematic director around an ideal defect with an isotropic core is

$$\phi = q\theta + \theta_0. \quad (4.38)$$

Here θ_0 is a constant. This constant is important for the dynamics of the topological defects since it gives the direction of the defect's polarity [84], which is illustrated in Fig. 4.4.

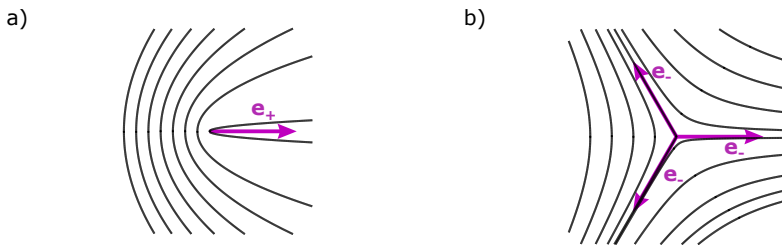


Figure 4.4: Sketch of a) the $+1/2$ and b) the $-1/2$ topological defects in a nematic liquid crystal with the polarities \mathbf{e}_+ and \mathbf{e}_- drawn in. Notice that the negative defect has three equivalent polarizations due to its three-fold symmetry. Figure from Paper (II).

The relation between the polarisation and the phase constant is $\mathbf{e}_+ = [\cos(2\theta_0), \sin(2\theta_0)]$ and $\mathbf{e}_- = [\cos(2\theta_0/3), \sin(2\theta_0/3)]$. The core structure and the far-field free energy related to the nematic defect can be found in the limit of an ideal defect if we neglect the flow field. Since the stationary equation for the complex field is identical to the stationary GPE, eq. (3.40), the calculations are identical to Section 3.4.2 and the result is that the complex field has the form $\psi_0 = \chi(r)e^{2i(q\theta + \theta_0)}$ for a stationary defect centered at $\mathbf{r} = 0$ [21, 81]. The core function $\chi(r)$ has the asymptotic $\chi(r) \sim r$ for $r \ll 1$ and $\chi(r) = 1$ for $r \gg 1$. Using the same argument as for the quantum vortex discussed in Section 3.4.2, we can show that the far-field energy of a nematic defect of charge q is proportional to q^2 . This makes the higher-order defects unstable so that they tend to decay into defects of lower charge.

The defect kinematics Similar to how we motivated the kinematics of the defects in the Bose-Einstein condensate in Section 3.5 we can also use the Halperin-Mazenko formalism to find the kinematics of defects in the nematics. The definition of the D field and its density current stays the same as for the BEC, with the following expression for the velocity of the defect labeled α

$$D = \frac{\epsilon_{ij}}{2i} \partial_i \psi^* \partial_j \psi, \quad (4.39)$$

$$j_i^D = \epsilon_{ij} \text{Im}(\partial_t \psi \partial_j \psi^*), \quad (4.40)$$

$$\mathbf{v}^\alpha = \frac{\mathbf{j}^D}{D}. \quad (4.41)$$

We see that mapping the Q -tensor to the complex order parameter ψ has allowed us to reuse the same formulas for the D field and its current density from Chapter 3. By using this common formalism, we avoid solving the same problem twice, and the method gives a general expression for the defect velocity, eq. (4.41), in terms of two fields, D and \mathbf{j}^D , that are straightforward to calculate numerically. As we will see below, eq. (4.41) can be combined with the system-specific equations of motion and the quasi-static defect approximation to derive an expression for the defect kinematics. In Paper (III) and (IV), we use the D field and its current to get insights into the creation and annihilation of defects as a gradual process of core formation, and demonstrated that the D field also tracks non-linear excitations. It is important to note that since the D field also captures non-linear perturbations, it has to be combined with additional methods to accurately separate smooth perturbations from topological defects.

We can use this to find the equation of motion for a nematic defect of charge q_α that is due to a non-zero velocity field and perturbations in the phase $\delta\phi$. Assuming that the core is not deformed when the defect moves we can use the ansatz $\psi = \psi_0(r, \theta)e^{2i\delta\phi}$, where $\psi_0(r, \theta)$ is the quasi-static ideal vortex solution, which is the same (up to the constant Λ) as the one for the Bose-Einstein condensate, see sec. (3.4.2), and $\delta\phi$ represents perturbations in the phase. The constant phase θ_0 is included in $\delta\phi$. Inserting this ansatz into eq. (4.18) and using that the order parameter decays to zero linearly at the phase singularity we get the following expression for the defect velocity [81]

$$\mathbf{v}^\alpha = \mathbf{u}(\mathbf{r}^\alpha) + 4q_\alpha \nabla^\perp \delta\phi + \lambda \mathbf{G}. \quad (4.42)$$

We have here introduced the vector $\mathbf{G} = [\text{Re}(G), \text{Im}(G)]$ as

$$G = \begin{cases} -\Lambda^{-1}, \partial_{\bar{z}} u e^{-2i\delta\phi} & \text{sgn}(q) > 0 \\ -\Lambda^{-1} \partial_z \bar{u} e^{2i\delta\phi}, & \text{sgn}(q) < 0, \end{cases} \quad (4.43)$$

and used that close to the singularity the wave function has the form $\psi_0 = \Lambda r e^{2i\theta}$ with Λ being a constant. See Section 3.4.2 for details. Looking at eq. (4.42) we see that the second term is due to the elasticity of the order parameter, and is equivalent to the term that in the BEC was due to thermal dissipation. We can in a similar way relate it to an effective Coulomb interaction between defects in the system.

The other two terms in eq. (4.42) are due to the non-zero flow field, where the first term is due to the advection and the last term is due to the flow alignment. In Paper (I) and (II), we study among other things the active self-propulsion of isolated defects, which is due to the flow fields the defects themselves induce through the active stress. To find the active flow field we insert the active stress of an isolated stationary defect into eq. (4.24) and (4.25) and solve the integrals

4. Hydrodynamics for Active Fluids

using the methods discussed in sec. 2.4. In addition to making the defects self-propel the first term in eq. (4.42) allows the defects to interact through the flow field [81]. We have not considered this for the nematics in the works presented here, but in Paper (V) we consider this for defects in a polar system.

The effect of vorticity We saw above that the vorticity does not appear in the equation for the defect velocity. It does however have some effect on the orientation of the defect. We can show this by first writing the wave function as $\psi = \tilde{S}e^{2i\phi}$ and inserting it into eq. (4.18). After dividing by $e^{2i\phi}$ and separating the real and the imaginary part of the equation we find the following set of equations for the phase and the length of the wave function

$$\partial_t \tilde{S} = -\mathbf{u} \cdot \nabla \tilde{S} + \nabla^2 \tilde{S} - 4\tilde{S} \nabla \theta \cdot \nabla \phi + (1 - \tilde{S}^2) \tilde{S}, \quad (4.44)$$

$$2\tilde{S} \partial_t \phi = -2\tilde{S} \mathbf{u} \cdot \nabla \phi + \omega \tilde{S} + 4\nabla \tilde{S} \cdot \nabla \phi + 2\tilde{S} \nabla^2 \phi. \quad (4.45)$$

The flow alignment parameter λ is set to zero and $\tilde{S} = S/2$. We can rewrite the equation for the angle as

$$\partial_t \phi = -\mathbf{u} \cdot \nabla \phi + \frac{1}{2} \omega + 2\nabla \ln(\tilde{S}) \cdot \nabla \phi + \nabla^2 \phi. \quad (4.46)$$

We now consider a positive defect placed at \mathbf{r}_0 . The polarity of this defect is [81]

$$\mathbf{e}_+ = \nabla \cdot Q|_{\mathbf{r}=\mathbf{r}_0}, \quad (4.47)$$

where we are going to insert the ansatz $\psi = \psi_0 e^{2i\delta\phi}$ for the complex order parameter. Here ψ_0 is the static vortex profile with the additional assumption that the defect is oriented in such a way that the defect does not spontaneously rotate. We show in Paper (II) that this is only true for specific values of θ_0 when the activity α is spatially varying. The deviation from the stable orientations is therefore taken to be part of $\delta\phi$. Inserting this ansatz into eq. (4.47) we find that the polarisation vector can be written as the complex number

$$e_+ = 2e^{2i\delta\phi}. \quad (4.48)$$

Taking the time derivative of this, we find

$$\frac{d}{dt} e^+ = \dot{e}^+ = 4ie^{2i\delta\phi} \partial_t \delta\phi + 4i\mathbf{u} e^{2i\delta\phi} \cdot \nabla \delta\phi. \quad (4.49)$$

We can now use that the angle for the ideal positive defect is assumed not to be explicitly time-dependent. Using eq. (4.46), neglecting the flow alignment and keeping only the terms that are due to the flow field we find

$$\dot{e}^+ \sim i\omega e^+, \quad (4.50)$$

which in real vector notation reads

$$\dot{\mathbf{e}}^+ \sim -\omega \boldsymbol{\epsilon} \cdot \mathbf{e}^+. \quad (4.51)$$

Here ϵ is the anti-symmetric tensor. From this, we see the effect of non-zero vorticity is, not surprisingly, to rotate the polarization of the defect. Doing the same exercise for the negative defect, we find that the vorticity rotates its polarity slower by a factor of $1/3$. This is used in Paper (II) to discuss how a spatially varying activity makes the defects rotate. As we see from eq. (4.46) there will also be contributions from gradients and divergences in the angle.

4.3 Polar active matter

The model that we discussed in the previous section is for an active system with nematic symmetry and it is well known to capture a lot of the dynamics seen in many active systems such as bacterial suspensions [34, 68]. In addition to the half-integer defects discussed in the previous section, there have been observed defects of charge ± 1 in biological systems such as motile bacteria [85, 86] and cells [87, 88]. The free energy considered in eq. (4.5) is not ideal for studying the dynamics of ± 1 defects, because they are energetically unstable and tend to decay into defects of charge $\pm 1/2$. We, therefore, change the free energy to allow ± 1 defects to be energetically stable.

The particles in a polar system are very similar to the ones in the nematic. The way they differ is that they have distinct heads and tails, and the interaction between them favors the heads to point in the same direction as shown in Fig. (4.5). Microscopically the polar entity labeled α is described by a polar director $\hat{\mathbf{p}}^{(\alpha)}$ which is a unit vector pointing from the tail to the head of the particle as shown in Fig. 4.5 a). The order parameter of the polar order is the coarse-grained polarity \mathbf{p} , which contrary to the coarse-grained nematic director \mathbf{n} is not a unit vector. The length of \mathbf{p} is a measure for the order, and it tends to zero when the particles are randomly oriented in the disordered phase.

In Ref. [89] they propose a free energy that allows for both ± 1 and $\pm 1/2$ defects by using the vector order parameter \mathbf{p} with the following free energy

$$F_p = \int d\mathbf{r} \left[\frac{K_p}{2} |\nabla \mathbf{p}|^2 + \frac{K_n}{2} (\nabla Q^p)^2 + \frac{A}{2} \left(-p^2 + \frac{p^4}{2} \right) \right], \quad (4.52)$$

with

$$Q_{ij}^p = p_i p_j - \frac{1}{2} p^2 \delta_{ij} \quad (4.53)$$

being a "nematic" tensor constructed from the polar order parameter. Note that since \mathbf{p} is not a unit vector, p^2 has taken the role of the parameter S . If the parameter $K_p = 0$ in the above eq. (4.52) then the lowest energy topological defects are those of charge $\pm 1/2$. In the other limit, with $K_n = 0$, the lowest order topological defects are ± 1 defects. If both K_n and K_p are non-zero, one can have coexistence of $\pm 1/2$ and ± 1 defects. We will mostly consider the case that has only stable ± 1 defects, i.e. $K_n = 0$, $K_p \neq 0$.

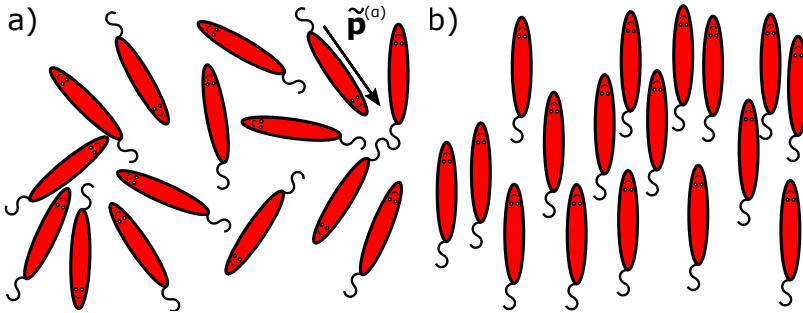


Figure 4.5: The figure shows the polar particles in a) an isotropic phase and b) a polar phase. The polar particles have a distinct head and tail in contrast to the nematic particles. The polar director $\tilde{\mathbf{p}}^{(\alpha)}$ of the particle labeled α is shown in the top right of a)

These active polar particles can become self-propelled either by swimming in the surrounding fluid or by interacting with (i.e. walking on) substrate. During the discussion on the nematic system, we argued that the active force due to the interaction with the surrounding fluid had to be dipolar because of momentum conservation. This also holds true for micro-swimmers with polar order. If we allow the active particles to exchange momentum with the substrate, we can relax this restriction and include a polar self-propulsion force into the flow equations. From the above free energy one can then write down a hydrodynamic model for the evolution of the vector order parameter [89]

$$\partial_t \mathbf{p} + \mathbf{u} \cdot \nabla \mathbf{p} + \Omega \cdot \mathbf{p} = \lambda E \cdot \mathbf{p} - \frac{1}{\gamma} \frac{\delta F_p}{\delta \mathbf{p}}, \quad (4.54)$$

$$(\Gamma - \eta \nabla^2) \mathbf{u} = \mathbf{F}^a - \nabla P + \mathbf{F}^p, \quad (4.55)$$

$$\nabla \cdot \mathbf{u} = 0. \quad (4.56)$$

Which, in the "dry" limit, reduces to a form similar to the Toner-Tu model discussed in sec. 4.1.

The structure of this system of equations is similar to eq. (4.8) - (4.11). It consists of an equation for the evolution of the order parameter, eq. (4.54), coupled to the incompressible Stokes equation which governs the flow. From this, we recognize the terms on the left-hand side of eq. (4.54) to be the corotational derivative with a term advecting the rods $\mathbf{u} \cdot \nabla \mathbf{p}$ and one that rotates them $\Omega \cdot \mathbf{p}$. On the right-hand side, we have the flow alignment $\lambda E \cdot \mathbf{p}$ and the relaxation of the free energy. Notice that if we neglect the terms that are due to the flow field, this reduces to the dissipative part of the dGPE eq. (3.7). For the flow field we have in addition to the dipolar active force $\mathbf{F}^a = \alpha_0 \nabla \cdot \mathbf{Q}$ included a polar self-propulsion force $\mathbf{F}^p = \alpha_p \mathbf{p}$ that is due to the polar entities moving on and exchanging momentum with the substrate. Notice that the role of the

velocity field in this model is a bit different than that in the Toner-Tu model given by eq. (4.1) and (4.2). In the model described above, eq. (4.54) -(4.56), the active polar particles are submerged in a surrounding fluid. The model does not separate between the velocity of the polar particles and the velocity of the surrounding fluid but has one velocity field \mathbf{u} that describes both. In the Toner-Tu model, one does not include the surrounding fluid and the velocity \mathbf{v} is that of the active gas. In addition the Toner-Tu model is compressible, while the polar system is incompressible.

Since the equations for the flow field eq. (4.56) are linear we can consider the effects of the active dipolar force \mathbf{F}^a and the polar self-propulsion force \mathbf{F}^p individually and use the superposition principle when considering the effects of having both. The flow field and pressure due to the dipolar force are therefore given as

$$\mathbf{u}^a(\mathbf{r}) = \frac{1}{2\pi\zeta^2} \int d\mathbf{r}' K_0 \left(\frac{|\mathbf{r} - \mathbf{r}'|}{\zeta} \right) (\mathbf{F}^a(\mathbf{r}') - \nabla' P^a(\mathbf{r}')) \quad (4.57)$$

$$P^a(\mathbf{r}) = \frac{1}{2\pi} \int d\mathbf{r}' \ln(|\mathbf{r} - \mathbf{r}'|) \nabla' \cdot \mathbf{F}^a. \quad (4.58)$$

And similarly for the flow field and pressure due to the polar force. In Paper (V) we use the active dipolar and polar forces related to single ideal defects and solve the above integrals to find the induced flow. An interesting result is that for the dipolar force, we find a flow reversal around the +1 defects in the limit $\Gamma = 0$. We also find that the flow field related to the polar self-propulsion force is non-decaying in the far-field. This is due to the polar self-propulsion force which, when neglecting pressure, gives the particles a constant velocity in their head direction. The homogeneous polar state will therefore in this model have a constant flow in the direction pointed out by the entities. We also find that, in the friction-dominated limit, the velocity-mediated interaction between the defects will not decay with the distance between the defects.

Polar defects As mentioned above when $K_p = 0$ the free energy in eq. (4.52) gives nematic defects which are the same as those we discussed in Section 4.2.2. Setting the parameters to $K_n = 0$ and $K_p > 0$ the free energy allows for ± 1 defects. These are the same as the defects in the Bose-Einstein condensate, but the phase gradient $\nabla\phi$ is in this case not the velocity of the fluid. Because of the coupling with the flow field \mathbf{u} the polar defects will behave a bit differently than the quantized vortices, but their structure is similar so that an ideal stationary defect of charge q at the origin has the order parameter

$$\mathbf{p}_0(r, \theta) = \chi(r) [\cos(q\theta + \theta_0), \sin(q\theta + \theta_0)], \quad (4.59)$$

where the core function χ can be found by doing an analysis similar to that in Section 3.4.2. The asymptotic behavior is also similar, with $\chi(r)$ having a linear decay to zero in the near field and tending to a constant value in the far-field.

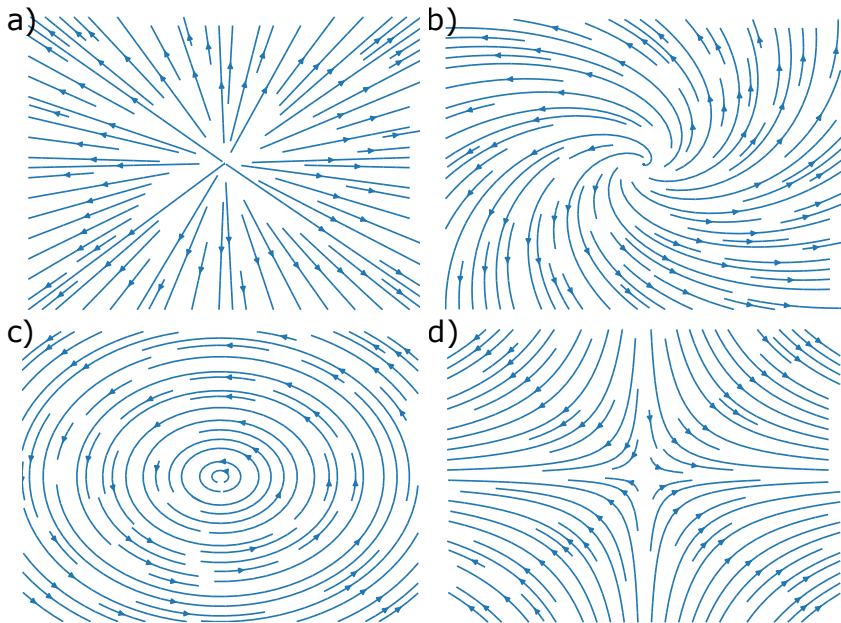


Figure 4.6: a)-c) different types of $+1$ defects. They are respectively the aster $\theta_0 = 0$, the spiral $\theta_0 = \pi/4$ and the vortex $\theta_0 = \pi/2$. Notice that they are rotationally invariant. d) a -1 defect at angle $\theta_0 = 0$.

Fig. 4.6 shows the orientation of the order parameter around ± 1 defects. Notice that the $+1$ defect is rotationally symmetric, and the constant θ_0 distinguishes the different shapes this defect can have. We refer to the defect as an aster when $\theta_0 = n\pi$ with n being an integer, a vortex for $\theta_0 = (2n - 1)\pi/2$, and a spiral for all other cases. Contrary to the other defects we have considered we can't set the constant θ_0 to zero by rotating the reference frame. We can see this by noting that the order parameter of the positive defect can be written as

$$\mathbf{p}_0(r, \theta) = \chi(r)R_{\theta_0}\mathbf{r}, \quad (4.60)$$

with

$$R_{\theta_0} = \begin{pmatrix} \cos \theta_0 & -\sin \theta_0 \\ \sin \theta_0 & \cos \theta_0 \end{pmatrix} \quad (4.61)$$

being the rotational matrix for a rotation of θ_0 . If we now rotate the reference frame by ϑ and use that rotational matrices in two dimensions commute we get that the vectorial order parameter transforms as

$$R_{\vartheta}\mathbf{p}_0 = \chi(r)R_{\theta_0}R_{\vartheta}\mathbf{r} = \chi(r')R_{\theta_0}\mathbf{r}', \quad (4.62)$$

where \mathbf{r}' is the position vector in the rotated frame. The $+1$ defect thus looks the same after a rotation, which can also be seen from Fig. 4.6. Therefore when

we consider the flow around polar defects in Paper (V) we have to keep the angle θ_0 when doing the calculations. We find that θ_0 does affect the flow and for certain values, the flow vanishes.

Defect kinematics The kinematics of the polar defects can also be found using the Halperin-Mazenko formalism. In this case the D field and its current have the form [7, 60]

$$D = \frac{1}{2!} \epsilon_{ij} \epsilon_{kl} \partial_i p_k \partial_j p_l, \quad (4.63)$$

$$j_i^D = -\epsilon_{ij} \epsilon_{kl} \partial_t p_k \partial_j p_l. \quad (4.64)$$

Putting this into the expression for the defect velocity, eq. (4.41) or (3.60) we find that the velocity of the defect labeled α is

$$\mathbf{v}^\alpha = \mathbf{u}(\mathbf{r}^\alpha) + \frac{2K_p}{\gamma} \sum_{\beta \neq \alpha} q_\alpha q_\beta \frac{\mathbf{r}^\alpha - \mathbf{r}^\beta}{|\mathbf{r}^\alpha - \mathbf{r}^\beta|^2}. \quad (4.65)$$

We have here used the quasi-static approximation of the core structure, which is the same assumption that we made to get eq. (3.67). Similar to that discussion we have assumed that all perturbations in the order parameter are in the phase and that they are due to other topological defects in the system. In Paper (V) we write this in dimensionless form, while here we have kept the units. From the discussion of the nematic point defect model 4.42 we recognize that the first term comes from the advection, while the second is from the relaxation of the free energy. One difference in this model is that the flow alignment does not appear explicitly in the equation governing the defects' kinematics. The reason for this is that the flow alignment term in eq. (4.54) is proportional to \mathbf{p} and goes therefore to zero at the phase singularity.

"Dry"-limit: In the limit of $\alpha_0 = 0$ and $\eta = 0$, the defect velocity from eq. (4.65) reduces to

$$\mathbf{v}^\alpha = -\frac{1}{\Gamma} \nabla P^p|_{\mathbf{r}=\mathbf{r}^\alpha} + \frac{2K_p}{\gamma} \sum_{\beta \neq \alpha} q_\alpha q_\beta \frac{\mathbf{r}^\alpha - \mathbf{r}^\beta}{|\mathbf{r}^\alpha - \mathbf{r}^\beta|^2}. \quad (4.66)$$

Here we have used that the flow field due to the polar self-propulsion force in the friction-dominated limit is given as $\Gamma \mathbf{u} = \alpha_p \mathbf{p} - \nabla P^p$, and that the polarity \mathbf{p} vanishes at the defect position.

We now take the "compressible" limit by neglecting the incompressibility constraint, hence the pressure gradients. The velocity of the defect, eq (4.65), reduces to the Coulomb-like interaction between defects given by

$$\mathbf{v}^\alpha = \frac{2K_p}{\gamma} \sum_{\beta \neq \alpha} q_\alpha q_\beta \frac{\mathbf{r}^\alpha - \mathbf{r}^\beta}{|\mathbf{r}^\alpha - \mathbf{r}^\beta|^2}. \quad (4.67)$$

Kinematics of a dipole If we have two defects of opposite charge at position \mathbf{r}^- (-1 defect) and \mathbf{r}^+ ($+1$ defect), we can subtract their kinematic equations eq. (4.65) to find an equation for the dipole displacement vector $\mathbf{R} = \mathbf{r}^- - \mathbf{r}^+$

$$\dot{\mathbf{R}} = \mathbf{u}(\mathbf{r}^-) - \mathbf{u}(\mathbf{r}^+) - \frac{4K_p}{\gamma} \frac{\mathbf{R}}{R^2}. \quad (4.68)$$

The effect of the polar flow field is discussed in Paper (V), we see there that the effective defect-defect interaction mediated through this flow field is only dependent on the orientation of \mathbf{R} , and not its length. This is in contrast to the passive attraction and the dipolar active flow field which both decay as $1/R$. We further show that the distance-independent interaction enhances the annihilation rate of the dipole. If we neglect the effect of the flow field, we find that the evolution of R is described by a differential equation in this form

$$\dot{R} = -\frac{C}{R}. \quad (4.69)$$

This is equivalent to the Coloumb interaction in two dimensions, meaning that the topological defects are in the quasi-static approximation following similar dynamics as electrically charged particles. The winding number, which is ± 1 , has taken a similar role as the electric charge. The solution of eq. (4.69) is of the form

$$R(t) = \sqrt{B - At}. \quad (4.70)$$

In Paper (V) we use linear regression to find the constants A and B that best match the results from a numerical simulation during a dipole annihilation with and without the polar self-propulsion force. We can find the coefficients analytically in an infinite system but in the numerical simulations, we get modifications due to the periodic boundary conditions. We also find that if we include the self-propulsion force R does not follow a curve of the form given in eq. (4.70).

Chapter 5

Numerical Methods

Here we are going to discuss the numerical methods that we have used in the different papers, namely finite element and pseudo-spectral methods. We are here restricting the discussion to two dimensions.

5.1 Finite elements

The finite elements method is a method for solving differential equations that we used to solve the Stokes equations for the active flows in Paper (I) and (II). We are here going to show the main ideas behind this method by using the Poisson equation as an example. To make the discussion easier we restrict ourselves to homogeneous Dirichlet boundary conditions. The Poisson equation reads

$$-(\kappa \nabla^2 u) = f, \text{ in } \Omega \tag{5.1}$$

$$u = 0, \text{ on } \partial\Omega. \tag{5.2}$$

Here, $\Omega \subset \mathbb{R}^2$ is the domain of interest and $\partial\Omega$ is the boundary of this domain. To solve this, we multiply the equation with a test function v and integrate the equation over the domain [90]. After an integration by parts, it reads

$$\int_{\Omega} d\mathbf{r} \kappa \nabla u \cdot \nabla v = \int_{\Omega} d\mathbf{r} f v. \tag{5.3}$$

The test function v is an element of a test function space \mathbb{V}_t , while our trial function u is in the trial function space \mathbb{V} . When we have homogeneous Dirichlet conditions the trial and test spaces are the same [90], and have the restriction that the functions have to go to zero on the boundary.

The problem now is to find the function u so that eq. (5.3) is satisfied for all test functions v in the space \mathbb{V} . To solve this on a computer we discretize the function spaces. Any function in the discrete function space \mathbb{V}_d can be written as a linear combination of the basis functions N_i . Our trial function u is now written on the form $u = u_j N_j$. Since eq. (5.3) should hold for any $v \in \mathbb{V}_d$ we need to show that it holds for all the basis functions. We, therefore, get the N equations

$$\int_{\Omega} d\mathbf{r} \kappa u_i \nabla N_i \cdot \nabla N_j = \int_{\Omega} d\mathbf{r} f N_j. \tag{5.4}$$

This can be written in matrix form as

$$\mathbf{A}\mathbf{u} = \mathbf{f}, \tag{5.5}$$

5. Numerical Methods

with $A_{ij} = \int_{\Omega} d\mathbf{r} \kappa \nabla N_i \cdot \nabla N_j$, $u_i = u_i$ and $f_i = \int_{\Omega} d\mathbf{r} f N_j$. The problem is now reduced to a linear set of equations. For this to be easy to solve, we need a smart choice of the discrete function space \mathbb{V}_d and its basis functions N_i .

The finite element method provides a way of constructing the discrete basis. The space and basis are constructed by first dividing the domain Ω into cells. In two dimensions, a popular choice for the shape of the cells is triangular, but other shapes are also popular and give different types of advantages and disadvantages [90]. Fig. 5.1 a) shows how a circular domain can be divided up into a mesh of triangular cells. When this is done, one defines a local function space \mathbb{V}_l for each of the cells and constructs the discrete function space \mathbb{V}_d as the collection of the local ones [90]. The basis functions live only inside the local func-

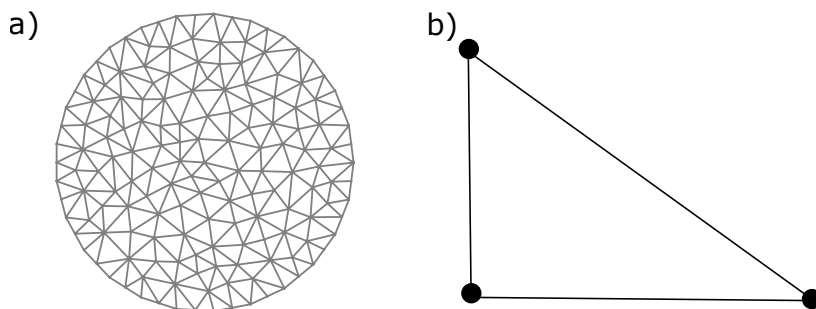


Figure 5.1: a) division of a circular domain into triangular cells. b) a triangular cell with nodes on the vertices.

tion spaces and each function in \mathbb{V}_d is constructed by linear combinations of these.

A popular choice of basis functions is linear Lagrangian functions. For the triangular cells, this basis is constructed by putting a node on each vertex as shown in Fig. 5.1 b) and choosing a basis of three functions that is zero on two of the nodes and one on the last. For example if the element has nodes on $(0, 0)$, $(0, 1)$ and $(1, 0)$ the basis will be [90]

$$f_1(x, y) = 1 - x - y, \quad (5.6)$$

$$f_2(x, y) = x, \quad (5.7)$$

$$f_3(x, y) = y. \quad (5.8)$$

For higher-degree polynomials, one simply puts more nodes on the elements. Once the basis vectors for each element are chosen, one has to stitch them together. For the piecewise linear functions described above one only needs to identify all the nodes, but other types of functions might require more care. The functions that are constructed by the piecewise linear basis are continuous. We can see this if we consider two neighboring elements that share two nodes and one edge. Since the basis functions are linear polynomials that have the

same value on the nodes they will also be equal on the entire line connecting the nodes. The function constructed by them is therefore continuous. The derivative is however not, and one should therefore be careful with taking second-order derivatives of functions in this space. Once the basis is created, one can calculate the matrix A in eq. (5.5) and solve the linear set of equations. Note that since all basis functions only live on one element the matrix A will be sparse.

In paper I and II we used finite elements to solve the set of equations

$$(\Gamma - \eta \nabla^2) \mathbf{u} = \mathbf{F} - \nabla p, \quad (5.9)$$

$$\nabla \cdot \mathbf{u} = 0, \quad (5.10)$$

with $\mathbf{u} = 0$ on the boundary. Here \mathbf{u} is the unknown velocity field, p is an unknown pressure, and \mathbf{F} is a known source. The first equation is a vector equation while the second is a scalar equation. We, therefore, need two sets of function spaces, the vector space \mathbb{V} and the scalar space \mathbb{Q} [90]. Both these spaces have corresponding trial and test spaces. Note that the pressure p is an unknown and is a linear trial function while the velocity \mathbf{u} is a vectorial trial function. We now multiply eq. (5.9) and eq. (5.10) with a vector test function \mathbf{b} and a scalar test function q respectively. We then integrate over all of the space and do integration by parts

$$\Gamma \int_{\Omega} d\mathbf{r} \mathbf{u} \cdot \mathbf{v} + \eta \int_{\Omega} d\mathbf{r} \partial_i u_j \partial_i v_j - \int_{\Omega} d\mathbf{r} p (\nabla \cdot \mathbf{v}) = \int_{\Omega} d\mathbf{r} \mathbf{F} \cdot \mathbf{v} \quad (5.11)$$

$$\int_{\Omega} d\mathbf{r} q \nabla \cdot \mathbf{u} = 0. \quad (5.12)$$

The surface term has been taken care of by the boundary condition (remember that $v = 0$ on the Dirichlet boundary). We add these equations and end up with

$$\Gamma \int_{\Omega} d\mathbf{r} \mathbf{u} \cdot \mathbf{v} + \eta \int_{\Omega} d\mathbf{r} \partial_i u_j \partial_i v_j - \int_{\Omega} d\mathbf{r} p (\nabla \cdot \mathbf{v}) + \int_{\Omega} d\mathbf{r} q \nabla \cdot \mathbf{u} = \int_{\Omega} d\mathbf{r} \mathbf{F} \cdot \mathbf{v}. \quad (5.13)$$

We now do the same as we did for the Poisson equation. That is, we write \mathbf{u} and p as a linear combination of the basis vectors and use that eq. (5.13) should hold for \mathbf{v} and q being any of the basis vectors. When implementing this, we use a mixed function space \mathbb{W} which contains the functions in \mathbb{V} and \mathbb{Q} and let the open source package FEniCS construct and solve the linear set of equations [90]. We only need to decide which function spaces we want to use. For this equation, we have chosen to use Taylor-Hood elements where the vector space is piecewise quadratic and the scalar space is piecewise linear. This is chosen because this construction is known to be Stokes stable, i.e., it is known to be able to solve eq. (5.13) when $\Gamma = 0$ [90].

5.2 Pseudospectral methods and exponential time differentiation

When working with periodic boundary conditions on a uniform grid, we can take advantage of the ease of finding derivatives of functions in Fourier space. Considering the derivative of the function $f(x)$ we can expand it in Fourier space to find

$$\partial_i f(x) = \frac{1}{(2\pi)^2} \partial_i \int d\mathbf{k} \tilde{f}(\mathbf{k}) e^{i\mathbf{k}\cdot\mathbf{r}} = \frac{1}{(2\pi)^2} \int d\mathbf{k} i k_i \tilde{f}(\mathbf{k}) e^{i\mathbf{k}\cdot\mathbf{r}}, \quad (5.14)$$

which means that the Fourier transform of $\partial_i f(x)$ is $i k_i \tilde{f}(\mathbf{k})$. This can be exploited to map an ordinary differential equation into N equations for the Fourier modes. For example the Poisson equation, eq. (5.1), can be solved in Fourier space as

$$\tilde{u}(\mathbf{k}) = \frac{1}{\kappa k^2} \tilde{f}(\mathbf{k}), \quad (5.15)$$

for $k > 0$. Note that the Poisson equation with periodic boundary conditions can only be solved up to a constant term that is given as the zero mode, $u_0 = \tilde{u}(k=0)$, meaning that an additional condition to set this. We need to solve the Poisson equation to find the pressure when solving the hydrodynamic equations for the active systems discussed in Chapter 4. The zero mode is then a constant term in the pressure and has no physical effect. We therefore set it to zero.

In addition to making the process of solving ODEs simple, the Fourier transform can be used to solve partial differential equations (PDE) by mapping them into ODEs for the Fourier modes. A simple example of this is the diffusion equation

$$\partial_t u(\mathbf{r}, t) = D \nabla^2 u(\mathbf{r}, t), \quad (5.16)$$

which in Fourier space takes the form

$$\partial_t \tilde{u}(\mathbf{k}, t) = -D k^2 \tilde{u}(\mathbf{k}, t). \quad (5.17)$$

This can be solved exactly. Given some initial conditions $\tilde{u}(\mathbf{k}, t=0) = \tilde{u}_0(k)$ it has the solution $\tilde{u}(\mathbf{k}, t) = \tilde{u}_0(k) e^{-D k^2 t}$.

We are however going to consider non-linear equations that can not be solved analytically. Consider an equation of the form [46, 47, 91]

$$\partial_t \psi(\mathbf{r}, t) = \omega(\nabla) \psi(\mathbf{r}, t) + N(\psi, t), \quad (5.18)$$

where $\omega(\nabla)$ is a linear differential operator and $N(\psi, t)$ is the non-linear part of the equation. In Fourier space, this equation takes the form

$$\partial_t \tilde{\psi}(\mathbf{k}, t) = \tilde{\omega}(k) \tilde{\psi}(\mathbf{k}, t) + \tilde{N}(\psi, t). \quad (5.19)$$

We now have one ODE for each Fourier node. Note that the linear part of these equations is stiff (unstable when using explicit methods) for large k , and therefore requires some extra care. We will take advantage of the fact that the linear part is exactly solvable, using what is known as an exponential time differencing scheme (ETD)[91].

We start by multiplying eq. (5.19) by the integrating factor $e^{-\tilde{\omega}(k)t}$ so that it becomes

$$\partial_t(\tilde{\psi}e^{-\tilde{\omega}t}) = e^{-\tilde{\omega}t}\tilde{N}(\psi, t). \quad (5.20)$$

We now integrate this equation from t to $t + \Delta t$. After some work, it takes the form [46, 47, 91]

$$\tilde{\psi}(t + \Delta t) = e^{\tilde{\omega}\Delta t}\tilde{\psi}(t) + e^{\tilde{\omega}\Delta t} \int_0^{\Delta t} d\tau e^{-\tilde{\omega}\tau} \tilde{N}(\psi, t + \tau), \quad (5.21)$$

so the problem is now reduced to finding an approximation for the integral of the function $e^{-\tilde{\omega}\tau}\tilde{N}(\psi, t)$. To do this, we are going to use a scheme analogous to the improved Euler method [91]. We start by evaluating the integral assuming that $N(t + \tau) = N_0$ is a constant in the interval $\tau \in (0, \Delta t)$. Doing this we get

$$\tilde{a}(t + \Delta t) = e^{\tilde{\omega}\Delta t}\tilde{\psi}(t) + \frac{\tilde{N}_0}{\tilde{\omega}} (e^{\tilde{\omega}\Delta t} - 1). \quad (5.22)$$

We could stop here and use $\tilde{a}(t + \Delta t)$ as the value for $\tilde{\psi}(t + \Delta t)$. That is the integration scheme known as the ETD1 scheme [91]. We are instead going to use \tilde{a} to get a better guess for $N(t + \tau)$ to improve the numerical integration. We then assume that N is linear in the interval of integration, so it is given by $N(\psi, t + \tau) = N_0 + N(a(t + \Delta t), t + \Delta t)\tau/\Delta t$. Performing the integral we get the following two-step scheme [46, 47, 91]

$$\tilde{a}(t + \Delta t) = e^{\tilde{\omega}\Delta t}\tilde{\psi}(t) + \frac{\tilde{N}_0}{\tilde{\omega}} (e^{\tilde{\omega}\Delta t} - 1), \quad (5.23)$$

$$\tilde{\psi}(t + \Delta t) = \tilde{a} + (N(\tilde{a}, t + \Delta t) - N_0) \frac{1}{\tilde{\omega}} \left((e^{\tilde{\omega}\Delta t} - 1) \frac{1}{\tilde{\omega}\Delta t} - 1 \right). \quad (5.24)$$

This is the ETDRK2 scheme. It is in a similar way possible to use higher order Runge-Kutta schemes to integrate eq. (5.21).

We have used the above scheme to solve the dGPE eq. (3.7) and to simulate the active nematic eq. (4.8) and the active polar system 4.54. For the active nematic, we use the scheme in Paper (IV) to look at how the active stress drives the system from an initially homogeneous nematic state with small perturbations in the phase to a defect-driven turbulent state. In Paper (V) we use this scheme to compare the annihilation of a defect dipole in a system with the polar self-propulsion force and one without. The defects are here initialized as phase singularities with a linear core. We then evolve the equation for a time of order

5. Numerical Methods

the relaxation time, $\tau = \gamma/A$, with the flow field set to zero to let the cores form. We can do this because the equation is dissipative and will evolve to a lower energy state and form the proper core function for the defects. For both the active nematic and the polar active matter we find the flow fields and pressures by solving the equations directly in Fourier space. For the BEC in Paper (III) and (IV) we evolve the dGPE in imaginary time to find the lowest energy state.

Chapter 6

Papers: Summary and Outlook

In this chapter, we summarise the papers and present an outlook for the direction of future works.

6.1 Paper I

Title : Flow around topological defects in active nematic films

Summary: The dynamics of the topological defects play a prominent role in the two-dimensional active nematic in the defect-laden turbulent phase. These defects are point-like, but unless they are screened by the presence of other defects, their presence will affect the entire system. The active stress creates a flow whenever there are inhomogeneities in the order parameter Q , and the presence of topological defects is therefore related to a non-zero flow. In this paper, we studied the flow field due to individual ideal point defects of charge $\pm 1/2$ in an active nematic by solving the incompressible Stokes equation eq. (4.20) analytically in an infinite system and numerically for bounded systems of radius R . This was done by putting the Q tensor related to an ideal defect, see Section 4.4.2 and 3.4.2, into the equations for the flow field. This setup has previously been studied for systems with no friction [92], and here we extend the analysis to also include the friction with the substrate Γ .

Including the friction has some notable effects on the flow for systems that are large compared to the hydrodynamic dissipation length $R \gg \ell_d = \sqrt{\eta/\Gamma}$, which is illustrated in the self-propulsion of the $+1/2$ defect. Due to its asymmetry in the axis defined by its polarization, there is a net active force acting on the $+1/2$ defect which induces a non-zero velocity at its core. The defect will therefore move either in the direction of its polarity for a contractile system $\alpha_0 > 0$ or opposite this direction for an extensile system $\alpha_0 < 0$. When ignoring the friction term $\Gamma = 0$ Ref. [92] found that the self-propulsion velocity is proportional to the system size R . When we include friction, we only get this behavior for small systems $R \ll \ell_d$ where the viscous effects are dominating. For large systems $R \gg \ell_d$ the friction with the substrate becomes important and the velocity saturates to a value proportional to ℓ_d . We, therefore, expect the corrections to Ref. [92] to become important when the distance between defects is large. That is, in systems where the density of defects is low. In addition to affecting the magnitude, the size of the system also affects the shape of the flow field. The flow fields created around the defects form two counter-rotating vortices around the $+1/2$ defect and six around the $-1/2$ defects. In the frictionless limit, the flow field has the same shape regardless of the value of R and the system size

only controls the magnitude of the velocity. When friction Γ is included one sees that the shape of the vortices changes, so that when R grows they get more elongated. In the infinite system limit the vortices extends to infinity and do not close.

In addition to finding the flow fields in the point defect approximation, we also look at core effects for the self-propulsion of the $+1/2$ defect. We do this by using the linear core approximation, where we assume that the parameter S is constant in the far-field and goes to zero linearly in the near field over the size of the coherence length ξ . Analytically, we can solve the equations at the phase singularity to get the self-propulsion velocity in the limit of an unbounded defect. The result is written as a function of the ratio $\zeta = \ell_d/\xi$ and in the limit $\xi \ll \ell_d$ we find that the defect speed becomes, in dimensional units,

$$v = \frac{\pi}{4} \frac{\alpha_0}{\Gamma \ell_d} \left[1 + \left(C_1 + C_2 \ln \left(\frac{\xi}{\ell_d} \right) \right) \frac{\xi}{\ell_d} \right], \quad (6.1)$$

with C_1 and C_2 being two constants. This converges to the point defect value in the limit of $\xi \rightarrow 0$.

Outlook In this paper, we studied the self-induced flow fields that are created around topological defects. To get analytically tractable results, we neglected that the non-zero flow will deform the defects which again will modify the flow that we found and the effects of the passive stress. It would thus be interesting to find the corrections to this.

Something else that we have neglected in the work considered here is that the defects have a non-zero velocity. As mentioned in the main text, the movement of a defect in a dissipative field tends to deform it which, in addition to affecting the active flow, leads to a velocity-dependent mobility [21, 62, 93]. This effect will lead to corrections to the self-induced velocity of the $+1/2$ defects and it would be interesting to consider what these effects are.

6.2 Paper II

Title: Defect self-propulsion in active nematic films with spatially-varying activity

Summary: In Paper (I) we studied the flow field and self-propulsion for lone defects in an active nematic system where the activity α_0 was assumed to be constant. In this follow-up paper, we looked at the effects of making this parameter spatially varying. This was inspired by recent work where they use spatially patterned activity to control the motion of topological defects [94–96]. We wanted to see how much of this dynamic could be described by considering the self-induced flow of idealized point defects. We, therefore, considered two setups that are analytically tractable. In the first setup, the activity had a constant gradient in the x direction, while in the second there was an interface

between two regions with different activities. In both cases, we considered ideal coreless defects placed at the origin in an otherwise unperturbed nematic and neglected that the self-induced flow fields will deform the defect.

For the first setup, we found that the self-propulsion of the positive defect is only determined by the local activity at its center. The constant gradient induces a circular flow around the $+1/2$ defect if the polarization is not pointing parallel or anti-parallel to the gradient. This has the effect of turning the defect and we found that the flow tends to reorient the defect so that it points opposite to the gradient. If the local activity is positive, it will tend to rotate so that it eventually moves down the gradient. If the activity is negative, the defect will eventually move up the gradient. In both cases, it is moving so that the absolute value of the local activity is lowered. So the effect of the gradient is to rotate the $+1/2$ defect so that it will move to regions with lower absolute activity and thus reduce the self-propulsion speed. For the $-1/2$ defect, the constant gradient does not induce any non-zero velocity or vorticity at the center so it stays stationary also in this case.

In the second setup, we had to neglect the pressure contributions to be able to get analytic solutions. The results show that the self-propulsion and reorientation of both defects are affected. For the positive defect, it tends to slow down and reorient so that it points perpendicular to the interface. The negative defect starts to rotate towards a preferred orientation relative to the interface. If it has this orientation, which depends on the sign of activity, it becomes attracted to the interface, while other orientations become repelled. Note that when the interface is steep, it will produce strong flows so the approximation that the flow does not affect the shape of the defects only holds when it is far from the interface.

Outlook Here we considered the self-induced flow and vorticity at the center of ideal defects in an active system with spatially varying activity. As mentioned, we neglect the deformation of the Q tensor here due to the flow field and only consider an ideal defect profile in an infinite system. In the case of the sharp active interface, there will be large stresses on the interface which will effectively induce anchoring conditions on the nematic director. This will deform the defects profile and have an effect on the flow and the motion of the defect and it would therefore be interesting to consider the effects of this. Numerically it would be interesting to imprint different geometries in the activity and study how this is affecting the dynamics of the defects.

6.3 Paper III

Title: Precursory patterns to vortex nucleation in stirred Bose-Einstein condensates

Summary: The Halperin-Mazenko formalism is very good for tracking topological defects, but it requires us to evaluate a delta function to get the defect density eq. (3.52). However, we can get a lot of information on the nucleation and kinematics of the defects using the D field alone. This is beneficial because it does not require us to introduce a singular field. In this paper, we studied defects that are nucleated in a Bose-Einstein condensate described by the Gross-Pitaevskii theory, see Chapter 3. The defects were nucleated by stirring the BEC with a Gaussian stirring potential, $\mathcal{U} = U_0 e^{-(\mathbf{r}-\mathbf{r}_0)^2/d^2}$, and we studied how the D field and its conserved current shows the formation of the defect core prior to the defect nucleation. The idea is that since D is a conserved quantity and we know it is non-zero in the core of topological defect, then D and its current $\mathbf{J}^{(D)}$ should capture the formation of the defect cores prior to the nucleation of the phase singularities and thereby act as a precursory event. We looked at two different coupling strengths for the potential, one that is weakly coupled $U_0 = 0.8\mu$ and one that is strongly coupled $U_0 = 10\mu$. For the strongly coupled potential, the nucleation of the vortices is preceded by the formation of a halo in the D field at the edge of the potential. At the same time, a phase slip is formed in the depleted region under the potential. If the velocity is below a critical velocity, one reaches a steady state where the phase slips are formed, but they never migrate to the bulk. These unshed phase slips are known as ghost vortices [97]. If the stirring velocity is higher than a critical velocity, the phase slips detach and move towards the edge. While the phase slips move to the edges the halo in the D field forms two blobs, which the phase slips eventually migrate into. For the weakly coupled potential, the D field shows the formation of two cores under the potential before the phase slip is formed. The cores are then created before the phase slip occurs and act as a precursor event. In this case, there is no steady state where the phase slip remains stable under the potential. Once they are formed inside the cores, the defects are shed. The conserved current $\mathbf{J}^{(D)}$ plays an important role in the formation of the cores since it is this current that creates the cores in the D field that will eventually harbor the phase singularities.

Outlook In this paper, we used the D field to study the nucleation of topological defects in a stirred Bose-Einstein condensate, with a focus on the formation of the defect's core and the role of the conserved current $\mathbf{J}^{(D)}$. Once the defects are nucleated, they are going to interact with perturbations in the condensate, both linear and non-linear. Both defects and non-linear excitations are captured by the D field and its conserved current, and it would therefore be interesting to use this formalism to study their interactions in detail.

6.4 Paper IV

Title: A unified field theory of topological defects and non-linear local excitations

Summary: The topic of this paper is a generalization of the formalism we used in Paper (III). Here we motivated the use of a coarse-grained topological density field to study topological defects and non-linear local excitations in a system with broken $O(n)$ symmetry. This field is proportional to the D field that we discussed in Section 3.5, and we generalize this density and its current to d spatial dimensions for a n dimensional order parameter giving a general expression for the velocity of the defects. To illustrate the versatility of the method we used it to study dipole annihilation in a Bose-Einstein condensate, the onset of active turbulence in an active nematic, and the nucleation of dislocations in the phase field model.

For the onset of active turbulence, we initialized a homogeneous nematic state with small perturbations in the angle of the director. The active stress enhances the initial perturbations and creates periodic arches, i.e., smectic-like distortions in the nematic field. When these arches appear the continuous translational symmetry of the homogeneous state becomes broken, and we can describe the newly formed periodic arched state by constructing a new order parameter. The periodic arch state has dislocations, which are topological defects in the order parameter of this state. These dislocations act as sources for the nucleation of $\pm 1/2$ defects in the nematic order. When the $\pm 1/2$ defects are nucleated the system goes into an active turbulent regime and the periodic order is melted in addition to the global orientational order.

This approach shows the route to active turbulence through competing symmetries. The onset of the turbulent state is here mediated by an intermediate striped phase, when the periodic arches are destroyed by the "splitting" of its dislocations into $\pm 1/2$ defects, which changes the global symmetry of the system. This route to active turbulence fits well with the usual interpretation of defect nucleation being favored in areas of high elastic energy [68], since the dislocations in the arches are areas with substantial deformations in the Q -tensor. These gradients are further enhanced by the active stress, leading up to the creation of the $\pm 1/2$ defects. Note that the mechanism for the nucleation of defects is different when friction with the substrate is neglected [68, 98]. Also in this case there are formed arches/walls in the nematic order and the defects are formed on the walls, without being seeded by dislocations.

For the dipole annihilation in the Bose-Einstein condensate, we initialized a dipole and evolved the system with the dGPE, and visualized the coarse-grained topological density field and the related velocity field. After the annihilation event, the depleted region in the condensate, corresponding to the overlapping defect cores that previously harbored the phase singularities, is no longer protected and diffuses into the condensate as a shock wave. The D field still captures the shock wave created during the annihilation and shows how it diffuses away into the condensate. The last example concerns dislocations in the phase field crystal where we also look at precursory patterns prior to nucleation, and the breakdown of this description when the underlying translational order is melted.

6. Papers: Summary and Outlook

For the phase field crystal, we also consider defects that have an anisotropic core structure.

Outlook The coarse-grained topological density current gives information about the nucleation process and acts as a precursor. In the example of the active nematic, we saw that the precursor event for the defect nucleation was to first break the translational symmetry by forming periodic arches. Evolving this in time we saw the formation of topological defects in the arched phase which were nucleated at the location where the defects in the nematic eventually nucleated, which in turn melted the order parameter of the arches. This suggests that there might be a hierarchy of topological defects. With this, we mean that the defects in an ordered system with some broken symmetry can act as seeds for defects of another ordered phase, restoring one of the broken symmetries of the former ordered system and melting the order parameter. This hierarchical structure is also hinted at in the three-dimensional APFC model where the grain boundaries of a bicrystal are created at the same location as a disclination network in the single crystal which simultaneously melts the crystal order. It would be interesting to see if other systems with multiple broken symmetries have the same hierarchical structure in the nucleation of defects, with defects in one order parameter spawning defects in another with more symmetries.

6.5 Paper V

Title: Spontaneous flows and dynamics of full-integer topological defects in polar active matter

Summary: In the last paper, we solved the flow equations around ideal point-like topological defects of charge ± 1 in the polar model described in Section 4.3, for both the dipolar active force $\alpha_0 \nabla \cdot Q_p$ and for the polar self-propulsion force $\alpha_p \mathbf{P}$. The dipolar active force gives a circular flow field around the $+1$ defects which vanishes for ideal asters or vortices, while the flow field around the -1 defect gets divided into eight regions of oppositely signed vorticity. In the limit where friction was neglected, we find that there should be a flow reversal around the $+1$ defect. The flow equations do not give the scale of the reversal since in the limit of point defects there is no length scale in the problem. We expect the reversal to happen on the scale of the neglected core size, which is confirmed numerically by averaging the flow fields around defects in large-scale simulations of eq. (4.54)–(4.56). We also found the flow field related to the polar self-propulsion force and saw that the flow induced by this force is non-decaying in the far-field.

In the last part of the paper, we considered a pair of oppositely charged point defects in an otherwise unperturbed system in the friction-dominated limit, and study how the defects interact through the activity-induced flow by evaluating the flow field at the positions of the defects. For the dipolar active force, the

interaction decays as $1/R$, with R being the distance between the defects. We also find that the interaction due to the polar self-propulsion is non-decaying in the far-field, and showed that this non-decaying interaction leads to enhanced defect annihilation. Simulations with and without the polar self-propulsion force show that it tends to speed up the annihilation rate, and we believe that this is the main mechanism behind the suppression of the defect density when this force is included.

Outlook In the first part of this paper, we studied the flow fields around the topological defects in a system of an individual coreless defect in a system with constant activity and friction with the substrate. There has been recent work on the active nematic where they vary the substrate geometry, which effectively makes the activity and friction spatially dependent [99]. It would be interesting to study the effects a spatially varying friction would have on the flow due to the polar self-propulsion force around single defects, and the effects on the dynamics of a pair of oppositely charged defects.

In the second part, we evaluated the flow field of a defect dipole at the center of the positions of the defects to consider the defect-defect interaction mediated through the flow. Here, we restricted ourselves to the friction-dominated limit, neglecting the effects of viscosity. It would therefore be interesting to see whether the viscous effects have any large impact on the results, especially once the distance between the defects becomes small. It would also be interesting to extend the analysis to N vortices of arbitrary charge to get a point defect model. For the superfluid and the active nematic, it is possible to coarse-grain the point defect model into a hydrodynamic description of the defect gas [81, 100]. It would be interesting to consider a similar construction for this polar system and see how including the polar self-propulsion flow modifies the behavior compared to the active nematic.

Chapter 7

Conclusion

We have seen that the topological defects in weakly interacting Bose-Einstein condensates and active matter with nematic and polar symmetries can, in two dimensions, be described using the Halperin-Mazenko formalism where the defects are tracked by introducing the defect density field D and its current \mathbf{j}^D . This formalism allows us to derive the defect's equation of motion using the quasi-static core approximation, and study the defect nucleation through the localization of the D field at the cores of the defects. We can use the same formalism because the ordered phase in these systems is due to the underlying rotational symmetry ($SO(2)$) and tied to the ϕ^4 free energy, which makes it possible to map their order parameters into each other. However, there are important dynamical differences that are reflected in the defect kinematics, nucleation, and interactions.

We saw in Chapter 3 that in the mean-field approximation, the dynamics of the Bose-Einstein condensate at zero temperature is conservative and dictated by the grand canonical Hamiltonian. To include interactions with the equilibrium thermal cloud, we introduced a dissipative part through a constant thermal drag γ . Using the Halperin-Mazenko formalism and the quasi-static core approximation, we find a kinematic model for the motion of the defects as discussed in Chapter 3 and Paper (III). We see that the distinction between the dissipative and conservative parts of the dGPE is reflected in the defect kinematics, i.e. γ introduces a Coulomb-like interaction between the defects, while the conservative part reproduces the Hamiltonian point defect model.

The hydrodynamics of active fluid, as discussed in Chapter 4, is described in terms of the dissipative dynamics of the Q tensor/ \mathbf{p} vector order parameter coupled with a Stokes flow. Similar to the BEC system, we used the Halperin-Mazenko formalism to show how this hydrodynamic description determines the motion of the defects. In addition to the Coulomb-like interaction due to the dissipative dynamics, the defects are moved by fluid flows. This flow field is coupled to the order parameter through configurational stresses so that the presence of defects causes flows that move defects and mediate interactions between them. In Paper. (I), (II) and (V) we studied the active flow induced by the defects, in order to get insight into their dynamics. Topological defects are non-linear excitations in the order parameter making them challenging to study, especially in the active turbulent regime where the density of defects is high. For analytical traceability, we, therefore, assumed idealized, pointwise defects to study the spontaneous flows due to their far-field structure.

7. Conclusion

In Paper. (I), and (II) we studied the flow field due to isolated $\pm 1/2$ defects in an active nematic. In Paper. (I) we found that the hydrodynamic length scale ℓ_d set by friction and viscosity, plays an important role for the defect self-propulsion speed and the far-field flow profile. In Paper (II) we study the defects self-propulsion and how they tend to rotate in a system where the activity is spatially varying. In Paper (V) one of the themes was the flow induced by ± 1 defects and the effects of the activity-induced flow fields on the defect-defect interaction. Here we studied the flow fields of ± 1 defects subject to both the active stress and the self-propulsion force. We predicted a flow reversal of the chiral active flow around a $+1$ defect in the limit of zero friction, and non-local mutual interaction between defects due to the self-propulsion force. Even though there may be corrections due to the defect core, our analysis was able to reproduce phenomena reported in previous numerical and experimental studies. For example, in Paper. (II) we predicted how $\pm 1/2$ defects reorient to a preferred direction as they approach an activity interface, as observed in numerical studies [101, 102]. Also, we theoretically predicted the accumulation of $-1/2$ defects next to an activity interface [94] and in Paper. (V) we predicted the suppression of ± 1 defects by the polar self-propulsion force [7]. The last effect is due to a non-local defect-defect interaction mediated through the flow field, while the two first effects are consequences of a spatially dependent activity as discussed in Paper (II).

In Chapter 3, we saw that the coarse-grained topological density field D is a conserved quantity. This is utilized in Paper (III) and (IV) where we study the defect nucleation as a process where the D field becomes localized around the defect cores, and the annihilation process where the D field disappears while the core diffuses into the bulk. The homogeneous nucleation of defects in these two systems looks a bit different, but they have much in common. Firstly, we need energy to be injected. In the Bose-Einstein condensate, the particles are passive so we need to inject the energy externally, e.g., by stirring it with a potential, while for the active fluids the energy injection happens at the single particle scale which comes into the hydrodynamic description as the active stress. Secondly, there has to be a seed for the defects to form, which for the active fluid is given by the initial perturbations. These perturbations grow into a striped phase with dislocations, and these dislocations then act as seeds for the defect nucleation. In the condensate, the defects are created by the potential. When the nucleation happens, it is in both systems shown as a gradual process where the D field localizes into the cores. The phase singularities are either created inside the cores or move into them from the depleted region under the potential.

In this thesis, we have bridged the fields of active matter and Bose-Einstein condensates using the Halperin-Mazenko formalism as a unified framework for studying the topological defects resulting from the broken $SO(2)$ symmetry. As discussed in Paper (IV) the theoretical formalism presented in this thesis can be extended to arbitrary dimensions. An interesting venue for further research is to extend the derivations beyond the frozen core approximation. It is an elegant, versatile, and minimal formalism that can be applied across several systems,

something we exemplify by using it to mathematically bridge the systems of active liquid crystals and superfluids.

Bibliography

- [1] Rønning, J., Marchetti, C. M., Bowick, M. J., and Angheluta, L. “Flow around topological defects in active nematic films”. In: *Proceedings of the Royal Society A* vol. 478, no. 2257 (2022), p. 20210879.
- [2] Rønning, J., Marchetti, M. C., and Angheluta, L. “Defect self-propulsion in active nematic films with spatially varying activity”. In: *Royal Society Open Science* vol. 10, no. 2 (2023), p. 221229.
- [3] Rønning, J. and Angheluta, L. “Precursory patterns to vortex nucleation in stirred Bose-Einstein condensates”. In: *Physical Review Research* vol. 5, no. 2 (2023), p. 023108.
- [4] Skogvoll, V., Rønning, J., Salvalaglio, M., and Angheluta, L. “A unified field theory of topological defects and non-linear local excitations”. In: *npj Computational Materials* vol. 9, no. 122 (2023).
- [5] Rønning, J., Renaud, J., Doostmohammadi, A., and Angheluta, L. “Spontaneous flows and dynamics of full-integer topological defects in polar active matter”. In: *Soft Matter* (2023).
- [6] Moen, E. Q. Z., Olsen, K. S., Rønning, J., and Angheluta, L. “Trapping of active Brownian and run-and-tumble particles: A first-passage time approach”. In: *Physical Review Research* vol. 4, no. 4 (2022), p. 043012.
- [7] Andersen, B. H., Renaud, J., Rønning, J., Angheluta, L., and Doostmohammadi, A. “Symmetry-restoring crossover from defect-free to defect-laden turbulence in polar active matter”. In: *Physical Review Fluids* vol. 8, no. 6 (2023), p. 063101.
- [8] Anderson, P. W. “More is different”. In: *Science* vol. 177, no. 4047 (1972), pp. 393–396.
- [9] Chaikin, P. M. and Lubensky, T. C. *Principles of condensed matter physics*. Cambridge: Cambridge University Press, 1995.
- [10] Martin, P. C., Parodi, O., and Pershan, P. S. “Unified hydrodynamic theory for crystals, liquid crystals, and normal fluids”. In: *Physical Review A* vol. 6, no. 6 (1972), p. 2401.
- [11] Sethna, J. P. *Statistical Mechanics: Entropy, Order Parameters and Complexity (Oxford Master Series In Statistical, Computational, and Theoretical Physics)*. Oxford: Oxford University Press, 2012.
- [12] Frank, F. C. “The influence of dislocations on crystal growth”. In: *Discussions of the Faraday Society* vol. 5 (1949), pp. 48–54.

- [13] Skaugen, A., Angheluta, L., and Viñals, J. “Dislocation dynamics and crystal plasticity in the phase-field crystal model”. In: *Physical Review B* vol. 97, no. 5 (2018), p. 054113.
- [14] Skogvoll, V., Angheluta, L., Skaugen, A., Salvalaglio, M., and Viñals, J. “A Phase Field Crystal Theory of the Kinematics of Dislocation Lines”. In: *Journal of the Mechanics and Physics of Solids* vol. 166 (Sept. 2022), p. 104932.
- [15] Gennes, P. G. d. *The physics of liquid crystals*. 2nd ed. Vol. 83. The International series of monographs on physics. Oxford: Clarendon Press, 1993.
- [16] Poulin, P., Stark, H., Lubensky, T., and Weitz, D. “Novel colloidal interactions in anisotropic fluids”. In: *Science* vol. 275, no. 5307 (1997), pp. 1770–1773.
- [17] Durrer, R., Kunz, M., and Melchiorri, A. “Cosmic structure formation with topological defects”. In: *Physics Reports* vol. 364, no. 1 (2002), pp. 1–81.
- [18] Svistunov, B. “Strongly non-equilibrium Bose–Einstein condensation in a trapped gas”. In: *Physics Letters A* vol. 287, no. 1-2 (2001), pp. 169–174.
- [19] Weiler, C. N., Neely, T. W., Scherer, D. R., Bradley, A. S., Davis, M. J., and Anderson, B. P. “Spontaneous vortices in the formation of Bose–Einstein condensates”. In: *Nature* vol. 455, no. 7215 (2008), pp. 948–951.
- [20] Maroudas-Sacks, Y., Garion, L., Shani-Zerbib, L., Livshits, A., Braun, E., and Keren, K. “Topological defects in the nematic order of actin fibres as organization centres of Hydra morphogenesis”. In: *Nature Physics* vol. 17, no. 2 (2021), pp. 251–259.
- [21] Pismen, L. *Vortices in Nonlinear Fields: From Liquid Crystals to Superfluids, From Non-Equilibrium Patterns to Cosmic Strings*. Oxford: Oxford university press, 1999.
- [22] Bray, A. J. “Theory of phase-ordering kinetics”. In: *Advances in Physics* vol. 51, no. 2 (2002), pp. 481–587.
- [23] Kwon, W. J., Moon, G., Seo, S. W., and Shin, Y.-i. “Critical velocity for vortex shedding in a Bose-Einstein condensate”. In: *Physical Review A* vol. 91, no. 5 (2015), p. 053615.
- [24] Doostmohammadi, A., Shendruk, T. N., Thijssen, K., and Yeomans, J. M. “Onset of meso-scale turbulence in active nematics”. In: *Nature communications* vol. 8, no. 1 (2017), pp. 1–7.
- [25] Nejad, M. R., Doostmohammadi, A., and Yeomans, J. M. “Memory effects, arches and polar defect ordering at the cross-over from wet to dry active nematics”. In: *arXiv preprint arXiv:2010.04200* (2020).

-
- [26] Raman, C., Köhl, M., Onofrio, R., Durfee, D., Kuklewicz, C., Hadzibabic, Z., and Ketterle, W. “Evidence for a critical velocity in a Bose-Einstein condensed gas”. In: *Physical Review Letters* vol. 83, no. 13 (1999), p. 2502.
- [27] Neely, T. W., Samson, E. C., Bradley, A. S., Davis, M. J., and Anderson, B. P. “Observation of vortex dipoles in an oblate Bose-Einstein condensate”. In: *Physical Review Letters* vol. 104, no. 16 (2010), p. 160401.
- [28] Abo-Shaeer, J. R., Raman, C., Vogels, J. M., and Ketterle, W. “Observation of vortex lattices in Bose-Einstein condensates”. In: *Science* vol. 292, no. 5516 (2001), pp. 476–479.
- [29] Fetter, A. L. “Rotating trapped Bose-Einstein condensates”. In: *Reviews of Modern Physics* vol. 81, no. 2 (2009), p. 647.
- [30] Andersen, J. O. *Introduction to Statistical Mechanics*. Bergen: Fagbokforlaget Vigmostad & Bjørke As, 2017.
- [31] Jeevanjee, N. *An Introduction to Tensors and Group Theory for Physicists*. eng. Cham, 2015.
- [32] Kardar, M. *Statistical Physics of Fields*. Cambridge: Cambridge University Press, 2007.
- [33] Landau, L. and Lifshitz, E. *Fluid Mechanics*. 2nd ed. Oxford: Elsevier Ltd, 2009.
- [34] Marchetti, M. C., Joanny, J.-F., Ramaswamy, S., Liverpool, T. B., Prost, J., Rao, M., and Simha, R. A. “Hydrodynamics of soft active matter”. In: *Reviews of Modern Physics* vol. 85, no. 3 (2013), p. 1143.
- [35] Feder, J., Flekkøy, E. G., and Hansen, A. *Physics of flow in porous media*. Cambridge: Cambridge University Press, 2022.
- [36] Kreyszig, E. *Advanced Engineering Mathematics (International Student Version)*. 10th ed. Hoboken: John Wiley & Sons, inc, 2011.
- [37] Stone, M. *Mathematics for physics : a guided tour for graduate students*. eng. Cambridge: Cambridge University Press, 2009.
- [38] Shi, H. and Griffin, A. “Finite-temperature excitations in a dilute Bose-condensed gas”. In: *Physics Reports* vol. 304, no. 1-2 (1998), pp. 1–87.
- [39] Kevrekidis, P. G., Frantzeskakis, D. J., and Carretero-González, R. *Emergent nonlinear phenomena in Bose-Einstein condensates: theory and experiment*. Vol. 45. Berlin: Springer, 2007.
- [40] Pitaevskii, L. and Stringari, S. *Bose-Einstein Condensation and Superfluidity*. Oxford University Press, Jan. 2016.
- [41] Rooney, S., Blakie, P., and Bradley, A. “Stochastic projected Gross-Pitaevskii equation”. In: *Physical Review A* vol. 86, no. 5 (2012), p. 053634.
- [42] Bradley, A. S. and Anderson, B. P. “Energy spectra of vortex distributions in two-dimensional quantum turbulence”. In: *Physical Review X* vol. 2, no. 4 (2012), p. 041001.

- [43] Gardiner, C., Anglin, J., and Fudge, T. “The stochastic gross-pitaevskii equation”. In: *Journal of Physics B: Atomic, Molecular and Optical Physics* vol. 35, no. 6 (2002), p. 1555.
- [44] Gardiner, C. and Davis, M. “The stochastic Gross–Pitaevskii equation: II”. In: *Journal of Physics B: Atomic, Molecular and Optical Physics* vol. 36, no. 23 (2003), p. 4731.
- [45] Rooney, S., Bradley, A., and Blakie, P. “Decay of a quantum vortex: Test of nonequilibrium theories for warm Bose-Einstein condensates”. In: *Physical Review A* vol. 81, no. 2 (2010), p. 023630.
- [46] Skaugen, A. “A unified perspective on two-dimensional quantum turbulence and plasticity”. PhD thesis. University of Oslo, Aug. 2018.
- [47] Rønning, J. “Dynamics of a 2D Bose-Einstein Condensate With an Impurity”. Master Thesis. University of Oslo, May 2020.
- [48] Rønning, J., Skaugen, A., Hernández-García, E., López, C., and Angheluta, L. “Classical analogies for the force acting on an impurity in a Bose-Einstein condensate”. In: *arXiv preprint arXiv:2002.05003* (2020).
- [49] Dalfovo, F., Giorgini, S., Pitaevskii, L. P., and Stringari, S. “Theory of Bose-Einstein condensation in trapped gases”. In: *Reviews of Modern Physics* vol. 71, no. 3 (1999), p. 463.
- [50] Khalatnikov, I. M. *Theory of Superfluidity (Frontiers in Physics)*. New York: W. A. Benjamin, 1965.
- [51] Pinsker, F. “Gaussian impurity moving through a Bose-Einstein superfluid”. In: *Physica B: Condensed Matter* vol. 521 (2017), pp. 36–42.
- [52] Astrakharchik, G. and Pitaevskii, L. “Motion of a heavy impurity through a Bose-Einstein condensate”. In: *Physical Review A* vol. 70, no. 1 (2004), p. 013608.
- [53] Newell, A. C. and Pomeau, Y. “Phase diffusion and phase propagation: interesting connections”. In: *Physica D: Nonlinear Phenomena* vol. 87, no. 1-4 (1995), pp. 216–232.
- [54] Berloff, N. G. and Roberts, P. H. “Motions in a Bose condensate: VII. Boundary-layer separation”. In: *Journal of Physics A: mathematical and general* vol. 33, no. 22 (2000), p. 4025.
- [55] Pinsker, F. and Berloff, N. G. “Transitions and excitations in a superfluid stream passing small impurities”. In: *Physical Review A* vol. 89, no. 5 (2014), p. 053605.
- [56] Kwak, H., Jung, J. H., and Shin, Y.-i. “Minimum critical velocity of a Gaussian obstacle in a Bose-Einstein condensate”. In: *arXiv preprint arXiv:2210.04403* (2022).
- [57] Mermin, N. D. “The Topological Theory of Defects in Ordered Media”. In: *Rev. Mod. Phys.* vol. 51, no. 3 (July 1979), pp. 591–648.

- [58] Sidi, A. “Some aspects of two-point Padé approximants”. In: *Journal of Computational and Applied Mathematics* vol. 6, no. 1 (1980), pp. 9–17.
- [59] Halperin, B. I. “Statistical Mechanics of Topological Defects”. In: *Physique Des Défauts/ Physics of Defects*. Ed. by Balian, R., Kléman, M., and Poirier, J.-P. Amsterdam: North-Holland, 1981, pp. 812–857.
- [60] Mazenko, G. F. “Vortex velocities in the $O(n)$ symmetric time-dependent Ginzburg-Landau model”. In: *Physical review letters* vol. 78, no. 3 (1997), p. 401.
- [61] Mazenko, G. F. “Velocity distribution for strings in phase-ordering kinetics”. In: *Physical Review E* vol. 59, no. 2 (1999), p. 1574.
- [62] Bodenschatz, E., Pesch, W., and Kramer, L. “Structure and dynamics of dislocations in an anisotropic pattern-forming systems”. In: *Physica D: Nonlinear Phenomena* vol. 32, no. 1 (1988), pp. 135–145.
- [63] Stockdale, O. R., Reeves, M. T., Yu, X., Gauthier, G., Goddard-Lee, K., Bowen, W. P., Neely, T. W., and Davis, M. J. “Universal dynamics in the expansion of vortex clusters in a dissipative two-dimensional superfluid”. In: *Physical Review Research* vol. 2, no. 3 (2020), p. 033138.
- [64] Mazenko, G. F. “Defect statistics in the two-dimensional complex Ginzburg-Landau model”. In: *Physical Review E* vol. 64, no. 1 (2001), p. 016110.
- [65] Törnkvist, O. and Schröder, E. “Vortex dynamics in dissipative systems”. In: *Physical review letters* vol. 78, no. 10 (1997), p. 1908.
- [66] Skaugen, A. and Angheluta, L. “Origin of the inverse energy cascade in two-dimensional quantum turbulence”. In: *Physical Review E* vol. 95, no. 5 (2017), p. 052144.
- [67] Newton, P. K. *The N-Vortex Problem : Analytical Techniques*. 1st ed. 2001. Vol. 145. Applied Mathematical Sciences. New York, NY: Springer Science & Business Media, 2001.
- [68] Doostmohammadi, A., Ignés-Mullol, J., Yeomans, J. M., and Sagués, F. “Active nematics”. In: *Nat. Commun.* vol. 9, no. 1 (2018), pp. 1–13.
- [69] Ballerini, M., Cabibbo, N., Candelier, R., Cavagna, A., Cisbani, E., Giardina, I., Lecomte, V., Orlandi, A., Parisi, G., Procaccini, A., et al. “Interaction ruling animal collective behavior depends on topological rather than metric distance: Evidence from a field study”. In: *Proceedings of the national academy of sciences* vol. 105, no. 4 (2008), pp. 1232–1237.
- [70] Sanchez, T., Chen, D. T., DeCamp, S. J., Heymann, M., and Dogic, Z. “Spontaneous motion in hierarchically assembled active matter”. In: *Nature* vol. 491, no. 7424 (2012), pp. 431–434.
- [71] Guillamat, P., Ignés-Mullol, J., and Sagués, F. “Taming active turbulence with patterned soft interfaces”. In: *Nature communications* vol. 8, no. 1 (2017), pp. 1–8.

- [72] Palacci, J., Abécassis, B., Cottin-Bizonne, C., Ybert, C., and Bocquet, L. “Colloidal motility and pattern formation under rectified diffusiophoresis”. In: *Physical review letters* vol. 104, no. 13 (2010), p. 138302.
- [73] Bickel, T., Zecua, G., and Würger, A. “Polarization of active Janus particles”. In: *Physical Review E* vol. 89, no. 5 (2014), p. 050303.
- [74] Wang, G., Phan, T. V., Li, S., Wombacher, M., Qu, J., Peng, Y., Chen, G., Goldman, D. I., Levin, S. A., Austin, R. H., et al. “Emergent field-driven robot swarm states”. In: *Physical review letters* vol. 126, no. 10 (2021), p. 108002.
- [75] Vicsek, T. and Zafeiris, A. “Collective motion”. In: *Physics reports* vol. 517, no. 3-4 (2012), pp. 71–140.
- [76] Vicsek, T., Czirók, A., Ben-Jacob, E., Cohen, I., and Shochet, O. “Novel type of phase transition in a system of self-driven particles”. In: *Physical review letters* vol. 75, no. 6 (1995), p. 1226.
- [77] Toner, J. and Tu, Y. “Long-range order in a two-dimensional dynamical XY model: how birds fly together”. In: *Physical review letters* vol. 75, no. 23 (1995), p. 4326.
- [78] Mermin, N. D. and Wagner, H. “Absence of ferromagnetism or antiferromagnetism in one-or two-dimensional isotropic Heisenberg models”. In: *Physical Review Letters* vol. 17, no. 22 (1966), p. 1133.
- [79] Toner, J. and Tu, Y. “Flocks, herds, and schools: A quantitative theory of flocking”. In: *Physical review E* vol. 58, no. 4 (1998), p. 4828.
- [80] Genkin, M. M., Sokolov, A., Lavrentovich, O. D., and Aranson, I. S. “Topological defects in a living nematic ensnare swimming bacteria”. In: *Physical Review X* vol. 7, no. 1 (2017), p. 011029.
- [81] Angheluta, L., Chen, Z., Marchetti, M. C., and Bowick, M. J. “The role of fluid flow in the dynamics of active nematic defects”. In: *New Journal of Physics* vol. 23, no. 3 (2021), p. 033009.
- [82] Simha, R. A. and Ramaswamy, S. “Hydrodynamic fluctuations and instabilities in ordered suspensions of self-propelled particles”. In: *Physical review letters* vol. 89, no. 5 (2002), p. 058101.
- [83] Thampi, S. P., Golestanian, R., and Yeomans, J. M. “Vorticity, defects and correlations in active turbulence”. In: *Philosophical Transactions of the Royal Society A: Mathematical, Physical and Engineering Sciences* vol. 372, no. 2029 (2014), p. 20130366.
- [84] Vromans, A. J. and Giomi, L. “Orientational properties of nematic disclinations”. In: *Soft matter* vol. 12, no. 30 (2016), pp. 6490–6495.
- [85] Meacock, O. J., Doostmohammadi, A., Foster, K. R., Yeomans, J. M., and Durham, W. M. “Bacteria solve the problem of crowding by moving slowly”. In: *Nature Physics* vol. 17, no. 2 (2021), pp. 205–210.
- [86] Ardaševa, A. and Doostmohammadi, A. “Topological defects in biological matter”. In: *Nature Reviews Physics* vol. 4, no. 6 (2022), pp. 354–356.

-
- [87] Guillaumat, P., Blanch-Mercader, C., Pernollet, G., Kruse, K., and Roux, A. “Integer topological defects organize stresses driving tissue morphogenesis”. In: *Nature materials* vol. 21, no. 5 (2022), pp. 588–597.
- [88] Endresen, K. D., Kim, M., Pittman, M., Chen, Y., and Serra, F. “Topological defects of integer charge in cell monolayers”. In: *Soft Matter* vol. 17, no. 24 (2021), pp. 5878–5887.
- [89] Amiri, A., Mueller, R., and Doostmohammadi, A. “Unifying polar and nematic active matter: emergence and co-existence of half-integer and full-integer topological defects”. In: *Journal of Physics A: Mathematical and Theoretical* vol. 55, no. 9 (Feb. 2022), p. 094002.
- [90] Logg, A., Mardal, K.-A., Wells, G. N., et al. *Automated Solution of Differential Equations by the Finite Element Method*. Ed. by Logg, A., Mardal, K.-A., and Wells, G. N. Berlin: Springer, 2012.
- [91] Cox, S. M. and Matthews, P. C. “Exponential time differencing for stiff systems”. In: *Journal of Computational Physics* vol. 176, no. 2 (2002), pp. 430–455.
- [92] Gomi, L., Bowick, M. J., Mishra, P., Sknepnek, R., and Cristina Marchetti, M. “Defect dynamics in active nematics”. In: *Philosophical Transactions of the Royal Society A: Mathematical, Physical and Engineering Sciences* vol. 372, no. 2029 (2014), p. 20130365.
- [93] Romano, J., Mahault, B., and Golestanian, R. “Dynamical theory of topological defects I: the multivalued solution of the diffusion equation”. In: *arXiv preprint arXiv:2304.02348* (2023).
- [94] Zhang, R., Redford, S. A., Ruijgrok, P. V., Kumar, N., Mozaffari, A., Zemsky, S., Dinner, A. R., Vitelli, V., Bryant, Z., Gardel, M. L., et al. “Spatiotemporal control of liquid crystal structure and dynamics through activity patterning”. In: *Nature materials* vol. 20, no. 6 (2021), pp. 875–882.
- [95] Mozaffari, A., Zhang, R., Atzin, N., and De Pablo, J. J. “Defect spirograph: Dynamical behavior of defects in spatially patterned active nematics”. In: *Physical Review Letters* vol. 126, no. 22 (2021), p. 227801.
- [96] Zhang, R., Mozaffari, A., and Pablo, J. J. de. “Logic operations with active topological defects”. In: *Science advances* vol. 8, no. 8 (2022), eabg9060.
- [97] Kunimi, M. and Kato, Y. “Metastability, excitations, fluctuations, and multiple-swallowtail structures of a superfluid in a Bose-Einstein condensate in the presence of a uniformly moving defect”. In: *Physical Review A* vol. 91, no. 5 (2015), p. 053608.
- [98] Thampi, S. and Yeomans, J. “Active turbulence in active nematics”. In: *The European Physical Journal Special Topics* vol. 225 (2016), pp. 651–662.

- [99] Thijssen, K., Khaladj, D. A., Aghvami, S. A., Gharbi, M. A., Fraden, S., Yeomans, J. M., Hirst, L. S., and Shendruk, T. N. “Submersed micropatterned structures control active nematic flow, topology, and concentration”. In: *Proceedings of the National Academy of Sciences* vol. 118, no. 38 (2021).
- [100] Yu, X. and Bradley, A. S. “Emergent non-eulerian hydrodynamics of quantum vortices in two dimensions”. In: *Physical review letters* vol. 119, no. 18 (2017), p. 185301.
- [101] Ruske, L. J. and Yeomans, J. M. “Activity gradients in two-and three-dimensional active nematics”. In: *Soft Matter* vol. 18, no. 30 (2022), pp. 5654–5661.
- [102] Shankar, S., Scharrer, L. V., Bowick, M. J., and Marchetti, M. C. “Spatiotemporal control of active topological defects”. In: *arXiv preprint arXiv:2212.00666* (2022).

Papers

Paper I

Flow around topological defects in active nematic films

Jonas Rønning, Cristina M. Marchetti, Mark J. Bowick, Luiza Angheluta

Research



Cite this article: Rønning J, Marchetti CM, Bowick MJ, Angheluta L. 2022 Flow around topological defects in active nematic films. *Proc. R. Soc. A* **478**: 20210879. <https://doi.org/10.1098/rspa.2021.0879>

Received: 16 November 2021

Accepted: 22 December 2021

Subject Areas:

statistical physics, fluid mechanics, biophysics

Keywords:

active nematics, topological defects, nematic liquid crystals, hydrodynamics

Author for correspondence:

Jonas Rønning

e-mail: jonason@uio.no

Flow around topological defects in active nematic films

Jonas Rønning¹, Cristina M. Marchetti²,

Mark J. Bowick³ and Luiza Angheluta¹

¹Njord Centre, Department of Physics, University of Oslo, PO Box 1048, Oslo 0316, Norway

²Department of Physics, University of California Santa Barbara, Santa Barbara, CA 93106, USA

³Kavli Institute for Theoretical Physics, University of California Santa Barbara, Santa Barbara, CA 93106, USA

JR, 0000-0001-5289-7276

We study the active flow around isolated defects and the self-propulsion velocity of $+1/2$ defects in an active nematic film with both viscous dissipation (with viscosity η) and frictional damping Γ with a substrate. The interplay between these two dissipation mechanisms is controlled by the hydrodynamic dissipation length $\ell_d = \sqrt{\eta/\Gamma}$ that screens the flows. For an isolated defect, in the absence of screening from other defects, the size of the shear vorticity around the defect is controlled by the system size R . In the presence of friction that leads to a finite value of ℓ_d , the vorticity field decays to zero on the lengthscales larger than ℓ_d . We show that the self-propulsion velocity of $+1/2$ defects grows with R in small systems where $R < \ell_d$, while in the infinite system limit or when $R \gg \ell_d$, it approaches a constant value determined by ℓ_d .

1. Introduction

Active matter consists of collections of individuals that dissipate energy taken from the environment to generate motion and forces and self-organize into a rich variety of ordered phases. Many active systems exhibit nematic order interrupted by orientational defects and advected by spontaneous flows driven by intrinsic activity of the self-propelled individuals. This behaviour is found in reconstituted systems, such as mixtures of cytoskeletal filaments and motor proteins [1–4], bacterial suspensions [5,6] and cell sheets [7,8], as well as synthetic systems, like vertically vibrated layers of granular rods [6,9].

© 2022 The Authors. Published by the Royal Society under the terms of the Creative Commons Attribution License <http://creativecommons.org/licenses/by/4.0/>, which permits unrestricted use, provided the original author and source are credited.

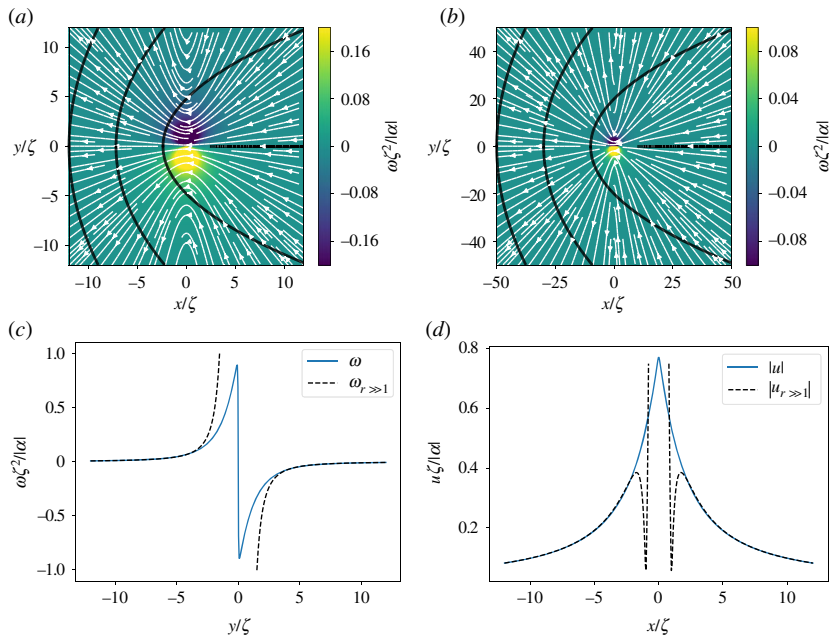


Figure 1. Flow streamlines (white arrow) around a $+1/2$ defect for $\alpha < 0$ obtained from (a) full solution and (b) asymptotic one. The nematic director field is shown in black lines and the background colour map denotes vorticity. To show the structure of the near-field, the vorticity scale is saturated at ± 0.2 in (a) and at ± 0.1 in (b). (c) Cross section of vorticity obtained from the exact solution (solid blue line) and the asymptotic limit (dotted black line) at $x = 0$ as a function of y . (d) Cross section of the velocity obtained from the exact solution (solid blue line) and the asymptotic limit (dotted black line) at $y = 0$ as a function of x . (Online version in colour.)

A central feature of active nematics is the feedback between active stresses, which distort orientational order and the spontaneous flow generated by such distortions. In hydrodynamic descriptions [6], the active stress σ_{ij}^a exerted by elongated active entities on the surrounding fluid is proportional to the nematic order parameter tensor Q_{ij} , namely $\sigma_{ij}^a = \alpha_0 Q_{ij}$ [10,11]. The activity coefficient α_0 embodies the microscale biomolecular processes that convert chemical energy into mechanical forces, and depends on the concentration of active entities, which in general may vary in space and time [12,13]. The sign of α_0 distinguishes between contractile ($\alpha_0 > 0$) stress generated by ‘puller’ swimmers, such as the algae *Chlamydomonas*, versus extensile ($\alpha_0 < 0$) stress generated by ‘pusher’ swimmers, e.g. most flagellated bacteria. Its magnitude controls the strength of the active flow. Fluctuations in orientational order yield active stresses and associated flows, which can in turn enhance the orientational distortions. The resulting feedback loop destabilizes the nematic order, driving the system to a state of self-sustained spatio-temporally chaotic flow, with proliferation of topological defects, and termed active turbulence [14,15].

The lowest-energy orientational defects in nematic films have half-integer topological charge and opposite sign. The $+1/2$ defects have a comet-like shape, while the $-1/2$ defects have a tri-fold symmetry (figures 1 and 2). Defects strongly disrupt orientational order and induce long-range nematic distortions. In active systems, such distortions generate flows with symmetry and profiles controlled by the defect geometry. The nematic distortion created by a $+1/2$ defect yields an active flow that is finite at the defect core. A $+1/2$ defect then rides along with the flow it itself generates, behaving like a motile particle with a non-vanishing self-propulsion velocity \mathbf{v}_+^a , even in the absence of external drive [12,16]. On the other hand, the active backflow generated by a $-1/2$ defect vanishes at the core due to the defect’s threefold symmetry (figure 2). Thus

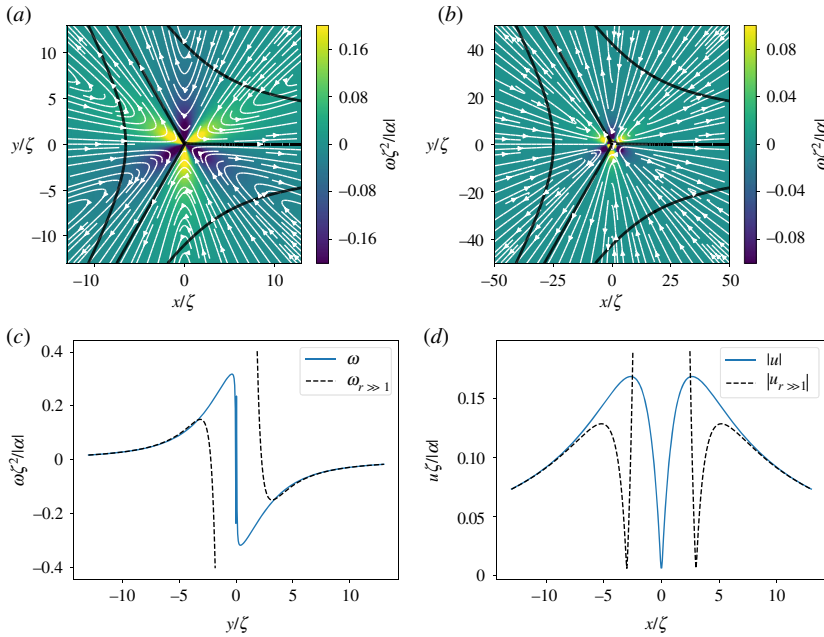


Figure 2. Flow streamlines (white arrow) around a $-1/2$ defect for $\alpha < 0$ obtained from (a) full solution and (b) asymptotic one. The nematic director field is shown in black lines and the background colour map denotes vorticity. To show the structure of the near-field, the vorticity scale is saturated at ± 0.2 in (a) and at ± 0.1 in (b). (c) Cross section of vorticity obtained from the exact solution (solid blue line) and the asymptotic limit (dotted black line) at $x = 0$ as a function of y . Note that the vortices changes sign rapidly at origin due to its multi-valued phase (see equation (4.6)). (d) Cross section of the velocity obtained from the exact solution (solid blue line) and the asymptotic limit (dotted black line) at $y = 0$ as a function of x . (Online version in colour.)

$-1/2$ defects behave like passive particles and have no spontaneous motility in the absence of external driving. A simple estimate demonstrates that \mathbf{v}_+^a is directed along the polar axis of the $+1/2$ defect and is proportional to the activity α_0 . In an extensile medium $+1/2$ defects self-propel in the direction of the head of the comet, while in a contractile system they move towards the comet’s tail [12,16,17]. The direction of motion of $+1/2$ defects can then be used as a metric for determining the nature of active stress in the system. Such measurements have, for instance, revealed the surprising dominance of extensile stresses in confluent tissue composed of tightly bound contractile individual cells [18–22].

The flow generated by defects and the resulting propulsive speed of the $+1/2$ also vary depending on the dissipative processes at play in the system and the role of fluid incompressibility. Specifically, important differences exist between ‘dry’ systems, where dissipation is dominated by friction Γ with a substrate or an external medium [23,24] and ‘wet’ systems, where dissipation is mainly controlled by viscosity η , resulting in long-range hydrodynamic effects [14,17,24,25]. In incompressible wet systems, activity is also a source of pressure gradients, which in turn contribute alongside with the nematic distortion to the self-motility of positive defects. In the limit of viscous dominated flows with no friction with the substrate, the self-propulsion speed scales as $|\mathbf{v}_+^a| \sim (|\alpha_0|/\eta)\ell$, where ℓ is a length scale given by the system size for an isolated defect [17] or by the mean separation between defects, which is, in turn, controlled by the active length scale $\ell_a = \sqrt{K/|\alpha_0|}$, with K the nematic stiffness [17]. In overdamped (dry) systems, where viscosity is negligible compared with frictional damping with the substrate, $|\mathbf{v}_+^a| \sim |\alpha_0|/(\xi\Gamma)$, where ξ is the nematic coherence length [23,24,26]. A complete

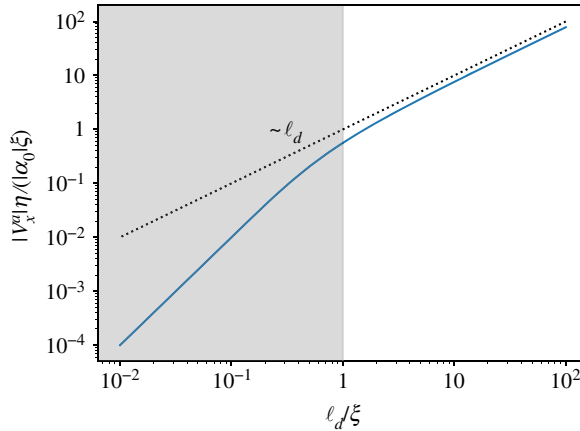


Figure 3. The self-propulsion speed of a $+1/2$ defect as function of ℓ_d/ξ in an unbounded system. The line is the exact analytical solution, while the dotted line shows the asymptotic scaling with ℓ_d , i.e. $v_x^a \eta \sim \ell_d$ for $\ell_d > \xi$. The grey area corresponds to the overdamped limit, where essentially v_x^a depends solely on friction. (Online version in colour.)

calculation of the active flows associated with defect configurations and of the propulsive speed of the $+1/2$ defect that bridges between the two limits is, however, not available. The need for such a calculation is further motivated by recent work that has shown that tuning frictional damping relative to viscous dissipation leads to different dynamical regimes and ordering behaviour of interacting defects [27].

In this paper, we present a detailed calculation of the flow around isolated $\pm 1/2$ defects and of the defect's self-propulsion velocity in an incompressible nematic film. We incorporate both viscous dissipation and frictional damping and examine the interplay between the two, as well as the long-range hydrodynamic effects arising from incompressibility. We evaluate the $+1/2$ self-propulsive speed $|v_+^a|$ as a function of the hydrodynamic dissipation length $\ell_d = \sqrt{\eta/\Gamma}$, which measures the competition between viscous dissipation and frictional damping. The result is summarized in figure 3. When dissipation is controlled by friction ($\ell_d \ll \xi$), one recovers the simple dimensional estimate $|v_+^a| \sim |\alpha_0|/(\xi \Gamma)$. We show, however, that to obtain this result it is not sufficient to consider the far flow field which diverges near the defect, but one must resolve the full flow field near the defect core. On the other hand, when viscous stresses dominate, the defect propulsive speed depends on the order of limits. If $\Gamma = 0$ from the outset, then a simple estimate yields $v_x^a \sim r$ due to the long-range nature of defect distortions. This limit, however, corresponds to a 'floating' layer and does not describe experimental situations where the active nematic film is supported by a substrate [25] or in contact with other fluids. It has been argued before that this unbounded growth should be cut off either by the system size or by the defect separation [17]. Our work shows that a finite friction cuts off the large-scale divergence of the defect self-propulsion speed at the scale ℓ_d , with $|v_+^a| \sim (|\alpha_0|/\eta)\ell_d$ in the limit $\zeta = \ell_d/\xi \gg 1$, where viscous dissipation exceeds frictional drag and provides an analytical expression for the defect self-propulsion over all values of friction and viscosity. We find that the structure of the flow field around a defect is also affected by the competition between viscosity and friction. At distances large compared with ℓ_d , the flow velocity decays in the far-field as $\sim 1/r$, due to friction with the substrate [25]. At distances smaller than ℓ_d , viscous dissipation dominates and smooths out the velocity field near the defect core. Our work is relevant to defects in thin film of microtubule nematics on a substrates, as well as to dense cell layers.

In §2, we describe the hydrodynamic model. In §§3 and 4, we provide analytical derivations of closed expressions for the velocity and pressure fields induced by $\pm 1/2$ defects in an infinite

system. One implication of the long-range interactions present in active nematics is that there are strong finite-size effects on the single defect flow field. This is discussed in §5, where we compare the analytical predictions with numerical integration of the Stokes equations in a disc of finite radius. Finally, the main results are discussed with concluding remarks in §6.

2. Hydrodynamic model

We consider a hydrodynamic model of an active nematic that couples flow velocity $\mathbf{u}(\mathbf{r})$ to the nematic order parameter $Q_{ij} = S(\hat{n}_i\hat{n}_j - \frac{1}{2}\delta_{ij})$, where S quantifies the degree of order and $\hat{\mathbf{n}}(\mathbf{r}) = (\cos\theta(\mathbf{r}), \sin\theta(\mathbf{r}))$ is the orientational director field with head-tail symmetry. In the simplest formulation, we consider that the \mathbf{Q} -tensor is a minimizer of the de Gennes–Landau free energy [6]

$$\mathcal{F} = \int d\mathbf{r} \left[\frac{K}{2} |\nabla Q|^2 + \frac{g}{4} \left(1 - \frac{1}{2} \text{Tr}(Q^2) \right)^2 \right], \quad (2.1)$$

with isotropic elastic constant $K > 0$ and g the strength of the local ordering potential. The uniform nematic ordered state corresponds to $S_0^2 = 1$. The flow field satisfies a Stokes equation that balances forces on a fluid element, given by [6]

$$(\Gamma - \eta \nabla^2) \mathbf{u} = \alpha_0 \nabla \cdot \mathbf{Q}(\mathbf{r}) - \nabla p(\mathbf{r}), \quad \nabla \cdot \mathbf{u} = 0, \quad (2.2)$$

where Γ is a friction coefficient per unit area, η is the dynamic viscosity and α_0 is the activity parameter, with dimensions of stress. For simplicity, we neglect the elastic stress as being of higher order in the gradients of \mathbf{Q} compared with the active stress and a more important contribution for nematic textures with many defects. Here, we consider the flow field generated by an isolated $\pm 1/2$ defect embedded in an otherwise uniform nematic field.

In two dimensions, the traceless \mathbf{Q} -tensor has two independent components and can be represented equivalently as a complex scalar order parameter $\psi = Q_{xx} + iQ_{xy}$. The configuration of a defect located at the origin can be written in terms of the ψ -field as $\psi(\mathbf{r}) = S(r)e^{2i\theta(r)}$, where $r \equiv |\mathbf{r}|$. The detailed form of core function $S(r)$ depends on the specific terms retained in the free energy, but it has the important generic asymptotic behaviours that $S(r) \rightarrow 1$ for $r \gg \xi$ and $S(r) \approx ar/\xi$ when $r \rightarrow 0$, where $\xi = \sqrt{K/g}$ is the coherence length that sets the scale of the defect core and a is a numerical constant $\mathcal{O}(1)$. Below we set $a = 1$, without loss of generality. The coherence length provides an ultraviolet cutoff to separate inner core-solution from outer-core solution. On long distances, the nematic orientation is a potential field that has a branch cut starting at the origin where there is an isolated defect of charge $q = \pm 1/2$ and can be written as [24,28]

$$\theta(\mathbf{r}) = q \arctan\left(\frac{y}{x}\right) + \theta_0, \quad (2.3)$$

where θ_0 is the uniform background orientation. Without loss of generality, we set $\theta_0 = 0$.

We rescale the Stokes equation in units of the nematic relaxation time $\tau = \gamma/g$ (where γ is the inverse of the rotational diffusivity) and the coherent length ξ , such that the dimensionless momentum equation takes the form

$$(1 - \zeta^2 \nabla^2) \mathbf{u} = \mathbf{F}^\pm - \nabla \tilde{p}(\mathbf{r}), \quad \nabla \cdot \mathbf{u} = 0, \quad (2.4)$$

where $\mathbf{F}^\pm = \alpha \nabla \cdot \mathbf{Q}$ is the active force generated by a defect. The rescaled activity and pressure are given by $\alpha = \alpha_0 \gamma / (\Gamma K)$ and $\tilde{p} = p \gamma / (\Gamma K)$. The dimensionless parameter $\zeta = \sqrt{\eta / (\Gamma \xi^2)} = \ell_d / \xi$ measures the hydrodynamic dissipation length $\ell_d = \sqrt{\eta / \Gamma}$ in units of the coherent length, ξ . In the following, we will omit the tilde and all quantities are dimensionless unless otherwise stated.

The components of the \mathbf{Q} tensor for an isolated $+1/2$ defect are given by $Q_{xx}(\mathbf{r}) = S(r)(x/r)$ and $Q_{xy} = S(r)(y/r)$. The active force density then reduces to

$$\mathbf{F}^+(\mathbf{r}) = \begin{cases} 2\alpha\mathbf{e}_x, & r \rightarrow 0, \\ \frac{\alpha}{r}\mathbf{e}_x, & r \gg 1. \end{cases} \quad (2.5)$$

Similarly, for a negative defect $Q_{xx} = S(r)(x/r)$ and $Q_{xy} = -S(r)(y/r)$, corresponding to an active force density given by

$$\mathbf{F}^-(\mathbf{e}) = \begin{cases} 0, & r \rightarrow 0 \\ -\alpha\frac{x^2-y^2}{r^3}\mathbf{e}_x + \alpha\frac{2xy}{r^3}\mathbf{e}_y, & r \gg 1. \end{cases} \quad (2.6)$$

The solutions for the flow velocity and pressure can be written in terms of the corresponding Green functions as

$$\mathbf{u}(\mathbf{r}) = \frac{1}{2\pi\zeta^2} \int d\mathbf{r}' K_0\left(\frac{|\mathbf{r}-\mathbf{r}'|}{\zeta}\right) [\mathbf{F}^\pm(\mathbf{r}') - \nabla' p(\mathbf{r}')] \equiv \mathbf{u}^a + \mathbf{u}^p \quad (2.7)$$

and

$$p(\mathbf{r}) = \frac{1}{2\pi} \int d\mathbf{r}' \ln(|\mathbf{r}-\mathbf{r}'|) \nabla' \cdot \mathbf{F}^\pm(\mathbf{r}'), \quad (2.8)$$

where \mathbf{u}^a and \mathbf{u}^p are the contributions to the flow velocity induced by the active stress and pressure gradients, respectively. Note that the latter also depends (indirectly) on activity. In the limit of no friction, equations (2.7) and (2.8) reduce to equations (3.7) and (3.8) of [17].

3. Positive nematic defect in an infinite system

(a) Defect self-propulsion

The net active flow at the defect core acts as an advective velocity that propels the defect with a velocity \mathbf{v}^a , which in turn is controlled by both the active stress and pressure gradients. Thus we write $\mathbf{v}^a = \mathbf{u}^a(0) + \mathbf{u}^p(0)$. The flow induced by the active stress at the origin is given by equation (2.7) evaluated at $\mathbf{r}=0$. The y -component vanishes due to symmetry considerations, and the x -component is given by

$$u_x^a(0) = 2\alpha \left[1 - \frac{1}{\zeta} K_1(\zeta^{-1}) \right] + \frac{\pi\alpha}{2\zeta} \left[1 - \frac{1}{\zeta} (L_{-1}(\zeta^{-1})K_0(\zeta^{-1}) + L_0(\zeta^{-1})K_1(\zeta^{-1})) \right], \quad (3.1)$$

where $\zeta = \ell_d/\xi$, $K_n(x)$ are modified Bessel functions and $L_n(x)$ modified Struve function.

The integral determining the pressure field given by equation (2.8) can be performed by a mapping to complex coordinates $(x', y') \rightarrow (w, \bar{w})$, $(x, y) \rightarrow (z, \bar{z})$ and then using the substitution to polar coordinates $w = r'\hat{w}$, $\hat{w} = e^{i\theta'}$. This yields

$$p(\mathbf{r}) = -\frac{\alpha}{2i\pi} \int_0^1 dr' r' \oint_\gamma d\hat{w} \left(\frac{1}{\hat{w}r'(\hat{w} - zr'^{-1})} - \frac{1}{\bar{z}(\hat{w} - r'\bar{z}^{-1})} \right) \\ - \frac{\alpha}{4i\pi} \int_1^\infty dr' r' \oint_\gamma d\hat{w} \left(\frac{1}{\hat{w}r'(\hat{w} - zr'^{-1})} - \frac{1}{\bar{z}(\hat{w} - r'\bar{z}^{-1})} \right) \quad (3.2)$$

with γ a contour of unit radius centred at origin. The pole at $\hat{w}=0$ is always inside the unit disc $|\hat{w}| < 1$, whereas the poles at $\hat{w} = zr'^{-1}$ and $\hat{w} = r'\bar{z}^{-1}$ are inside the unit disc when $|z| < r'$ or $|z| > r'$, respectively. The contour integrals are then evaluated using the residue theorem. Integrating over

r' , we finally obtain

$$p(\mathbf{r}) = \begin{cases} \alpha x, & r < 1, \\ \frac{\alpha x}{r}, & \text{if } r > 1. \end{cases} \quad (3.3)$$

Consequently, the defect self-propulsion induced by pressure gradient has only an x -component, which counteracts that induced by the active stress, and given by

$$\begin{aligned} u_x^p(0) &= -\alpha \left(1 - \frac{1}{\zeta} K_1(\zeta^{-1}) \right) - \frac{\pi\alpha}{4\zeta} \left[1 - \frac{1}{\zeta} [L_{-1}(\zeta^{-1})K_0(\zeta^{-1}) + L_0(\zeta^{-1})K_1(\zeta^{-1})] \right] \\ &= -\frac{u_x^a(0)}{2}. \end{aligned} \quad (3.4)$$

Combining these results, we find that the self-propulsion velocity of an isolated $+1/2$ defect oriented along the x -axis is $\mathbf{v}^a = v_x^a \hat{\mathbf{e}}$, where v_x^a has the following scaling form:

$$v_x^a = \alpha F(\zeta), \quad (3.5)$$

where

$$F(\zeta) = \left(1 - \frac{1}{\zeta} K_1(\zeta^{-1}) \right) + \frac{\alpha\pi}{4\zeta} \left[1 - \frac{1}{\zeta} [L_{-1}(\zeta^{-1})K_0(\zeta^{-1}) + L_0(\zeta^{-1})K_1(\zeta^{-1})] \right]. \quad (3.6)$$

When $\zeta \gg 1$, we can simplify the expression by expanding in powers of ζ^{-1} , and, to leading order, we obtain,

$$F(\zeta) \underset{\zeta \gg 1}{\approx} \frac{\pi}{4\zeta} + \frac{1}{2\zeta^2} (\gamma - 1 - \ln(2\zeta)) - \frac{1}{4\zeta^2} (2\gamma - 1 - 2 \ln(2\zeta)), \quad (3.7)$$

where $\gamma \approx 0.577$ is the Euler–Mascheroni constant. Similarly, we also take the other limit $\zeta \ll 1$, where the scaling function approaches a constant value. The dependence of the scaling function F on ζ is plotted in figure 4 and its asymptotic scaling at $\zeta \gg 1$ as $F \sim \zeta^{-1}$ is included as the dotted line. We can discuss the implications of these results better when we use dimensional quantities and write the asymptotic behaviour of the self-propulsion speed as

$$v_x^a \approx \begin{cases} \frac{\pi}{4} \frac{\alpha_0}{\Gamma \ell_d} = \frac{\pi}{4} \frac{\alpha_0 \ell_d}{\eta}, & \zeta \gg 1 \\ \frac{\alpha_0}{\Gamma \xi}, & \zeta \rightarrow 0. \end{cases} \quad (3.8)$$

As anticipated from dimensional analysis, $v_x^a \sim (\alpha_0/\Gamma\xi)$, in the overdamped limit where dissipation is controlled only by frictional drag [23,24,26]. In the underdamped limit, where the effect of drag is much smaller than viscous dissipation, hydrodynamic lengthscale becomes important in screening the divergence of the self-propulsion speed with system size, such that v_x^a scales instead as $v_x^a \sim \alpha_0/\sqrt{\eta\Gamma}$. In this case, the self-driven motion of $+1/2$ defect is reduced by both friction and viscosity.

As discussed in the introduction, the presence of a finite drag always cuts off the large-scale divergence of the speed of a single defect obtained in a purely viscous two-dimensional layer at the dissipation length ℓ_d . When the flow equations for a thin nematic film of thickness h on a substrate are derived via a lubrication approximation, the effective friction coefficient relates to the film thickness and the viscosity of the substrate bulk fluid (oil), and scales as $\Gamma \sim \bar{\eta}/h^2$ [29]. A more detailed calculation relevant to active microtubule suspensions confined between water and oil shows that the bulk viscosity plays an important role as an additional source of dissipation in the nematic layer affecting the individual defect self-propulsion [30], as well as the vortex statistics in the active turbulence regime [31]. Note that [30] shows that the $+1/2$ defect speed decays algebraically with the bulk oil viscosity (that controls the drag) in the regime where the flow dissipation comes from the viscous dissipation in the nematic layer, consistent with our formulation. When the flow dissipation is dominated by the oil bulk viscosity, there is, however, a logarithmic decay with increasing oil viscosity and, indirectly, drag.

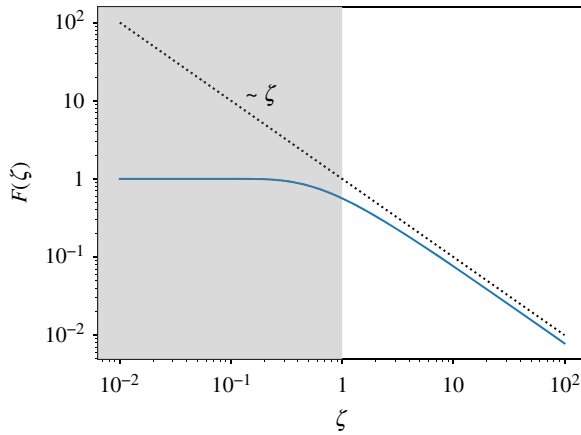


Figure 4. Scaling function $F(\zeta)$ as a function of ζ . The grey region corresponds to the overdamped limit where v_x^a depends only on friction. The dotted black line is the asymptotic limit for $\zeta \gg 1$. (Online version in colour.)

(b) Flow field away from the defect

Outside the core, we treat the defect as a point source. From symmetry considerations, the flow velocity due to σ^a is again non-zero only along the x -direction and it is given by

$$u_x^a(\mathbf{r}) = \frac{\alpha}{2\pi\zeta^2} \int \frac{d\mathbf{r}'}{r'} K_0\left(\frac{|\mathbf{r}' - \mathbf{r}|}{\zeta}\right). \quad (3.9)$$

The flow velocity associated with pressure gradients is finite also in the y -direction and it is given by

$$u_i^p(\mathbf{r}) = -\frac{\alpha}{2\pi\zeta^2} \int d\mathbf{r}' K_0\left(\frac{|\mathbf{r}' - \mathbf{r}|}{\zeta}\right) \left(\frac{\delta_{ix}}{r'} - \frac{x' r'_i}{r'^3}\right). \quad (3.10)$$

The term proportional to the δ function in equation (3.10) cancels u_x^a from equation (3.9), such that the total active fluid flow is entirely determined by pressure flow, with

$$u_i(\mathbf{r}) = \frac{\alpha}{2\pi\zeta^2} \int d\mathbf{r}' K_0\left(\frac{|\mathbf{r}' - \mathbf{r}|}{\zeta}\right) \frac{x' r'_i}{r'^3}. \quad (3.11)$$

To evaluate this integral, we use a complex representation $u = u_x + iu_y$ and evaluate the resulting contour integrals as shown in appendix A where we express them in terms of complete elliptic integrals of first and second kind. We further use the power series representation of these elliptic integrals, which allows us to write the active fluid velocity as a series expansion in integrals over the zeroth-order modified Bessel function, namely

$$u^+(r, \phi) = \frac{\alpha}{2\zeta^2} \sum_{n=0}^{\infty} \left(1 - \frac{2n+1}{2n-1} e^{2i\phi}\right) \left(\frac{(2n-1)!!}{(2n)!!}\right)^2 \int_0^r dr' K_0\left(\frac{r'}{\zeta}\right) \left(\frac{r'}{r}\right)^{2n+1} + \frac{\alpha}{2\zeta^2} \sum_{n=0}^{\infty} \left(1 - \frac{n}{n+1} e^{2i\phi}\right) \left(\frac{(2n-1)!!}{(2n)!!}\right)^2 \int_r^{\infty} dr' K_0\left(\frac{r'}{\zeta}\right) \left(\frac{r'}{r}\right)^{2n}. \quad (3.12)$$

The $K_0(x)$ integrals are computed in appendix B. After some mathematical manipulations the velocity reduces to

$$u^+(r, \phi) = \frac{\alpha}{4\zeta} \left[\pi \left(I_0\left(\frac{r}{\zeta}\right) - I_2\left(\frac{r}{\zeta}\right) e^{2i\phi} \right) + \sum_{k,n=0}^{\infty} (\kappa_1^+(n, k) + \kappa_2^+(n, k) e^{2i\phi}) \frac{1}{(k!)^2} \left(\frac{r}{2\zeta}\right)^{2k+1} \right], \quad (3.13)$$

with

$$\kappa_1^+(n, k) = \left(\frac{(2n-1)!!}{(2n)!!} \right)^2 \left(\frac{-(4n+1)(4k+3)}{(n+k+1)^2(2n-1-2k)^2} \right) \quad (3.14)$$

and

$$\kappa_2^+(n, k) = \left(\frac{(2n-1)!!}{(2n)!!} \right)^2 \frac{[(2n-1)(4k(n+1)+1+n)-4k^2](4n+1)}{(n+1+k)^2(2n-1-2k)^2(n+1)(2n-1)}. \quad (3.15)$$

The corresponding vorticity is given by

$$\begin{aligned} \omega^+(r, \phi) = & -\frac{\alpha}{8\zeta^2} \sin(\phi) \left(4\pi I_1 \left(\frac{r}{\zeta} \right) + \sum_{n,k} [(2k+1)\kappa_1^+(n, k) \right. \\ & \left. - (2k+3)\kappa_2^+(n, k)] \frac{1}{(k!)^2} \left(\frac{r}{2\zeta} \right)^{2k} \right). \end{aligned} \quad (3.16)$$

Both velocity and vorticity are shown in figure 1.

(i) Asymptotic far-field flow

The flow field greatly simplifies in the far-field $r/\zeta \gg 1$, corresponding to distances much larger than the hydrodynamic dissipation length. Then, the second term in equation (3.12) vanishes due to the exponential decay of the Bessel function. In the first integral, we can replace the upper limit r with ∞ and perform it analytically with the result given as

$$u^+(r, \phi) = \frac{\alpha}{2r} \left(e^{2i\phi} + 1 + \left(\frac{\zeta}{r} \right)^2 (1 - 3e^{2i\phi}) \right), \quad (3.17)$$

where we have kept the two first terms in the expansion. The slow $1/r$ -decay term in equation (3.17) is independent of viscosity η and identical to the one derived in Ref. [24] in the friction-dominated regime. Corrections due to viscosity give rise to faster $1/r^3$ decay. The corresponding far-field vorticity is

$$\omega^+(r, \phi) = \frac{\alpha}{r^2} \sin \phi \left(1 + 3 \left(\frac{\zeta}{r} \right)^2 \right). \quad (3.18)$$

The far-field solutions are singular at the origin, which is not the case for the full series solution that resolves the near core field. This is demonstrated visually in figure 1c,d where we plot cross sections of the velocity and vorticity profiles for both the full solution and the far-field solution. The form of the expressions makes it natural to scale the position, velocity and vorticity with ζ , $\zeta/|\alpha|$ and $\zeta^2/|\alpha|$ respectively. The only free parameter is then the sign of α . Panels (a) and (b) show the flow streamlines and the vorticity field in the background for the full and the far-field solutions, respectively, for an extensile system ($\alpha < 0$). The velocity magnitude is highest near the defect core and decays as a power law following the far-field asymptote. The velocity streamlines point towards the defect in the right half-plane, and away from the defect in the left half-plane. For positive α , the flow direction is reversed. In an infinite system, the flow streamlines around an isolated defect are not closed. On the other hand, as discussed later, in bounded domains, the system size controls the size of the eddies formed around the defect. For more realistic configurations with many defects, the system size is typically replaced by the mean defect separation. It may be that other intrinsic length scales controlled by elastic stresses are also important in stabilizing finite-size vortices. These effects are left for future investigation.

4. Negative nematic defect in an infinite system

By similar calculations as in §3, we find that the velocity induced by the active stress at the position of the negative defect vanishes as expected from symmetry consideration. After performing the integral in the complex plane and subsequently integrating over the integrand with the Bessel

function, we determine the pressure field induced by the $-1/2$ defect vanishes inside the defect core and non-zero outside given by

$$p(\mathbf{r}) = \begin{cases} 0, & r < 1, \\ -\alpha \frac{x^3 - 3xy^2}{3r^3}, & r > 1 \end{cases} \quad (4.1)$$

and its gradient vanishes at the origin, hence no advective pressure-flow of the negative defect. Thus, an isolated $-1/2$ defect is stationary in a uniform nematic field, regardless of activity.

(a) Flow field away from the defect

The flow field induced by the $-1/2$ defect can also be expressed analytically as a series expansion of the elliptic integrals as detailed in appendix C, with the resulting expression of the velocity field in the complex representation $u^- = u_x^- + iu_y^-$ given as

$$u^-(r, \phi) = -\frac{\alpha}{2\xi^2} \sum_{n=0}^{\infty} \left(\frac{(2n-1)!!}{(2n)!!} \right)^2 \frac{2n+1}{2n-1} \left[e^{4i\phi} \frac{2n+3}{2n-3} - e^{-2i\phi} \right] \int_0^r dr' K_0 \left(\frac{r'}{\xi} \right) \left(\frac{r'}{r} \right)^{2n+1} \\ - \frac{\alpha}{2\xi^2} \sum_{n=0}^{\infty} \left(\frac{(2n-1)!!}{(2n)!!} \right)^2 \frac{n}{n+1} \left[e^{4i\phi} \frac{n-1}{n+2} - e^{-2i\phi} \right] \int_r^{\infty} dr' K_0 \left(\frac{r'}{\xi} \right) \left(\frac{r}{r'} \right)^{2n}. \quad (4.2)$$

The integrals over the Bessel functions are evaluated in appendix B, and the final expression is then given as

$$u^-(r, \phi) = \frac{\alpha}{8\xi} \left(2\pi \left[I_2 \left(\frac{r}{\xi} \right) e^{-2i\phi} - I_4 \left(\frac{r}{\xi} \right) e^{4i\phi} \right] \right. \\ \left. + \sum_{k,n} [\kappa_1^-(n, k) e^{-2i\phi} + \kappa_2^-(n, k) e^{4i\phi}] \frac{2}{(k!)^2} \left(\frac{r}{2\xi} \right)^{2k+1} \right) \quad (4.3)$$

with the coefficients

$$\kappa_1^-(n, k) = \left(\frac{(2n-1)!!}{(2n)!!} \right)^2 \frac{(4n+1)[4k^2 - (2n-1)(4k+1)(n+1)]}{(2n-1)(n+1)(n+1+k)^2(2n-1-2k)^2} \quad (4.4)$$

and

$$\kappa_2^-(n, k) = \left(\frac{(2n-1)!!}{(2n)!!} \right)^2 \left[\frac{4n(n-1)}{(n+1)(n+2)(2n-1-2k)^2} \right. \\ \left. - \frac{(2n+1)(2n+3)}{(2n-1)(2n-3)(n+k+1)^2} \right]. \quad (4.5)$$

The corresponding vorticity field as function of the polar coordinates follows as:

$$\omega^-(r, \phi) = -\frac{\alpha}{8\xi^2} \sin(3\phi) \left(4\pi I_3 \left(\frac{r}{\xi} \right) + \sum_{k,n} [(2k-1)\kappa_1^-(n, k) \right. \\ \left. - (2k+5)\kappa_2^-(n, k)] \frac{1}{(k!)^2} \left(\frac{r}{2\xi} \right)^{2k} \right). \quad (4.6)$$

(b) Asymptotic far-field flow

As with the $+1/2$ defect, the far-field asymptotic flow is dominated by the leading order terms in the expansion, which can also be computed directly from equation (4.2) in the limit of $r/\xi \rightarrow \infty$.

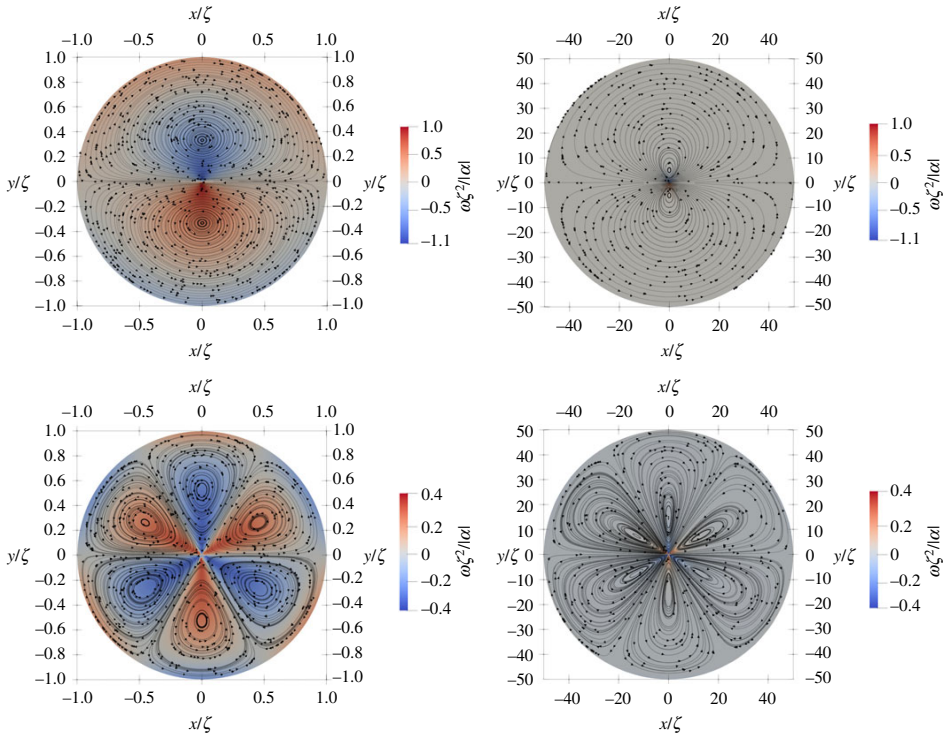


Figure 5. Flow streamlines (black lines) with vorticity as a colour map background generated by a $+1/2$ (a, b) and a $-1/2$ (c, d) defect in discs of different radii R for an extensile system ($\alpha < 0$). (a) and (c) are for $R = 1$ and (b) and (d) $R = 50$. (Online version in colour.)

The result of this calculation is that

$$u^-(r, \phi) \underset{\xi \gg 1}{\approx} = \frac{\alpha}{2r} \left[\left(\frac{\xi}{r} \right)^2 (15e^{4i\phi} + 3e^{-2i\phi}) - (e^{4i\phi} + e^{-2i\phi}) \right]. \quad (4.7)$$

As for equation (3.17) the $1/r$ term here was also obtained in [24]. The vorticity related to this velocity is

$$\omega^-(r, \phi) = \frac{3\alpha \sin(3\phi)}{r^2} \left(5 \left(\frac{\xi}{r} \right)^2 - 1 \right). \quad (4.8)$$

In this asymptotic approximation, the flow field is singular at the origin. This singularity is however lifted by the higher order terms in the series expansions, so that the exact flow is smooth everywhere. Figure 2 shows the flow streamlines with the vorticity field as the colour map for the asymptotic (in a) and the exact solutions (in b), with the values scaled in the same way as for figure 1. Cross sections of the vorticity and velocity at $y = 0$ are plotted in (c, d) showing the singular behaviour of the asymptotic approximation at the origin, while it captures very well the far-field behaviour. The plots correspond to an extensile system with $\alpha < 0$. The $\sin(3\phi)$ factor in the vorticity divides the plane in six regions where the sign of the vorticity is altered and making it multi-valued at the origin. The size of the velocity is zero at origin as we discussed above. It increases a bit outside before it starts to decay with increasing r following the far-field asymptotic behaviour.

As for the $+1/2$ defect, the flow streamlines never closed in an infinite system, thus there are no finite size vortices. In the next section, we discuss how the picture changes once the defect is placed in bounded domain.

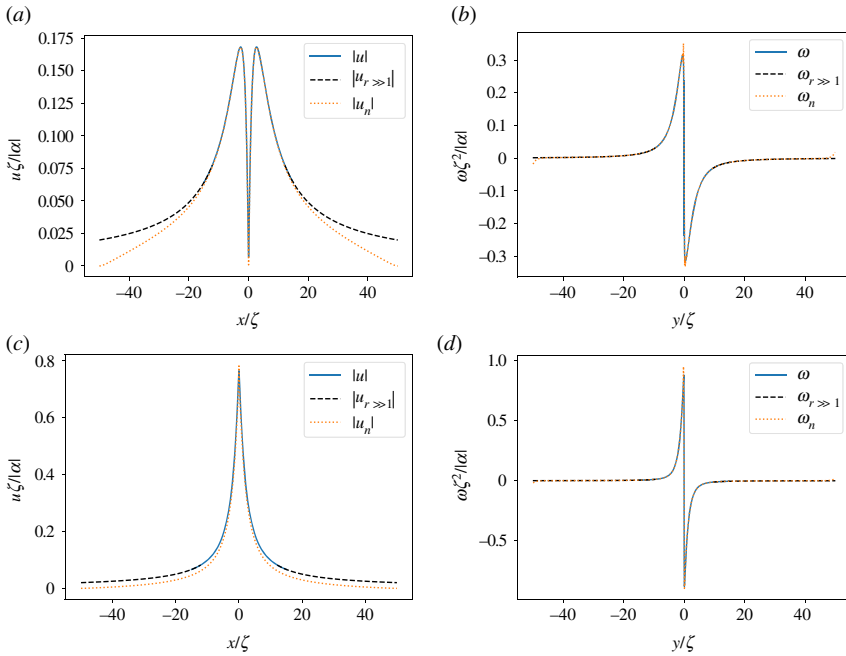


Figure 6. Cross sections of the numerically obtained velocity (a,c) and vorticity (b,d) profiles for $R = 50$ (in units of ℓ_d) (orange dotted lines) are compared with the analytical solution for an infinite system (solid blue lines) for a negative (a,b) and positive (c,d) defect. x and y are also in units of ℓ_d . The dashed black lines are the asymptotic solutions. (Online version in colour.)

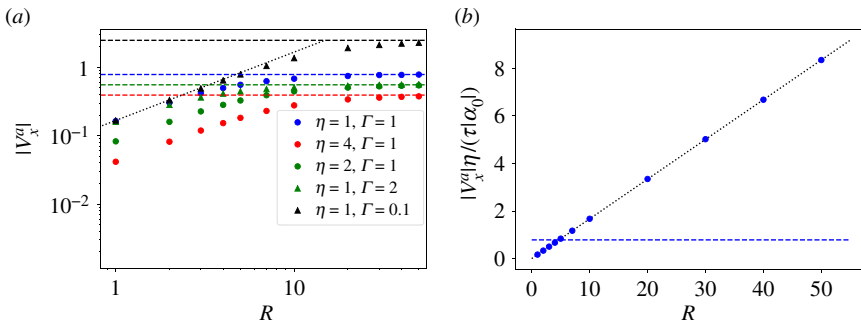


Figure 7. The self-propulsion speed of a $+1/2$ defect as a function of the disc radius, R for (a) different values of the parameters η and Γ and (b) $\Gamma = 0$. The black dotted line is a best fit line for the system in (b), it is also plotted for the $\Gamma \neq 0$ systems ignoring the constant term. Horizontal dashed lines are the analytical prediction for an infinite system $v_+^{(a)} = \pi \alpha_0 / (4\sqrt{\eta\tau})$ with the rescaled activity $|\alpha_0| = 1$. (Online version in colour.)

5. Isolated defect in a bounded active nematic

The problem of finding the flow field around defects in a bounded domain is challenging to solve analytically. Thus, we resort to numerical solutions of the Stokes flow given by equation (2.4) in a disc of radius R using finite-element methods and homogeneous boundary conditions (zero velocity). In addition, we use the simplification that a single defect is imprinted in an

uniform nematic field, while the changes in the nematic orientation induced by confinement are ignored [17].

The Stokes flow equation (2.4) is solved with FEniCS using Taylor–Hood elements, which are quadratic for the velocity and linear for the pressure and vorticity [32,33].

Figure 1 shows the flow streamlines induced by a single $+1/2$ (a,b) and $-1/2$ (c,d) defect in a disc of radius R for an extensile system for $\eta \neq 0$ and $\Gamma \neq 0$. The left and right columns correspond to $R = 1$ and $R = 50$, respectively. In a bounded system, the vortical flows around each defect span the system size, as also reported in [17] for $\Gamma = 0$. However, due to friction with the substrate, the flow decays on length scales larger than ℓ_d . This is evident by comparing the values in the far-field of vorticity in the left and right columns from figure 5, corresponding to $R = 1$ (in units of ℓ_d) in (a,c) and $R = 50$ (in units of ℓ_d) in (b,d). We note that the centre of a vortex is not fixed at the maximum of the vorticity. This is due to the fact that the $\pm 1/2$ defects generate shear flows that localize shear vorticity next to the defect cores. However, unlike curvature vorticity in rotating flows which peaks at the vortex core, shear vorticity is not necessarily an indication of the presence of vortices or their location. In fact, with increasing R , the flow gradients near the defect cores become sharper, the streamlines near the cores are ‘stretched’ in the radial direction, and the eyes of vortices move further from the origin. In the limit $R \rightarrow \infty$, we expect vortices to get stretched out so that flow streamlines close at infinity, and we recover the analytic flow profiles.

In figure 6, we compare the cross-sectional profiles of velocity and vorticity obtained from the numerical solution for a large system, $R = 50$ (ℓ_d) to the analytical solutions. The analytical solutions is obtained by truncating the summation in the full solution at $n = 5000$ and $k = 500$ up to $r = 15$ and then using the asymptotic solution for $r > 15$. The plots of velocity in panels (a,c) show that the numerical and analytical solutions agree very well close to the defect cores, but deviate from each other near the boundary. This is due to the imposed boundary conditions of the vanishing velocity field. The vorticity in panels (b,d) agrees well in the entire domain, with a small boundary effect due to vanishing velocity and vortices spanning the system size. This effect is perhaps more visible for the negative defect and decreases with increasing R .

The self-propulsion speed v_x^a of the $+1/2$ defect is also affected by the system size. If $\Gamma = 0$ at the outset $v_x^a \sim R$, as noted in [17]. Frictional damping screens out this divergence, yielding the finite value given in equation (3.7) for $R \rightarrow \infty$. The numerical calculation shows, however, that for smaller R there are finite-size corrections to the defect propulsive speed. These are displayed in figure 7, where we plot $|v_x^a|$ as a function of R obtained from the numerical solution of equation (2.4) for different values of η and Γ . The horizontal dashed lines are the analytical solution in the limit of an infinite system, as given by $v_x^{(a)} \approx (\pi/4)(\alpha_0/\sqrt{\eta\Gamma})$, while the dotted black lines show the linear scaling with R in the limit of zero friction. We note that viscosity η determines the slope for R dependence in small systems, while friction Γ controls the cross-over to the intrinsic constant speed. Note that the asymptotic constant values of v_x^a agree very well with the analytical prediction at $\zeta \gg 1$ because in the numerical computations the vortex core is actually set to zero (hydrodynamic regime with $S = 1$). For comparison, we also show in figure 7b the defect propulsion speed in the absence of friction $\Gamma = 0$ from the outset, where the speed increases linearly with the system size. The dotted black line represents the analytical prediction as found in [17].

6. Conclusion

In summary, we have evaluated the flow field induced by an isolated $\pm 1/2$ defect in an incompressible active nematic film on a substrate both for an infinite system and a finite-size disc. While the self-propulsion speed of a $+1/2$ defect diverges with system size for an isolated film, we show analytically that the presence of finite substrate friction Γ cures this divergence resulting in a finite speed $v_x^{(a)} \approx (\pi/4)(\alpha_0/\sqrt{\eta\Gamma}) = (\pi/4)(\alpha_0/\eta)\ell_d$ that increases with the hydrodynamic dissipation length ℓ_d . This is also confirmed numerically in a finite disc with $R > \ell_d$. For small discs with $R < \ell_d$, the active speed scales instead linearly with R .

Stable shear vortical flows are formed around the defects. In finite systems, the size of the flow vortices is controlled by the dissipation length ℓ_d , hence spans the whole system if $\ell_d > R$. The eye of the vortices shifts away from the defect core with increasing R . For infinite-size systems, the flow streamlines close at infinity as predicted by the far-field analytical solution. In the same limit, we showed that the absolute value of the velocity decreases as $1/r$ for distances that are large compared with the dissipation length scale, in agreement with previous studies. The $1/r$ far-field decay of the flow created by defects may seem surprising as it suggests that a defect acts like a point force. This behaviour arises from the long-range nature of the distortion of the texture created by defects. When other defects are present (as required in the plane to guarantee zero net topological charge), this decay is cut off by the defect separation. In finite domains, it is cut off by the system size. The $1/r$ decay indicates, however, that a multi-defect approach is needed to describe the defect gas, as attempted in [34,35].

In this work, we have neglected the effect of the elastic stress. An interesting extension would be to study the effects it would have on the flow field, and also considering the effect of having multiple interacting defects.

Data accessibility. This is primarily theoretical work and does not have any experimental data. The computational data and codes for FEniCS are available on GitHub: <https://github.com/jonason/Defect-Flows>.

Authors' contributions. J.R.: formal analysis, software, visualization, writing-original draft, writing review and editing; C.M.M.: validation, writing review and editing; M.J.B.: validation, writing review and editing; L.A.: conceptualization, supervision, validation, writing original draft, writing review and editing.

Competing interests. We declare we have no competing interests.

Funding. J.R. and L.A. acknowledge support from the Research Council of Norway through the Center of Excellence funding scheme, Project no. 262644 (PoreLab). M.C.M. was supported by the US National Science Foundation through Grant No. DMR-2041459.

Appendix A. Integrals for the $+1/2$ defect

Here, we provide the detailed steps that are taken to arrive at equation (3.12) from equation (3.11). We start by changing to a complex representation $u = u_x + iu_y$ with complex coordinates $z = x + iy$ and $z' = x' + iy'$. By changing variables to $t = z' - z$, and then to polar coordinates $t = r'e^{i\theta} = r'\hat{z}$, we write equation (3.11) as

$$u = \frac{\alpha}{4i\pi\zeta^2} \int dr' r' K_0 \left(\frac{r'}{\zeta} \right) \oint_{\gamma} d\hat{z} \times \left(\frac{r'\hat{z}^2 + z\hat{z}}{(r' + \bar{z}\hat{z})\sqrt{\hat{z}(r'\hat{z} + z)(r' + \bar{z}\hat{z})}} + \frac{1}{\sqrt{\hat{z}(r'\hat{z} + z)(r' + \bar{z}\hat{z})}} \right), \quad (\text{A } 1)$$

where γ is the unit circle. We note that the integral over \hat{z} is over three branch points. $\hat{z} = 0$ is always in the unit circle, $\hat{z} = -z/r$ is inside when $|z| < r$ and $\hat{z} = -r/\bar{z}$ when $|z| > r$. We consider the integral over \hat{z} and start by looking at the last term. Splitting up the square root, we write it as

$$\frac{1}{\sqrt{\bar{z}r'}} \oint_{\gamma} d\hat{z} \frac{1}{\sqrt{\bar{z}}\sqrt{(\hat{z} + \frac{z}{r})}\sqrt{(\hat{z} + \frac{r'}{\bar{z}})}}. \quad (\text{A } 2)$$

We see that for all values of r' we have two branch points inside of the contour. Therefore, we write the integral as

$$\frac{1}{\sqrt{\bar{z}r'}} \oint_{\gamma} d\hat{z} \frac{1}{\sqrt{\bar{z}}\sqrt{(\hat{z} + a)}\sqrt{(\hat{z} + b)}}. \quad (\text{A } 3)$$

From here, $-a$ is the branch point inside of the contour, while $-b$ is the point outside of the contour. We note that the complex numbers a and b have the same argument ϕ so we can write it

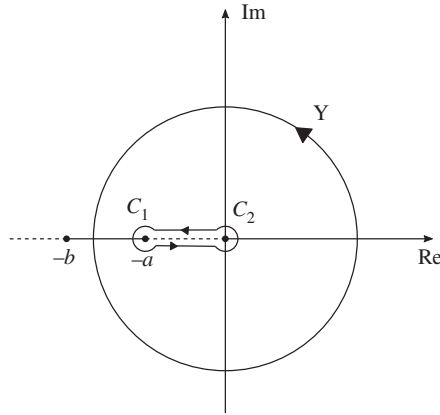


Figure 8. Sketch of the keyhole contour in the complex plane associated with the integral in equation (A 4).

as

$$\frac{1}{\sqrt{z}r'} \oint_{\gamma} d\hat{z} \frac{1}{\sqrt{\hat{z}}\sqrt{(\hat{z} + ae^{i\phi})}\sqrt{(\hat{z} + be^{i\phi})}}. \quad (\text{A } 4)$$

a and b are now either r/r' and r'/r . If we change our integral variable from \hat{z} to $\hat{u} = \hat{z}e^{-i\phi}$, we get

$$\begin{aligned} & \frac{1}{\sqrt{z}r'} \oint_{\gamma} d\hat{u} e^{i\phi} \frac{1}{\sqrt{e^{i\phi}\hat{u}}\sqrt{(e^{i\phi}\hat{u} + ae^{i\phi})}\sqrt{(e^{i\phi}\hat{u} + be^{i\phi})}} \\ &= \frac{e^{-i\phi/2}}{\sqrt{z}r'} \oint_{\gamma} d\hat{u} \frac{1}{\sqrt{\hat{u}}\sqrt{(\hat{u} + a)}\sqrt{(\hat{u} + b)}}. \end{aligned} \quad (\text{A } 5)$$

Note that all branch points $\hat{z} = 0$, $-a$ and $-b$ are now located on the real axis. We now have to consider what branch cuts we want to use to perform this integral. We consider the integral over the domain as shown in figure 8. Here, we have cut out a area around the branch cut in order to avoid problems. The key hole consists of a circle C_1 with radius ϵ around $-a$, the circle C_2 around the origin and the lines connecting them which is ϵ above or below the real line as shown in figure 8. Since there are no poles in the domain between the two contours, the integral of them has to be the same [36]. The contour integral becomes

$$\begin{aligned} & \int_{\gamma} \frac{e^{-i\phi/2}}{\sqrt{z}r'} d\hat{u} \frac{1}{\sqrt{\hat{u}}\sqrt{(\hat{u} + a)}\sqrt{(\hat{u} + b)}} \\ &= \left(\int_{-a-i\epsilon \rightarrow -i\epsilon} + \int_{i\epsilon \rightarrow -a+i\epsilon} + \int_{C_1} + \int_{C_2} \right) \frac{e^{-i\phi/2}}{\sqrt{z}r'} \frac{d\hat{u}}{\sqrt{\hat{u}}\sqrt{(\hat{u} + a)}\sqrt{(\hat{u} + b)}}. \end{aligned} \quad (\text{A } 6)$$

When $\epsilon \rightarrow 0$, the integrals over C_1 and C_2 disappears. The integral above the real line is just above the branch cut and therefore positive, while the one below is negative. We therefore get

$$\oint_{\gamma} \frac{e^{-i\phi/2}}{\sqrt{z}r'} d\hat{u} \frac{1}{\sqrt{\hat{u}}\sqrt{(\hat{u} + a)}\sqrt{(\hat{u} + b)}} = -2 \frac{e^{-i\phi/2}}{\sqrt{z}r'} \int_{-a}^0 d\hat{u} \frac{1}{\sqrt{\hat{u}}\sqrt{(\hat{u} + a)}\sqrt{(\hat{u} + b)}}. \quad (\text{A } 7)$$

Evaluating this integral, we obtain

$$\oint_{\gamma} \frac{e^{-i\phi/2}}{\sqrt{z}r'} d\hat{u} \frac{1}{\sqrt{\hat{u}}\sqrt{(\hat{u} + a)}\sqrt{(\hat{u} + b)}} = 4i \frac{e^{-i\phi/2}}{\sqrt{z}r'} \frac{1}{\sqrt{b}} K\left(\frac{a}{b}\right). \quad (\text{A } 8)$$

Here, K is the complete elliptic integral of the first kind with the power series

$$K(x) = \frac{\pi}{2} \sum_{n=0}^{\infty} \left(\frac{(2n-1)!!}{(2n)!!} \right)^2 x^n. \quad (\text{A } 9)$$

With the double factorial $(2n)!! = 2 \cdot 4 \cdot 6 \cdots (2n-2) \cdot 2n$.

We now consider the other integral over \hat{z} in equation (A 1):

$$\oint_{\gamma} d\hat{z} \frac{r'\hat{z}^2 + z\hat{z}}{(r' + \hat{z}\hat{z})\sqrt{\hat{z}(r'\hat{z} + z)(r' + \hat{z}\hat{z})}}. \quad (\text{A } 10)$$

This is not symmetric in the branch points as the other integral was. We can write this as

$$r^{1/2}\bar{z}^{-3/2} \oint_{\gamma} d\hat{z} \frac{\hat{z}^{1/2}(\hat{z} + e^{i\phi}r/r')^{1/2}}{(\hat{z} + e^{i\phi}r'/r)^{3/2}}, \quad (\text{A } 11)$$

and we can rotate the integral variable to $u = \hat{z}e^{-i\phi}$ and get

$$\begin{aligned} r^{1/2}\bar{z}^{-3/2} \oint_{\gamma} d\hat{u} e^{i\phi} \frac{\hat{u}^{1/2}e^{i\phi/2}(\hat{u}e^{i\phi} + e^{i\phi}r/r')^{1/2}}{(\hat{u}e^{i\phi} + e^{i\phi}r'/r)^{3/2}} \\ = r^{1/2}\bar{z}^{-3/2} e^{i\phi/2} \oint_{\gamma} d\hat{u} \frac{\hat{u}^{1/2}(\hat{u} + r/r')^{1/2}}{(\hat{u} + r'/r)^{3/2}}. \end{aligned} \quad (\text{A } 12)$$

Which of the branch points that are inside of the integral depends on the value of r' . If $r' > r$ then r/r' is inside of the unit circle. We can then use the same branch cuts and arguments as before and find

$$\begin{aligned} r^{1/2}\bar{z}^{-3/2} e^{i\phi/2} \oint_{\gamma} d\hat{u} \frac{\hat{u}^{1/2}(\hat{u} + r/r')^{1/2}}{(\hat{u} + r'/r)^{3/2}} \\ = -2r^{1/2}\bar{z}^{-3/2} e^{i\phi/2} \int_{-r/r'}^0 d\hat{u} \frac{\hat{u}^{1/2}(\hat{u} + r/r')^{1/2}}{(\hat{u} + r'/r)^{3/2}}. \end{aligned} \quad (\text{A } 13)$$

We can perform the integral and find that it equals

$$-2r^{1/2}\bar{z}^{-3/2} e^{i\phi/2} \frac{2i}{\sqrt{r'/r}} \left[\left(\frac{2r'}{r} - \frac{r}{r'} \right) K\left(\frac{r^2}{r'^2}\right) - \frac{2r'}{r} E\left(\frac{r^2}{r'^2}\right) \right]. \quad (\text{A } 14)$$

Here, $E(x)$ is the complete elliptic integral of the second kind with the power series

$$E(x) = \frac{\pi}{2} \left(1 - \sum_{n=1}^{\infty} \left(\frac{(2n-1)!!}{(2n)!!} \right)^2 \frac{x^n}{2n-1} \right). \quad (\text{A } 15)$$

The other possibility is that $r' < r$. Now it is the $-3/2$ root that is inside of the integral domain. In this case, we cannot use the above approach since the integrand does not go to zero when \hat{z} goes to r'/r . However, we can use the binomial expansion that is valid for $|x| < 1$. We have that

$$r^{1/2}\bar{z}^{-3/2} e^{i\phi/2} \oint_{\gamma} d\hat{u} \frac{\hat{u}^{1/2}(\hat{u} + a)^{1/2}}{(\hat{u} + b)^{3/2}}. \quad (\text{A } 16)$$

Doing a change of variables to $h = \sqrt{\hat{u}}$ with $dh = du/(2\sqrt{\hat{u}})$. We then get (remembering a factor half since because integrating once around h we have gone twice around u)

$$r^{1/2}\bar{z}^{-3/2} e^{i\phi/2} \oint_{\gamma} dh \frac{h^2(h^2 + a)^{1/2}}{(h^2 + b)^{3/2}}. \quad (\text{A } 17)$$

We have that $|h| = 1$, $a > 1$ and $b < 1$. We therefore write this

$$r^{1/2}\bar{z}^{-3/2} e^{i\phi/2} \oint_{\gamma} dh \frac{\sqrt{a}(1 + h^2/a)^{1/2}}{h(1 + b/h^2)^{3/2}}. \quad (\text{A } 18)$$

We now use the binomial expansion

$$(1+x)^r = \sum_{n=0}^{\infty} \binom{r}{n} x^n, \quad (\text{A } 19)$$

and the integral becomes

$$r^{1/2} \bar{z}^{-3/2} e^{i\phi/2} \sqrt{a} \oint_{\gamma} \frac{dh}{h} \left(\sum_{n=0}^{\infty} \binom{1/2}{n} \left(\frac{h^2}{a} \right)^n \right) \left(\sum_{k=0}^{\infty} \binom{-3/2}{k} \left(\frac{b}{h^2} \right)^k \right). \quad (\text{A } 20)$$

By the residue theorem only the terms where $k = n$ is contributing to the integral. We therefore get

$$\begin{aligned} & r^{1/2} \bar{z}^{-3/2} e^{i\phi/2} \sqrt{a} \oint_{\gamma} \frac{dh}{h} \left(\sum_{n=0}^{\infty} \binom{1/2}{n} \binom{-3/2}{n} \left(\frac{b}{a} \right)^n \right) \\ &= 2\pi i r^{1/2} \bar{z}^{-3/2} e^{i\phi/2} \sqrt{a} \left(\sum_{n=0}^{\infty} \binom{1/2}{n} \binom{-3/2}{n} \left(\frac{b}{a} \right)^n \right). \end{aligned} \quad (\text{A } 21)$$

Inserting the expressions for a and b , we find

$$2\pi i \bar{z}^{-3/2} e^{i\phi/2} \sqrt{r} \sum_{n=0}^{\infty} \binom{1/2}{n} \binom{-3/2}{n} \left(\frac{r'}{r} \right)^{2n}. \quad (\text{A } 22)$$

Now we have solved the integral over the angles \hat{z} . Inserting this into the equation (A1), we find

$$\begin{aligned} u &= \frac{\alpha}{4i\pi \zeta^2} \int_0^r dr' r' K_0(r'/\zeta) \left(2\pi i \bar{z}^{-3/2} e^{i\phi/2} \sqrt{r} \sum_{n=0}^{\infty} \binom{1/2}{n} \binom{-3/2}{n} \left(\frac{r'}{r} \right)^{2n} \right. \\ &\quad \left. + \frac{4ie^{-i\phi/2}}{\sqrt{\bar{z}r'}} \sqrt{\frac{r'}{r}} K \left(\frac{r'^2}{r^2} \right) \right) + \frac{\alpha}{4i\pi \zeta^2} \int_r^{\infty} dr' r' K_0(r'/\zeta) \\ &\quad \times \left(\frac{4ie^{i\phi/2} \sqrt{r}}{\bar{z}^{3/2}} \left[\left(\frac{r}{r'} - 2 \frac{r'}{r} \right) K \left(\frac{r^2}{r'^2} \right) + 2 \frac{r'}{r} E \left(\frac{r^2}{r'^2} \right) \right] \right. \\ &\quad \left. + \frac{4ie^{-i\phi/2}}{\sqrt{\bar{z}r'}} \sqrt{\frac{r}{r'}} K \left(\frac{r^2}{r'^2} \right) \right) \end{aligned} \quad (\text{A } 23)$$

Using that $\bar{z} = re^{-i\phi}$ and inserting the expressions for the K and E this becomes

$$\begin{aligned} u &= \frac{\alpha}{2\zeta^2} \int_0^r dr' K_0 \left(\frac{r'}{\zeta} \right) \left(\frac{r'}{r} \right)^{2n+1} \left(e^{2i\phi} \sum_{n=0}^{\infty} \binom{1/2}{n} \binom{-3/2}{n} + \sum_{n=0}^{\infty} \left(\frac{(2n-1)!!}{(2n)!!} \right)^2 \right) \\ &\quad + \frac{\alpha}{2\zeta^2} \int_r^{\infty} dr' K_0 \left(\frac{r'}{\zeta} \right) \left(\frac{r}{r'} \right)^{2n} \left(\sum_{n=0}^{\infty} \left[\left(\frac{(2n-1)!!}{(2n)!!} \right)^2 - 2 \left(\frac{(2n+1)!!}{(2n+2)!!} \right)^2 \frac{2n+2}{2n+1} \right] e^{2i\phi} \right. \\ &\quad \left. + \sum_{n=0}^{\infty} \left(\frac{(2n-1)!!}{(2n)!!} \right)^2 \right). \end{aligned} \quad (\text{A } 24)$$

We can simplify this by using that

$$\sum_{n=0}^{\infty} \left(\frac{(2n-1)!!}{(2n)!!} \right)^2 - 2 \left(\frac{(2n+1)!!}{(2n+2)!!} \right)^2 \frac{2n+2}{2n+1} = - \sum_{n=0}^{\infty} \left(\frac{(2n-1)!!}{(2n)!!} \right)^2 \frac{n}{n+1}, \quad (\text{A } 25)$$

and for the binomial

$$\binom{1/2}{n} \binom{-3/2}{n} = - \frac{2n+1}{2n-1} \left(\frac{(2n-1)!!}{(2n)!!} \right)^2. \quad (\text{A } 26)$$

Inserting this we finally arrive at

$$u = \frac{\alpha}{2\xi^2} \sum_{n=0}^{\infty} \left(\frac{(2n-1)!!}{(2n)!!} \right)^2 \left(1 - \frac{2n+1}{2n-1} e^{2i\phi} \right) \int_0^r dr' K_0 \left(\frac{r'}{\xi} \right) \left(\frac{r'}{r} \right)^{2n+1} + \frac{\alpha}{2\xi^2} \sum_{n=0}^{\infty} \left(\frac{(2n-1)!!}{(2n)!!} \right)^2 \left(1 - \frac{n}{n+1} e^{2i\phi} \right) \int_r^{\infty} dr' K_0 \left(\frac{r'}{\xi} \right) \left(\frac{r}{r'} \right)^{2n}. \quad (\text{A } 27)$$

Appendix B. Integrals over the Bessel function

We start a change of variables to $r'' = \xi^{-1}r'$, and then evaluate the integrals over the Bessel functions as

$$\begin{aligned} & \xi^{2n+2} \int_0^{r/\xi} dr'' K_0(r'') r''^{2n+1} \\ &= \frac{1}{4} r^{2n+2} n! \left[n! {}_2\tilde{F}_3 \left(1+n, 1+n; 1, 2+n, 2+n; \frac{r^2}{4\xi^2} \right) \right. \\ & \quad - 2 {}_1\tilde{F}_2 \left(1+n; 1, 2+n; \frac{r^2}{4\xi^2} \right) \left(\gamma + \ln \left(\frac{r}{2\xi} \right) \right) \\ & \quad \left. + 2 \frac{\partial}{\partial a_1} {}_2\tilde{F}_3 \left(a_1, 1+n; 1, 1, 2+n; \frac{r^2}{4\xi^2} \right) \Big|_{a_1=1} \right] \\ &= \frac{1}{4} r^{2n+2} F^{r' < r} \left(n, \frac{r}{\xi} \right) \end{aligned} \quad (\text{B1})$$

and

$$\begin{aligned} & \xi^{1-2n} \int_{r/\xi}^{\infty} dr' K_0(r') \left(\frac{1}{r'} \right)^{2n} \\ &= \frac{1}{4} r^{-2n+1} \Gamma \left(\frac{1}{2} - n \right) \left[4^{-n} \Gamma \left(\frac{1}{2} - n \right) \left(2 \left(\frac{r}{\xi} \right)^{2n-1} \right. \right. \\ & \quad \left. \left. - 4^n {}_2\tilde{F}_3 \left(\frac{1}{2} - n, \frac{1}{2} - n; 1, \frac{3}{2} - n, \frac{3}{2} - n; \frac{r^2}{4\xi^2} \right) \right) \right. \\ & \quad \left. + 2 {}_1\tilde{F}_2 \left(\frac{1}{2} - n; 1, \frac{3}{2} - n; \frac{r^2}{4\xi^2} \right) \left(\gamma + \ln \left(\frac{r}{2\xi} \right) \right) \right. \\ & \quad \left. - 2 \frac{\partial}{\partial a_1} {}_2\tilde{F}_3 \left(a_1, \frac{1}{2} - n; 1, \frac{3}{2} - n; \frac{r^2}{4\xi^2} \right) \Big|_{a_1=1} \right] \\ &= \frac{1}{4} r^{-2n+1} F^{r' > r} \left(n, \frac{r}{\xi} \right). \end{aligned} \quad (\text{B2})$$

Here, the regularized hypergeometric function is defined as

$${}_p\tilde{F}_q(a_1, \dots, a_p; b_1, \dots, b_q; x) = \frac{1}{\Gamma(b_1) \dots \Gamma(b_q)} \sum_{k=0}^{\infty} \frac{(a_1)_k \dots (a_p)_k x^k}{(b_1)_k \dots (b_q)_k k!}, \quad (\text{B3})$$

where $(a)_k = a \cdot (a+1) \dots (a+k-1)$ is the rising factorial. These expressions can be simplified. Using that $\Gamma(x) = (x-1)\Gamma(x-1)$, it follows that the Pochhammer symbol is given as

$$(a)_k = \frac{\Gamma(a+k)}{\Gamma(a)}, \quad (\text{B4})$$

with the derivative

$$\partial_a(a)_k|_{a=1} = (a)_k(\psi^{(0)}(a+k) - \psi^{(0)}(a))|_{a=1} = k!(\psi^{(0)}(1+k) - \psi^{(0)}(1)). \quad (\text{B5})$$

Here, $\psi^{(0)}(k)$ is the digamma function, that is the first derivative of the logarithm of the gamma function. For integer arguments, it is given as

$$\psi^{(0)}(n) = -\gamma + \sum_{l=1}^{n-1} \frac{1}{l}. \quad (\text{B6})$$

Using the relations above, we find after some algebra that the moments are given by the power series

$$\begin{aligned} F^{r' < r} \left(n, \frac{r}{\zeta} \right) &= \sum_{k=0}^{\infty} \left[\frac{1}{(n+k+1)} - 2 \left(\gamma + \ln \left(\frac{r}{2\zeta} \right) \right) + 2 \sum_{l=1}^k \frac{1}{l} \right] \\ &\times \frac{1}{(n+k+1)(k!)^2} \left(\frac{r}{2\zeta} \right)^{2k} \end{aligned} \quad (\text{B7})$$

and

$$\begin{aligned} F^{r' > r} \left(n, \frac{r}{\zeta} \right) &= 4 \sum_{k=0}^{\infty} \left[\sum_{l=1}^k \frac{1}{l} - \left(\gamma + \ln \left(\frac{r}{2\zeta} \right) \right) - \frac{1}{2n-1-2k} \right] \frac{1}{(2n-1-2k)(k!)^2} \\ &\times \left(\frac{r}{2\zeta} \right)^{2k} + \frac{2\pi}{((2n-1)!)^2} \left(\frac{r}{\zeta} \right)^{2n-1}. \end{aligned} \quad (\text{B8})$$

Appendix C. Integrals for the $-1/2$ defect

Here, we provide details of the calculation leading to equation (4.2). Using the complex representation with similar coordinate transformations as for the $+1/2$ -defect, the corresponding active flow velocity, $u^- = u_x^- + iu_y^-$ induced by active stress and pressure gradient from equation (2.7) reads as

$$u^- = -\frac{\alpha}{4i\pi\zeta^2} \int dr' r' K_0 \left(\frac{r'}{\zeta} \right) \oint_{\gamma} \frac{d\hat{z}}{\hat{z}} \left(\frac{1}{r'\hat{z}+z} \sqrt{\frac{r'\hat{z}^{-1}+\bar{z}}{r'\hat{z}+z}} + \frac{r'\hat{z}+z}{(r'\hat{z}^{-1}+\bar{z})^2} \sqrt{\frac{r'\hat{z}+z}{r'\hat{z}^{-1}+\bar{z}}} \right). \quad (\text{C1})$$

We start by looking at the integral over \hat{z} and we will first consider the second term:

$$\oint_{\gamma} \frac{d\hat{z}}{\hat{z}} \frac{r'\hat{z}+z}{(r'\hat{z}^{-1}+\bar{z})^2} \sqrt{\frac{r'\hat{z}+z}{r'\hat{z}^{-1}+\bar{z}}} = \frac{r'^{3/2}}{\bar{z}^{5/2}} \oint_{\gamma} d\hat{z} \frac{\hat{z}^{3/2}(\hat{z}+z/r')^{3/2}}{(\hat{z}+r'/\bar{z})^{5/2}}. \quad (\text{C2})$$

Using that $z = re^{i\phi}$ and changing variable to $u = e^{i\phi}\hat{z}$ we get

$$\frac{r'^{3/2}}{\bar{z}^{5/2}} \oint_{\gamma} d\hat{z} \frac{\hat{z}^{3/2}(\hat{z}+e^{i\phi}r/r')^{3/2}}{(\hat{z}+e^{i\phi}r'/\bar{z})^{5/2}} = \frac{r'^{3/2}}{r^{5/2}} e^{4i\phi} \oint_{\gamma} du \frac{u^{3/2}(u+(r/r'))^{3/2}}{(u+(r'/r))^{5/2}}. \quad (\text{C3})$$

This integral has three branch points on the real axis. Two of these points are inside the integration domain and give troubles. If $r' > r$ we have the two points $u=0$ and $u=r/r'$ inside of the unit circle. In this case, one uses the same key hole contour technique as (A7) and gets

$$\frac{r'^{3/2}}{r^{5/2}} e^{4i\phi} \oint_{\gamma} du \frac{u^{3/2}(u+(r/r'))^{3/2}}{(u+(r'/r))^{5/2}} = -2 \frac{r'^{3/2}}{r^{5/2}} e^{4i\phi} \int_{-r/r'}^0 du \frac{u^{3/2}(u+(r/r'))^{3/2}}{(u+(r'/r))^{5/2}}. \quad (\text{C4})$$

Performing this integral, we arrive at

$$\frac{4i}{3} e^{4i\phi} \frac{r'}{r^2} \left(\left[3 \left(\frac{r}{r'} \right)^2 - 16 + 16 \left(\frac{r'}{r} \right)^2 \right] K \left(\frac{r^2}{r'^2} \right) + \left[8 - 16 \left(\frac{r'}{r} \right)^2 \right] E \left(\frac{r^2}{r'^2} \right) \right), \quad (\text{C5})$$

where the functions K and E are defined in appendix A. Now let us look at the integral when $r' < r$. In this case, we can not use the contour approach because the integrand diverges near the r'/r pole. We, therefore, use the binomial expansion to evaluate this integral. We first change the variable to $h = \sqrt{u}$. The integral is then

$$\frac{r'^{3/2}}{r^{5/2}} e^{4i\phi} \oint_{\gamma} du \frac{u^{3/2}(u + (r/r'))^{3/2}}{(u + (r'/r))^{5/2}} = \frac{r'^{3/2}}{r^{5/2}} e^{4i\phi} \oint_{\gamma} dh \frac{h^4(h^2 + a)^{3/2}}{(h^2 + b)^{5/2}}. \quad (\text{C6})$$

We have introduced $a = r/r'$ and $b = r'/r$ and $|h| = 1$, $|b| < 1$ and $|a| > 1$. We therefore write this as

$$\begin{aligned} & \frac{r'^{3/2}}{r^{5/2}} a^{3/2} e^{4i\phi} \oint_{\gamma} dh \frac{h^4(1 + h^2/a)^{3/2}}{h^5(1 + b/h^2)^{5/2}} \\ &= \frac{1}{r} e^{4i\phi} \oint_{\gamma} \frac{dh}{h} \left(\sum_{k=0}^{\infty} \binom{3/2}{k} \left(\frac{h^2}{a}\right)^k \right) \left(\sum_{n=0}^{\infty} \binom{-5/2}{n} \left(\frac{b}{h^2}\right)^n \right). \end{aligned} \quad (\text{C7})$$

The residual theorem makes it so that only the terms with $k = n$ is relevant. The integral finally becomes

$$\frac{2\pi i}{r} e^{4i\phi} \sum_{n=0}^{\infty} \binom{3/2}{n} \binom{-5/2}{n} \left(\frac{r'}{r}\right)^{2n}. \quad (\text{C8})$$

We now turn to the first term in the integral over \hat{z} in equation (C1). It is

$$\oint_{\gamma} \frac{d\hat{z}}{\hat{z}} \frac{1}{r'\hat{z} + z} \sqrt{\frac{r'\hat{z} - 1 + \bar{z}}{r'\hat{z} + z}}. \quad (\text{C9})$$

We change variables to $t = 1/\hat{z}$ with $dt = -d\hat{z}/\hat{z}^2$. In addition there comes a negative sign because we must reverse the contour. This integral is then

$$\oint_{\gamma} \frac{dt}{t} \frac{1}{r't - 1 + z} \sqrt{\frac{r't + \bar{z}}{r't - 1 + z'}} \quad (\text{C10})$$

which is same integral as in equation (A10) with z and \bar{z} interchanged. We can therefore use the solution we found in appendix A with $\phi \rightarrow -\phi$. The velocity field is then

$$\begin{aligned} u = & -\frac{\alpha}{4i\pi\zeta^2} \int_0^r dr' r' K_0 \left(\frac{r'}{\zeta}\right) \left\{ \frac{2\pi i}{r} e^{4i\phi} \sum_{n=0}^{\infty} \binom{3/2}{n} \binom{-5/2}{n} \left(\frac{r'}{r}\right)^{2n} \right. \\ & + \left. \frac{2\pi i}{r} e^{-2i\phi} \sum_{n=0}^{\infty} \binom{1/2}{n} \binom{-3/2}{n} \left(\frac{r'}{r}\right)^{2n} \right\} \\ & - \frac{\alpha}{4i\pi\zeta^2} \int_r^{\infty} dr' r' K_0 \left(\frac{r'}{\zeta}\right) \left\{ \frac{4i}{3} e^{4i\phi} \frac{r'}{r^2} \left(\left[3 \left(\frac{r}{r'}\right)^2 - 16 + 16 \left(\frac{r}{r'}\right)^2 \right] K \left(\frac{r^2}{r'^2}\right) \right. \right. \\ & + \left. \left. \left[8 - 16 \left(\frac{r}{r'}\right)^2 \right] E \left(\frac{r^2}{r'^2}\right) \right) + 4ie^{-2i\phi} \frac{1}{r} \left[\left(\frac{r}{r'} - 2\frac{r'}{r}\right) K \left(\frac{r^2}{r'^2}\right) + \frac{2r'}{r} E \left(\frac{r^2}{r'^2}\right) \right] \right\}. \end{aligned} \quad (\text{C11})$$

Inserting the expressions for K and E , and using equation (A26) and

$$\sum_{n=0}^{\infty} \binom{3/2}{n} \binom{-5/2}{n} = \frac{(2n+1)(2n+3)}{(2n-1)(2n-3)} \left(\frac{(2n-1)!!}{(2n)!!} \right)^2. \quad (\text{C12})$$

We finally arrive at

$$\begin{aligned} u^-(r, \phi) = & -\frac{\alpha}{2\zeta^2} \sum_{n=0}^{\infty} \left(\frac{(2n-1)!!}{(2n)!!} \right)^2 \frac{2n+1}{2n-1} \left[e^{4i\phi} \frac{2n+3}{2n-3} - e^{-2i\phi} \right] \int_0^r dr' K_0 \left(\frac{r'}{\zeta}\right) \left(\frac{r'}{r}\right)^{2n+1} \\ & - \frac{\alpha}{2\zeta^2} \sum_{n=0}^{\infty} \left(\frac{(2n-1)!!}{(2n)!!} \right)^2 \frac{n}{n+1} \left[e^{4i\phi} \frac{n-1}{n+2} - e^{-2i\phi} \right] \int_r^{\infty} dr' K_0 \left(\frac{r'}{\zeta}\right) \left(\frac{r'}{r}\right)^{2n}. \end{aligned} \quad (\text{C13})$$

References

- Sanchez T, Chen DT, DeCamp SJ, Heymann M, Dogic Z. 2012 Spontaneous motion in hierarchically assembled active matter. *Nature* **491**, 431–434. (doi:10.1038/nature11591)
- Guillamat P, Ignés-Mullol J, Sagués F. 2017 Taming active turbulence with patterned soft interfaces. *Nat. Commun.* **8**, 1–8. (doi:10.1038/s41467-017-00617-1)
- Needleman D, Dogic Z. 2017 Active matter at the interface between materials science and cell biology. *Nat. Rev. Mater.* **2**, 1–14. (doi:10.1038/natrevmats.2017.48)
- Kumar N, Zhang R, De Pablo JJ, Gardel ML. 2018 Tunable structure and dynamics of active liquid crystals. *Sci. Adv.* **4**, eaat7779. (doi:10.1126/sciadv.aat7779)
- Doostmohammadi A, Ignés-Mullol J, Yeomans JM, Sagués F. 2018 Active nematics. *Nat. Commun.* **9**, 1–13. (doi:10.1038/s41467-018-05666-8)
- Marchetti MC, Joanny JF, Ramaswamy S, Liverpool TB, Prost J, Rao M, Simha RA. 2013 Hydrodynamics of soft active matter. *Rev. Mod. Phys.* **85**, 1143–1189. (doi:10.1103/RevModPhys.85.1143)
- Saw TB, Xi W, Ladoux B, Lim CT. 2018 Biological tissues as active nematic liquid crystals. *Adv. Mater.* **30**, 1802579. (doi:10.1002/adma.v30.47)
- Mueller R, Yeomans JM, Doostmohammadi A. 2019 Emergence of active nematic behavior in monolayers of isotropic cells. *Phys. Rev. Lett.* **122**, 048004. (doi:10.1103/PhysRevLett.122.048004)
- Kudrolli A, Lumay G, Volfson D, Tsimring LS. 2008 Swarming and swirling in self-propelled polar granular rods. *Phys. Rev. Lett.* **100**, 058001. (doi:10.1103/PhysRevLett.100.058001)
- Simha RA, Ramaswamy S. 2002 Hydrodynamic fluctuations and instabilities in ordered suspensions of self-propelled particles. *Phys. Rev. Lett.* **89**, 058101. (doi:10.1103/PhysRevLett.89.058101)
- Juelicher F, Kruse K, Prost J, Joanny JF. 2007 Active behavior of the cytoskeleton. *Phys. Rep.* **449**, 3–28. (doi:10.1016/j.physrep.2007.02.018)
- Giomi L, Bowick MJ, Ma X, Marchetti MC. 2013 Defect annihilation and proliferation in active nematics. *Phys. Rev. Lett.* **110**, 228101. (doi:10.1103/PhysRevLett.110.228101)
- Lemma LM, DeCamp SJ, You Z, Giomi L, Dogic Z. 2019 Statistical properties of autonomous flows in 2D active nematics. *Soft Matter* **15**, 3264–3272. (doi:10.1039/C8SM01877D)
- Thampi SP, Golestanian R, Yeomans JM. 2014 Vorticity, defects and correlations in active turbulence. *Phil. Trans. R. Soc. A* **372**, 20130366. (doi:10.1098/rsta.2013.0366)
- Doostmohammadi A, Shendruk TN, Thijssen K, Yeomans JM. 2017 Onset of meso-scale turbulence in active nematics. *Nat. Commun.* **8**, 1–7. (doi:10.1038/ncomms15326)
- Pismen LM. 2013 Dynamics of defects in an active nematic layer. *Phys. Rev. E* **88**, 050502. (doi:10.1103/PhysRevE.88.050502)
- Giomi L, Bowick MJ, Mishra P, Sknepnek R, Cristina Marchetti M. 2014 Defect dynamics in active nematics. *Phil. Trans. R. Soc. A* **372**, 20130365. (doi:10.1098/rsta.2013.0365)
- Kawaguchi K, Kageyama R, Sano M. 2017 Topological defects control collective dynamics in neural progenitor cell cultures. *Nature* **545**, 327–331. (doi:10.1038/nature22321)
- Saw TB *et al.* 2017 Topological defects in epithelia govern cell death and extrusion. *Nature* **544**, 212–216. (doi:10.1038/nature21718)
- Balasubramaniam L *et al.* 2020 Nature of active forces in tissues: how contractile cells can form extensile monolayers. *bioRxiv*.
- Vafa F, Bowick MJ, Shraiman BI, Marchetti MC. 2021 Fluctuations can induce local nematic order and extensile stress in monolayers of motile cells. *Soft Matter* **17**, 3068–3073. (doi:10.1039/D0SM02027C)
- Killeen A, Bertrand T, Lee CF. 2021 Polar fluctuations lead to extensile nematic behavior in confluent tissues. Preprint. (<https://arxiv.org/abs/2107.03838>)
- Shankar S, Ramaswamy S, Marchetti MC, Bowick MJ. 2018 Defect unbinding in active nematics. *Phys. Rev. Lett.* **121**, 108002. (doi:10.1103/PhysRevLett.121.108002)
- Angheluta L, Chen Z, Marchetti MC, Bowick MJ. 2021 The role of fluid flow in the dynamics of active nematic defects. *New J. Phys.* **23**, 033009. (doi:10.1088/1367-2630/abe8a8)
- Pismen LM, Sagués F. 2017 Viscous dissipation and dynamics of defects in an active nematic interface? *Eur. Phys. J. E* **40**, 92. (doi:10.1140/epje/i2017-11582-8)
- Shankar S, Marchetti MC. 2019 Hydrodynamics of active defects: from order to chaos to defect ordering. *Phys. Rev. X* **9**, 041047.

27. Thijssen K, Nejad MR, Yeomans JM. 2020 Role of friction in multidefect ordering. *Phys. Rev. Lett.* **125**, 218004. (doi:10.1103/PhysRevLett.125.218004)
28. Pismen LM *et al.* 1999 *Vortices in nonlinear fields: from liquid crystals to superfluids, from non-equilibrium patterns to cosmic strings*, vol. **100**. Oxford, UK: Oxford University Press.
29. Maitra A, Srivastava P, Marchetti MC, Lintuvuori JS, Ramaswamy S, Lenz M. 2018 A nonequilibrium force can stabilize 2D active nematics. *Proc. Natl Acad. Sci. USA* **115**, 6934–6939. (doi:10.1073/pnas.1720607115)
30. Guillamat P, Ignés-Mullol J, Shankar S, Marchetti MC, Sagués F. 2016 Probing the shear viscosity of an active nematic film. *Phys. Rev. E* **94**, 060602. (doi:10.1103/PhysRevE.94.060602)
31. Martínez-Prat B, Alert R, Meng F, Ignés-Mullol J, Joanny JF, Casademunt J, Golestanian R, Sagués F. 2021 Scaling regimes of active turbulence with external dissipation. Preprint. (<https://arxiv.org/abs/2101.11570>)
32. Alnæs Met *al.* 2015 The FEniCS project version 1.5. *Arch. Numer. Softw.* **3**, 9–23.
33. Logg A, Mardal KA, Wells GN. 2012 *Automated solution of differential equations by the finite element method*. Berlin, Germany: Springer.
34. Vafa F, Bowick MJ, Marchetti MC, Shraiman BI. 2020 Multi-defect dynamics in active nematics. Preprint. (<https://arxiv.org/abs/2007.02947>)
35. Zhang YH, Deserno M, Tu ZC. 2020 Dynamics of active nematic defects on the surface of a sphere. *Phys. Rev. E* **102**, 012607. (doi:10.1103/PhysRevE.102.012607)
36. Kreyszig E. 2011 *Advanced engineering mathematics (International student version)*, 10th edn. Hoboken: John Wiley & Sons, Inc.

Paper II

Defect self-propulsion in active nematic films with spatially varying activity

Jonas Rønning, M. Cristina Marchetti, Luiza Angheluta



Research



Cite this article: Rønning J, Marchetti MC, Angheluta L. 2023 Defect self-propulsion in active nematic films with spatially varying activity. *R. Soc. Open Sci.* **10**: 221229. <https://doi.org/10.1098/rsos.221229>

Received: 21 September 2022

Accepted: 24 January 2023

Subject Category:

Physics and biophysics

Subject Areas:

biophysics/fluid mechanics/statistical physics

Keywords:

active nematics, topological defects, nematic liquid crystals, hydrodynamics

Author for correspondence:

Jonas Rønning

e-mail: jonasron@uio.no

Defect self-propulsion in active nematic films with spatially varying activity

Jonas Rønning¹, M. Cristina Marchetti² and Luiza Angheluta¹

¹Njord Centre, Department of Physics, University of Oslo, PO Box 1048, Oslo 0316, Norway

²Department of Physics and Biomolecular Science and Engineering Program, University of California Santa Barbara, Santa Barbara, CA 93106, USA

JR, 0000-0001-5289-7276; MCM, 0000-0003-3583-4999; LA, 0000-0001-7231-6694

We study the dynamics of topological defects in active nematic films with spatially varying activity and consider two set-ups: (i) a constant activity gradient and (ii) a sharp jump in activity. A constant gradient of extensile (contractile) activity endows the comet-like $+1/2$ defect with a finite vorticity that drives the defect to align its nose in the direction of decreasing (increasing) gradient. A constant gradient does not, however, affect the known self-propulsion of the $+1/2$ defect and has no effect on the $-1/2$ that remains a non-motile particle. A sharp jump in activity acts like a wall that traps the defects, affecting the translational and rotational motion of both charges. The $+1/2$ defect slows down as it approaches the interface and the net vorticity tends to reorient the defect polarization so that it becomes perpendicular to the interface. The $-1/2$ defect acquires a self-propulsion towards the activity interface, while the vorticity-induced active torque tends to align the defect to a preferred orientation. This effective attraction of the negative defects to the wall is consistent with the observation of an accumulation of negative topological charge at both active/passive interfaces and physical boundaries.

1. Introduction

Active nematics are collections of elongated apolar particles that consume energy from their surroundings to generate dipolar forces that drive self-sustained flows [1]. Much progress in understanding the rich dynamics of these active liquid crystals has been achieved through a minimal hydrodynamic theory that couples orientational order and flow and captures the behaviour of biological systems from subcellular to multicellular scales [2].

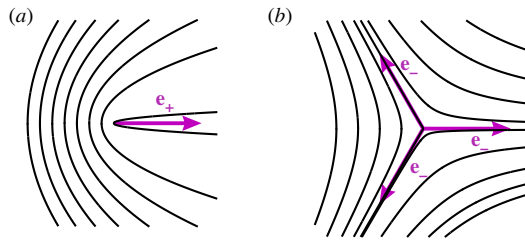


Figure 1. Illustration of (a) the $+1/2$ defect and (b) the $-1/2$ defect and their corresponding polarizations for $\theta_0 = 0$. The negative defect has three equivalent polarizations.

Within the biological realm, the active nematic paradigm describes mixtures of cytoskeletal filaments and motor proteins [3–6], bacterial suspensions [1,7] and confluent cell monolayers [8,9].

What distinguishes the hydrodynamics of active nematics from that of their passive counterparts is the presence of an active stress generated by active processes, which sets up spontaneous spatio-temporally chaotic flows [7]. The active stress is given by $\sigma_{ij}^a = \alpha Q_{ij}$ with \mathbf{Q} the nematic order parameter and α a scalar activity parameter that encapsulates the biochemical processes that generate active forces [10–13]. It can have either sign: $\alpha > 0$ corresponds to a system of ‘pullers’ generating contractile stresses on their surroundings, whereas $\alpha < 0$ reflects a system of ‘pushers’ and their induced extensile active stresses. With increasing activity, active flows are induced spontaneously and create large distortions of the nematic order, including the formation of pairs of topological defects that sustain active turbulence [3,14].

The lowest energy topological defects in active nematic films have half-integer charge, corresponding to the comet-shaped $+1/2$ with polarity \mathbf{e} , defined by a head–tail arrow, and the $-1/2$ which has threefold symmetry (see figure 1). These defects disrupt the nematic order locally and induce long-range distortions in the orientation field, generating active stresses, which in turn lead to spontaneous active flows surrounding the defects [12,15,16]. There is a net active flow through the core of the polar $+1/2$ defect which makes it intrinsically motile and is referred to as the defect self-propulsion. For an isolated $+1/2$ defect, the self-propulsion velocity aligns with the polarity vector and, depending on the contractile/extensile properties of the active nematic, the defect moves in/opposite to the direction of its polarization. The $-1/2$ defect does not create any net flow at the defect position and, thus, is not self-propelled in systems with uniform activity. The motion of defects in the presence of spatially inhomogeneous activity is far less understood and explored [17].

There are several approaches to realize experimentally systems with spatially dependent activity. In [18], a varying substrate topography is used to control the frictional damping in a film of a microtubule-kinesin suspension. This results in spatial variations of the concentration of active agents, thus indirectly in the local activity. In [19], a similar effect is achieved by manipulating light-sensitive myosin motors that activate the microtubules. Both studies find that the $-1/2$ defects localize near the interface separating the region of higher activity from that of lower activity. In [19], it was reported that the $+1/2$ defects are deflected by the active/passive interface. Analytical work based on a hydrodynamic theory of the defect gas has predicted that a passive/active interface can be used to separate positive and negative topological charge [17]. Numerical studies of how the defect dynamics is affected by the spatially dependent activity show that the polarity of the $+1/2$ defect tends to align parallel to the activity gradient [19–23], and that the confinement and motion of defects can be manipulated by varying the steepness of the activity gradients [24,25]. A recent numerical study also shows that the formation of defect dipoles can be controlled by imprinting special geometries into the activity profile [22].

In this paper, we provide a theoretical study of how spatially varying activity affects the self-propulsion and reorientation of isolated topological defects. We consider the representative basic set-ups where the spatial activity profile is given either by a constant activity gradient (linear profile) or a sharp interface separating two regions of constant bulk activity (Heaviside function profile). For constant activity gradients, the $+1/2$ defect rotates due to a vorticity-induced active torque acting on the defect polarization until the defect aligns parallel to the activity gradient and moves in the direction of lower magnitude of activity. Thus the defect slows down. We show analytically that the vorticity at the $+1/2$ defect core is proportional to the hydrodynamic dissipation length $\ell_d = \sqrt{\eta/T}$, which measures the strength of viscous dissipation η relative to friction T . Numerical simulations of

the active flow generated in a disc of radius R show that the vorticity depends on the system size for small R , and crosses over to the analytically predicted value for large systems. The vorticity field induced by an activity gradient parallel to the $+1/2$ defect's polarization has a quadruple structure with regions of alternating vorticity. This is confirmed by numerical simulations for a disc geometry where four vortices are formed around the $+1/2$ defect. By contrast, the vorticity induced by constant activity gradients at a $-1/2$ defect has an eightfold symmetry that leads to eight vortices with alternating circulation in a finite domain. We also calculate the net translational self-propulsion and reorientation that both $\pm 1/2$ defects acquire near a sharp active/passive interface. The $+1/2$ defect slows down as it moves towards the interface, and the vorticity-induced torque tends to reorient it such that its polarization becomes normal to the interface regardless of the sign of activity. The $-1/2$ defect also acquires a preferred orientation at the interface, and those that approach the interface with this stable orientation are then attracted by it.

The structure of the paper is as follows. We start in §2 by introducing the minimal hydrodynamic model active nematic films on a substrate. In §3, we derive and discuss the self-propulsion and spontaneous rotation of $+1/2$ defects in the presence of a constant activity gradient. Section 4 focuses on the analytical derivation of the self-propulsion and vorticity of $\pm 1/2$ defects close to a sharp active/passive interface. Summary and concluding remarks are presented in §5.

2. Hydrodynamics of active nematics with spatially varying activity

We consider the familiar hydrodynamic model of a 2D active nematics that couples the flow velocity $\mathbf{u}(\mathbf{r})$ to the nematic order parameter $Q_{ij} = S(\hat{n}_i\hat{n}_j - \frac{1}{2}\delta_{ij})$, where S quantifies the degree of order and $\hat{\mathbf{n}}(\mathbf{r}) = (\cos \theta(\mathbf{r}), \sin \theta(\mathbf{r}))$ is the orientational director field with head–tail symmetry. In the simplest formulation, the \mathbf{Q} -tensor is a minimizer of the de Gennes–Landau free energy [7]

$$\mathcal{F} = \int d\mathbf{r} \left[\frac{\kappa}{2} |\partial_i Q_{jk}|^2 + \frac{g}{4} (1 - \frac{1}{2} \text{Tr}(\mathbf{Q}^2))^2 \right], \quad (2.1)$$

with isotropic elastic constant $K > 0$ and g the strength of the local ordering potential. The uniform nematic ordered state corresponds to $S_0 = 2$. The flow field satisfies a Stokes equation that balances forces on a fluid element, given by [7]

$$(\Gamma - \eta \nabla^2) \mathbf{u} = \nabla \cdot [\alpha(\mathbf{r}) \mathbf{Q}(\mathbf{r})] - \nabla p(\mathbf{r}), \quad \nabla \cdot \mathbf{u} = 0, \quad (2.2)$$

where Γ is a friction coefficient per unit area, η is the shear viscosity and α is the activity coefficient, with dimensions of stress. For simplicity, we neglect the contributions from the passive stresses and flow alignment to focus, instead, on the active flows generated by an isolated $\pm 1/2$ in the presence of non-homogeneous activity $\alpha(\mathbf{r})$.

We rescale the Stokes equation in units of the nematic relaxation time $\tau = \gamma/g$ (where γ is the nematic rotational friction) [16,26] and the coherence length $\xi = \sqrt{K/g}$. Different dynamical regimes are then controlled by one dimensionless number $\zeta = \ell_d/\xi$, where $\ell_d = \sqrt{\eta/\Gamma}$, and the rescaled activity $\alpha(\mathbf{r}) \rightarrow \alpha(\mathbf{r})\gamma/(TK)$. The dimensionless form of the Stokes equation reads as

$$(1 - \zeta^2 \nabla^2) \mathbf{u} = \mathbf{F}_\pm - \nabla p, \quad \nabla \cdot \mathbf{u} = 0, \quad (2.3)$$

where the active force field induced by an isolated $\pm 1/2$ defect is given by

$$\mathbf{F}_\pm = \mathbf{Q}(\mathbf{r}) \cdot \nabla \alpha(\mathbf{r}) + \alpha(\mathbf{r}) \nabla \cdot \mathbf{Q}(\mathbf{r}) = \mathbf{F}_\pm^I + \mathbf{F}_\pm^B. \quad (2.4)$$

The first contribution is an interfacial force \mathbf{F}_\pm^I originating from activity gradients. The second term is a bulk force \mathbf{F}_\pm^B due to nematic distortions. The defect self-propulsion velocity \mathbf{v}_\pm is defined as the net active flow through the defect core, and thus can be computed from the active flow velocity \mathbf{u} obtained from the solution of equation (2.3) evaluated at the origin [26]. Due to viscosity, it depends nonlinearly and non-locally on the force field through the integral solution of equation (2.3) given by

$$\mathbf{v}_\pm = \frac{1}{2\pi\zeta^2} \int d\mathbf{r} K_0\left(\frac{r}{\zeta}\right) [\mathbf{F}_\pm(\mathbf{r}) - \nabla p(\mathbf{r})] = \mathbf{v}_\pm^I + \mathbf{v}_\pm^B, \quad (2.5)$$

where $K_0(r)$ is the zeroth order Bessel function which is the Green's function of equation (2.3) without the incompressibility constraint. We distinguish the interfacial contributions \mathbf{v}_\pm^I from the bulk contributions \mathbf{v}_\pm^B . The incompressibility constraint gives rise to pressure gradients which may affect the defect

kinematics. The pressure field is the solution of the corresponding Poisson's equation

$$\nabla^2 p = \nabla \cdot \mathbf{F}_\pm(\mathbf{r}). \quad (2.6)$$

The net vorticity at the defect core is also obtained from measuring the vorticity of the flow field induced by the defect distortion, given by $\omega = \partial_x u_y - \partial_y u_x = -\nabla^\perp \cdot \mathbf{u}$. Using equation (2.5) and evaluating it at the defect position $\mathbf{r}_0 = 0$, we obtain an expression for the defect vorticity

$$\omega_\pm = -\frac{1}{2\pi\xi^2} \int d\mathbf{r} K_0\left(\frac{r}{\xi}\right) \nabla^\perp \cdot \mathbf{F}_\pm(\mathbf{r}) = \omega_\pm^I + \omega_\pm^B. \quad (2.7)$$

Vorticity is also written as sums of interfacial ω_\pm^I and bulk ω_\pm^B contributions which depend on the defect polarization \mathbf{e}_\pm and are computed analytically in the next sections.

For isolated $\pm 1/2$ point-like defects, we can parametrize the \mathbf{Q} -tensor order parameter in the quasi-static phase approximation as [26]

$$Q_{xx}^\pm(\mathbf{r}) = \cos(\pm\phi(\mathbf{r}) + 2\theta_0) \quad \text{and} \quad Q_{xy}^\pm(\mathbf{r}) = \sin(\pm\phi(\mathbf{r}) + 2\theta_0), \quad (2.8)$$

where $\phi(\mathbf{r}) = \arctan(y/x)$ is the singular part of the nematic orientation due to a $\pm 1/2$ defect located at the origin, and θ_0 is the slowly varying part of the background orientation of the nematic director. The $+1/2$ defect has a well-defined polarization which is determined by the background nematic orientation θ_0 as

$$\mathbf{e}_+ = \left(\frac{\nabla \cdot \mathbf{Q}}{|\nabla \cdot \mathbf{Q}|} \right)_{\mathbf{r}=0} = [\cos(2\theta_0), \sin(2\theta_0)]. \quad (2.9)$$

For the $-1/2$ defect, we can also introduce a polarization vector determined by θ_0 and aligning with one of the principal axes of the threefold symmetry [26]

$$\mathbf{e}_- = \left[\cos\left(\frac{2\theta_0}{3}\right), \sin\left(\frac{2\theta_0}{3}\right) \right]. \quad (2.10)$$

Both nematic defects and their respective polarizations are illustrated in figure 1.

It can be shown that a net vorticity at the defect core induces an active torque that tends to rotate the defect polarization. This follows straightforwardly from taking the time derivative of the polarization in equations (2.9) and (2.10), and using the evolution of the \mathbf{Q} -tensor [17,26] to account for the change in the background nematic field θ_0 due to vorticity as $\partial_t \theta_0 \approx \omega/2$. Thus, the evolution of the defect polarization controlled by vorticity is

$$\dot{\mathbf{e}}_\pm \approx -3^{-1/2+q} \omega_\pm \mathbf{e}_\pm^\perp, \quad (2.11)$$

where the defect charge is $q = \pm 1/2$ and $\mathbf{e}^\perp = [e_y, -e_x]$ represents the 90° clockwise rotation of the polarization vector. For motile defects, there are additional torques due to defect interactions, the elastic stiffness K or the coupling to the flow alignment [17,26]. Here, we focus on the active torque induced by a non-zero vorticity which emerges from spatially varying activity alone. In the subsequent sections, we investigate how this active torque reorients the defect polarization relative to activity gradients for two set-ups: (i) a constant activity gradient and (ii) an interface with a sharp jump in activity.

3. Constant activity gradient

We first study the kinematics of an isolated defect in a region where the activity gradient is locally constant. Without loss of generality, we consider an activity gradient in the x -direction such that the activity has the linear profile $a(\mathbf{r}) = a_0 + \alpha_g x$. The defect orientation is arbitrary and controlled by the background nematic orientation θ_0 . We demonstrate that a constant gradient α_g does not modify the defect self-propulsion velocity as compared with what was obtained for uniform bulk activity a_0 . An activity gradient across the texture of a $+1/2$ defect generates, however, a flow that may yield a finite vorticity at the defect core, which tends to align the defect polarization according to equation (2.11) in the direction of the gradient. The $-1/2$ defect remains stationary both in its motion and orientation.

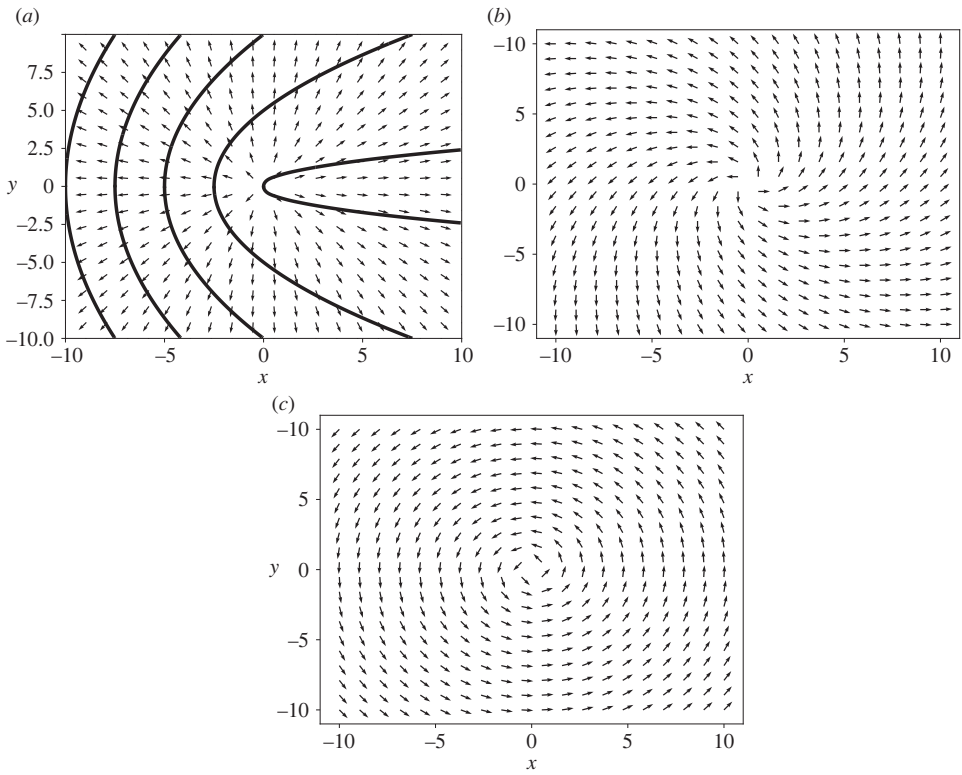


Figure 2. Interfacial active force field from equation (3.1) induced by a $+1/2$ defect with (a) $\theta_0 = 0$, (b) $\theta_0 = \pi/8$ and (c) $\theta_0 = \pi/4$. Note that cases (b,c) lead to rotation of the defect together with the nematic field until the defect polarization aligns with the direction of the activity gradient. The dark solid lines in (a) show the nematic field around the $+1/2$ defect oriented in the x direction.

3.1. $+1/2$ defect

The interfacial active force given in equation (2.4) arising from a constant activity gradient α_g is

$$\mathbf{F}_+^I(\mathbf{r}) = \alpha_g [\cos(2\theta_0)\hat{\mathbf{r}} - \sin(2\theta_0)\hat{\mathbf{r}}^\perp], \tag{3.1}$$

where $\hat{\mathbf{r}}$ is the radial unit vector and $\hat{\mathbf{r}}^\perp = (\hat{y}, -\hat{x})$. This expression corresponds to the Helmholtz decomposition of \mathbf{F}_+^I into a curl-free part ($\sim \hat{\mathbf{r}}$) and a divergence-free part ($\sim \hat{\mathbf{r}}^\perp$). These two contributions are plotted in figure 2. The divergence-free part gives a net vorticity at the defect core which tends to rotate its polarization until it aligns with the activity gradient. This is most easily demonstrated in the friction-dominated limit where the active flow velocity is $\Gamma\mathbf{u} = \mathbf{F}_+^I - \nabla p$. The incompressibility constraint thereby removes the curl-free contribution through the contribution of the interfacial pressure which is radially symmetric and given by

$$p_+^I(\mathbf{r}) = \alpha_g \cos(2\theta_0)(r - L), \tag{3.2}$$

making the interface flow purely rotational. Here the constant L is a length comparable with the system size which controls the divergent terms. More generally, to incorporate viscous dissipation we need to evaluate the integral expression for the defect velocity given in equation (2.5). In an infinite system, the symmetry of the integrand leads to no contribution to the defect speed from the interfacial active force, thus $\mathbf{v}_+^I = 0$. This contribution may become finite in non-radially symmetric bounded domains.

The contribution from the bulk active force in equation (2.4) reduces to

$$\mathbf{F}_+^B(\mathbf{r}) = \mathbf{F}_+^0(\mathbf{r}) + \alpha_g x \nabla \cdot \mathbf{Q}_+ = \mathbf{F}_+^0(\mathbf{r}) + \alpha_g \frac{x}{r} (\cos(2\theta_0)\hat{\mathbf{x}} + \sin(2\theta_0)\hat{\mathbf{y}}), \tag{3.3}$$

where $\mathbf{F}_+^0(\mathbf{r})$ is the known active force corresponding to a constant activity a_0 which leads to a constant self-propulsion velocity [16,26]. Since the contribution due to activity gradient α_g is antisymmetric

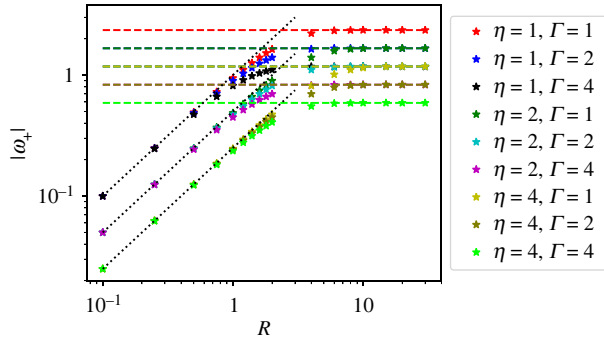


Figure 3. Magnitude of the angular velocity of the $+1/2$ defect for different values of dissipation parameters η and Γ , $\alpha_g = 1$ and $\theta_0 = -\pi/4$. The dashed horizontal lines are the analytical prediction for an unbounded domain. The dotted lines show the linear scaling with R and with slopes $1/\eta$.

around the defect position, its integral according to equation (2.5) vanishes. Therefore, there is no contribution from activity gradients to the defect self-propulsion. This is not changed when we add the gradient of the bulk pressure which is given as

$$p_+^B(\mathbf{r}) = p_+^0(\mathbf{r}) + \frac{\alpha_g \cos(2\theta_0)}{6} \left(\frac{(x^2 - y^2)}{r} + 3(r - L) \right) - \frac{\alpha_g \sin(2\theta_0) xy}{3r}. \quad (3.4)$$

Here p_+^0 is the pressure for the constant activity term α_0 [16].

Activity gradients induce, however, a vortical flow that is finite at the defect core, resulting in an angular velocity of the $+1/2$ defect, given by

$$\omega_+ = \frac{\alpha_g}{2\pi\zeta^2} \sin(2\theta_0) \int d\mathbf{r} K_0 \left(\frac{r}{\zeta} \right) \left(\frac{1}{r} + \frac{x^2}{r^3} \right), \quad (3.5)$$

where the first term in the bracket originates from the interfacial active force and the second is due to the bulk force. The integral can be carried out in polar coordinates, with the result

$$\omega_+ = \frac{3\pi\alpha_g}{4\zeta} \sin(2\theta_0). \quad (3.6)$$

We can rewrite this equivalently in physical units as

$$\omega_+ = \frac{3\pi\alpha_g}{4\Gamma l_d} \sin(2\theta_0) = \frac{3\pi\alpha_g}{4\sqrt{\Gamma\eta}} \sin(2\theta_0) = \frac{3\pi\alpha_g}{4\eta} \ell_d \sin(2\theta_0), \quad (3.7)$$

to highlight that the defect angular velocity scales linearly with the hydrodynamic dissipation length l_d , similar to the self-propulsion speed of a defect in a constant activity [16]. The effect of this vorticity is to align the polarization so that it is pointing opposite to the activity gradient. This is consistent with recent numerical results, where defects align normal on soft interfaces separating extensile and contractile regions [23].

To test the validity of these analytical predictions for a bounded system, we have solved numerically the Stokes flow from equation (2.3) in a disc of radius R . Equation (2.2) is solved with non-slip boundary conditions using the finite-element package FEniCS [27,28]. The active stress is computed from the analytical form of the Q tensor corresponding to a single point defect in a uniform background nematics.

In figure 3, we show that the defect angular velocity is proportional to R for radii smaller than l_d , and crosses over to the asymptotic value for an infinite system given by equation (3.7) at large R . We have also computed the vorticity field for $\alpha_0 = 0$ and different defect orientations relative to the activity gradient, as shown in figure 4. When the defect polarization is parallel to the activity gradient ($\theta_0 = 0$), we observe a quadruple structure of the vortical flow. This is consistent with the analytical prediction in the friction-dominated limit, where the vorticity field away from the defect is determined by the activity gradient α_g as (for $\alpha_0 = 0$)

$$\omega_+(r, \phi) = \frac{\alpha_g \sin(2\phi)}{2\Gamma r} \cos(2\theta_0) + \frac{\alpha_g}{\Gamma r} \sin(2\theta_0)(1 + \cos^2(\phi)), \quad (3.8)$$

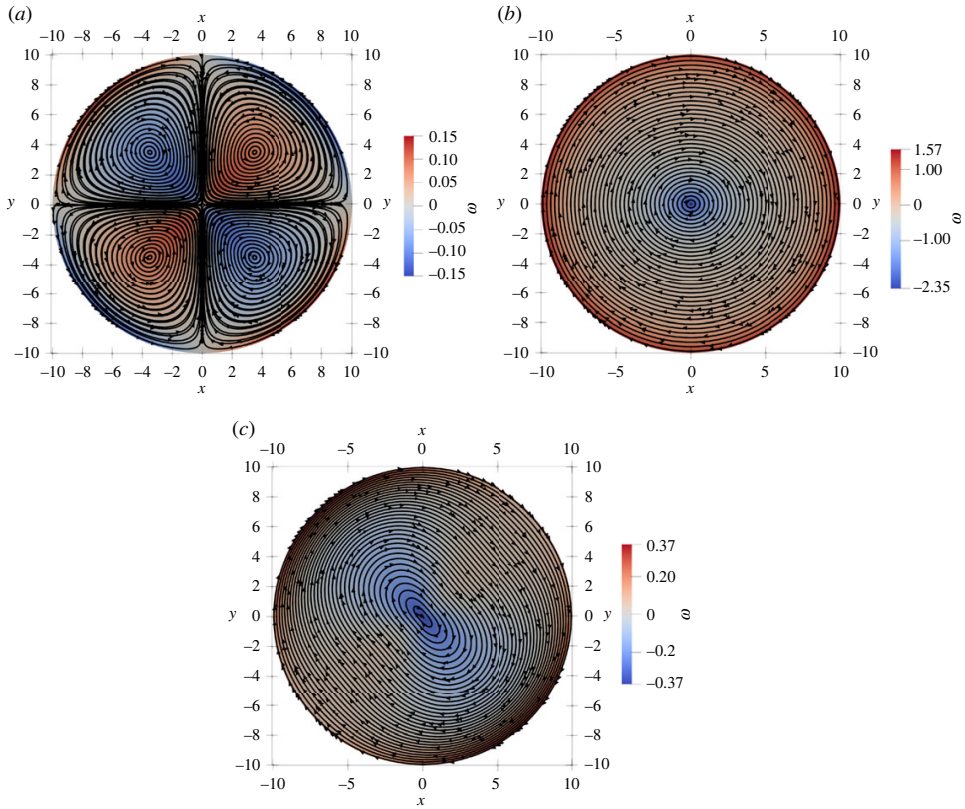


Figure 4. Active flow streamlines induced by a uniform activity gradient along x -direction with $\alpha_0 = 0$ and by a $+1/2$ defect with orientation (a) $\theta_0 = 0$, (b) $\theta_0 = -\pi/4$ and (c) $\theta = -\pi/40$. Since $\alpha_0 = 0$, the flow velocity vanishes at the defect core. The background colourmap represents the vorticity field. When $\theta_0 \neq 0$, the defect acquires a non-zero vorticity at its centre as predicted theoretically. The fourfold vortex structure is only visible for small values of θ_0 , i.e. when the defect is closely aligned with the direction of the activity gradient.

where r and ϕ are the polar coordinates centred at the defect position. By contrast, when the defect polarization is normal to the activity gradient ($\theta_0 = \pi/2$), we obtain a single vortex centred at the core of the defect.

3.2. $-1/2$ defect

A similar analytical calculation can be carried out for the $-1/2$ defect using the parametrization of the \mathbf{Q} -tensor in equation (2.8). The interfacial and bulk components of the active force field are obtained from equation (2.4) as

$$\mathbf{F}_-^I(\mathbf{r}) = \frac{\alpha_g}{r} [(x\hat{x} - y\hat{y}) \cos(2\theta_0) + (y\hat{x} + x\hat{y}) \sin(2\theta_0)] \quad (3.9)$$

and

$$\mathbf{F}_-^B(\mathbf{r}) = \frac{\alpha_g x}{r^3} [(y^2 - x^2)(\cos(2\theta_0)\hat{x} + \sin(2\theta_0)\hat{y}) + 2xy(\cos(2\theta_0)\hat{y} - \sin(2\theta_0)\hat{x})]. \quad (3.10)$$

From symmetry considerations these forces as well as their curl vanish upon integration. This implies that a constant activity gradient alone does not induce any self-propulsion of the $-1/2$ defect nor a rotation of its orientation. Including the pressure contributions does not alter this effect.

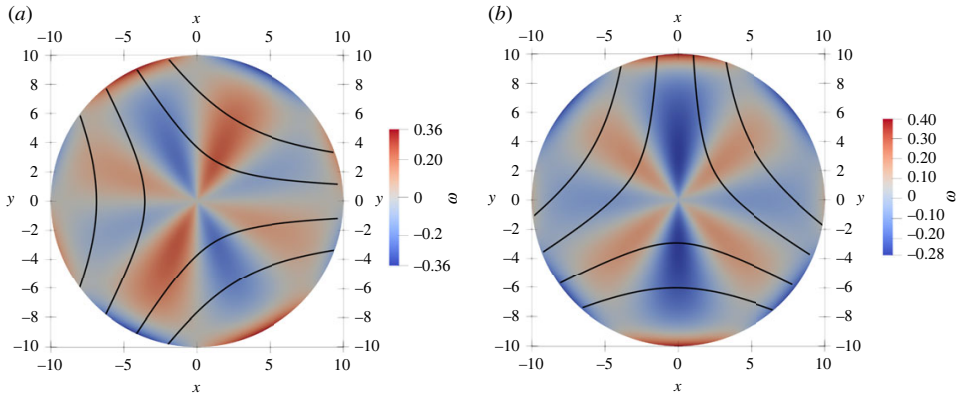


Figure 5. The vorticity field induced by an uniform activity gradient along the x -direction for $\alpha_0=0$ and a $-1/2$ defect with orientation (a) $\theta_0=0$ and (b) $\theta_0=-\pi/4$. The black lines shows the director field.

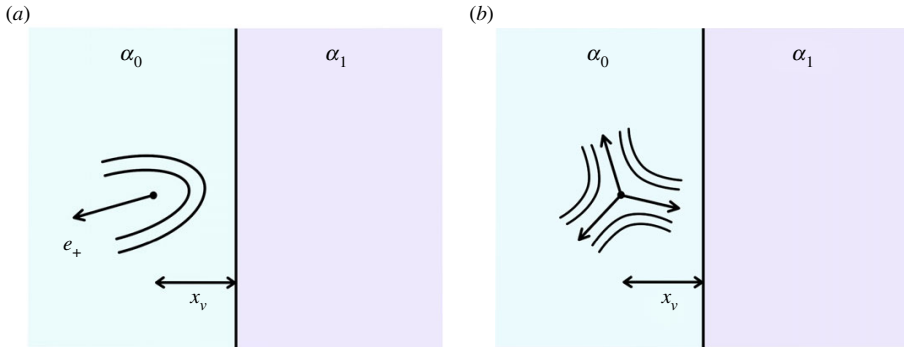


Figure 6. Set-up of (a) $+1/2$ defect and (b) $-1/2$ defect at a sharp interface separating a region with higher activity α_0 from that with lower activity α_1 .

In the friction-dominated limit and for $\alpha_0=0$, we can evaluate the vorticity field, and show that a constant activity gradient α_g induces eight counter-rotating vortices, with a vortical flow given by

$$\omega_-(r, \phi) = -\frac{\alpha_g \cos(2\theta_0)}{2\Gamma r} (3 \sin(4\phi) - \sin(2\phi)) + \frac{\alpha_g \sin(2\theta_0)}{2\Gamma r} (3 \cos(4\phi) - \cos(2\phi)). \quad (3.11)$$

The same structure is observed in bounded domains where the vorticity forms vortices of alternating circulation, as shown in figure 5 for a disc geometry.

4. Activity jump at an interface

We now consider an activity profile corresponding to a sharp interface separating a region of high activity α_0 from a region of low activity α_1 . Isolated $\pm 1/2$ defects are situated at a distance x_v from the interface in the region of high activity, α_0 , as illustrated in figure 6. The activity profile across this interface is given by the Heaviside step function

$$\alpha(\mathbf{r}) = \alpha_0 - \Delta\alpha H(x - x_v),$$

corresponding to a singular activity gradient $\partial_x \alpha = -\Delta\alpha \delta(x - x_v)$ with $\Delta\alpha = \alpha_0 - \alpha_1$ the interfacial jump in activity. An active/passive interface corresponds to $\alpha_1=0$ and $\Delta\alpha = \alpha_0$. In this case, we find that the self-propulsion of the $+1/2$ defect is reduced as the defect approaches the interface. The vorticity-induced active torque tends to reorient the $\pm 1/2$ defects moving toward the interface to preferred orientations that depend on extensile/contractile activity. The $-1/2$ defect that already has the selected orientation is attracted to the wall, while that with different polarizations might be repelled.

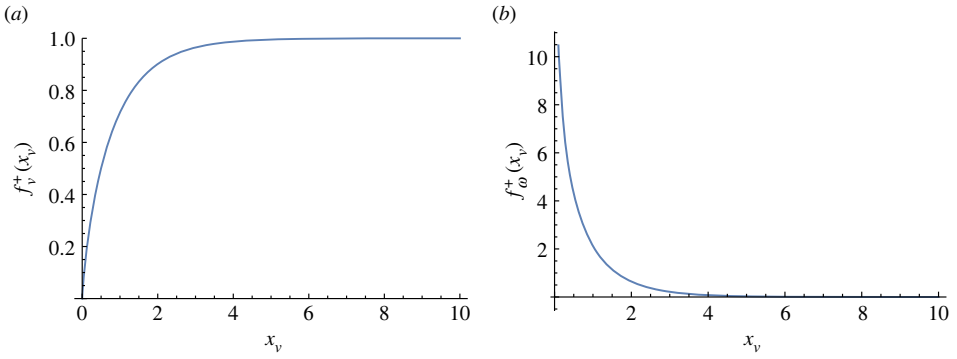


Figure 7. Plot of (a) f_v^+ and (b) f_ω^+ as functions of the distance x_v of the +1/2 defect from the interface. Note that f_ω^+ diverges at $x_v = 0$ due to the bulk terms.

4.1. +1/2 defect

The active force field induced by a +1/2 defect located at a distance x_v from a sharp interface is given by

$$\mathbf{F}_+^I(\mathbf{r}) = -\Delta\alpha\delta(x - x_v)(\cos(2\theta_0)\hat{\mathbf{r}} - \sin(2\theta_0)\hat{\mathbf{r}}^\perp) \quad (4.1)$$

and

$$\mathbf{F}_+^B(\mathbf{r}) = \left(\frac{\alpha_0}{r} - \frac{\Delta\alpha}{r}H(x - x_v) \right) \hat{\mathbf{e}}^+. \quad (4.2)$$

Inserting these expressions in equation (2.5), we obtain the contributions to the self-propulsion velocity from interfacial and bulk active forces as

$$\mathbf{v}_+^B = \frac{\alpha_0\pi}{4\zeta} \hat{\mathbf{e}}^+ - \frac{\Delta\alpha}{2\pi\zeta^2} \hat{\mathbf{e}}^+ \int \mathrm{d}\mathbf{r} K_0\left(\frac{r}{\zeta}\right) H(x - x_v) \frac{1}{r} \quad (4.3)$$

and

$$\mathbf{v}_+^I = -\frac{\Delta\alpha}{2\pi\zeta^2} \hat{\mathbf{e}}^+ \int_{-\infty}^{\infty} \mathrm{d}y K_0\left(\frac{\sqrt{x_v^2 + y^2}}{\zeta}\right) \frac{x_v}{\sqrt{x_v^2 + y^2}}. \quad (4.4)$$

The first term in the bulk contribution is the well-known constant self-propulsion velocity from a constant activity α_0 [16]. The second term is the additional drift due to the activity jump $\Delta\alpha$ and depends on the distance x_v from the interface. As we will see below, this contribution suppresses the defect self-propulsion near the interface.

If we now specialize to the case of an active/passive interface, i.e. $\Delta\alpha = \alpha_0$. In dimensional units, the self-propulsion velocity of the +1/2 defect is then given by

$$\mathbf{v}_+ = \frac{\alpha_0}{4\eta} \pi \ell_d f_v^+(x_v) \hat{\mathbf{e}}^+, \quad (4.5)$$

with

$$f_v^+(x_v) = 1 - \frac{2}{\pi^2} \int_{-\infty}^{\infty} \mathrm{d}y \left[K_0\left(\sqrt{x_v^2 + y^2}\right) \frac{x_v}{\sqrt{x_v^2 + y^2}} + \int_{x_v}^{\infty} \mathrm{d}x K_0(r) \frac{1}{r} \right]. \quad (4.6)$$

The function $f_v^+(x_v)$ is plotted in figure 7a. We note that the self-propulsion speed vanishes as the defect hits the interface $x_v = 0$. In other words, the defect slows down as it approaches the interface, and eventually remains at rest at the interface. We note that equation (4.5) is obtained by incorporating the incompressibility constraint only in the \mathbf{v}_+^I term. Additional pressure gradients may arise due to activity jump. These are, however, difficult to obtain analytically and are not included in this study.

We now compute the vorticity at the defect position to investigate how its contribution to the active torque tends to reorient the defect as it approaches the interface to a stable orientation. From equation

(2.7), we obtain the following expressions for interfacial and bulk contributions

$$\begin{aligned} \omega_+^I = & -\frac{\Delta\alpha}{2\pi\zeta^2} \sin(2\theta_0) \int_{-\infty}^{\infty} dy \left[K_0 \left(\frac{\sqrt{x_v^2 + y^2}}{\zeta} \right) \frac{x_v^2}{(x_v^2 + y^2)^{3/2}} \right. \\ & \left. + K_1 \left(\frac{\sqrt{x_v^2 + y^2}}{\zeta} \right) \frac{x_v^2}{\zeta(x_v^2 + y^2)} \right], \end{aligned} \quad (4.7)$$

and

$$\begin{aligned} \omega_{\pm}^B = & -\frac{\Delta\alpha}{2\pi\zeta^2} \sin 2\theta_0 \int_{-\infty}^{\infty} dy \left[K_0 \left(\frac{\sqrt{x_v^2 + y^2}}{\zeta} \right) \right. \\ & \left. \times \frac{1}{\sqrt{x_v^2 + y^2}} - \int_{x_v}^{\infty} dx K_0 \left(\frac{r}{\zeta} \right) \frac{x}{r^3} \right], \end{aligned} \quad (4.8)$$

where the bulk vorticity diverges at $x_v = 0$. The total defect angular velocity is given by the sum of these two contributions evaluated at the defect core. In dimensional units, it is given by

$$\omega_+(x_v, \theta_0) = -\frac{\Delta\alpha}{2\pi\eta} \sin(2\theta_0) f_{\omega}^+(x_v), \quad (4.9)$$

where the wall-dependence function $f_{\omega}^+(x_v)$ is plotted in figure 7b. Hence, near an active/passive interface, the vorticity-induced rotation is at a rate $\dot{\theta}_0 = \frac{1}{2} \omega_+(x_v, \theta_0)$ until $\omega_+(x_v, \theta_0) = 0$. It is clear from figure 7b that reorientation only occurs within a distance of order ℓ_d from the wall. As the $+1/2$ defect approaches the wall, f_{ω}^+ increases and eventually diverges at $x_v \rightarrow 0$. This means that the defect tends to reorient its polarization until $\sin(2\theta_0) = 0$. From the stability criterion that $(d\omega_+/d\theta_0) < 0$, this corresponds to the stable orientation $2\theta_0 = \pi$ for $\alpha_0 < 0$ (extensile) and $2\theta_0 = 0$ for $\alpha_0 > 0$ (contractile). In both cases, the defect polarization is normal to the interface $\mathbf{e}_+ = [\mp 1, 0]$ and points away from the interface for extensile systems and into the interface for contractile systems, respectively. Numerical simulations [19] report that $+1/2$ defects tend to reorient and drift parallel to the boundary when the angle between the interface and the incoming velocity is below a critical value that depends on activity. Above this critical angle, i.e. more head-on collisions, the defect hits the wall and tunnels through it. This effect is probably coming from the additional contributions to the active torque that are not considered here, namely the interactions between defects, deformations in the nematic order parameter due to the wall and the coupling to flow alignment. It is likely that these terms are important close to the interface, both for determining the defect orientation and the tunnelling effect observed both experimentally and numerically [19].

4.2. $-1/2$ defect

The components of the interfacial active force due to a $-1/2$ defect at a distance x_v from the activity jump are given by

$$F_{x-}^I = -\frac{\Delta\alpha}{r} \delta(x - x_v) (x \cos 2\theta_0 + y \sin 2\theta_0) \quad (4.10)$$

and

$$F_{y-}^I = -\frac{\Delta\alpha}{r} \delta(x - x_v) (-y \cos 2\theta_0 + x \sin 2\theta_0). \quad (4.11)$$

The corresponding bulk active force is

$$F_{x-}^B = (\alpha_0 - \Delta\alpha H(x - x_v)) \frac{1}{r^3} [(y^2 - x^2) \cos 2\theta_0 - 2xy \sin 2\theta_0] \quad (4.12)$$

and

$$F_{y-}^B = (\alpha_0 - \Delta\alpha H(x - x_v)) \frac{1}{r^3} [(y^2 - x^2) \sin 2\theta_0 + 2xy \cos 2\theta_0]. \quad (4.13)$$

Using these expressions, and neglecting the contribution from the pressure gradient, the net drift velocity of the defect can be written as

$$\mathbf{v}_-(x_v) = -\frac{\Delta\alpha}{2\pi\eta} \ell_d f_{\mathbf{v}}^-(x_v) \hat{\mathbf{n}}^-, \quad (4.14)$$

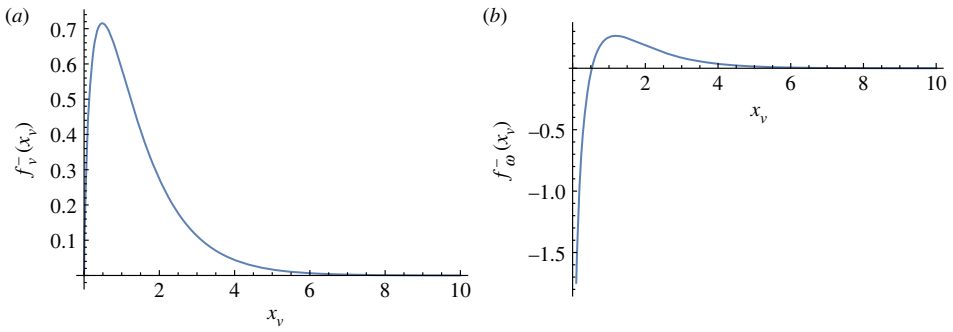


Figure 8. Profile of (a) $f_v^-(x_v)$ and (b) $f_\omega^-(x_v)$ as function of x_v . Note that the function $f_\omega^-(x_v)$ diverges at $x_v = 0$.

where $\hat{\mathbf{n}}^- = \cos(2\theta_0)\hat{\mathbf{x}} + \sin(2\theta_0)\hat{\mathbf{y}}$. The function $f_v^-(x_v)$ describes the dependence on the distance x_v to the interface and is given by

$$f_v^-(x_v) = \int_{-\infty}^{\infty} dy K_0(\sqrt{x_v^2 + y^2}) \frac{x_v}{\sqrt{x_v^2 + y^2}} - \int_{x_v}^{\infty} \int_{-\infty}^{\infty} dx dy K_0(r) \frac{x^2 - y^2}{r^3}.$$

It has been evaluated numerically and is plotted in figure 8a. The $-1/2$ defect acquires a finite self-propulsion close to the wall in a region of thickness of order ℓ_d near the activity jump. Its motion is either towards or away from the boundary, depending on the defect's orientation and the sign of the activity.

To see how the $-1/2$ reorients as it approaches the interface, we evaluate the flow vorticity at the defect core as a function of the wall distance. Again, there are contributions to the vorticity from both flows driven by interfacial and bulk forces, given by

$$\omega_-^I = -\frac{\Delta\alpha}{2\pi\zeta^2} \sin 2\theta_0 \int_{-\infty}^{\infty} dy \left[K_1\left(\frac{r}{\zeta}\right) \times \frac{x_v^2}{\zeta(x_v^2 + y^2)} - K_0\left(\frac{\sqrt{x_v^2 + y^2}}{\zeta}\right) \frac{x_v^2}{\sqrt{x_v^2 + y^2}^3} \right] \quad (4.15)$$

and

$$\omega_-^B = -\frac{\Delta\alpha}{2\pi\zeta^2} \sin 2\theta_0 \int d\mathbf{r} K_0\left(\frac{r}{\zeta}\right) \left(\delta(x - x_v) \frac{y^2 - x^2}{r^3} + H(x - x_v) \frac{3x(x^2 - 3y^2)}{r^5} \right). \quad (4.16)$$

Note that the bulk term diverges when $x_v \rightarrow 0$. The total angular velocity of the $-1/2$ defect can then be written as

$$\omega_-(x_v, \theta_0) = -\frac{\alpha_0}{2\pi\eta} \sin(2\theta_0) f_\omega^-(x_v). \quad (4.17)$$

The function $f_\omega^-(x_v)$ has been calculated numerically and is shown in figure 8b. The dependence on the wall distance x_v changes sign near the wall, indicating that the vorticity tends to rotate the defect to a preferred orientation at the wall. The preferred orientation is determined by the stationary condition $\sin 2\theta_0 = 0$, and the stability criterion $(d\omega_-/d\theta_0) < 0$, which implies that $\theta_0 = 0$ for $\alpha_0 < 0$ and $2\theta_0 = \pi$ for $\alpha_0 > 0$. In other words for extensile activity the stable orientation of a $-1/2$ defect at a sharp active/passive interface corresponds to a polarization $\mathbf{e}_- = [1, 0]$. Therefore, as a result of both their self-induced translational and rotational motion, in an extensile system $-1/2$ defects are attracted to a sharp active/passive interface and orient themselves with one of the three axis normal to the interface. This is consistent with the accumulation of negative topological charge observed in experiments at active/passive interfaces [18,19] and near physical walls [29], as well as in simulations [24,25].

5. Conclusion

Activity gradients or sharp jumps can guide the motion and orientation of nematic defects. In a constant activity gradient, $+1/2$ defects acquire an angular velocity that may rotate their orientation such that the defect polarization aligns parallel to the activity gradient. The defects then self-propel in the direction of the gradient, always moving towards regions of lower magnitude of activity, where it is less motile. Thus, we expect that activity gradients will introduce more circular motion in the trajectories of the $+1/2$ defects. By contrast, a constant activity gradient yields no net vorticity or active force at the core of the $-1/2$ defect, which remains stationary.

We find that the self-propulsion velocity of $+1/2$ defects moving towards a sharp active/passive interface is also reduced, and that the defect will eventually stagnate at the wall. By contrast, $-1/2$ defects acquire a finite propulsion speed in the interfacial region and can overcome the positive defects, explaining the observation of negative charge accumulation in experiments and simulations [18,19,24,25,29]. We also predict that the active torque acting on a $+1/2$ defect that reaches the interface tends to reorient it toward a preferred polarization that is perpendicular to the interface and points away/toward it depending on extensile/contractile activity. The vorticity-induced active torque also acts on the orientation of a $-1/2$ defect migrating toward interface, by rotating the defect until it reaches the stable orientation which minimizes the net vorticity at the defect position. We show that a $-1/2$ defect with a stable orientation gets attracted to a sharp interface. This stable orientation is selected by the sign of activity, i.e. whether the system is contractile or extensile. Tunnelling across the interface observed numerically may be due to soft interfaces where the activity gradients are not sufficiently steep, as well as due to defect interactions and other hydrodynamic effects. Here, we have neglected additional contributions of pressure gradients induced by activity gradients, as well as elastic stresses, flow alignment, nematic distortions due to the active/passive interface and defect interactions, which may change qualitatively the defect dynamics.

Our results offer a simple understanding of the dynamics of nematic defects in the presence of spatially varying activity. They can provide the starting point for designing structures capable of controlling defect dynamics and associated active flows.

Data accessibility. Data and relevant code for this research work are stored in GitHub: <https://github.com/jonasron/Defect-Flows> and have been archived within the Zenodo repository: <http://doi.org/10.5281/zenodo.7562394> [30].
Authors' contributions. J.R.: formal analysis, software, writing—original draft; M.C.M.: conceptualization, supervision, writing—original draft; L.A.: conceptualization, supervision, validation, writing—original draft.

All authors gave final approval for publication and agreed to be held accountable for the work performed therein.
Conflict of interest declaration. We declare we have no competing interests.

Funding. M.C.M. was supported by the US National Science Foundation grant no. DMR-2041459. J.R. and L.A. acknowledge support from the Research Council of Norway through the Center of Excellence funding scheme, project no. 262644 (PoreLab).

Acknowledgements. M.C.M. thanks Mark Bowick, Luca Scharrer and Suraj Shankar for illuminating discussions. L.A. and J.R. are thankful to Jorge Viñals for stimulating discussions.

References

- Doostmohammadi A, Ignés-Mullol J, Yeomans JM, Sagués F. 2018 Active nematics. *Nat. Commun.* **9**, 3246. (doi:10.1038/s41467-018-05666-8)
- Balazsramaniam L, Mège RM, Ladoux B. 2022 Active nematics across scales from cytoskeleton organization to tissue morphogenesis. *Curr. Opin. Genet. Dev.* **73**, 101897. (doi:10.1016/j.gde.2021.101897)
- Sanchez T, Chen DT, DeCamp SJ, Heymann M, Dogic Z. 2012 Spontaneous motion in hierarchically assembled active matter. *Nature* **491**, 431–434. (doi:10.1038/nature11591)
- Guillamat P, Ignés-Mullol J, Sagués F. 2017 Taming active turbulence with patterned soft interfaces. *Nat. Commun.* **8**, 1–8. (doi:10.1038/s41467-017-00617-1)
- Needleman D, Dogic Z. 2017 Active matter at the interface between materials science and cell biology. *Nat. Rev. Mater.* **2**, 1–14. (doi:10.1038/natrevmats.2017.48)
- Kumar N, Zhang R, De Pablo JJ, Gardel ML. 2018 Tunable structure and dynamics of active liquid crystals. *Sci. Adv.* **4**, eaat7779. (doi:10.1126/sciadv.aat7779)
- Marchetti MC, Joanny JF, Ramaswamy S, Liverpool TB, Prost J, Rao M, Simha RA. 2013 Hydrodynamics of soft active matter. *Rev. Mod. Phys.* **85**, 1143–1189. (doi:10.1103/RevModPhys.85.1143)
- Saw TB, Xi W, Ladoux B, Lim CT. 2018 Biological tissues as active nematic liquid crystals. *Adv. Mater.* **30**, 1802579. (doi:10.1002/adma.201802579)
- Mueller R, Yeomans JM, Doostmohammadi A. 2019 Emergence of active nematic behavior in monolayers of isotropic cells. *Phys. Rev. Lett.* **122**, 048004. (doi:10.1103/PhysRevLett.122.048004)
- Simha RA, Ramaswamy S. 2002 Hydrodynamic fluctuations and instabilities in ordered suspensions of self-propelled particles. *Phys. Rev. Lett.* **89**, 058101.
- Juelicher F, Kruse K, Prost J, Joanny JF. 2007 Active behavior of the cytoskeleton. *Phys. Rep.* **449**, 3–28.
- Giomi L, Bowick MJ, Ma X, Marchetti MC. 2013 Defect annihilation and proliferation in active nematics. *Phys. Rev. Lett.* **110**, 228101. (doi:10.1103/PhysRevLett.110.228101)
- Lemma LM, DeCamp SJ, You Z, Giomi L, Dogic Z. 2019 Statistical properties of autonomous



- flows in 2D active nematics. *Soft Matter* **15**, 3264–3272. (doi:10.1039/C8SM01877D)
14. Alert R, Casademunt J, Joanny JF. 2022 Active turbulence. *Ann. Rev. Condens. Matter Phys.* **13**, 143–170. (doi:10.1146/annurev-conmatphys-082321-035957)
 15. Pismen LM. 2013 Dynamics of defects in an active nematic layer. *Phys. Rev. E* **88**, 050502. (doi:10.1103/PhysRevE.88.050502)
 16. Rønning J, Marchetti CM, Bowick MJ, Angheluta L. 2022 Flow around topological defects in active nematic films. *Proc. R. Soc. A* **478**, 20210879. (doi:10.1098/rspa.2021.0879)
 17. Shankar S, Marchetti MC. 2019 Hydrodynamics of active defects: from order to chaos to defect ordering. *Phys. Rev. X* **9**, 041047.
 18. Thijsen K, Khaladj DA, Aghvami SA, Gharbi MA, Fraden S, Yeomans JM, Hirst LS, Shendruk TN. 2021 Submersed micropatterned structures control active nematic flow, topology, and concentration. *Proc. Natl Acad. Sci. USA* **118**, e2106038118. (doi:10.1073/pnas.2106038118)
 19. Zhang R *et al.* 2021 Spatiotemporal control of liquid crystal structure and dynamics through activity patterning. *Nat. Mater.* **20**, 875–882. (doi:10.1038/s41563-020-00901-4)
 20. Tang X, Selinger JV. 2021 Alignment of a topological defect by an activity gradient. *Phys. Rev. E* **103**, 022703. (doi:10.1103/PhysRevE.103.022703)
 21. Mozaffari A, Zhang R, Atzin N, De Pablo JJ. 2021 Defect spirograph: dynamical behavior of defects in spatially patterned active nematics. *Phys. Rev. Lett.* **126**, 227801. (doi:10.1103/PhysRevLett.126.227801)
 22. Zhang R, Mozaffari A, de Pablo JJ. 2022 Logic operations with active topological defects. *Sci. Adv.* **8**, eabg9060. (doi:10.1126/sciadv.abg9060)
 23. Ruske LJ, Yeomans JM. 2022 Activity gradients in two- and three-dimensional active nematics. *arXiv preprint* (<https://arxiv.org/abs/2206.06499>).
 24. Scharer L. 2022 Dynamics of topological defects in spatially patterned activity. B.S. thesis, University of California Santa Barbara.
 25. Scharer L, Shankar S, Bowick MJ, Marchetti MC. 2022 Spatiotemporal control of active topological defects. *arXiv preprint* (<https://arxiv.org/abs/2212.00666>).
 26. Angheluta L, Chen Z, Marchetti MC, Bowick MJ. 2021 The role of fluid flow in the dynamics of active nematic defects. *New J. Phys.* **23**, 033009. (doi:10.1088/1367-2630/abe8a8)
 27. Alnæs M *et al.* 2015 The FEniCS project version 1.5. *Arch. Numer. Softw.* **3**, 9–23.
 28. Logg A, Mardal KA, Wells GN. 2012 *Automated solution of differential equations by the finite element method*. Heidelberg, Germany: Springer Berlin.
 29. Hardoïin J, Laurent J, Lopez-Leon T, Ignés-Mullol J, Sagués F. 2020 Active boundary layers. *arXiv preprint* (<https://arxiv.org/abs/2012.02740>).
 30. Rønning J, Marchetti MC, Angheluta L. 2023 Defect self-propulsion in active nematic films with spatially varying activity. Zenodo. (doi:10.5281/zenodo.7562394)

Paper III

Precursory patterns to vortex nucleation in stirred Bose-Einstein condensates

Jonas Rønning, Luiza Angheluta

Precursory patterns to vortex nucleation in stirred Bose-Einstein condensates

Jonas Rønning  and Luiza Angheluta *The Njord Center, Department of Physics, University of Oslo, Blindern, 0316 Oslo, Norway*

(Received 26 October 2022; accepted 25 April 2023; published 18 May 2023)

Within the Gross-Pitaevskii theory, we study precursory pattern formations to the nucleation of vortex dipoles in a two-dimensional Bose-Einstein condensate stirred by a Gaussian potential. We introduce a smooth superfluid vorticity field and its conservative current, which capture very well the gradual process of vortex nucleation as a mechanism of topological singularities acquiring smooth cores. This is characterized by the localization of the superfluid vorticity into core regions which harbor the phase slips. For more impenetrable obstacles, we find that there are additional phase slips that do not acquire cores, thus remaining pinned as ghost vortices to the potential. We show that the vortex kinematics is slaved to the superfluid vorticity current, which determines not only the onset of nucleation but also the shedding dynamics.

DOI: [10.1103/PhysRevResearch.5.023108](https://doi.org/10.1103/PhysRevResearch.5.023108)

I. INTRODUCTION

Topological defects are the fingerprints of broken continuous symmetries and are widely encountered in ordered systems, such as disclinations in liquid crystals [1,2], dislocations in solid crystals [3–5], orientational defects in biological active matter [6–8], quantized vortices in quantum fluids [9–11], or cosmic strings [12]. The formation and dynamics of topological defects during phase ordering kinetics through temperature quenches from the disordered phase have been well studied for decades [13]. Going beyond the relaxation to equilibrium, more recent theoretical approaches have focused on the collective behavior in driven ordered systems through the dynamics of topological defects.

The topological defects in an atomic Bose-Einstein condensate (BEC) are quantum vortices where the condensate is locally melted while losing its phase coherence. This induces persistent circulating superfluid flow about the vortex cores [14]. With the advent of tailored experimental realizations of BECs comes also a surge in theoretical studies focused on understanding and tracking nonthermal nucleation and dynamics of quantized vortices in driven Bose-Einstein condensates. Two main frameworks are currently applied to study the vortex nucleation in two-dimensional BECs, either by rotating the condensate [15–17] or by coupling the condensate with a moving obstacle [18–22]. The nucleation criterion is based on the energetic argument that the superfluid flow reaches a critical velocity above which the condensate phase gradient undergoes phase slips. In rotating BEC systems, vortices of the same circulation are created when the total amount of angular momentum exceeds a critical threshold for the vortex formation. Same-sign vortices form at the edge of the

condensate and migrate into the bulk, where they eventually form vortex lattices after reequilibration [15,23–26].

The vortex nucleation in condensates stirred by a moving obstacle has also been studied [27–31] and observed experimentally [21,22]. Here, the nucleation criterion relies on the height U_0 of the repulsive Gaussian potential representing the coupling of the stirring obstacle to the condensate. A hard potential corresponds to an almost impenetrable obstacle when $U_0 > \mu$, where μ is the chemical potential, such that the condensate density rapidly decreases and nearly vanishes inside the potential. By contrast, a soft potential corresponds to a penetrable obstacle for $U_0 < \mu$ such that the condensate density is gently depleted inside the obstacle. The onset of vortex nucleation induced by a hard obstacle occurs when the local condensate velocity reaches the critical velocity for phonon emission, whereas for the soft obstacle this is a necessary but not a sufficient requirement [27,28]. Stirring obstacles are typically modelled as Gaussian potentials with varying height and width [30,31]. In Ref. [31] the vortex nucleation induced by a repulsive Gaussian potential of different strengths is studied numerically. It is found that near the critical velocity for vortex nucleation, the energy gap between the ground state and the excited state goes to zero as a power law, while ghost vortices, i.e., phase slips, are formed inside the potential. By contrast, no such ghost vortices develop in the case of soft potentials. In addition to tuning the degree of permeability of the obstacle, different vortex shedding regimes, from vortex dipoles, pairs, and clusters [32–34], can be induced by varying the size of the obstacle through the width of the potential, which also changes the critical stirring velocity [21,35]. Once vortices are being shed into the condensate they interact with each other, forming dynamic clusters that sustain energy cascades and two-dimensional quantum turbulence [11,34,36–39].

Even though compressibility effects, due to shock waves and phonons, are particularly important in the nucleation and the annihilation of vortex dipoles, they are typically overlooked in the quantum turbulence regime where turbulent

Published by the American Physical Society under the terms of the Creative Commons Attribution 4.0 International license. Further distribution of this work must maintain attribution to the author(s) and the published article's title, journal citation, and DOI.

energy spectra and clustering behavior is attributed mostly to the mutual interactions between vortices [37,40]. The point vortex modeling approach has been employed to characterize different quantum turbulence regimes [41–45]. In point vortex models, vortices are reduced to charged point particles with an overdamped dynamics where their velocity is determined by the mutual interaction potential or external potentials. While the point vortex approach is suitable for studying collective vortex dynamics, it cannot model fast processes such as vortex annihilation or creation events without ad hoc rules since, by construction, it overlooks the finite vortex core and compressibility effects, which are crucial to fast events.

An accurate, nonperturbative method of deriving the velocity of topological defects directly from the evolution of the order parameter of the O(2) broken rotational symmetry has been developed by Halperin and Mazenko [46–48]. Topological defects are located as zeros in the 2D vector order parameter, where the magnitude of order vanishes to regularize the core region where the phase of the order parameter becomes undefined. The defect velocity is determined by the magnitude of the defect density current at the defect position. In the frozen-phase approximation, where the phase of the order parameter is stationary apart from its moving singularities, the vortex kinematics determined by the evolution of the order parameter reduces to a point vortex model [45,47]. Within the Gross-Pitaevskii theory, the order parameter is the condensate wave function, and the frozen-phase approximation is the regime where the dynamics of phonon modes can be neglected. This is a versatile formalism which has been applied to various systems, from tracking of point dislocations [4] and dislocation lines [5] in crystals, point orientational defects in active nematics [49] and active polar systems [50], disclination lines in nematic liquid crystals [51] and vortex lines in BECs [52].

In this paper we adopt the Halperin-Mazenko formalism to gain further theoretical insights into the process of vortex nucleation as a mechanism by which phase singularities acquire a finite core to form a vortex. In Sec. II we present this formalism for two-dimensional (2D) BECs and show that the defect density field D represents a generalized, smooth vorticity, defined as the curl of the superfluid current, and its evolution determines the vortex velocity. This method circumvents the need of operating directly with the singularities in the condensate phase, which are harder to manipulate both theoretically and numerically. In Sec. III we study the pattern formations developed in the superfluid vorticity D and its current density $\mathbf{J}^{(D)}$ during the nucleation process and show that the superfluid vorticity condensed into well-defined cores which harbor phase slips. In Sec. IV we show that the superfluid vorticity current which determines vortex dynamics reduces to the point vortex model in the frozen-phase approximation and derive the kinematics of point vortices in the presence of both superfluid flow and nonuniform condensate density. Concluding remarks and a summary are presented in Sec. V.

II. VORTICES AS MOVING ZEROS

The superfluid flow and the topological structure of a weakly interacting BEC are described by the evolution of

its macroscopic wave function $\psi = |\psi|e^{i\theta}$, where $|\psi|$ is the magnitude of the condensate wave function and θ is the condensate phase. Disturbances in the condensate phase generate a superfluid flow with a current (momentum) density

$$\mathcal{J} = |\psi|^2 \nabla \theta = \text{Im}(\psi^* \nabla \psi), \quad (1)$$

such that gradients in the condensate phase define the superfluid flow velocity, which is irrotational everywhere except at the points \mathbf{r}_α where the condensate phase loses its coherence and becomes undetermined (singular), namely,

$$\nabla \times \nabla \theta = 2\pi q_\alpha \delta^2(\mathbf{r} - \mathbf{r}_\alpha). \quad (2)$$

This phase singularity has a topological nature determined by a $2\pi q_\alpha$ phase jump upon going counterclockwise around a loop C_α enclosing it, where $q_\alpha = \pm 1$ is the topological charge of the lowest energy quantum vortex, namely,

$$2\pi q_\alpha = \oint_{C_\alpha} d\theta = \oint_{C_\alpha} d\mathbf{l} \cdot \nabla \theta, \quad (3)$$

which is equivalent to the differential form in Eq. (2). Thus, for configurations of well-separated vortices punctuating an otherwise uniform condensate, the singular vortex charge density field is a superposition of δ functions centered at the vortex positions,

$$\rho_v(\mathbf{r}, t) = \sum_\alpha q_\alpha \delta^2[\mathbf{r} - \mathbf{r}^{(\alpha)}(t)], \quad (4)$$

and it represents the singular vorticity field as the curl of the superfluid flow velocity. From the single-valuedness of the condensate wave function everywhere, it follows that the condensate density vanishes where the condensate phase is undetermined. Hence, quantum vortices are located at zeros of the condensate wave function ψ as exploited by Halperin and Mazenko [46,47]. By representing the complex ψ field as an O(2)-symmetric real vector field $\vec{\Psi} = [\Psi_1; \Psi_2]$, where $\Psi_1 = \text{Re}(\psi)$ and $\Psi_2 = \text{Im}(\psi)$, we notice that $\vec{\Psi}(\mathbf{r})$ maps a point \mathbf{r} to a point in the (Ψ_1, Ψ_2) disk centered at the origin and of unit radius (i.e., the uniform condensate density in rescaled units). Regions of uniform condensate density map to the unit circle, whereas vortices located at various positions \mathbf{r}_α in the real space reside at the origin of the (Ψ_1, Ψ_2) disk. The coordinate transformation between the physical (x, y) space to the (Ψ_1, Ψ_2) disk is determined by the Jacobi determinant

$$D = \begin{vmatrix} \partial_x \Psi_1 & \partial_x \Psi_2 \\ \partial_y \Psi_1 & \partial_y \Psi_2 \end{vmatrix} = \epsilon_{ij} \partial_i \Psi_1 \partial_j \Psi_2 = \frac{\epsilon_{ij}}{2i} \partial_i \psi^* \partial_j \psi, \quad (5)$$

where ϵ_{ij} is the Levi-Civita tensor and Einstein's summation convention is used. The D field is a scalar field that vanishes in regions of uniform condensate phase and is non zero otherwise, as it is the case around vortices. By a coordinate transformation of the Dirac δ function in Eq. (4), we can rewrite the singular vortex density in terms of the zeros of the $\vec{\Psi}$ as

$$\rho_v(\mathbf{r}, t) = D(\mathbf{r}, t) \delta^2(\vec{\Psi}). \quad (6)$$

In fact, the D field is a measure of the nonsingular vorticity as the curl of the superfluid current [52]

$$\epsilon_{ij} \partial_j \mathcal{J}_i = \epsilon_{ij} \text{Im}(\partial_i \psi^* \partial_j \psi) = 2D. \quad (7)$$

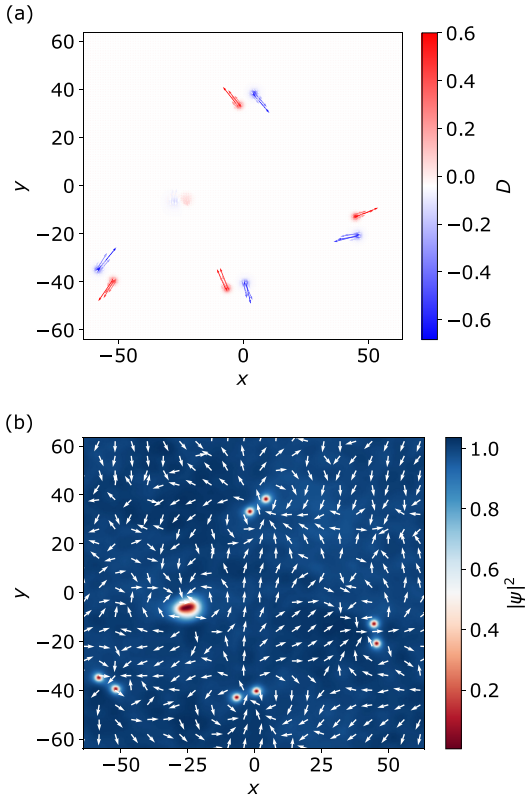


FIG. 1. Snapshot of (a) D field and (b) condensate density $|\psi|^2$ around a stirring Gaussian potential when vortex dipoles are being shed. The vector fields are (a) defect current $\mathbf{J}^{(D)}$ and (b) director of the superfluid current \mathcal{J} , respectively. Negative vortices move in the opposite direction of $\mathbf{J}^{(D)}$. System size is represented in units of the healing length.

This is also reflected in the fact that the singular, topological structure in the condensate phase is regularized by vanishing density which introduces a finite core size of the condensate vortices. The D field as a superfluid vorticity locates both the core and the circulation of the vortices as illustrated in Fig. 1(a). To show that the D field indeed captures the topological phase slips, we integrate Eq. (7) over an area S containing vortices

$$\int_S d^2\mathbf{r}D = \frac{1}{2} \int_{\partial S} d\mathbf{l} \cdot \mathcal{J} = \frac{1}{2} \int_{\partial S} |\psi|^2 \nabla\theta \cdot d\mathbf{l}. \quad (8)$$

In the assumption that the contour ∂S enclosing the area S is sufficiently far away from well-separated vortices, i.e., the superfluid density equals its uniform bulk value $|\psi_0|^2 = 1$ along the integration contour, the above integral reduces to

$$\int_S d^2\mathbf{r}D = \pi \sum_{\alpha \in S} q_\alpha, \quad (9)$$

where the sum is over all vortices inside the contour. Equivalently, integrating the absolute value of D , we obtain instead the total number N of vortices enclosed by the contour,

$$\int_S d^2\mathbf{r}|D| = \sum_\alpha q_\alpha \int_{S_\alpha} d^2\mathbf{r}D = N\pi, \quad (10)$$

which is the limit case of a uniform condensate punctuated by well-separated vortices.

However, the generalized vorticity D field picks up not only topological defects but any phase gradient (flow) disturbances modulated by the superfluid density, which may be induced by compressible modes, trapping, or stirring potentials. These nonsingular contributions become particularly important for the nucleation of vortices as discussed in Sec. III and have been overlooked in earlier studies using the Halperin-Mazenko formalism.

Flow disturbances with a topological origin can be dissociated from the rest by the value of the generalized vorticity determined by the condensate density profile near a vortex. Namely, if we consider Eq. (8) for a disk S of radius much smaller than the healing length and centered at an isolated vortex in an otherwise homogeneous condensate, we find that the value of the D field reaches in magnitude a value given by

$$|D_0| = \Lambda^2 \approx 0.7, \quad (11)$$

using the near-vortex profile of the condensate $|\psi|(r) = \Lambda r$ [53], and the numerical value for the steepness Λ of the density gradients taken from Ref. [39].

This superfluid vorticity is a topologically conserved quantity given by [47]

$$\partial_t D = -\partial_i J_i^{(D)}, \quad (12)$$

with its corresponding superfluid vorticity current

$$J_i^{(D)} = \epsilon_{ij} \text{Im}(\partial_i \psi \partial_j \psi^*), \quad (13)$$

determined uniquely by the evolution of the ψ field and accurately tracking the motion of the vortices as also illustrated in Fig. 1(a) for a snapshot of a stirred condensate with several dipoles. This current density is nonzero where the superfluid flow is nonuniform, particularly through the vortex cores where there are phase slips, as seen in Fig. 1(a). Figure 1(b) represents a color map of condensate density and the vector field of the normalized superfluid current showing vortical flow around vortices for the same snapshot as in panel (a). The Gaussian stirring potential is the larger indentation in the condensate density.

When the D field tracks vortices, it determines the topological invariance of the singular defect charge density ρ_v , namely, that

$$\partial_t \rho_v = -\partial_i J_i^{(\rho_v)}, \quad (14)$$

with the corresponding singular vortex current density being (see Appendix)

$$\begin{aligned} \mathbf{J}^{(\rho_v)}(\mathbf{r}, t) &= \mathbf{J}^{(D)}(\mathbf{r}, t) \delta^2(\vec{\Psi}) \\ &= \sum_\alpha q_\alpha \frac{\mathbf{J}^{(D)}(\mathbf{r}_\alpha)}{D(\mathbf{r}_\alpha)} \delta^2(\mathbf{r} - \mathbf{r}_\alpha). \end{aligned} \quad (15)$$

In the frozen-phase approximation, the vortex core is rigid and the equilibrium vortex wave-function profile remains stationary in the vortex comoving frame. In this case the vortex current is identical to the advective current $\sum_{\alpha} q_{\alpha} \mathbf{v}_{\alpha} \delta^2(\mathbf{r} - \mathbf{r}_{\alpha})$ [54]. Within this approximation, the velocity is uniform or slowly varying through the vortex core and given as

$$\mathbf{v}_{\alpha} = \frac{\mathbf{J}^{(D)}(\mathbf{r}_{\alpha})}{D(\mathbf{r}_{\alpha})}. \quad (16)$$

This relation provides an accurate measurement of the vortex velocity and can be reduced to the point vortex model as discussed further in Sec. IV. Within the Gross-Pitaevskii theory, the evolution of the condensate wave function ψ in the presence of a potential field $U(\mathbf{r}, t)$ containing both a static trapping potential and a time-dependent stirring potential can be described by a damped Gross-Pitaevskii equation (dGPE), which in dimensionless units reads as [11,38,39]

$$\partial_t \psi = (i + \gamma) \left[\frac{1}{2} \nabla^2 \psi + (1 - U - |\psi|^2) \psi \right], \quad (17)$$

where the damping coefficient γ is an effective thermal drag that represents the coupling of the condensate with a static thermal bath and particle exchanges [55]. The dimensional units used in the rescaling are given by the chemical potential μ , the healing length $\xi = \hbar / \sqrt{m\mu}$ and the sound velocity $c = \mu/m$. The wave function is rescaled in units of $\sqrt{\mu/g}$, where m is the mass of the bosons and g is an effective scattering parameter for the interactions between bosons.

By inserting Eq. (17) into the conservation law of the D field in Eq. (12), we express the evolution of the generalized superfluid vorticity as

$$\begin{aligned} \partial_t D = & -\frac{1}{2} \epsilon_{ij} \partial_i \partial_k \text{Re}(\partial_k \psi^* \partial_j \psi) + \frac{\epsilon_{ij}}{2} \partial_i U \partial_j |\psi|^2 \\ & + \frac{\gamma}{2} \nabla^2 D + 2\gamma D [1 - U - 2|\psi|^2] \\ & + \gamma \mathcal{J} \cdot \nabla^{\perp} U + \frac{\gamma}{2} \epsilon_{ij} \text{Im}[\partial_i \partial_k \psi \partial_j \partial_k \psi^*]. \end{aligned} \quad (18)$$

The first term on rhs is a sink/source superfluid vorticity coming from the kinetic energy. The second term corresponds to the coupling with an external potential and gives a nonzero contribution (as a sink/source) only when the gradient in the condensate density is normal to the gradient force. The remaining terms are the different contributions of the thermal damping to the dissipation of superfluid vorticity, such as diffusion, sink/sources from the coupling with a potential U , and a thermal drag induced by superfluid flow.

Since the condensate density vanishes at the vortex position, the only nonzero contribution to the generalized vorticity current density at the vortex position comes from the kinetic energy; thus the general formula for the vortex velocity can be expressed as

$$\mathbf{v}_{\alpha} = i \left. \frac{\text{Re}(\nabla^2 \psi^* \nabla^{\perp} \psi) + \gamma \text{Im}(\nabla^2 \psi \nabla^{\perp} \psi^*)}{\nabla \psi^* \cdot \nabla^{\perp} \psi} \right|_{\mathbf{r}=\mathbf{r}_{\alpha}}, \quad (19)$$

and reduces in certain approximations to the point vortex dynamics as detailed in Sec. IV. However, the sink/source contribution from the external potential U plays an important role in the nucleation and shedding of vortices as discussed next.

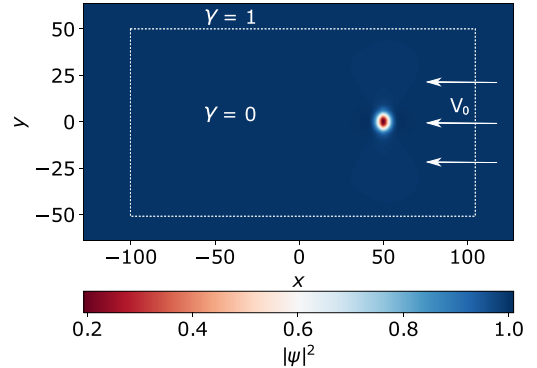


FIG. 2. Numerical setup of the condensate in the comoving frame of the Gaussian potential (uniform flow direction shown by the arrows). The color map represents the condensate density. The dotted lines show the thermal buffer interfaces.

III. VORTEX NUCLEATION

To study the onset of vortex nucleation, we consider a uniform Bose-Einstein condensate at zero temperature that is coupled with a Gaussian potential moving at a constant speed V_0 along the x axis. Using the Galilean invariance of the GPE at $\gamma = 0$, we can transform it to the comoving frame by boosting the wave function with the phase factor $\exp(iV_0 x + i\frac{V_0^2}{2} t)$ to account for the shift in the kinetic energy [56]. The form of the GPE is invariant under Galilean transformation only when $\gamma = 0$.

In the comoving frame, this is equivalent to having a static potential in a uniform superfluid flow described by

$$\partial_t \psi + V_0 \partial_x \psi = i \left[\frac{1}{2} \nabla^2 + (1 - |\psi|^2) - U_0 e^{-\frac{(x-y_0)^2}{d^2}} \right] \psi, \quad (20)$$

where d is the width of the potential and U_0 is the coupling strength.

In numerical simulations we consider a thermal buffer on the edge of the periodic domain where the damping coefficient is nonzero to avoid recirculation of the shed vortex dipoles and to dampen wave interference as illustrated in Fig. 2. A similar computational trick was used in previous studies of the vortex shedding [33] and the formation of a phonon wake [56]. The width of the stirring potential is set to $d = 4$, and we vary its speed V_0 and its height U_0 . We use a rectangular domain $[-128, 128] \times [-64, 64]$ (corresponding to a 512×256 rectangular grid) and a fixed time step $dt = 0.01$. The potential is centered in the middle of the domain at $(x_0, y_0) = (50, 0)$. For the dissipative buffer we set the thermal drag to $\gamma(\mathbf{r}) = \max[\gamma_x(x), \gamma_y(y)]$, which is effectively equal to 1, as shown in Fig. 2. The smooth, but sharp transition between the buffer and bulk values is mediated by the interfacial profiles along the x and y directions given by

$$\gamma_x(x) = \frac{1}{2} (2 + \tanh[(x - x_w)/\Delta] - \tanh[(x + x_w)/\Delta]),$$

and similarly for $\gamma_y(y)$. Here $x = \pm x_w$ and $y = \pm y_w$ locate the positions of the top and bottom buffer interfaces along

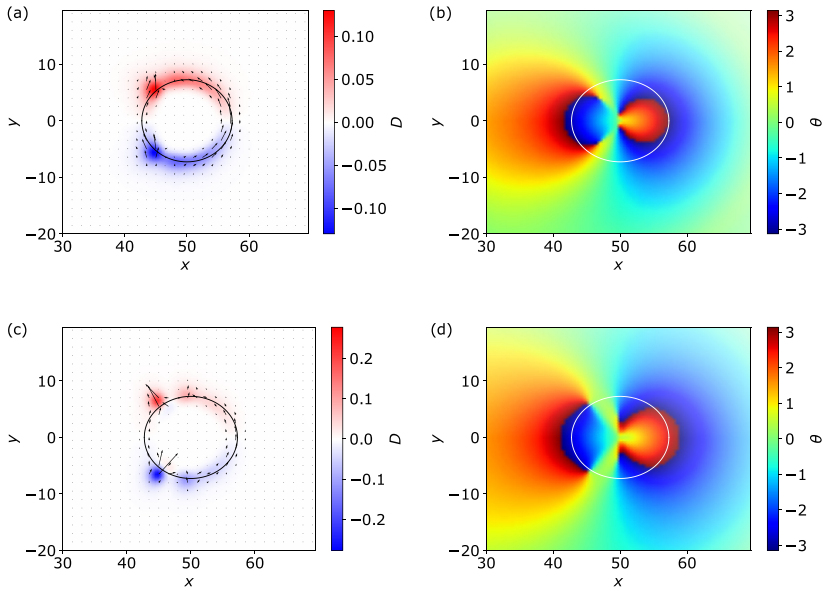


FIG. 3. (a) D field and (b) condensate phase θ around a hard potential at $t = 19$ prior to a nucleation. Two dipoles of phase slips reside inside the potential. (c) D field and (d) θ at $t = 28$ (at the nucleation onset) when one dipole of phase slips have migrated to occupy the two vorticity blobs. White/black circle is the radius where the potential becomes e^{-1} . The vector field in (a), and (c) represents the superfluid vorticity current. The potential strength is $U_0 = 10$, and the stirring speed is $V_0 = 0.4$, slightly above the estimated critical speed for this value of U_0 , $V_{0c} \approx 0.38$.

the x direction, while Δ is the width of interface. The buffer parameters are set to $w_x = 100$, $w_y = 50$, and $\Delta = 7$.

We start by relaxing the initial Thomas-Fermi ground state in imaginary time to find the steady state at $V_0 = 0$ and then evolve the condensate wave function according to Eq. (20) for a given V_0 . However, since the initial state is not the ground state of this equation, there will be an initial disturbance forming around the potential which may lead to defect nucleation even below the critical velocity. Thus we first let the system relax this initial disturbance before we analyze the nucleation process. The regime with $U_0 > 1$ (in units of the chemical potential) corresponds to a hard potential whereby the condensate density almost vanishes inside the obstacle, akin to the homogeneous boundary condition imposed at an impenetrable boundary which melts the condensate phase coherence at any stirring velocity. Conversely, for soft-indenting potentials equivalent to $U_0 < 1$, the condensate density is more gently depleted such that phase coherence is preserved below a critical speed. The transition from soft to hard potential obstacle occurs around $U_0 \sim 1$, where the potential induces a dipole of phase slips pinned inside the obstacle [35].

The superfluid vorticity D field and its current density turn out to be advantageous tools to unravel and explore the distinct precursory patterns to the onset of vortex nucleation and shedding for different stirring conditions as discussed next. For hard potentials, one dipole of phase slips develops and remained pinned inside the obstacle where the condensate density is close to zero for stirring velocities above and slightly below the critical value as visualized in Figs. 3(b)

and 3(d) (above the critical velocity) and Fig. 4(b) (below the critical velocity). However, it turns out that the presence of this dipole does not necessarily lead to nucleation. From the profile of the superfluid vorticity D field around the stirring potential, we can get a more in-depth understanding of the dynamical pattern formation leading to the nucleation of a vortex dipole. Below the critical speed we observe that a steady-state profile of the superfluid vorticity concentrated in a diffuse halo surrounding the edge of the potential such that the circulation changes sign symmetrically about the direction of motion as shown the Fig. 4(a). In this steady state, the superfluid vorticity current vanishes and results in no shedding event, even though there is one dipole of phase slips pinned in the middle of the potential [see Fig. 4(b)]. For this reason, this dipole was also termed as a ghost vortice in Ref. [31]. Above the critical velocity, which depends on U_0 as studied in Ref. [35], there is no steady state in the superfluid vorticity. Instead, the diffusive halo around the potential tends to localize over time into two blobs of opposite circulation as shown in Figs. 3(a) and 3(c), corresponding to the formation of two vortex cores. While the cores are forming on the edge, two dipoles of phase slips have formed inside the potential, where one detaches and migrates towards the vorticity cores while the other stays pinned. The onset of vortex nucleation corresponds to the moment when the two vorticity cores are hosting one phase slip each. The subsequent vortex shedding is precisely determined by the D -field current, which endows the vortices with a net velocity away from the potential as shown in Fig. 3(c). Thus the vortex shedding pattern and frequency could be further studied from

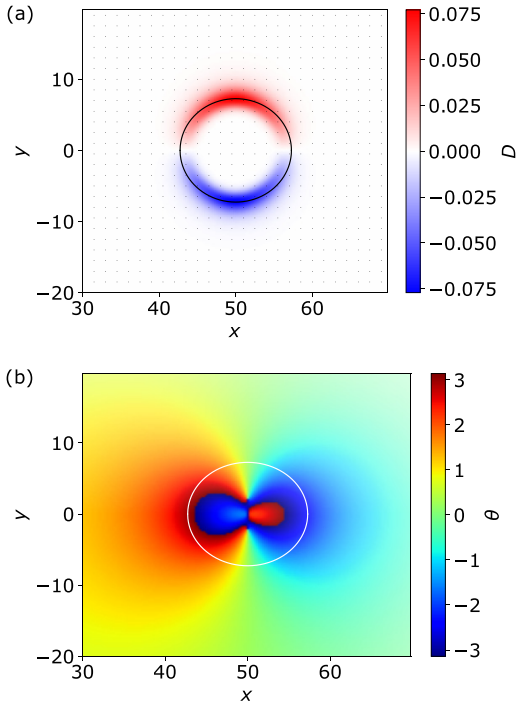


FIG. 4. (a) Steady-state profile of the D field for a hard potential $U_0 = 10$ with the stirring speed $V_0 = 0.35$ (below the critical value). (b) Ghost dipole of phase slips inside the hard obstacle.

the D -field current. We also note that this formalism allows us to make a clear distinction between real versus ghost vortices. The latter are really due to the hard potential breaking the phase coherence. It is the second dipole of phase slips which controls the nucleation process.

As argued earlier, the important distinction of soft and hard potentials is the presence of ghost vortices. The D field is a powerful tool to further investigate the influence of ghost vortices on the nucleation mechanism, which is a challenging task. We can do this by contrasting it with the scenario where there are no ghost vortices, as is the case for soft-indenting potentials. Here, the D field develops two smeared-out regions of superfluid vorticity with alternating circulating and spanning the stirring potential. This is accompanied by smooth phase gradients as shown in Figs. 5(a) and 5(b). The locations of the regions with opposite superfluid vorticity are determined by the phase gradients through the curl of the superfluid current, as predicted by Eq. (7). Below a critical speed, this D -field pattern remains stable with its corresponding vorticity current $\mathbf{J}^{(D)}$ vanishing as illustrated in Fig. 6. Notice that the pattern in the D field is also symmetric about the direction of motion, which also determines the orientation of the phase-slip dipole. At sufficiently high V_0 a dipole of phase slips forms inside the soft potential and corresponds to the localization of the D field around two blobs with opposite circulation [Figs. 5(c) and 5(d)]. Interestingly, in this case the phase slips develop already

inside the vorticity cores to form vortices. Since the D -field current tracks the motion of these vortices, it also reveals the direction in which vortices are being shed, as shown in Fig. 5(c).

Based on this analysis, we get new insights into the vortex nucleation as a fundamental gradual process of topological singularities acquiring a finite core. This basic mechanism is common to both hard and soft potentials. The main difference is that for the soft potential, the phase slips develop inside the vorticity core, whereas for the hard potential, the phase slips form inside the potential and migrate to vorticity cores. In this case phase slips can form as ghost vortices without there being any vorticity localization, as seen in Fig. 4(b). We have considered the homogeneous vortex nucleation and shedding away from a stirring potential in a uniform condensate. Because of the symmetry of the initial configuration, only dipoles are being nucleated and shed. However, a small noise added to the uniform condensate wave function breaks the symmetry of the initial state and may lead to vortex nucleation beyond simple dipoles [32,33]. The nucleation event remains symmetrical through the formation of dipoles of phase slips inside the potential. However, the shedding can become more irregular depending on the noise amplitude and stirring velocity.

To get a more quantitative measure of the nucleation event, we use the spatial average of the magnitude of the generalized vorticity $|D|$ as a proxy to the total number of nucleated vortices. The deviation from the theoretical prediction from Eq. (10) corresponding to a uniform superfluid punctuated by well-separated vortices informs us about the presence of additional density heterogeneities due to compressible modes or induced by the obstacle potential, as discussed earlier and shown in Figs. 3–5. In Fig. 7 we have plotted this global measure as a function of time for a soft versus hard potential and for different stirring speeds. The integration domain is a square surrounding the obstacle of size $l = 40$, i.e., the same domain that is shown in Figs. 3–6.

Below the critical speed $V_0 < V_{0c}$, the net circulation plateaus at a value lower than the predicted threshold for vortices. This corresponds to the regime where superfluid vorticity is smeared diffusively around the potential in the absence of any phase slips or vortex nucleation, as is the case for soft potentials and illustrated in Fig. 7(a).

As V_0 approaches the critical speed from below (in the absence of noise), the net circulation reaches above the 2π threshold, signaling the presence of a vortex dipole. This is common to both soft and hard potentials as shown in Figs. 7(a) and 7(b). Once the nucleated vortex dipole drifts out of the integration domain, the value of the circulation drops and shows only the contribution of the vorticity around the potential. When $V_0 > V_{0c}$, the gradual process of phase slips acquiring finite cores becomes recurrent and results in repeating vortex nucleation and shedding. Periodic shedding is observed near the critical speed, and more irregular shedding occurs with higher speeds, as shown in Figs. 7(a) and 7(b).

IV. VORTEX KINEMATICS

Using the formalism presented in Sec. II, we now derive a closed expression for the vortex kinematics in the presence

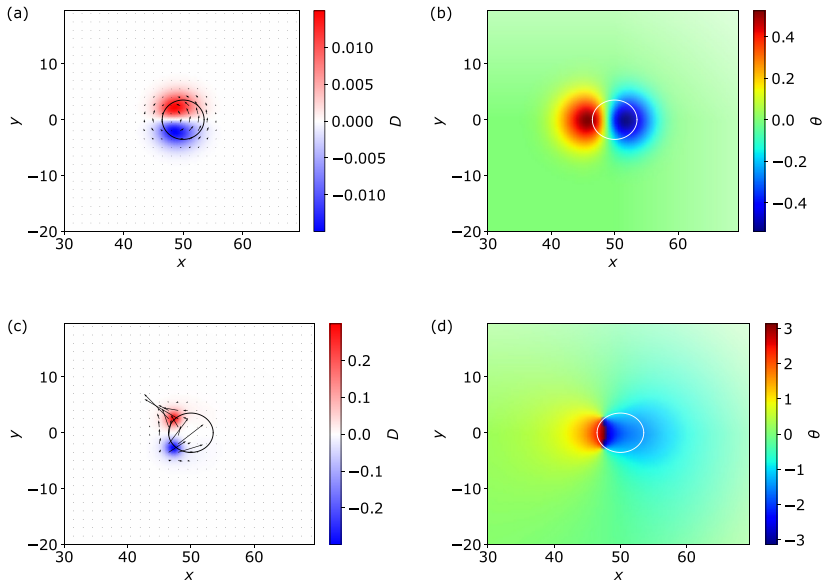


FIG. 5. D field with defect current (a), (c) and condensate phase (b), (d) around the soft potential during a dipole nucleation. Before the phase slips formed, $t = 5$ (a), (b), the D field spreads diffusively inside the potential. This region condenses into two cores which detach from the potential after they acquire phase slips at $t = 29$ (c), (d). Potential strength is $U_0 = 0.8$ and stirring speed is $V_0 = 0.42$, slightly above the estimated critical value $V_{0c} \approx 0.4$.

of both background superfluid flow and heterogeneities in the condensate density. In this section we also consider the dissipative effect of the thermal drag on the vortex dynamics. First we consider a uniform condensate punctuated at the origin with a vortex. The profile of the condensate wave function near the defect is approximated as $\psi_0 \approx r e^{i q \theta}$, where r is the distance to the vortex with circulation $q = \pm 1$ and $r \ll 1$, which is a solution of the stationary vortex, $\partial_t \psi_0 = 0$. We now introduce a smooth phase perturbation $\psi(\mathbf{r}, t) = \psi_0(\mathbf{r}) e^{i \phi(\mathbf{r}, t)}$ which accounts for the net superfluid flow at the vortex position while keeping the steady-state density profile. Near the defect position, the time evolution of the wave function is dominated by the kinetic energy contribution,

$$\partial_t \psi|_{\mathbf{r}=0} \approx (i + \gamma) \frac{1}{2} \nabla^2 \psi = (-1 + i\gamma) \nabla \psi_0 \cdot \nabla \phi e^{i \phi}. \quad (21)$$

Thus, evaluating the vorticity current using the near-vortex evolution of the condensate wave function we arrive at the following expression:

$$J_i^{(D)} = \epsilon_{ij} [-\epsilon_{jk} D + \gamma q \epsilon_{kl} \epsilon_{jk} D] \partial_k \phi, \quad (22)$$

which together with Eq. (16) implies that the vortex velocity is determined by the phase gradients,

$$v_i = (\partial_i \phi + \gamma q \epsilon_{ij} \partial_j \phi)_{\mathbf{r}=0}, \quad (23)$$

which is the basic overdamped vortex dynamics in the point vortex model [57,58]. However, this model does not include the effect of condensate density disturbances due to the presence of trapping or stirring potentials.

We now apply the same method to compute the contribution of density variations to the vortex velocity. For this, the wave function is perturbed both in magnitude and phase:

$\psi = \psi_0 e^{\lambda + i \phi}$, where ϕ and λ are smooth real fields [45,48]. The generalized vorticity D field acquires an additional contribution from the density perturbations and is given by

$$D = e^{2\lambda} \frac{1}{2i} \epsilon_{ij} \partial_i \psi_0 \partial_j \psi_0. \quad (24)$$

The corresponding vortex velocity becomes

$$v_i = (\partial_i \phi - \gamma \partial_i \lambda + \gamma q \epsilon_{ij} \partial_j \phi + q \epsilon_{ij} \partial_j \lambda)_{\mathbf{r}=0}, \quad (25)$$

which is consistent with the dissipative vortex dynamics obtained by a different approach in Ref. [59]. A similar dissipative dynamics in the absence of density variations has also been used in Ref. [60] to study the diffusive expansion of a vortex cluster and compare with experimental observations. This equation reduces to the expressions obtained in Refs. [45,48] for $\gamma = 0$. In Ref. [45] it was shown that the density inhomogeneities due to an harmonic trap induces an orbital motion or a vortex imprinted in the condensate. This is precisely determined by last term in Eq. (25) due to the spatial profile of the condensate density. The effect of thermal drag is that it makes oppositely charged vortices attract each other according to the third term in Eq. (25). Also, vortices move down gradients in the background condensate density as given by the second term. For the harmonic trap this implies that vortices have instead a spiral motion towards the edge of the trap.

To illustrate this we track the trajectory of a single vortex imprinted in a BEC coupled to a harmonic potential. At zero temperature the vortex moves in an orbit of constant radius around the center of the harmonic trap. As a dissipative effect of the effective thermal drag, the vortex acquires a radial

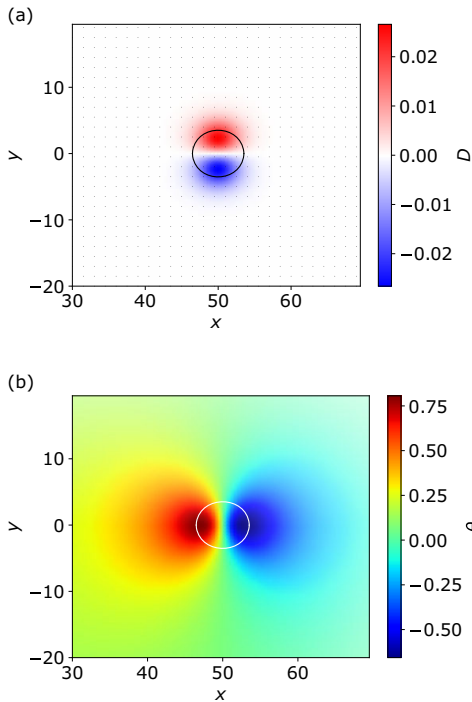


FIG. 6. (a) Steady-state profile of the D field for a soft potential $U_0 = 0.8$ at velocity $V_0 = 0.38$ (below the estimated critical value ≈ 0.4). (b) Smooth-steady-state profile of the condensate phase.

velocity and spirals out towards the edge of the trap. The angular v_θ and radial v_r velocity components as functions of time are shown in Fig. 8. We notice that velocity obtained by the slope of the vortex trajectory is a noisy signal compared to the velocity from Eq. (16).

V. DISCUSSION AND CONCLUSIONS

In summary, we have extended the Halperin-Mazenko formalism to characterize the nucleation and dynamics of vortices in a stirred Bose-Einstein condensate. We introduce a smooth superfluid vorticity D field as a topologically conserved quantity with its associated current density which tracks all the localized disturbances in the condensate both singular (vortices) and nonsingular (shock waves and disturbances induced by external potentials).

When the uniform condensate is stirred by a Gaussian potential, the onset to vortex nucleation is signalled by the precursory pattern formations in the superfluid vorticity D field which captures the process of phase slips acquiring finite cores. The D field is nonzero only around the stirring potential, where it develops two diffusive regions with alternating vorticity distributed symmetrically about the direction of motion. This also determines the orientation of the phase slip nucleating first inside the potential. The onset to nucleation is signaled by the localization of the superfluid vorticity into two

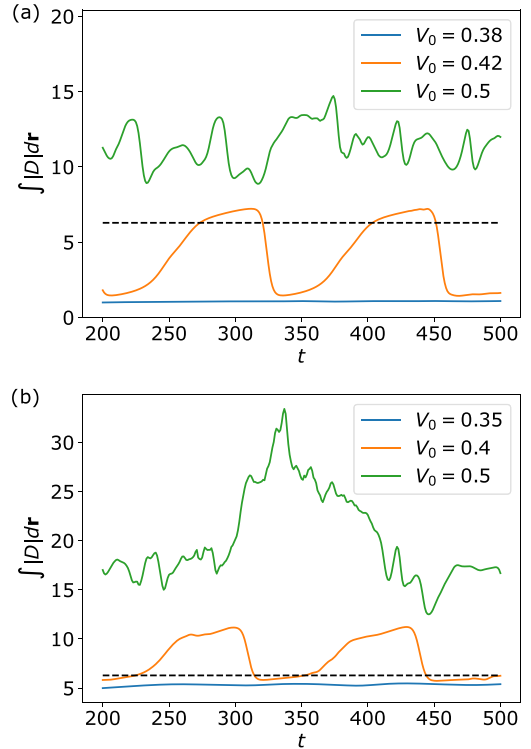


FIG. 7. Net generalized vorticity for soft potential $U_0 = 0.8$ (a) and hard potential $U_0 = 10$ (b) for different V_0 just below (blue), just above (orange), and well above (green) the critical speed. The integral is performed over the area around the potential shown in Figs. 3 and 5. The dotted line is the expected value corresponding to a single vortex dipole at the critical speed.

blobs that harbor the dipole of phase slips. While this process of acquiring a finite core occurs inside the potential, the actual nucleation is manifested into the condensate by the shedding of the vortex dipole.

In addition, for the hard potential, the D field localizes around the rim, signaling the presence of a ghost dipole of phase slips forming near and above the critical velocity. This ghost dipole is pinned to obstacle and aligns perpendicular to the stirring direction. Above the critical velocity an additional dipole of phase slips develops at the onset of nucleation and the previous ghost dipole is quickly migrating where vorticity localizes into vortex cores.

The superfluid vorticity current $\mathbf{J}^{(D)}$ plays an important role during the process of acquiring a core since it develops the vortex cores harboring phase slips. It also controls the vortex kinematics and thus is the quantity that dictates the shedding direction and frequency. From the general relation to this current density, we derive closed expressions for the vortex velocity depending on phase gradients and density disturbances. It is worth noting that the Halperin-Mazenko formalism may be extended also to analyzing experimental

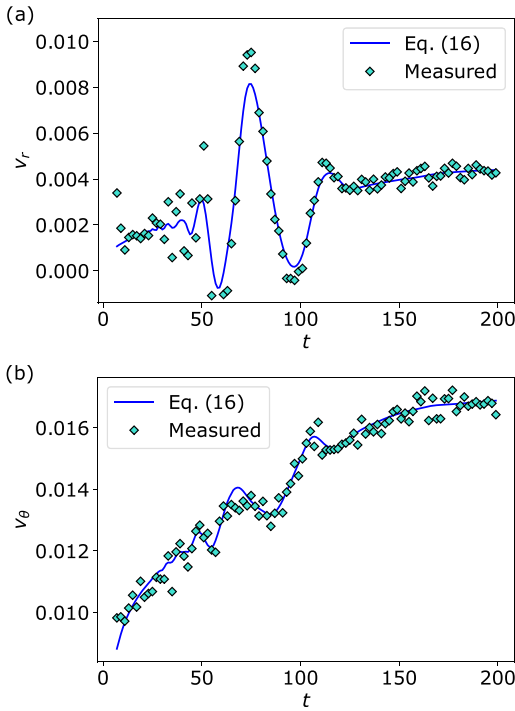


FIG. 8. (a) Radial velocity component v_r , and (b) angular velocity component v_θ of a single vortex in a harmonic potential with $R_{rf} = 60$ obtained from Eq. (16) (blue line) and from tracking the position of the defect (turquoise diamonds). The thermal drag is set to $\gamma = 0.05$.

data and identifying different types of condensate disturbances.

ACKNOWLEDGMENTS

We are grateful to Vidar Skogvoll, Marco Salvalaglio, and Jorge Viñals for many fruitful discussions.

APPENDIX

Here we derive the expression of the defect density current,

$$\mathbf{J}^{(\rho_v)}(\mathbf{r}, t) = \mathbf{J}^{(D)}(\mathbf{r}, t)\delta^2(\vec{\Psi}),$$

where $\delta^2(\vec{\Psi}) = \delta(\Psi_1)\delta(\Psi_2)$. We first start by multiplying Eq. (12) with $\delta^2(\vec{\Psi})$,

$$\begin{aligned} \delta^2(\vec{\Psi})\partial_t D &= -(\partial_i J_i^{(D)})\delta^2(\vec{\Psi}) \\ \partial_t \rho_v - D\partial_t \delta^2(\vec{\Psi}) &= -\partial_i (J_i^{(D)}\delta^2(\vec{\Psi})) + J_i^{(D)}\partial_i \delta^2(\vec{\Psi}), \end{aligned} \quad (A1)$$

where the last term on the right-hand side can be expressed as

$$\begin{aligned} J_i^{(D)}\partial_i \delta^2(\vec{\Psi}) &= \epsilon_{ij}\epsilon_{kl}\partial_j \Psi_k \partial_l \Psi_i \Psi_m \frac{d}{d\Psi_m} \delta^2(\vec{\Psi}) \\ &= \epsilon_{kl}(\epsilon_{ij}\partial_i \Psi_m \partial_j \Psi_k)\partial_l \Psi_i \frac{d}{d\Psi_m} \delta^2(\vec{\Psi}). \end{aligned} \quad (A2)$$

Note that ∂_j and ∂_i acting on the same $\vec{\Psi}$ component lead to a vanishing term due to the Levi-Civita tensor. Thus the only nonzero contributions contain $D = \epsilon_{ij}\partial_j \Psi_1 \partial_i \Psi_2$ and therefore

$$J_i^{(D)}\partial_i \delta^2(\vec{\Psi}) = -D\partial_t \delta^2(\vec{\Psi}). \quad (A3)$$

Inserting this into Eq. (A1), we arrive at

$$\partial_t \rho_v = -\partial_i (J_i^{(D)}\delta^2(\vec{\Psi})),$$

from which the current density of ρ_v follows.

[1] P. G. de Gennes, *The Physics of Liquid Crystals*, 2nd ed., The International Series of Monographs on Physics Vol. 83 (Clarendon Press, Oxford, 1993).
 [2] P. Poulin, H. Stark, T. Lubensky, and D. Weitz, Novel colloidal interactions in anisotropic fluids, *Science* **275**, 1770 (1997).
 [3] F. C. Frank, The influence of dislocations on crystal growth, *Discuss. Faraday Soc.* **5**, 48 (1949).
 [4] A. Skaugen, L. Angheluta, and J. Viñals, Dislocation dynamics and crystal plasticity in the phase-field crystal model, *Phys. Rev. B* **97**, 054113 (2018).
 [5] V. Skogvoll, L. Angheluta, A. Skaugen, M. Salvalaglio, and J. Viñals, A phase field crystal theory of the kinematics of dislocation lines, *J. Mech. Phys. Solids* **166**, 104932 (2022).
 [6] S. P. Thampi, R. Golestanian, and J. M. Yeomans, Vorticity, defects and correlations in active turbulence, *Philos. Trans. R. Soc. A* **372**, 20130366 (2014).
 [7] A. Doostmohammadi, T. N. Shendruk, K. Thijssen, and J. M. Yeomans, Onset of meso-scale turbulence in active nematics, *Nat. Commun.* **8**, 15326 (2017).
 [8] A. Amiri, R. Mueller, and A. Doostmohammadi, Unifying polar and nematic active matter: Emergence and co-existence of

half-integer and full-integer topological defects, *J. Phys. A: Math. Theor.* **55**, 094002 (2022).
 [9] W. F. Vinen, The detection of single quanta of circulation in liquid helium II, *Proc. R. Soc. London A* **260**, 218 (1961).
 [10] I. M. Khalatnikov, *Theory of Superfluidity (Frontiers in Physics)* (W. A. Benjamin, New York, 1965).
 [11] A. Skaugen and L. Angheluta, Vortex clustering and universal scaling laws in two-dimensional quantum turbulence, *Phys. Rev. E* **93**, 032106 (2016).
 [12] R. Durrer, M. Kunz, and A. Melchiorri, Cosmic structure formation with topological defects, *Phys. Rep.* **364**, 1 (2002).
 [13] A. J. Bray, Theory of phase-ordering kinetics, *Adv. Phys.* **51**, 481 (2002).
 [14] P. G. Kevrekidis, D. J. Frantzeskakis, and R. Carretero-González, *Emergent Nonlinear Phenomena in Bose-Einstein Condensates: Theory and Experiment* (Springer Science & Business Media, 2007), Vol. 45.
 [15] J. R. Abo-Shaer, C. Raman, J. M. Vogels, and W. Ketterle, Observation of vortex lattices in Bose-Einstein condensates, *Science* **292**, 476 (2001).

- [16] A. L. Fetter and A. A. Svidzinsky, Vortices in a trapped dilute Bose-Einstein condensate, *J. Phys.: Condens. Matter* **13**, R135 (2001).
- [17] A. L. Fetter, Rotating trapped Bose-Einstein condensates, *Rev. Mod. Phys.* **81**, 647 (2009).
- [18] C. Raman, M. Köhl, R. Onofrio, D. S. Durfee, C. E. Kuklewicz, Z. Hadzibabic, and W. Ketterle, Evidence for a Critical Velocity in a Bose-Einstein Condensed Gas, *Phys. Rev. Lett.* **83**, 2502 (1999).
- [19] R. Onofrio, C. Raman, J. M. Vogels, J. R. Abo-Shaeer, A. P. Chikkatur, and W. Ketterle, Observation of Superfluid Flow in a Bose-Einstein Condensed Gas, *Phys. Rev. Lett.* **85**, 2228 (2000).
- [20] W. Weimer, K. Morgener, V. P. Singh, J. Siegl, K. Hueck, N. Luick, L. Mathey, and H. Moritz, Critical Velocity in the BEC-BCS Crossover, *Phys. Rev. Lett.* **114**, 095301 (2015).
- [21] W. J. Kwon, G. Moon, S. W. Seo, and Y.-i. Shin, Critical velocity for vortex shedding in a Bose-Einstein condensate, *Phys. Rev. A* **91**, 053615 (2015).
- [22] T. W. Neely, E. C. Samson, A. S. Bradley, M. J. Davis, and B. P. Anderson, Observation of Vortex Dipoles in an Oblate Bose-Einstein Condensate, *Phys. Rev. Lett.* **104**, 160401 (2010).
- [23] I. Coddington, P. Engels, V. Schweikhard, and E. A. Cornell, Observation of Tkachenko Oscillations in Rapidly Rotating Bose-Einstein Condensates, *Phys. Rev. Lett.* **91**, 100402 (2003).
- [24] D. Butts and D. Rokhsar, Predicted signatures of rotating Bose-Einstein condensates, *Nature (London)* **397**, 327 (1999).
- [25] G. M. Kavoulakis, B. Mottelson, and C. J. Pethick, Weakly interacting Bose-Einstein condensates under rotation, *Phys. Rev. A* **62**, 063605 (2000).
- [26] A. A. Penckwitt, R. J. Ballagh, and C. W. Gardiner, Nucleation, Growth, and Stabilization of Bose-Einstein Condensate Vortex Lattices, *Phys. Rev. Lett.* **89**, 260402 (2002).
- [27] C. Josslerand, Y. Pomeau, and S. Rica, Cavitation versus Vortex Nucleation in a Superfluid Model, *Phys. Rev. Lett.* **75**, 3150 (1995).
- [28] A. C. Newell and Y. Pomeau, Phase diffusion and phase propagation: Interesting connections, *Physica D* **87**, 216 (1995).
- [29] M. Crescimanno, C. G. Koay, R. Peterson, and R. Walsworth, Analytical estimate of the critical velocity for vortex pair creation in trapped Bose condensates, *Phys. Rev. A* **62**, 063612 (2000).
- [30] T. Aoi, T. Kadokura, T. Kishimoto, and H. Saito, Controlled Generation and Manipulation of Vortex Dipoles in a Bose-Einstein Condensate, *Phys. Rev. X* **1**, 021003 (2011).
- [31] M. Kunimi and Y. Kato, Metastability, excitations, fluctuations, and multiple-swallowtail structures of a superfluid in a Bose-Einstein condensate in the presence of a uniformly moving defect, *Phys. Rev. A* **91**, 053608 (2015).
- [32] K. Sasaki, N. Suzuki, and H. Saito, Bénard-von Kármán Vortex Street in a Bose-Einstein Condensate, *Phys. Rev. Lett.* **104**, 150404 (2010).
- [33] M. T. Reeves, T. P. Billam, B. P. Anderson, and A. S. Bradley, Identifying a Superfluid Reynolds Number via Dynamical Similarity, *Phys. Rev. Lett.* **114**, 155302 (2015).
- [34] W. J. Kwon, J. H. Kim, S. W. Seo, and Y.-i. Shin, Observation of von Kármán Vortex Street in an Atomic Superfluid Gas, *Phys. Rev. Lett.* **117**, 245301 (2016).
- [35] H. Kwak, J. H. Jung, and Y.-i. Shin, Minimum critical velocity of a Gaussian obstacle in a Bose-Einstein condensate, *Phys. Rev. A* **107**, 023310 (2022).
- [36] T. W. Neely, A. S. Bradley, E. C. Samson, S. J. Rooney, E. M. Wright, K. J. H. Law, R. Carretero-González, P. Kevrekidis, M. Davis, and B. P. Anderson, Characteristics of Two-Dimensional Quantum Turbulence in a Compressible Superfluid, *Phys. Rev. Lett.* **111**, 235301 (2013).
- [37] T. P. Billam, M. T. Reeves, B. P. Anderson, and A. S. Bradley, Onsager-Kraichnan Condensation in Decaying Two-Dimensional Quantum Turbulence, *Phys. Rev. Lett.* **112**, 145301 (2014).
- [38] M. T. Reeves, T. P. Billam, B. P. Anderson, and A. S. Bradley, Inverse Energy Cascade in Forced Two-Dimensional Quantum Turbulence, *Phys. Rev. Lett.* **110**, 104501 (2013).
- [39] A. S. Bradley and B. P. Anderson, Energy Spectra of Vortex Distributions in Two-Dimensional Quantum Turbulence, *Phys. Rev. X* **2**, 041001 (2012).
- [40] X. Yu and A. S. Bradley, Emergent Non-Eulerian Hydrodynamics of Quantum Vortices in Two Dimensions, *Phys. Rev. Lett.* **119**, 185301 (2017).
- [41] G. Hess, Angular momentum of superfluid helium in a rotating cylinder, *Phys. Rev.* **161**, 189 (1967).
- [42] S. Middelkamp, P. Torres, P. Kevrekidis, D. Frantzeskakis, R. Carretero-González, P. Schmelcher, D. Freilich, and D. Hall, Guiding-center dynamics of vortex dipoles in Bose-Einstein condensates, *Phys. Rev. A* **84**, 011605(R) (2011).
- [43] R. Navarro, R. Carretero-González, P. J. Torres, P. G. Kevrekidis, D. J. Frantzeskakis, M. W. Ray, E. Altuntaş, and D. S. Hall, Dynamics of a Few Corotating Vortices in Bose-Einstein Condensates, *Phys. Rev. Lett.* **110**, 225301 (2013).
- [44] A. Skaugen and L. Angheluta, Velocity statistics for nonuniform configurations of point vortices, *Phys. Rev. E* **93**, 042137 (2016).
- [45] A. J. Groszek, D. M. Paganin, K. Helmersson, and T. P. Simula, Motion of vortices in inhomogeneous Bose-Einstein condensates, *Phys. Rev. A* **97**, 023617 (2018).
- [46] B. Halperin, published in *Physics of Defects, Proceedings of Les Houches*, Session XXXV, 1980 NATO ASI, edited by Balian, Kléman, and Poirier (North Holland, Amsterdam, 1981).
- [47] G. F. Mazenko, Vortex Velocities in the O(n) Symmetric Time-Dependent Ginzburg-Landau Model, *Phys. Rev. Lett.* **78**, 401 (1997).
- [48] G. F. Mazenko, Defect statistics in the two-dimensional complex Ginzburg-Landau model, *Phys. Rev. E* **64**, 016110 (2001).
- [49] L. Angheluta, Z. Chen, M. C. Marchetti, and M. J. Bowick, The role of fluid flow in the dynamics of active nematic defects, *New J. Phys.* **23**, 033009 (2021).
- [50] B. H. Andersen, J. Renaud, J. Rønning, L. Angheluta, and A. Doostmohammadi, Symmetry-breaking transition between defect-free and defect-laden turbulence in polar active matter, arXiv:2209.10916.
- [51] C. D. Schimming and J. Viñals, Singularity identification for the characterization of topology, geometry, and motion of nematic disclination lines, *Soft Matter* **18**, 2234 (2022).
- [52] A. Vilhois, D. Proment, and G. Krstulovic, Universal and nonuniversal aspects of vortex reconnections in superfluids, *Phys. Rev. Fluids* **2**, 044701 (2017).

- [53] L. Pismen, *Vortices in Nonlinear Fields: From Liquid Crystals to Superfluids, From Non-Equilibrium Patterns to Cosmic Strings* (Oxford University Press, Oxford, 1999).
- [54] V. Skogvoll, J. Rønning, M. Salvalaglio, and L. Angheluta, A unified field theory of topological defects and non-linear local excitations, [arXiv:2302.03035](https://arxiv.org/abs/2302.03035).
- [55] C. Gardiner and M. Davis, The stochastic Gross–Pitaevskii equation: II, *J. Phys. B: At., Mol. Opt. Phys.* **36**, 4731 (2003).
- [56] J. Rønning, A. Skaugen, E. Hernández-García, C. López, and L. Angheluta, Classical analogies for the force acting on an impurity in a Bose-Einstein condensate, *New J. Phys.* **22**, 073018 (2020).
- [57] J. H. Kim, W. J. Kwon, and Y.-i. Shin, Role of thermal friction in relaxation of turbulent Bose-Einstein condensates, *Phys. Rev. A* **94**, 033612 (2016).
- [58] A. Skaugen and L. Angheluta, Origin of the inverse energy cascade in two-dimensional quantum turbulence, *Phys. Rev. E* **95**, 052144 (2017).
- [59] O. Törnkvist and E. Schröder, Vortex Dynamics in Dissipative Systems, *Phys. Rev. Lett.* **78**, 1908 (1997).
- [60] O. R. Stockdale, M. T. Reeves, X. Yu, G. Gauthier, K. Goddard-Lee, W. P. Bowen, T. W. Neely, and M. J. Davis, Universal dynamics in the expansion of vortex clusters in a dissipative two-dimensional superfluid, *Phys. Rev. Res.* **2**, 033138 (2020).

Paper IV

A unified field theory of topological defects and non-linear local excitations

Vidar Skogvol, Jonas Rønning, Marco Salvalagli, Luiza Anghe-luta

ARTICLE OPEN



A unified field theory of topological defects and non-linear local excitations

Vidar Skogvoll ^{1,✉}, Jonas Rønning ¹, Marco Salvalaglio ^{2,3} and Luiza Angheluta¹

Topological defects and smooth excitations determine the properties of systems showing collective order. We introduce a generic non-singular field theory that comprehensively describes defects and excitations in systems with $O(n)$ broken rotational symmetry. Within this formalism, we explore fast events, such as defect nucleation/annihilation and dynamical phase transitions where the interplay between topological defects and non-linear excitations is particularly important. To highlight its versatility, we apply this formalism in the context of Bose-Einstein condensates, active nematics, and crystal lattices.

npj Computational Materials (2023)9:122; <https://doi.org/10.1038/s41524-023-01077-6>

INTRODUCTION

Topological defects are hallmarks of systems exhibiting collective order. They are widely encountered from condensed matter, including biological systems, to elementary particles, and the very early Universe^{1–8}. The small-scale dynamics of interacting topological defects are crucial for the emergence of large-scale non-equilibrium phenomena, such as quantum turbulence in superfluids⁹, spontaneous flows in active matter¹⁰, or dislocation plasticity in crystals¹¹. In fact, classical discrete modeling approaches such as point vortex models¹² and discrete dislocation dynamics¹³ describe turbulence and plasticity in terms of the collective dynamics of topological defects as interacting charged points (in 2D) or line defects (in 3D). In most of these theories, the interactions of topological defects are modeled through the linear excitations that they induce in the far fields. The physics of events on short time- and length scales, such as core energies, nucleation conditions, defect interaction, etc., are often introduced by ad-hoc rules, such as cut-off parameters, Schmidt stress nucleation criteria, and defect line recombination rules. However, the dynamics of these events play a vital role in the transitions between different dynamical regimes. This is the case, for example, in stirred Bose-Einstein condensates where different superfluid flow regimes are observed depending on the size and speed of the moving obstacle^{14–19}, and where there is a subtle interplay between vortices and shock waves. Active nematic fluids are characterized by a dynamic transition to active turbulence at a sufficiently large activity where the spontaneous flows are sustained by the creation and annihilation of orientational defects^{20,21}. During plastic deformation of polycrystals, grains are progressively fragmented, a process governed by the nucleation and patterning of dislocations²². A number of macroscopic criteria exist for the nucleation of topological defects in crystals^{23–25}. Due to the highly non-linear nature of this process, however, it still remains poorly understood.

In this paper, we present a formalism to describe the evolution of ordered systems from the dynamics of their topological defects and their interactions with smooth but localized excitations. The versatility of the approach allows us to gain insight into defect annihilation, the onset of collective behavior, and perspectives on defect structures. In particular, we apply the method to systems of

increasing topological and dynamical complexity. First, we study the motion of isolated vortices in Bose-Einstein condensates, which, in addition to confirming that the method correctly identifies topological defects and their velocities, sheds light on changes in quantum pressure arising from the interplay between phase slips and shock waves. For active nematics, we observe that the onset of active turbulence as a melting of periodic arches is signaled by the formation of bound dipoles of nematic defects at the core of dislocations in the nematic arches. Similarly, bound dipoles of phase slips are also associated with the nucleation of dislocations in a crystal lattice.

The proposed approach builds upon the classical method introduced by Halperin and Mazenko (hereafter called the HM-method)^{26,27} to track and derive analytical results for topological defects. Therefore, in the section “Classical description of topological defects”, we begin with preliminary details of homotopy theory for topological defects and how the HM-method can be used for $O(n)$ -symmetric theories to track their location and kinematics. In the section “Non-singular defect fields”, we then develop a non-singular field theory as a generalization of the HM-method which constitutes our primary reduced defect field. The method is then applied to the aforementioned physical systems in the sections “Defect annihilation: vortices in Bose-Einstein condensates”, “Onset of collective behavior: active nematics”, and “Defect structures: solid crystals”. For the sake of readability, a rigorous derivation of the theoretical framework for arbitrary dimensions and details of the numerical simulations are reported in the Supplementary Notes. Conclusions and perspectives for further study are outlined in the section “Discussion”.

Classical description of topological defects

Collective order is typically described by an order parameter field representative of symmetries and carrying information about topological defects and smooth, localized excitations. Although the order parameters are well-established for conventional systems, one often needs to define them for more exotic systems^{28,29}. In this paper, we focus on well-known order parameters for systems with broken $O(n)$ rotational symmetries, where n is the intrinsic dimension of the order parameter.

¹PoreLab, Njord Centre, Department of Physics, University of Oslo, P. O. Box 1048, 0316 Oslo, Norway. ²Institute of Scientific Computing, TU Dresden, 01062 Dresden, Germany.

³Dresden Center for Computational Materials Science, TU Dresden, 01062 Dresden, Germany. ✉email: vidarsko@uio.no

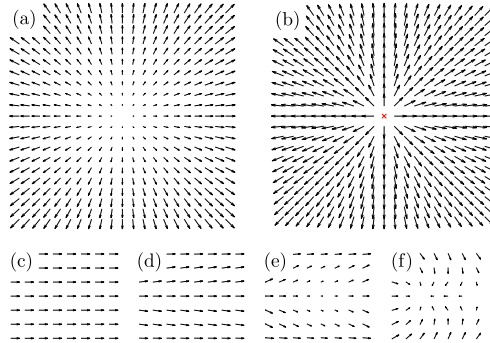


Fig. 1 Different types of excitations in a 2D vector field theory. **a** +1 defect is shown in **a** the order parameter field Ψ and **b** in the unit vector field $\mathbf{u} = \Psi/|\Psi|$. Excitations of **c** the ground state can be categorized into **d** linear excitations with variations in the orientation of Ψ , **(e)** local non-linear excitations for which also the magnitude $|\Psi|$ varies and **f** topological defects.

Homotopy theory provides a valuable identification and classification of topological defects¹. The fundamental idea of homotopy theory is that the order parameter can be mapped onto a particular topological space R and the homotopy group of R classify topological defects. For example, in the XY -model of ferromagnetism, and more generally for any system with $O(2)$ broken symmetry, the order parameter is mapped by a 2D unit vector \mathbf{u} onto $R = S^1$, the unit circle. On S^1 , we may define classes of closed circuits (loops), where loops of the same class are homotopic, i.e., they can be continuously deformed into each other. These classes, together with an appropriate binary operation, define the homotopy group of S^1 . This group is isomorphic to \mathbb{Z} under addition since the difference between two loops that are not homotopic is how many times they have looped around the circle S^1 . Therefore, in regions of space where \mathbf{u} is continuous and well-defined, a closed circuit $\partial\mathcal{M}$ in real space corresponds to a closed circuit in S^1 , and the topological charge s_{top} contained in $\partial\mathcal{M}$ is given as an integer by the isomorphism between homotopy group of S^1 and \mathbb{Z} . This topological charge is obtained from $\mathbf{u} = (\cos\theta, \sin\theta)$, by the contour integral

$$s_{\text{top}} = \frac{1}{2\pi} \oint_{\partial\mathcal{M}} d\theta, \quad (1)$$

which is invariant under any smooth deformations of $\partial\mathcal{M}$. This also implies that by shrinking $\partial\mathcal{M}$ down to a point and given that s_{top} is a constant, there must be regions inside $\partial\mathcal{M}$ where \mathbf{u} is undefined. These are the topological defects that have a s_{top} charge. Therefore, topological defects for $R = S^1$ in 2D are points with their charge determined by corresponding loop integration. On the other hand, such topological defects (with $R = S^1$) in three dimensions are lines.

In field theories of symmetry-breaking transitions, the ground state of the order parameter minimizes a free energy constructed from symmetry considerations. For broken rotational symmetries, the order parameter is a vector field Ψ , which in the ordered (ground) state has a constant magnitude $|\Psi| = \Psi_0$, meaning that the ground state manifold is S^{n-1} , where n is the number of components of Ψ . The link between the order parameter Ψ , and 2D unit vector (director) field $\mathbf{u} \in S^1$ is given by $\mathbf{u} = \Psi/|\Psi|$ and topological defects are located at positions where \mathbf{u} is undefined, which corresponds to $|\Psi| = 0$ as shown in Fig. 1a, b.

A description of topological defects as zeros of order parameters in $O(n)$ models and their kinematics was proposed originally by Halperin and Mazenko in the context of phase-ordering kinetics^{26,27} and extended to systems driven out of equilibrium, such as in stirred Bose-Einstein condensation^{18,30,31},

active nematics^{32,33}, and deformed crystals^{34–36}. Sticking to $O(2)$ -symmetry in two dimensions and using the definition of a topological charge given in Eq. (1), it is possible to express the topological defect density in terms of the zeros of the order parameter Ψ ²⁶ tracked by Dirac-delta functions as

$$\rho_{\text{top}}(\mathbf{r}) \equiv \sum_a q_a \delta^{(2)}(\mathbf{r} - \mathbf{r}_a) = D(\mathbf{r}) \delta^{(2)}(\Psi), \quad (2)$$

where q_a and \mathbf{r}_a are, respectively, the charge and position of the topological defect a , $\delta^{(2)}(\Psi) = \delta(\Psi_1)\delta(\Psi_2)$, and $D(\mathbf{r})$ is the (signed) Jacobian determinant of the map Ψ ,

$$D = \frac{\partial(\Psi_1, \Psi_2)}{\partial(x, y)} = \partial_x \Psi_1 \partial_y \Psi_2 - \partial_x \Psi_2 \partial_y \Psi_1 \\ = \frac{1}{2} \epsilon^{ij} \tilde{\epsilon}^{mn} (\partial_i \Psi_m) (\partial_j \Psi_n), \quad (3)$$

where ϵ^{ij} are the components of the Levi-Civita tensor in real space. The Levi-Civita tensor $\tilde{\epsilon}$ in order parameter space is written with a tilde to emphasize that it is contracted with the order parameter Ψ . In the Cartesian space, both ϵ and $\tilde{\epsilon}$ are simply the Levi-Civita (permutation) symbols. Note that Eq. (2) is the usual scaling property of the delta function taking Ψ as input, apart from the sign of D carrying information of the charge q_a of the topological defects. This result was shown in ref. ²⁶ by considering as explicit ansatz a negative point defect, but can, in general, be justified using differential forms. Nominally, the D field in Eq. (3) is evaluated at the location of the defect only, because of the δ -function in Eq. (2).

RESULTS

Non-singular defect fields

The δ -function in the topological charge density of Eq. (2) locates the topological defects at singular points where \mathbf{u} is undefined. In $O(2)$ models, however, even though the ground state manifold is S^1 , the topological excitations have a finite core over which the magnitude of the order parameter goes smoothly to zero. This feature is also seen in physical systems, for instance, in liquid crystals, where optical retardance is an order parameter that goes to zero at the core. This has been used to quantify the size and structure of the defect cores in liquid crystals³⁷. Motivated by this, we seek to generalize Eq. (2) in a way that will avoid singularities in the resulting charge density.

Since the equilibrium value Ψ_0 of $|\Psi|$ is constant, the order parameter effectively resides in D^2 , the unit disk. We propose in this paper that the simplest generalization of s_{top} is to consider the relative area of D^2 swept by Ψ on the circuit $\partial\mathcal{M}$. During an

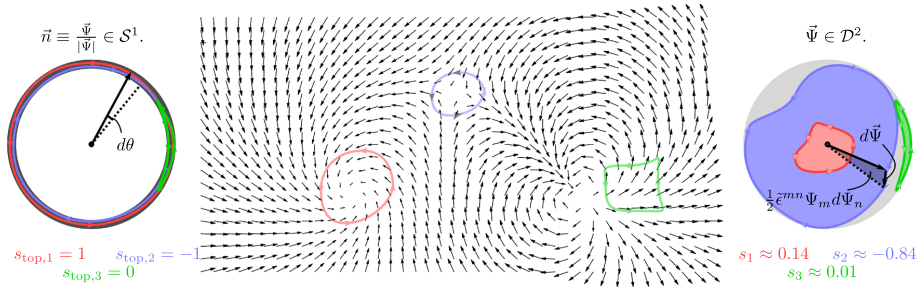


Fig. 2 A continuous field $\Psi(r)$ containing defects with integer charges $+1$, -1 , and $+2$. The net integer topological charge contained in the circuits is given by the winding number of the unit vector field u in S^1 . The (signed) relative area gives the value of s for the circuits spanned by the order parameter Ψ in D^2 .

infinitesimal displacement along $\partial\mathcal{M}$, Ψ sweeps the infinitesimal area given by half of the parallelogram spanned by Ψ and $d\Psi$. This (signed) area is given by $\frac{1}{2}\epsilon^{mn}\Psi_m d\Psi_n$, see Fig. 2. The complete area of D^2 is $\pi\Psi_0^2$, and we define the charge s as the area swept by Ψ relative to the area of D^2 ,

$$s = \frac{1}{\pi\Psi_0^2} \oint_{\partial\mathcal{M}} \frac{1}{2}\epsilon^{mn}\Psi_m d\Psi_n, \tag{4}$$

where $\partial\mathcal{M}$ is defined as in Eq. (1). Naming s a “charge” suggests that it satisfies a global conservation law, which we shall prove shortly. The connection between s and s_{top} is made by recognizing that for a path $\partial\mathcal{M}$ in the far field of a topological defect, where $|\Psi| = \Psi_0$, $s = s_{\text{top}}$. To see this, note that if $|\Psi| = \Psi_0$, then the infinitesimal area swept by Ψ is simply $\frac{1}{2}\Psi_0^2 d\theta$, which inserted into Eq. (4) gives Eq. (1). Closer to the core, however, the magnitude $|\Psi|$ decreases and s is no longer an integer, which is why the associated defect density will give information about the core extent. Using Green’s theorem, we get

$$s = \frac{1}{2\pi\Psi_0^2} \oint_{\partial\mathcal{M}} \epsilon^{mn}\Psi_m \partial_k \Psi_n d\ell^k = \int_{\mathcal{M}} d^2r \rho(r), \tag{5}$$

where $\rho(r)$ is the charge density of s , given by

$$\rho(r) = \frac{D(r)}{\pi\Psi_0^2}. \tag{6}$$

Whereas ρ_{top} describes topological defects as point singularities in the physical space, ρ describes topological defects with a finite core size.

The time derivative of Eq. (6) gives a continuity equation

$$\partial_t \rho + \nabla \cdot \mathbf{J} = 0, \tag{7}$$

with the current density determined by the evolution of the order parameter

$$\mathbf{J}^j = -\frac{1}{\pi\Psi_0^2} \epsilon^{ij} \epsilon^{mn} (\partial_t \Psi_m) (\partial_j \Psi_n). \tag{8}$$

Thus, ρ is a globally conserved quantity, and the change in s contained in a circuit $\partial\mathcal{M}$ is given by

$$\partial_t s = \partial_t \int_{\mathcal{M}} d^2r \rho(r) = \int_{\partial\mathcal{M}} \mathbf{J} \cdot d\mathbf{n}, \tag{9}$$

where $d\mathbf{n}$ is an infinitesimal surface area normal to the circuit $\partial\mathcal{M}$. Far away from defects, $|\Psi| = \Psi_0$ and the time evolution of Ψ is carried by its phase $\theta(r, t)$ through $\Psi = \Psi_0(\cos \theta, \sin \theta)$ which can be inserted in Eq. (8) to show that $\mathbf{J} = \mathbf{0}$. This means that linear perturbations of the ground state, which affect the orientation of Ψ only, are not described by the charge density ρ . However, it describes a certain type of local non-linear perturbations, where the magnitude is affected; see Fig. 1c-f. We will exemplify this

distribution in the applications. Due to the standard continuity form of Eq. (7), we can connect it to a velocity field \mathbf{v} through the charge flux $\rho\mathbf{v}$. Equation (7) only determines the current $\rho\mathbf{v}$ up to an unknown divergence free contribution \mathbf{K} , i.e., $\mathbf{v} = \frac{1}{\rho}(\mathbf{J} + \mathbf{K})$, where $\nabla \cdot \mathbf{K} = 0$. However, when $\rho \neq 0$, there exists a unique velocity field $\mathbf{v}^{(\Psi)}$ such that the evolution of Ψ can be written in a generic advection form $\partial_t \Psi + (\mathbf{v}^{(\Psi)} \cdot \nabla) \Psi = 0$, equivalently expressed as

$$\begin{pmatrix} \partial_t \Psi_1 \\ \partial_t \Psi_2 \end{pmatrix} + \begin{pmatrix} \partial_1 \Psi_1 & \partial_2 \Psi_1 \\ \partial_1 \Psi_2 & \partial_2 \Psi_2 \end{pmatrix} \begin{pmatrix} v_1^{(\Psi)} \\ v_2^{(\Psi)} \end{pmatrix} = 0. \tag{10}$$

This equation can be inverted to uniquely determine $\mathbf{v}^{(\Psi)}$ if $\det(\partial_i \Psi_n) = D(r) \neq 0$. To find $\mathbf{v}^{(\Psi)}$ where this condition holds true, i.e., the regions of interest where also $\rho(r) \neq 0$ from Eq. (6), it is then possible to invert Eq. (10). However, it is easier to insert $\partial_t \Psi = -(\mathbf{v}^{(\Psi)} \cdot \nabla) \Psi$ into the expression \mathbf{J}/ρ and see that it is the solution of Eq. (10). Thus, to fix the gauge on \mathbf{v} , we set $\mathbf{K} = 0$ to get $\mathbf{v} = \mathbf{v}^{(\Psi)}$ and find

$$v^j = \frac{J^j}{\rho} = -2 \frac{\epsilon^{ij} \epsilon^{mn} (\partial_t \Psi_m) (\partial_j \Psi_n)}{\epsilon^{ij} \epsilon^{mn} (\partial_i \Psi_m) (\partial_j \Psi_n)}, \tag{11}$$

where it is implied that repeated indices are summed over independently in the numerator and denominator. It should be noted that the velocity \mathbf{v} only describes the velocity of the defect density ρ and is not, in general, the same as the advection velocity of the order parameter. We have only shown that if $\rho \neq 0$ in some region then it is possible to write the evolution of Ψ in this way. If the actual evolution of Ψ is given as the advection \mathbf{v}_D of a density field (i.e., including the term $\Psi \nabla \cdot \mathbf{v}_D$), then $\mathbf{v} \neq \mathbf{v}_D$, because the compressible part of the advection will not directly translate into the motion of topological defects. However, if a localized topological defect moves without changing its core structure, i.e., with a frozen core, Eq. (11) will give this velocity in the region of the core, which we will show in the section “Defect annihilation: vortices in Bose-Einstein condensates”. While the expression for the current of D and the velocity equation (11) have previously been used in the HM-method, several important distinctions can be highlighted. Firstly, the derivation of the ρ field from the redefined charge, Eq. (6), shows that the field carries topological information and does not only serve as auxiliary transformation determinants of δ -functions. Secondly, the velocity field has previously only been rigorously shown to apply to topological defects. In contrast, this derivation also describes the velocity of ρ for other non-linear excitations. Thirdly, the fixing of the gauge \mathbf{K} has not been adequately addressed in previous works to the authors’ knowledge. While the derivation above was done for a $n = 2$ order parameter in $d = 2$ spatial dimensions for simplicity, topological defects exist whenever $d \geq n$. Equation (4) can be generalized to arbitrary dimensions by replacing the integrand

with the volume of the n -sphere spanned by $\Psi = (\Psi_1, \dots, \Psi_n)$ and normalizing by the volume $V_n \Psi_0^n$ of the n -sphere. We show in the Supplementary Notes the formal derivation, and here we state the result that the charge density becomes

$$\begin{aligned} n = 1: \quad \rho_i &= \frac{\partial_i \Psi}{2\Psi_0} \\ n \geq 2: \quad \rho_{i_1 \dots i_{d-n}} &= \frac{D_{i_1 \dots i_{d-n}}}{V_n \Psi_0^n} \end{aligned} \quad (12)$$

with

$$D_{i_1 \dots i_{d-n}} = \frac{1}{n!} \epsilon^{i_1 \dots i_{d-n} \mu_1 \dots \mu_n} \tilde{\epsilon}^{v_1 \dots v_n} (\partial_{\mu_1} \Psi_{v_1}) \dots (\partial_{\mu_n} \Psi_{v_n}). \quad (13)$$

Generalizing the derivation of the defect kinematics, we find general expressions for the reduced defect velocity field

$$v^{\mu_i} = -n \frac{\delta_{v_1}^{i_1} \delta_{v_2}^{i_2} \dots \delta_{v_n}^{i_n} (\partial_{\mu_1} \Psi_{v_1}) (\partial_{\mu_2} \Psi_{v_2}) \dots (\partial_{\mu_n} \Psi_{v_n})}{\delta_{v_1}^{i_1} \delta_{v_2}^{i_2} \dots \delta_{v_n}^{i_n} \prod_{l=1}^n (\partial_{\mu_l} \Psi_{v_l}) (\partial_{\mu_l} \Psi_{v_l})}, \quad (14)$$

$$\text{Special case } n = d: \quad v^{\mu_i} = -n \frac{\epsilon^{\mu_1 \mu_2 \dots \mu_n} \tilde{\epsilon}^{v_1 \dots v_n} (\partial_{\mu_1} \Psi_{v_1}) \dots (\partial_{\mu_n} \Psi_{v_n})}{\epsilon^{\mu_1 \dots \mu_n} \tilde{\epsilon}^{v_1 \dots v_n} \prod_{l=1}^n \partial_{\mu_l} \Psi_{v_l}}, \quad (15)$$

where $[v_1 v_2 \dots v_n]$ is the antisymmetrization over the indices $v_1 v_2 \dots v_n$. Equation (15) is the special case of $n = d$, where the velocity can be written in a simpler way. Still, Eq. (14) looks complicated due to the arbitrary number of dimensions and so we have summarized the most important cases of $n \leq d \leq 3$ in Supplementary Figure 2 of the Supplementary Notes. Thus, Eqs. (12) and (14) are the primary general expressions of the reduced defect field. The equations generalize the description of topological defects in the HM-method to include both topological defects and non-linear excitations.

There are two important notes to be made on the generalization beyond the case $d = n = 2$. Firstly, for $n \geq 2$, the charge density is a rank $(d - n)$ tensor that represents the defect density per n -dimensional volume-oriented *normal* to the manifold, e.g., how the charge density on a 2D surface is expressed in terms of the *normal* vector to the surface. The case of $n = 1$ is special because densities on one-dimensional manifolds are usually expressed in terms of the density *along* the manifold, i.e., the charge density per length *along* the curve. Secondly, in the case of $n < d$, the gauge \mathbf{K} cannot be uniquely determined by looking at the evolution of Ψ alone. Therefore, another condition is required to obtain Eq. (14). This condition implies that topological defects live effectively on a $d - n$ dimensional submanifold and will move perpendicular to this structure, e.g., how the motion of a line defect is given by the velocity normal to its tangent vector. Due to the difference in definitions of the integrals to yield the topological content, this translates to the velocity being parallel to the charge density for $n = 1$ and perpendicular to it for $n \geq 2$. This velocity will be normal to topological structures in the case of topological lines or walls. While the systems of study in this manuscript exhibit ground state manifolds with S^1 symmetries ($n = 2$), the generalization can be directly applied to systems with $n = 1$, where the defect density represents domain walls in interfacial systems such as viscous fingering³⁸, or with $n = 3$, such as the 3D Heisenberg model of ferromagnetism, where the defect density will show emergent magnetic monopoles³⁹. For further discussions, see the Supplementary Notes.

With the method at hand, we study phenomena involving both topological charges and non-linear local excitations through the reduced defect field and the information it conveys, such as the velocity of topological defects. This is done by considering progressively such phenomena in three representative systems with broken $O(2)$ symmetry and featuring increasing complexity in terms of order parameters and collective behaviors. Both system-specific information and general behaviors will be outlined. As a starting point, we consider a Bose-Einstein condensate where the

order parameter is isomorphic to $\Psi \in \mathcal{D}^2$ so that the method can be directly applied.

Defect annihilation: vortices in Bose-Einstein condensates

Within the Gross Pitaevskii theory of a superfluid Bose-Einstein condensate (BEC), the condensed bosons are described by a macroscopic wavefunction ψ , and its evolution can be described by damped Gross Pitaevskii equation^{18,40}

$$i\hbar \partial_t \psi = (1 - i\gamma) \left(-\frac{\hbar^2}{2m} \nabla^2 + g|\psi|^2 - \mu \right) \psi, \quad (16)$$

where g is an effective scattering parameter between condensate atoms, $\gamma > 0$ is an effective thermal damping coefficient and μ is the chemical potential. The complex condensate wavefunction ψ is isomorphic to a real 2D vector order parameter $\Psi = (\Psi_1, \Psi_2)$ through $\psi = \Psi_1 + i\Psi_2$, the norm of which is given by the absolute value $|\psi|$. In the equilibrium ground state, the phase of ψ (and therefore the direction of Ψ) is constant, and the magnitude is given by $|\psi| = \Psi_0 = \sqrt{\mu/g}$. Topological defects in the orientational (unit vector) field correspond to quantized vortices captured by the charge density field

$$\rho^{(\psi)}(\mathbf{r}) = \frac{gD(\mathbf{r})}{\pi\mu}. \quad (17)$$

In this context, the D field (calculated from Ψ) has the physical interpretation of the generalized superfluid vorticity³¹. Linear perturbations of the ground state are phonons, which are characterized by traveling waves in the phase of the order parameter ψ , and will not be signaled in the defect density field ρ . Non-linear local perturbations, e.g., brought on by external stirring potentials or obstacles, will lead to a decrease in the magnitude of the order parameter near the obstacle^{14,16,17,41}, leading to an increase in the quantum pressure, defined as

$$P = -\frac{\hbar^2}{2m} \frac{\nabla^2 |\psi|}{|\psi|}. \quad (18)$$

Such excitations are detected by $\rho^{(\psi)}$, and mediate the nucleation or annihilation of topological defects. To showcase this, we simulate a BEC as dictated by Eq. (16) with an initial condition featuring two vortices at $(x, y) = (\pm 5, 0)$. Numerical details are reported in the “Methods” section. Dimensionless units are defined so that $\hbar = m = g = \mu = 1$ and the damping coefficient is set to $\gamma = 0.1$. Figure 3 illustrates the defect density from Eq. (17) during the fast event of annihilating a vortex with an anti-vortex due to a small thermal drag.

The velocity field from Eq. (14) is plotted close to vortices and shows two exciting features. At the beginning of the simulations ($t = 5$), the non-uniform velocity over the vortex core indicates the early core deformation induced by the initial conditions. After this relaxation, however, vortices retain stationary or rigid cores and consistently feature a uniform velocity. After the annihilation event, we can see traces of their diffusive cores in the excitations produced by the vortex annihilation, as seen by the quantum pressure in the system, which is shown in Fig. 3c. We will see in the following that similar traces appear as precursory patterns for defect nucleation. Moreover, after having dealt with a system with only one broken symmetry, we now consider systems that have multiple rotational or translational symmetries.

Onset of collective behavior: active nematics

In this section, we consider the case of an active nematic system. This system is peculiar as we can construct the defect density from different order parameters. By applying the proposed formalism we can investigate the transition among different regimes and the interplay among defects. Interestingly, we will show that defects in

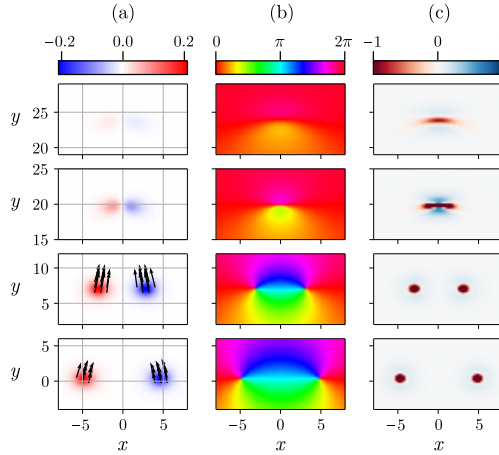


Fig. 3 Annihilation of a vortex dipole in a Bose-Einstein condensate. Snapshots of **a** defect density, **b** condensate phase $\arg(\psi)$, and **c** quantum pressure at different times from bottom to top: at $t = 5$, $t = 60$ (before annihilation), $t = 105$ (after) and $t = 110$. **a** Defect velocity is included prior before annihilation. Notice in **(b)** the large phase gradients after the annihilation due to the induced shock-waves which can also be seen in the **(c)** quantum pressure profiles. The plots in column **(c)** have saturated colorbars because of the singular pressure at the defect core.

one broken symmetry are the nucleation sites of defects for a separate order.

Within the hydrodynamic approach⁴², the nematic orientational order of active matter in two dimensions is described by a rank-2 symmetric and traceless tensor Q determined by the nematic director $\mathbf{n} = (\cos(\theta), \sin(\theta))$

$$Q = S \begin{pmatrix} n_1 n_1 - \frac{1}{2} & n_1 n_2 \\ n_2 n_1 & n_2 n_2 - \frac{1}{2} \end{pmatrix} \equiv \begin{pmatrix} \Psi_1 & \Psi_2 \\ \Psi_2 & -\Psi_1 \end{pmatrix}, \quad (19)$$

where S is an order parameter which is 0 in the disordered phase. Q is thus related to the D^2 order parameter Ψ field by $\Psi = \frac{S}{2}(\cos(2\theta), \sin(2\theta))$. The evolution of the Q -tensor follows dissipative dynamics coupled with an incompressible Stokes flow with substrate friction⁴³. Details on the evolution equation and its numerical method are reported in the “Methods” section. The system is here initialized in a homogeneous nematic phase with small perturbations in the angle of the director field. These perturbations are enhanced by the active stress creating a striped phase that is further destabilized and eventually melts due to the creation of topological defects leading into active turbulence. The ground state corresponds to a constant magnitude $|\Psi| \equiv \Psi_0 = \sqrt{B}/2$ dependent on the parameter B , which is defined in the “Methods” section. Within the framework introduced in the section “Non-singular defect fields”, this gives the following expression for the defect density

$$\rho^{(Q)} = \frac{4D(\mathbf{r})}{\pi B}, \quad (20)$$

which supports orientational defects with half-integer charge $s_{\text{top}} = \pm 1/2$. In Fig. 4a, we show the nematic orientation θ in the colorbar to emphasize the breaking of translational symmetry and the formation of a (transient) striped order. The striped order arises from modulations in the nematic orientation which, to first order, do not change the magnitude of the order parameter Ψ . Thus, these are linear perturbations not signaled by $\rho^{(Q)}$.

The inset of Fig. 4a shows a dislocation in the periodic arches in the nematic director. To describe these defects, we represent the parameter Ψ as a complex field $\psi = |\Psi|e^{i\theta}$ and decompose it into a

slowly-varying amplitude field of the periodic arch mode as

$$\psi(\mathbf{r}) = \psi_0(\mathbf{r}) + \eta_{\mathbf{k}}(\mathbf{r})e^{i\mathbf{k}\cdot\mathbf{r}} + \eta_{-\mathbf{k}}(\mathbf{r})e^{-i\mathbf{k}\cdot\mathbf{r}}, \quad (21)$$

where $\psi_0(\mathbf{r})$, $\eta_{\mathbf{k}}$, $\eta_{-\mathbf{k}}$ are slowly-varying complex fields on the length scale a_0 of the director field modulations. \mathbf{k} is the wave vector of the modulations which is $\mathbf{k} = \frac{2\pi}{a_0}\mathbf{e}_x$ due to the initial condition. We can extract the complex amplitude of a \mathbf{k} mode by a demodulation of ψ ,

$$\eta_{\mathbf{k}} = \langle \psi e^{-i\mathbf{k}\cdot\mathbf{r}} \rangle, \quad (22)$$

through the convolution with a Gaussian kernel denoted by $\langle \cdot \rangle$, which filters out the small-scale variations, Eq. (40). The modulation length scale a_0 and the equilibrium value η_0 of $|\eta_{\mathbf{k}}|$ are found numerically to be $a_0 = 10.6$ and $\eta_0 = 0.20$ for the given parameters. From the order parameter $\eta_{\mathbf{k}}$, we can construct the defect density $\rho^{(\eta_{\mathbf{k}})}$ as for the complex wavefunction in the BEC. This field locates the dislocations from the nematic arches as shown in panel (b) at $t = 240$, just prior to the nucleation of nematic defects.

By also showing the reduced defect field $\rho^{(Q)}$ associated with the rotational symmetry (Fig. 4c), we clearly notice that each dislocation detected by $\rho^{(\eta_{\mathbf{k}})}$ is a source for the nucleation of a dipole of half-integer defects. The precursory pattern of the two bound defects prior to nucleation is similar to the pattern retained by the dipole annihilation in the BEC. However, for active nematics, the bound state is associated with a dislocation in the periodic arches, while for BECs it is a source of quantum pressure. We observe numerically that the melting of the smectic-like arches is mediated by the dissociation of the dislocations into dipoles of $\pm 1/2$ nematic defects. This occurs very fast and simultaneously at various locations, such that the system quickly transitions to active turbulence. Notice also that the core size of the dislocations in the periodic arches is bigger than the core size of the $\pm 1/2$ nematic defects that form in the transition. To quantify such nucleation events, we compute the defect velocity Eq. (11) associated to the charged defect density $\rho^{(Q)}$ which is localized in well-defined blobs of opposite signs around a dislocation as illustrated in Fig. 4b, c. By averaging the speed around these blobs, we can track the defect speed $v = \langle |v| \rangle$ as function of time and show that prior to dissociation, the defects are in a bound state

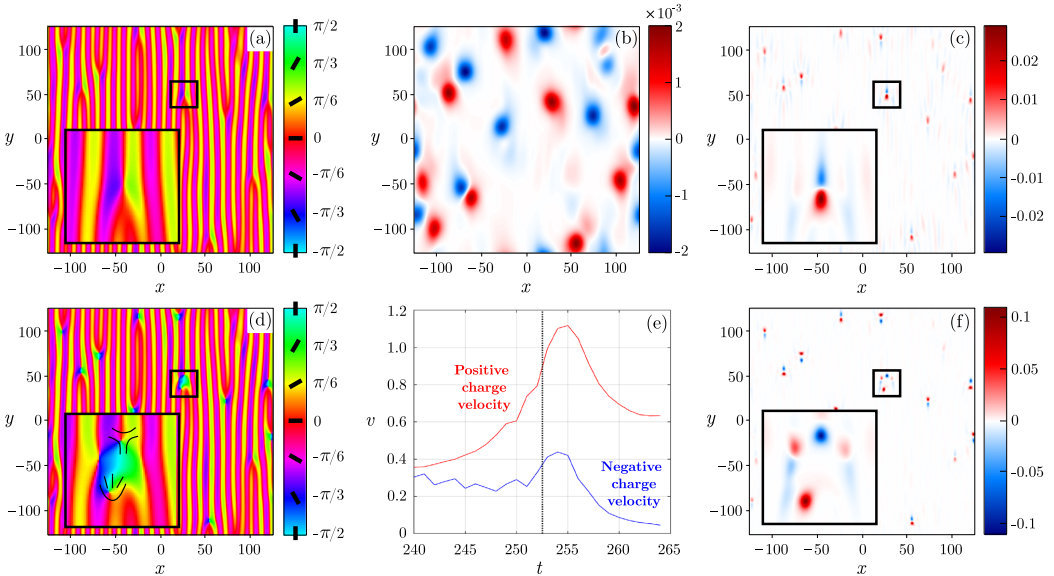


Fig. 4 Onset of active turbulence in a nematic liquid crystal mediated by the nucleation of topological defects. **a** The angle of the nematic director at $t = 240$, prior to nucleation of half-integer defects from the unstable periodic arches, and **d** at $t = 260$, after nucleation. **b** The defect density $\rho^{(nk)}$ at $t = 240$, corresponding to the broken translational symmetry, shows the charge signature of dislocations with large core structures. The dislocation core harbors a bound dipole (inset) shown in **(c)** the defect density $\rho^{(Q)}$ associated to the nematic order at $t = 240$, which splits into fully formed $\pm \frac{1}{2}$ defects after nucleation as shown in **(f)** $\rho^{(Q)}$ at $t = 260$. Panel **(e)** shows the speed $v = \langle |\mathbf{v}| \rangle$ of the two localized blobs in the charged defect density $\rho^{(Q)}$ around the nucleation site. After the nucleation event indicated by the dashed line, these correspond to the speed of the $\pm 1/2$ defects.

while afterwards they move apart as $\pm 1/2$ defects with different speeds as shown in Fig. 4e. Notice that the $-1/2$ defect slows down while the $+1/2$ acquires a net speed related to its self-propulsion.

To summarize this part, our analysis offers an alternative perspective on the onset of active turbulence using the presence of competing symmetries. The transition to a turbulent state from a periodic arch state seems to be mediated by the dissociation of one type of topological defect into a different kind associated with changes in the global symmetries. In the following section, we study a system where the order parameters with $O(n)$ -symmetry are found by decomposing a more complicated topological space.

Defect structures: solid crystals

We focus here on the study of defects and collective order in crystals. The ground state manifold of the crystal can be factorized in fundamental S^1 spaces, which has a straightforward physical interpretation related to the crystal's Bravais reference lattice reflecting the broken translational symmetry. As discussed below, this implies that a dislocation, i.e., a topological defect in the crystal, can be represented by bound vortices in the amplitudes of the fundamental periodic modes. Indeed, by applying the formalism introduced in the section "Non-singular defect fields", analogies with previously discussed systems emerge, as well as peculiar features that will be discussed in detail.

In the conserved Swift-Hohenberg modeling of crystal lattices, commonly named phase-field crystal (PFC)^{44,45}, the order parameter is a weakly distorted periodic scalar field $\psi(\mathbf{r})$, and can be

approximated as

$$\psi(\mathbf{r}) = \bar{\psi} + \sum_{n=1}^N \eta_n e^{i\mathbf{q}^{(n)} \cdot \mathbf{r}}, \quad (23)$$

where $\bar{\psi}$ and $\{\eta_n\}_{n=1}^N$ are slowly varying (on the lattice unit length scale) amplitude fields, and N is the number of reciprocal lattice vectors $\{\mathbf{q}^{(n)}\}_{n=1}^N$ taken into consideration. Disordered or liquid phases are described by $\eta_n(\mathbf{r}) = 0$. For a perfect lattice, $\bar{\psi}(\mathbf{r}) = \psi_0$ and $\eta_n(\mathbf{r}) = \eta_0$ are constant, and an affine displacement $\mathbf{r} \rightarrow \mathbf{r} - \mathbf{u}$ amounts to a phase change $\eta_n = \eta_0 e^{-\mathbf{q}^{(n)} \cdot \mathbf{u}}$. The displacement field \mathbf{u} supports dislocations, which are line topological defects. For a path $\partial\mathcal{M}$ in real space circling one dislocation, the charge is given by the vector difference between the end and starting point, namely the Burgers' vector \mathbf{b} ,

$$\oint_{\partial\mathcal{M}} d\mathbf{u} = -\mathbf{b}, \quad (24)$$

(minus sign by convention). The corresponding dislocation density tensor a_{ij} is defined through the integral of some 2D surface \mathcal{M} bounded by $\partial\mathcal{M}$

$$\int_{\mathcal{M}} a_{ij} n^i dS = b_j, \quad (25)$$

where \mathbf{n} is the normal vector to the surface element dS . By multiplying Eq. (24) with a reciprocal lattice vector $\mathbf{q}^{(n)}$ of the structure, we get

$$\oint_{\partial\mathcal{M}} d(\mathbf{q}^{(n)} \cdot \mathbf{u}) = -2\pi s_n, \quad (26)$$

where s_n is an integer by definition of the reciprocal lattice vector. This shows that the phase of an amplitude $\theta_n \equiv (-\mathbf{q}^{(n)} \cdot \mathbf{u})$ is a

topological order parameter that has integer winding numbers, i.e., $\theta_n \in \mathbb{S}^1$.

The amplitude η_n acts as an order parameter in \mathcal{D}^2 , i.e., $\Psi^{(n)} = \Re(\eta_n)$ and $\Psi_2^{(n)} = \Im(\eta_n)$. A topological description of dislocations using the HM-framework has been provided in two and three dimensions in refs. 34,36. Here, we adopt an alternative and convenient description using the charge density from Eq. (12), which is a vector field for 3D lattices

$$\rho_i^{(n)} = \frac{D_i^{(n)}}{\pi\Psi_0^2}, \quad (27)$$

where

$$\mathbf{D}^{(n)} = \begin{pmatrix} (\partial_x \Psi_1^{(n)})(\partial_z \Psi_2^{(n)}) - (\partial_y \Psi_2^{(n)})(\partial_z \Psi_1^{(n)}) \\ (\partial_x \Psi_2^{(n)})(\partial_y \Psi_1^{(n)}) - (\partial_x \Psi_1^{(n)})(\partial_z \Psi_2^{(n)}) \\ (\partial_x \Psi_1^{(n)})(\partial_y \Psi_2^{(n)}) - (\partial_x \Psi_2^{(n)})(\partial_y \Psi_1^{(n)}) \end{pmatrix}. \quad (28)$$

By contracting Eq. (25) with q^i , we can relate the dislocation density tensor with the defect charge density in a given amplitude³⁶

$$a_{ij} = \frac{2d}{N\eta_0^2} \sum_{n=1}^N D_i^{(n)} q_j^{(n)}, \quad (29)$$

where d is the spatial dimension. The amplitudes η_n used to calculate $\mathbf{D}^{(n)}$ are extracted from the phase-field ψ as in Eq. (22), and only the modes corresponding to the shortest reciprocal lattice vectors are used to calculate a_{ij} .

Next, we focus on two examples to highlight insights obtained from using this approach. We consider the nucleation of dislocations in a square lattice from the point of view of its precursory pattern formations and quantify the dislocation core size. Then, we consider the classical inclusion problem of a rotated spherical crystal embedded in another crystal with the same lattice symmetry, to show how the surface of the inclusion changes its topology as a function of the lattice misorientation.

Dislocations in 2D square lattices. A minimal PFC free energy which can be minimized by a square lattice reads^{46,47}

$$F_\psi^{\text{sq}} = \int d^2r \left(\frac{1}{2} (\mathcal{L}_1 \mathcal{L}_2 \psi)^2 + \frac{r}{2} \psi^2 + \frac{1}{4} \psi^4 \right), \quad (30)$$

where $\mathcal{L}_X = X + \nabla^2$ and r is a parameter. We recall that PFC energy functionals describe order–disorder (solid–liquid) phase transitions. The minimizer field ψ of (30), for certain model parameters, has a perfect square lattice symmetry with an accurate two-mode amplitude expansion

$$\psi = \bar{\psi} + \sum_{n=1}^2 \eta_n e^{i\mathbf{q}^{(n)} \cdot \mathbf{r}} + \sum_{n=3}^4 \eta_n e^{i\mathbf{q}^{(n)} \cdot \mathbf{r}} + \text{c.c.}, \quad (31)$$

where $\{\mathbf{q}^{(n)}\} = \{(1, 0), (0, 1), (1, 1), (1, -1)\}$ are the reciprocal lattice vectors of the square lattice with lengths 1 and $\sqrt{2}$. This sets the characteristic length $a_0 = 2\pi$ of the system, which is the width of the square unit cell. At equilibrium, the amplitude field η_n goes to the equilibrium values $\eta_{1,2} \rightarrow A_{\text{sq}}, \eta_{3,4} \rightarrow B_{\text{sq}}$. The characteristic unit of stress is given by the elastic shear modulus $\mu = 16B_{\text{sq}}^2$ ⁴⁷. The dislocation density tensor can be factorized as $a_{ij} = t_i \mathcal{B}_{ij}$, where \mathcal{B} is a 2D Burgers vector density and \mathbf{t} the tangent vector to the dislocation line. In two dimensions, we define \mathbf{t} to point out-of-plane so that the Burgers vector density is given by

$$\mathcal{B} = (a_{31}, a_{32}), \quad (32)$$

where a_{ij} can be computed by using $\mathbf{q}^{(1,2)}$. We initiate a perfect square lattice of 101×101 unit cells and use the sHPFC model of ref. 48 to apply a local stress in the central region which causes the nucleation of a dislocation dipole. The PFC deforms gradually, trying to account for the externally imposed stress, increasing

from linear to non-linear strains until nucleation of a pure $\pm a_0 e_x$ dislocation dipole. Once formed, these dislocations move under the action of the Peach-Koehler force⁴⁹, namely they separate at large speeds due to the external stress and slow down as they reach the far-field regions of the crystal. Simulation details are given in the “Methods” section. Figure 5 shows the region of applied stress during the nucleation event. Like for the nucleation of nematic defects, the nucleation is singled by a precursory localized pattern formation in the Burgers vector density, which corresponds to a bound dipole of phase slips. While variations only in the phase of the complex amplitudes are associated with linear elastic perturbations, non-linear elastic strains cause a decrease in the equilibrium value of the amplitudes⁵⁰ and so produce a signal in the reduced defect density given by the expression of the dislocation density. Thus, the excitations visible in the dislocation density \mathcal{B} prior to nucleation are due to non-linear elastic strains. From the signal profile, Fig. 5c, we observe that these large non-linear elastic strains can be connected to a bound dislocation dipole.

From the defect density corresponding to η_1 for $\mathbf{q} = (1, 0)$, we can also determine the average speed $v = \langle |\mathbf{v}| \rangle$ of dislocations with positive and negative charge before and after nucleation. The defect speed as a function of time is shown in Fig. 5e. Like for the nucleation of defects in the active nematic, we observe a speed build up prior to nucleation succeeded by a relaxation to a constant speed. Unlike the $\pm 1/2$ defects in active nematics, however, both dislocations are equally mobile in this case.

The Burgers vector density, in addition to describing the process of nucleation itself, provides us with useful information about the defect core. To extract the core size directly from the Burger vector density without free-tuning parameters, we consider a coarse-grained version of the PFC model, namely its amplitude expansion (APFC)^{51,52}. This approach gives access to phases and lattice deformation directly rather than through the demodulation of Eq. (22). It builds on the definition of a free energy functional F_η derived from the PFC free energy F_ψ^{sq} under the approximation of slowly-varying amplitudes. We simulate a square lattice hosting dislocations in a static, periodic configuration, and focus on a single defect therein. The expression for F_η , the choice of $\mathbf{q}^{(n)}$, and details of the simulation setup are given in the “Methods” section. For the given lattice structure, the extension of its core depends on the parameters r' and s in the free energy F_η . The parameter r' corresponds to a phenomenological temperature controlling a first-order order–disorder phase transition at $r' = r_0$ with r_0 the critical point and ordered (disordered) phase for $r' < r_0$ ($r' > r_0$), and s is a constant scaling the elastic moduli^{53,54}. $\Delta r = r_0 - r'$ is referred to as the quenching depth. These parameters affect the competition among gradient terms and the bulk energy terms in F_η . Figure 6a, b illustrates two different core sizes for the same dislocation obtained with different values for r' and s . They show the reconstructed densities obtained by computing Eq. (23) with the numerical solution for the amplitudes (first column), the Burgers vector density component \mathcal{B}_x (second column), a plot of $\mathcal{B}_x(x, 0)$ and $\mathcal{B}_x(0, y)$ (third column, empty symbols) with Gaussian fits (solid lines). The data fitting is obtained via $G \exp(-x^2/2\sigma_x^2 - y^2/2\sigma_y^2)$ with G , σ_x and σ_y fitting parameters (dashed lines), well reproducing its shape and allowing for an estimation of the core size. The definition here introduced for the Burgers vector density fully characterizes the loss of coherency at the dislocation core. Importantly, it realizes a spreading of the topological charge at the core similar to non-singular continuum theories based either on regularization of singularities⁵⁵ or within strain-gradient elasticity theories^{56,57}.

The amplitude expansion defined in Eq. (23), and thus the density field ψ , correspond to the sum of plane waves (Fourier modes) which are periodic stripe phases similar to the one shown in Fig. 4. The dislocation in the crystal then corresponds to the superposition of defects in such stripe phases. Interestingly,

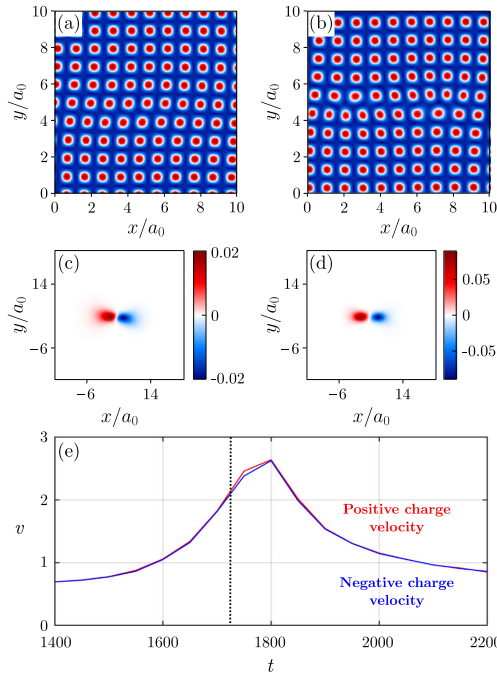


Fig. 5 Nucleation of a dislocation dipole in a square PFC model. **a** The PFC at $t = 1600$ prior to the nucleation of **(b)** a dislocation dipole at $t = 1800$. Panels **(c)** and **(d)** show the x -component B_x of the dislocation density B at $t = 1600$ and $t = 1800$, respectively. The magnitude of B_x is, in both cases, two orders of magnitude smaller and not shown. **e** The average speed $v = \langle |v| \rangle$ at the nucleation site of positive charge ($B_x > 0$) and negative charge ($B_x < 0$) where the dashed line indicates the time of nucleation (see text).

dislocations do not necessarily correspond to a defect for all the coupled stripe phases. Indeed, by applying Eq. (1) to the phase of the amplitudes one gets $-f\mathbf{q}^{(n)} \cdot \mathbf{u} = 2\pi\mathbf{q}^{(n)} \cdot \mathbf{b}$. At least for perfect dislocations, those having a translation vector of the lattice as Burgers vector, we have that $\mathbf{q}^{(n)} \cdot \mathbf{b} = 0$, for some n . Therefore, at the dislocation core, a different ordered phase forms as some amplitudes may have non-singular phases and, in turn, do not vanish. This differs from the case of dislocations forming in pure stripe phases, e.g., in Fig. 4, where the single complex amplitude vanishes, pointing to a disordered phase. In Fig. 6c, the fields $\eta_n e^{i\mathbf{q}^{(n)} \cdot \mathbf{r}}$ entering the sum in Eq. (23) are reported. Three out of four stripe phases ($n = 1, 3, 4$) vanish at the core, while one ($n = 2$) features a small variation of its amplitudes with no topological content.

The defect core can then be interpreted as a transition region between two different ordered phases, one of which is present at the dislocation core only. To explore the analogy with phase interfaces, we compare its extension with the width of a solid-liquid (order-disorder) interface, w , which measures the correlation length for these phases. We find some analogies and differences in the dependence on the parameters entering the free energy. Traveling-wave solutions exist for solid-liquid (order-disorder) interfaces with amplitudes having hyperbolic tangent profiles, $\eta \propto (\eta_0/2)\{1 - \tanh[(x - Vt)/w]\}$ with $w \propto \sqrt{g}/(1 + \sqrt{1 - 8r'/9r_0})$, V the interface velocity along its normal and g a parameter in the free energy which multiplies gradient terms and scales the elastic constants^{54,58,59} (see also “Methods”). For a given set of parameters, we determine the specific amplitude profile and w by fitting the result of numerical calculations with the hyperbolic tangent profile mentioned above for an interface with normal along the

x -axis ($\langle 10 \rangle$ crystallographic direction, further details are reported in the “Methods” section). Measuring the size of the dislocation core through σ_x and σ_y from a Gaussian fit as in Fig. 6a, b, we find that it scales linearly with w when varying g , while a different scaling is observed when varying r' , c.f. Fig. 6d. Here g is an energy scale associated with amplitudes gradients, similar to theories based on Ginzburg-Landau energy functionals⁵⁹. r' , instead, affects the equilibrium values of the amplitudes, which are qualitatively different for an interface, where they all vanish in the disordered phase, and a defect, where some amplitudes are non-zero owing to a non-singular phase (see Fig. 6c). Also, for $r' \neq r_0$, interfaces move, which affects the width w ⁶⁰. A more detailed analysis would require finding a solution for the amplitudes’ profile at defects, which goes beyond the goals of this investigation and will be addressed in future work.

The evaluation of the Burgers vector density also allows for the characterization of anisotropies in the behavior of phases at the core as illustrated in Fig. 6d. $\sigma_y/\sigma_x \approx 0.75$ throughout the whole range of parameters investigated here as also illustrated in Fig. 6e. This may be ascribed to the asymmetry introduced by the specific orientation of the Burgers vector. We conclude that, for systems described by order parameters as in the phase-field crystal model, as well as in descriptions exploited in previous sections, the defect density may be exploited to characterize the loss of coherency at defects.

Order transition for 3D crystal inclusions. Like the melting of translational order in the nematic liquid crystal through the nucleation of defects in the nematic field, the global translational order in a single crystal is also destroyed under large deformations

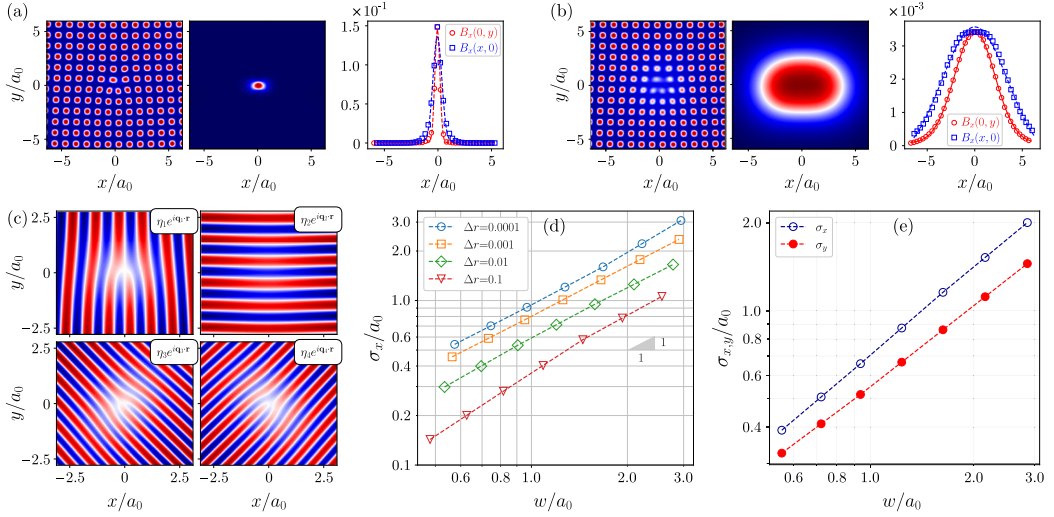


Fig. 6 Dislocation core size near melting by APFC modeling. **a, b** Reconstructed density (left), B_x (center), and B_x along x and y direction for a relatively small and large core size, respectively obtained with **a** $\Delta r = 10^{-4}$, $s = 3.16$ and **b** $\Delta r = 10^{-1}$, $s = 1$, with $r_0 = 7.455 \times 10^{-2}$ the critical point. Symbols show values from APFC simulations; dashed lines correspond to Gaussian fits. The latter are exploited to quantify the size of the core in terms of σ_x and σ_y as a function of the order-disorder correlation length w , for various values of s and r' (the latter shown by different colors and symbols). **c** Periodic modes $\eta_n e^{iq_n r} + c.c.$ for the density in panel **(b)**. **d** Core size in terms of σ_x and σ_y as a function of the variance along x and y , namely σ_x and σ_y . **e** Comparison of σ_x and σ_y as function of w for $\Delta r = 0.00464$ and $s \in [10^{-1}, 3.16]$.

and rotations. To highlight this, we use a full 3D PFC model corresponding to a cubic lattice for which the PFC density in the one-mode approximation reads as

$$\psi(\mathbf{r}) = \psi_0 + \sum_{\mathbf{q} \in \mathcal{R}_{\text{bcc}}^{(1)}} \eta_0 e^{i\mathbf{q}^{(n)} \cdot \mathbf{r}}, \quad (33)$$

where $\mathcal{R}_{\text{bcc}}^{(1)}$ are the reciprocal lattice vectors of the bcc Bravais lattice with unit length⁴⁷. This sets the length of the bcc unit cell as $a_0 = 2\pi\sqrt{2}$. We consider spherical inclusions with radius $17a_0$, rotated at an angle θ_{rot} about the $[1, 1, 1]$ -axis. The initial condition is relaxed by dissipative dynamics with an appropriate symmetry-conserving free energy; see further details in the “Methods” section. We choose three representative angles θ_{rot} and calculate the Frobenius norm $|a| = \sqrt{a^j a_j}$ of a at each angle. Since $|a| > 0$, we plot its isosurface at half its maximum value $|a|_M = \max_r(|a|(\mathbf{r}))$ in Fig. 7 for three representative misorientation angles θ_{rot} . For small lattice misorientations, $|a| \ll 1$, indicating only slight non-linear elastic excitations (and no fully formed dislocations) at the interface between the inclusion and the matrix. As expected, these non-linear strains are largest in the plane perpendicular to the rotation axis, since the rotation deformation field scales with distance from the rotation axis. Notably, we observe a three-fold symmetry in the profile of $|a|$, which can be ascribed to the underlying crystallographic orientation. For larger values of θ_{rot} , the non-linear distortions increase and localize into a network of dislocations. Notice that such a defect network is determined directly by the Burgers vector density rather than through arbitrary reconstructions^{61,62}. The description breaks down at large misorientations, as witnessed by the decrease in the magnitude of the defect density field since there is no longer a global translational order. Indeed, large misorientations lead to the nucleation of grain boundaries which are fully described by accounting for the bicrystallography of the two crystals meeting at the interface rather than the deformation with respect to a reference lattice⁶³. Such a regime shift echoes

the onset of active turbulence in the nematic liquid, where the description in terms of the order parameter $\rho^{(n)}$ also breaks down.

DISCUSSION

In-depth understanding and tailoring of collective behaviors require a unified description of defects associated with symmetry breaking and the non-topological excitations of ground states. Here, we proposed a systematic way of deriving reduced defect fields from order parameters associated with $O(n)$ broken symmetries which captures topological defects, localized non-linear excitations, and their dynamics. This enables the non-singular description of defects and their interaction, accounting for precursors and resulting patterns involving non-topological excitations. In this way, short-scale interactions between topological defects may be more accurately described, since features such as core overlap and high-energy excitations become more prominent at shorter length scales. This paves the way for a more thorough characterization of defect interactions, particularly in cases where the defects get close or are annihilated, as in the applications shown above. Moreover, the proposed framework can be used to study concurrent symmetry breakings and order transitions. Applications to systems of general interest, such as superfluids, active nematics, and solid crystals, are shown to showcase the considered framework, while we envisage applications in many other contexts.

We have shown that the method accurately tracks topological defects since these appear as localized blobs in the defect density field. The associated current density and velocity field determine the kinematics of the defects, and its utility has been shown to extend beyond tracking the velocity of topological defects. For example, in the case of the motion of vortices in a BEC, the velocity field accounts for both the overall velocity of the defect and local variations associated with the early-stage rearrangements of the defect core evolving towards its stationary shape.

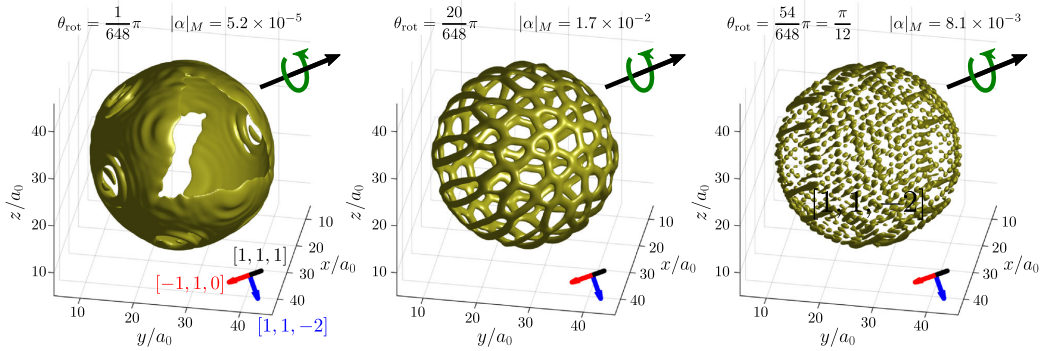


Fig. 7 Rotated inclusions in the bcc PFC model. The panels show, for three representative rotation angles θ_{rot} the isosurface of the Frobenius norm of the coarse dislocation density tensor $|\alpha| = \sqrt{\alpha^i \alpha_j}$ at 50% of its maximal value $|\alpha|_M = \max_r(|\alpha(r)|)$, which is given in the panels.

Thus, the uniformity of the velocity field over the core extent tests whether the frozen-core approximation¹ is valid. For active nematics and solid crystals, the velocity formula is shown to track the dynamics of defect dipoles, during, and after the nucleation of topological defects, pointing at interesting analogies and differences between processes in different physical systems. The rigorous derivation of these fields given in the Supplementary Notes for any dimensions makes the equations readily applicable to tracking topological defects and localized excitations in general.

We have found interesting features and insights about the evolution of these systems with broken symmetries. After the annihilation of the vortex dipole in the BEC, the remaining shock wave produces a signal in the defect density field that echoes the charge density pattern of the dipole, remnant also of other similar observations during mass-driven vortex collision⁶⁴. In active nematics, the large cores of the dislocation in the translational order harbor a bound dipole of orientational defects associated with the rotational order. This picture presents the idea of a hierarchy of topological defects, where the defects associated with one symmetry can spontaneously dissociate into stable defects for a different symmetry and melt the former ordered state. This is a non-equilibrium transition that echoes the equilibrium Kosterlitz-Thouless transition for melting of 2D crystals via the hexatic phase⁶⁵.

In the case of a 3D crystal, a rotated inclusion was shown to be described as a network of topological defects (dislocations) up to a point before these dissociated into other types of defects (grain boundaries) and the global orientational order was destroyed. The best topological description of polycrystalline materials is an open challenge, even though candidates, such as interacting disconnections⁶³, exist. Applying this formalism to such topologies is a fascinating avenue of research. Employing the APFC framework, where the periodic nature of crystal densities is inherently coarse-grained, we have shown that dislocation cores in Swift-Hohenberg theories emerge as transition regions from crystalline to pointwise stripe-like phases. When approaching the solid-liquid coexistence limit, analogies between the dislocation core size and the extensions of order-disordered interfaces have been found.

Finally, while the whole framework is presented for systems with one broken rotational symmetry, it is a powerful tool that can be generalized to systems with multiple broken symmetries and reveal hidden hierarchies of topological defects associated with each symmetry, laying the foundation for unified theories in systems characterized by collective behaviors.

METHODS

Bose-Einstein condensates

The damped Gross Pitaevskii equation, Eq. (16), is solved by using a Fourier pseudo-spectral integration scheme which is described in detail in ref. ³⁰. We use a periodic grid of size $[-32, 32] \times [-32, 32]$ with spatial discretization $\Delta x = \Delta y = 0.25$. To initialize the dipole we use the ansatz $\psi = \prod_{\alpha=1}^2 \chi(|r - r_{\alpha}|) e^{i q_{\alpha} \theta_{\alpha}}$, where r_{α} is the position of the vortex labeled α , $\theta_{\alpha} = \arctan[(y - y_{\alpha}) / (x - x_{\alpha})]$, and

$$\chi(r) = \begin{cases} r, & r < 1 \\ 1, & r > 1 \end{cases} \quad (34)$$

This order parameter is then evolved in imaginary time, $t \rightarrow i\tau$, with $\gamma = 0$ to lower the energy and find a better estimate for the core structure of the vortices we use as the initial condition.

Active nematic liquid crystals

The evolution of the Q -tensor follows dissipative dynamics coupled with an incompressible Stokes flow⁴³

$$\partial_t Q_{ij} + \mathbf{v} \cdot \nabla Q_{ij} - Q_{ik} \Omega_{kj} + \Omega_{ik} Q_{kj} = \lambda \mathcal{W}_{ij} + \gamma^{-1} H_{ij}, \quad (35)$$

$$(\Gamma - \eta \nabla^2) v_i = \partial_j (\alpha Q_{ij}) - \nabla p, \quad \nabla \cdot \mathbf{v} = 0, \quad (36)$$

where \mathbf{v} is the flow velocity that advects the nematic structure, p is the fluid pressure, Γ is the friction with a substrate, η is the viscosity and αQ is the active stress. The vorticity tensor $2\Omega_{ij} = (\partial_i v_j - \partial_j v_i)$ rotates the nematic structure, λ is the flow alignment parameter which aligns the nematic orientation in the direction of shear

$$\mathcal{W}_{ij} = E_{ij} + (E_{ik} Q_{kj} + Q_{ik} E_{kj}) - Q_{ik} E_{kl} (\delta_{ij} + Q_{ij}),$$

with the trace less strain rate $2E_{ij} = (\partial_i v_j + \partial_j v_i - \delta_{ij} \partial_k v_k)$. The molecular field

$$H_{ij} = K \nabla^2 Q_{ij} + A(B - 2Q_{kk}^2) Q_{ij}. \quad (37)$$

controls the relaxation to equilibrium with γ as the rotational diffusivity. We have here assumed a single Frank elastic constant K , treating splay and bend distortions similarly. The second term in the molecular field is a relaxation to a homogeneous nematic state. The parameter A is the quench depth and B sets the value of the order parameter $S_0 = \sqrt{B}$ in the homogeneous state. We discretize the above equations on a $[-64, 64] \times [-64, 64]$ grid with spatial discretization $\Delta x = \Delta y = 0.5$, and solve the system using pseudo-spectral methods. The parameters are set to $K = \Gamma = \gamma = 1$, $A = \lambda = \eta = 0.5$, $B = 2$ and $\alpha = -1.4$. The initial state is $S = \sqrt{2}$ with the angle of the director θ being uniformly distributed in the

interval $(-0.05, 0.05)$. We solve the equations for the flow field, Eq. (36), in Fourier space and evolve the equation for the Q tensor, Eq. (35), using the same scheme as for the BEC.

2D square lattice PFC

To simulate the PFC dynamics, we use the sHPFC model proposed in ref. 48, namely

$$\partial_t \psi = \Gamma \nabla^2 \frac{\delta F_{\psi}^{\text{sq}}}{\delta \psi} - \mathbf{v} \cdot \nabla \psi, \quad (38)$$

coupled to a momentum equation for $\partial_t \mathbf{v}$

$$\rho_0 \partial_t \mathbf{v} = \langle \tilde{\mu}_c \nabla \psi - \nabla \tilde{f} \rangle + \Gamma_5 \nabla^2 \mathbf{v} + \mathbf{f}^{(\text{ext})}. \quad (39)$$

$\langle \cdot \rangle$ is a convolution with a Gaussian kernel given by

$$\langle \tilde{X} \rangle = \int d\mathbf{r}' \frac{X(\mathbf{r}')}{2\pi w^2} \exp\left(-\frac{(\mathbf{r}-\mathbf{r}')^2}{2w^2}\right), \quad (40)$$

which filters out variations on length scales smaller than w . The quench depth in Eq. (30) is set to $r = -0.3$ and the average density to $\bar{\psi} = -0.3$. Parameters are set to $\Gamma = 1, \rho_0 = \Gamma_5 = 2^{-6}$, and an initial velocity field $\mathbf{v} = 0$. We solve the system of coupled equations with a Fourier pseudo-spectral method. The spatial grid of the simulation is set to $\Delta x = \Delta y = a_0/7$. Further details can be found in ref. 48.

In the simulation reported in Fig. 5, the perfect lattice is indented by an applied external force density given by a Gaussian profile $\mathbf{f}^{(\text{ext})} = f_0 \frac{(y-y_0)}{a_0} \exp(-\frac{(x-x_0)^2}{2w^2}) \mathbf{e}_x$. Above a critical strength $f_0 = 3.5\mu/a_0$ and width $w = a_0$, this force causes the nucleation of a dislocation dipole.

2D square lattice APFC

The evolution of the amplitudes as delivered by the APFC model can then be directly expressed as

$$\frac{\partial \eta_n}{\partial t} = -|\mathbf{q}^{(n)}|^2 \frac{\delta F_{\eta}}{\delta \eta_n}, \quad (41)$$

with F_{η} the free energy depending on $\{\eta_n\}$ that can be derived by substituting (31) in F_{ψ}^{sq} and integrating over the unit cell⁵⁹. By assuming constant $\bar{\psi}$ it reads

$$F_{\eta} = \int d^2 r \left(g \sum_{n=1}^N |\mathcal{G}_n \eta_n|^2 + W(\{\eta_n\}) + C(\bar{\psi}) \right), \quad (42)$$

with $\mathcal{G}_n = (\nabla^2 + 2i\mathbf{q}^{(n)} \cdot \nabla)$, g a coefficient that controls elastic constants, $W(\{\eta_n\}) = r'\Phi/2 + (3/4)\Phi^2 - (3/4)\sum_{n=1}^N |\eta_n|^4 + f^s(\{\eta_n\})$, $r' = r + 3\bar{\psi}^2$, $\Phi = \sum_{n=1}^N |\eta_n|^2$, and $f^s(\{\eta_n\})$ a symmetry-dependent polynomial in the amplitudes. For the square symmetry as encoded in Eq. (30) and the choice $\mathbf{q}^{(1)} = (1, 0)$, $\mathbf{q}^{(2)} = (0, 1)$, $\mathbf{q}^{(3)} = (1, 1)$, $\mathbf{q}^{(4)} = (-1, 1)$ and $\{\mathbf{q}^{(n)}\} = \{-\mathbf{q}^{(n-4)}\}$ for $n = 5, \dots, 8$, we have $f^s(\{\eta_n\}) = 2\bar{\psi}(\eta_1 \eta_2 \eta_3^* + \eta_1 \eta_2^* \eta_4) + 3(\eta_1^* \eta_3^* \eta_4 + \eta_2^* \eta_3^* \eta_4^*) + \text{c.c.}$, with $\{\eta_n^*\} = \{\eta_{n-4}\}$ for $n = 5, \dots, 8$ as ψ is a real function. Therefore, one may consider just η_n with $n = 1, \dots, 4$ as variables. $C(\bar{\psi})$ is a constant depending on $\bar{\psi}$ ⁵⁹, set here to $\bar{\psi} = -0.3$ as set in the corresponding PFC modeling of the 2D square lattice. r' corresponds to a phenomenological temperature. With r_0 the solid–liquid critical point, the solid crystalline phase is favored for $r' < r_0$.

We simulate a stationary system hosting dislocations with the APFC model exploiting the (FEM) numerical approach with adaptive grid refinement outlined in refs. 66,67. The semi-implicit integration scheme adopted for numerical simulations can be found therein. We consider dislocations with spacing $L = 50a_0$ arranged in a periodic, 2D matrix with alternating Burgers vectors $\pm a_0 \hat{x}$. The system is initialized by setting the displacement field of dislocation known from classical continuum mechanics⁴⁹ in the

phase of amplitudes, $-\mathbf{q}^{(n)} \cdot \mathbf{u}$, and let relaxed according to the amplitudes evolution law (41). We can consider a system $2L \times 2L$ by exploiting periodic boundary conditions.

In the section “Defect structures: solid crystals”, we characterize the extension of the core of dislocations through the field $\mathbf{D}^{(n)}$ as entering the definition of the dislocation density tensor α , Eq. (29). We compare the size of the defects extracted with the aid of Gaussian fits (see Fig. 6a, b) with the extension of a solid–liquid interface, w , computed numerically as the average of interface width for single amplitudes. This is obtained by initializing the solid phase with a straight interface having normal along the x -axis and letting the system evolve by Eq. (41) until reaching a steady state. Then, a fit of each amplitude with a function $\phi_i = \bar{A}_i [1 - \tanh(x - \bar{x}_i)/\bar{w}_i]$, representing a traveling wave solution for a solid–liquid interface^{54,58,60}, is performed with \bar{A}_i , \bar{x}_i and \bar{w}_i parameters and the solid–liquid interface thickness extracted as $w = \sum_{i=1}^4 \bar{w}_i/4$.

3D bcc lattice PFC

Numerical simulations reported in the section “Defect structures: solid crystals” are obtained by solving the classical PFC equation encoding dissipative dynamics,

$$\partial_t \psi = \nabla^2 \frac{\delta F_{\psi}^{\text{bcc}}}{\delta \psi}, \quad (43)$$

where F_{ψ}^{bcc} is a free energy functional that produces a stable bcc lattice, given by

$$F_{\psi}^{\text{bcc}} = \int d^3 r \frac{1}{2} (\mathcal{L}_1 \psi)^2 + \frac{r}{2} \psi^2 + \frac{1}{4} \psi^4. \quad (44)$$

As parameters, we use $r = -0.3$ and $\psi_0 = -0.325$ with spatial discretization $\Delta x = \Delta y = \Delta z = a_0/7$ and exploiting a Fourier pseudo-spectral integration scheme. We consider a $51 \times 51 \times 51$ cubic crystal as matrix in which we embed a spherical inclusion with radius $17a_0$ rotated at an angle θ_{rot} about the $[1, 1, 1]$ -axis. This initial condition is obtained just by a rotation of grid points inside the inclusion. This leaves a sharp (and unphysical) interface which is regularized by letting this initial condition relax as dictated by Eq. (43) for 300 time steps with $\Delta t = 0.1$.

DATA AVAILABILITY

The data will be provided by the corresponding author upon reasonable request.

CODE AVAILABILITY

The code will be provided by the corresponding author upon reasonable request.

Received: 17 February 2023; Accepted: 25 June 2023;

Published online: 13 July 2023

REFERENCES

- Mermin, N. D. The topological theory of defects in ordered media. *Rev. Mod. Phys.* **51**, 591–648 (1979).
- Kibble, T. W. B. Topology of cosmic domains and strings. *J. Phys. A* **9**, 1387 (1976).
- Michel, L. Symmetry defects and broken symmetry. Configurations hidden symmetry. *Rev. Mod. Phys.* **52**, 617 (1980).
- Vilenkin, A. & Shellard, E. P. S. *Cosmic Strings and Other Topological Defects* (Cambridge University Press, 2000).
- Chaikin, P. M. & Lubensky, T. C. *Principles of Condensed Matter Physics* (Cambridge University Press, 1995).
- Nelson, D. R. *Defects and Geometry in Condensed Matter Physics* 1st edn (Cambridge University Press, 2002).
- Ozawa, T. et al. Topological photonics. *Rev. Mod. Phys.* **91**, 015006 (2019).
- Ardaševa, A. & Doostmohammadi, A. Topological defects in biological matter. *Nat. Rev. Phys.* **4**, 354–356 (2022).

9. Madeira, L., Caracanhas, M. A., dos Santos, F. & Bagnato, V. S. Quantum turbulence in quantum gases. *Annu. Rev. Condens. Matter Phys.* **11**, 37–56 (2020).
10. Alert, R., Casademunt, J. & Joanny, J.-F. Active turbulence. *Annu. Rev. Condens. Matter Phys.* **13**, 143 – 170 (2022).
11. Papanikolaou, S., Cui, Y. & Ghoniem, N. Avalanches and plastic flow in crystal plasticity: an overview. *Model. Simul. Mat. Sci. Eng.* **26**, 013001 (2017).
12. Eyink, G. L. & Sreenivasan, K. R. Onsager and the theory of hydrodynamic turbulence. *Rev. Mod. Phys.* **78**, 87 (2006).
13. Zhou, C., Biner, S. B. & LeSar, R. Discrete dislocation dynamics simulations of plasticity at small scales. *Acta Mater.* **58**, 1565–1577 (2010).
14. Neely, T. W., Samson, E. C., Bradley, A. S., Davis, M. J. & Anderson, B. P. Observation of vortex dipoles in an oblate bose-einstein condensate. *Phys. Rev. Lett.* **104**, 160401 (2010).
15. Kwon, W. J., Moon, G., Seo, S. W. & Shin, Y.-i. Critical velocity for vortex shedding in a Bose-Einstein condensate. *Phys. Rev. A* **91**, 053615 (2015).
16. Aioi, T., Kadokura, T., Kishimoto, T. & Saito, H. Controlled generation and manipulation of vortex dipoles in a Bose-Einstein condensate. *Phys. Rev. X* **1**, 021003 (2011).
17. Kunimi, M. & Kato, Y. Metastability, excitations, fluctuations, and multiple-swallowtail structures of a superfluid in a Bose-Einstein condensate in the presence of a uniformly moving defect. *Phys. Rev. A* **91**, 053608 (2015).
18. Skaugen, A. & Angheluta, L. Vortex clustering and universal scaling laws in two-dimensional quantum turbulence. *Phys. Rev. E* **93**, 032106 (2016).
19. Neely, T. et al. Characteristics of two-dimensional quantum turbulence in a compressible superfluid. *Phys. Rev. Lett.* **111**, 235301 (2013).
20. Thampi, S. P., Golestanian, R. & Yeomans, J. M. Vorticity, defects and correlations in active turbulence. *Philos. Trans. Royal Soc. A* **372**, 20130366 (2014).
21. Doostmohammadi, A., Shendruk, T. N., Thijssen, K. & Yeomans, J. M. Onset of meso-scale turbulence in active nematics. *Nat. Commun.* **8**, 1–7 (2017).
22. Zolotarevsky, N., Rybin, V., Ushanova, E., Ermakova, N. & Perevezentsev, V. Large-scale fragmentation of grains in plastically deformed polycrystalline iron. *Mater. Today Commun.* **31**, 103816 (2022).
23. Li, J., Zhu, T., Yip, S., Vliet, K. J. V. & Suresh, S. Elastic criterion for dislocation nucleation. *Mater. Sci. Eng. A* **365**, 25–30 (2004).
24. Miller, R. E. & Acharya, A. A stress-gradient based criterion for dislocation nucleation in crystals. *J. Mech. Phys. Solids* **52**, 1507–1525 (2004).
25. Garg, A., Acharya, A. & Maloney, C. E. A study of conditions for dislocation nucleation in coarser-than-atomistic scale models. *J. Mech. Phys. Solids* **75**, 76–92 (2015).
26. Halperin, B. I. In *Physique Des Défauts/Physics of Defects* (eds. Balian, R., Kléman, M. & Poirier, J.-P.) 812–857 (North-Holland, 1981).
27. Mazenko, G. F. Vortex velocities in the O(n) symmetric time-dependent ginzburg-landau model. *Phys. Rev. Lett.* **78**, 401–404 (1997).
28. Mietke, A. & Dunkel, J. Anyonic defect braiding and spontaneous chiral symmetry breaking in dihedral liquid crystals. *Phys. Rev. X* **12**, 011027 (2022).
29. Monderkamp, P. A. et al. Topological fine structure of smectic grain boundaries and tetratic disclination lines within three-dimensional smectic liquid crystals. *Phys. Chem. Chem. Phys.* **24**, 15691–15704 (2022).
30. Rønning, J., Skaugen, A., Hernández-García, E., Lopez, C. & Angheluta, L. Classical analogies for the force acting on an impurity in a Bose-Einstein condensate. *New J. Phys.* **22**, 073018 (2020).
31. Rønning, J. & Angheluta, L. Precursor patterns to vortex nucleation in stirred Bose-Einstein condensates. *Phys. Rev. Res* **5**, 023108 (2023).
32. Angheluta, L., Chen, Z., Marchetti, M. C. & Bowick, M. J. The role of fluid flow in the dynamics of active nematic defects. *New J. Phys.* **23**, 033009 (2021).
33. Rønning, J., Marchetti, C. M., Bowick, M. J. & Angheluta, L. Flow around topological defects in active nematic films. *Proc. R. Soc. A* **478**, 20210879 (2022).
34. Skaugen, A., Angheluta, L. & Viñals, J. Dislocation dynamics and crystal plasticity in the phase-field crystal model. *Phys. Rev. B* **97**, 054113 (2018).
35. Skogvoll, V., Skaugen, A., Angheluta, L. & Viñals, J. Dislocation nucleation in the phase-field crystal model. *Phys. Rev. B* **103**, 014107 (2021).
36. Skogvoll, V., Angheluta, L., Skaugen, A., Salvalaglio, M. & Viñals, J. A phase field crystal theory of the kinematics of dislocation lines. *J. Mech. Phys. Solids* **166**, 104932 (2022).
37. Zhou, S., Shiyonovskii, S. V., Park, H.-S. & Lavrentovich, O. D. Fine structure of the topological defect cores studied for disclinations in lyotropic chromonic liquid crystals. *Nat. Commun.* **8**, 14974 (2017).
38. Nguyen, S., Folch, R., Verma, V. K., Henry, H. & Plapp, M. Phase-field simulations of viscous fingering in shear-thinning fluids. *Phys. Fluids* **22**, 103102 (2010).
39. Kanazawa, N. et al. Direct observation of the statics and dynamics of emergent magnetic monopoles in a chiral magnet. *Phys. Rev. Lett* **125**, 137202 (2020).
40. Reeves, M. T., Billam, T. P., Anderson, B. P. & Bradley, A. S. Inverse energy cascade in forced two-dimensional quantum turbulence. *Phys. Rev. Lett.* **110**, 104501 (2013).
41. Astrakharchik, G. & Pitaevskii, L. Motion of a heavy impurity through a bose-einstein condensate. *Phys. Rev. A* **70**, 013608 (2004).
42. Marchetti, M. C. et al. Hydrodynamics of soft active matter. *Rev. Mod. Phys.* **85**, 1143 (2013).
43. Nejad, M. R., Doostmohammadi, A. & Yeomans, J. M. Memory effects, arches and polar defect ordering at the cross-over from wet to dry active nematics. *Soft Matter* **17**, 2500–2511 (2021).
44. Elder, K. R., Katakowski, M., Haataja, M. & Grant, M. Modeling elasticity in crystal growth. *Phys. Rev. Lett.* **88**, 245701 (2002).
45. Elder, K. R. & Grant, M. Modeling elastic and plastic deformations in non-equilibrium processing using phase field crystals. *Phys. Rev. E* **70**, 051605 (2004).
46. Emdadi, A., Asle Zaeem, M. & Asadi, E. Revisiting phase diagrams of two-mode phase-field crystal models. *Comput. Mater. Sci.* **123**, 139–147 (2016).
47. Skogvoll, V., Skaugen, A. & Angheluta, L. Stress in ordered systems: Ginzburg-Landau-type density field theory. *Phys. Rev. B* **103**, 224107 (2021).
48. Skogvoll, V., Salvalaglio, M. & Angheluta, L. Hydrodynamic phase field crystal approach to interfaces, dislocations and multi-grain networks. *Model. Simul. Mater. Sci. Eng.* **30**, 084002 (2022).
49. Anderson, P. M., Hirth, J. P. & Lothe, J. *Theory of Dislocations* 3rd edn (Cambridge University Press, 2017).
50. Hüter, C. et al. Nonlinear elastic effects in phase field crystal and amplitude equations: Comparison to ab initio simulations of bcc metals and graphene. *Phys. Rev. B* **93**, 214105 (2016).
51. Goldenfeld, N., Athreya, B. P. & Dantzig, J. A. Renormalization group approach to multiscale simulation of polycrystalline materials using the phase field crystal model. *Phys. Rev. E* **72**, 020601 (2005).
52. Athreya, B. P., Nigel, G. & Dantzig, J. A. Renormalization-group theory for the phase field crystal model. *Phys. Rev. E* **74**, 011601 (2006).
53. Elder, K. R., Provatas, N., Berry, J., Stefanovic, P. & Grant, M. Phase-field crystal modeling and classical density functional theory of freezing. *Phys. Rev. B* **75**, 064107 (2007).
54. Galenko, P., Sanches, F. I. & Elder, K. Traveling wave profiles for a crystalline front invading liquid states: Analytical and numerical solutions. *Phys. D: Nonlinear Phenom.* **308**, 1–10 (2015).
55. Cai, W., Arsenlis, A., Weinberger, C. & Bulatov, V. A non-singular continuum theory of dislocations. *J. Mech. Phys. Solids* **54**, 561–587 (2006).
56. Lazar, M. & Maugin, G. A. Nonsingular stress and strain fields of dislocations and disclinations in first strain gradient elasticity. *Int. J. Eng. Sci.* **43**, 1157–1184 (2005).
57. Lazar, M., Maugin, G. A. & Aifantis, E. C. Dislocations in second strain gradient elasticity. *Int. J. Solids Struct.* **43**, 1787–1817 (2006).
58. Ankudinov, V., Elder, K. R. & Galenko, P. K. Traveling waves of the solidification and melting of cubic crystal lattices. *Phys. Rev. E* **102**, 062802 (2020).
59. Salvalaglio, M. & Elder, K. R. Coarse-grained modeling of crystals by the amplitude expansion of the phase-field crystal model: an overview. *Model. Simul. Mater. Sci. Eng.* **30**, 053001 (2022).
60. Nizovtseva, I. G. & Galenko, P. K. Travelling-wave amplitudes as solutions of the phase-field crystal equation. *Philos. Trans. R. Soc. A* **376**, 20170202 (2018).
61. Yamanaka, A., McReynolds, K. & Voorhees, P. W. Phase field crystal simulation of grain boundary motion, grain rotation and dislocation reactions in a BCC bicrystal. *Acta Mater.* **133**, 160–171 (2017).
62. Salvalaglio, M., Backofen, R., Elder, K. R. & Voigt, A. Defects at grain boundaries: a coarse-grained, three-dimensional description by the amplitude expansion of the phase-field crystal model. *Phys. Rev. Mater.* **2**, 053804 (2018).
63. Han, J., Thomas, S. L. & Srolovitz, D. J. Grain-boundary kinetics: a unified approach. *Prog. Mater. Sci.* **98**, 386–476 (2018).
64. Richaud, A., Lamporesi, G., Capone, M. & Recati, A. Mass-driven vortex collisions in flat superfluids. *Phys. Rev. A* **107**, 053317 (2023).
65. Nelson, D. R. & Halperin, B. Dislocation-mediated melting in two dimensions. *Phys. Rev. B* **19**, 2457 (1979).
66. Salvalaglio, M., Backofen, R., Voigt, A. & Elder, K. R. Controlling the energy of defects and interfaces in the amplitude expansion of the phase-field crystal model. *Phys. Rev. E* **96**, 023301 (2017).
67. Praetorius, S., Salvalaglio, M. & Voigt, A. An efficient numerical framework for the amplitude expansion of the phase-field crystal model. *Model. Simul. Mater. Sci. Eng.* **27**, 044004 (2019).

ACKNOWLEDGEMENTS

We are grateful to Jorge Viñals for many interesting discussions. M.S. acknowledges support from the German Research Foundation (DFG) under Grant No. SA4032/2-1. Computing resources have been provided by the Center for Information Services and High-Performance Computing (ZIH) at TU-Dresden.

AUTHOR CONTRIBUTIONS

V.S.: concept and theory development, simulations, data analysis, manuscript writings. J.R.: concept and theory development, simulations, data analysis, manuscript writings. M.S.: concept and theory development, supervision, simulations, manuscript writings. L.A.: concept and theory development, supervision, manuscript writings.

COMPETING INTERESTS

The authors declare no competing interests.

ADDITIONAL INFORMATION

Supplementary information The online version contains supplementary material available at <https://doi.org/10.1038/s41524-023-01077-6>.

Correspondence and requests for materials should be addressed to Vidar Skogvoll.

Reprints and permission information is available at <http://www.nature.com/reprints>

Publisher's note Springer Nature remains neutral with regard to jurisdictional claims in published maps and institutional affiliations.



Open Access This article is licensed under a Creative Commons Attribution 4.0 International License, which permits use, sharing, adaptation, distribution and reproduction in any medium or format, as long as you give appropriate credit to the original author(s) and the source, provide a link to the Creative Commons license, and indicate if changes were made. The images or other third party material in this article are included in the article's Creative Commons license, unless indicated otherwise in a credit line to the material. If material is not included in the article's Creative Commons license and your intended use is not permitted by statutory regulation or exceeds the permitted use, you will need to obtain permission directly from the copyright holder. To view a copy of this license, visit <http://creativecommons.org/licenses/by/4.0/>.

© The Author(s) 2023

Paper V

Spontaneous flows and dynamics of full-integer topological defects in polar active matter

**Jonas Rønning, Julian Renaud, Amin Doostmohammadi,
Luiza Angheluta**



Spontaneous flows and dynamics of full-integer topological defects in polar active matter†

Cite this: DOI: 10.1039/d3sm00316g

Jonas Rønning,^a Julian Renaud,^{bc} Amin Doostmohammadi^{bd} and Luiza Angheluta^{ba*}

Polar active matter of self-propelled particles sustain spontaneous flows through the full-integer topological defects. We study theoretically the incompressible flow profiles around ± 1 defects induced by polar and dipolar active forces. We show that dipolar forces induce vortical flows around the +1 defect, while the flow around the -1 defect has an 8-fold rotational symmetry. The vortical flow changes its chirality near the +1 defect core in the absence of the friction with a substrate. We show analytically that the flow induced by polar active forces is vortical near the +1 defect and is 4-fold symmetric near the -1 defect, while it becomes uniform in the far-field. For a pair of oppositely charged defects, this polar flow contributes to a mutual interaction force that depends only on the orientation of the defect pair relative to the background polarization, and that enhances defect pair annihilation. This is in contradiction with the effect of dipolar active forces which decay inversely proportional with the defect separation distance. As such, our analyses reveals a long-ranged mechanism for the pairwise interaction between topological defects in polar active matter.

Received 13th March 2023,
Accepted 20th July 2023

DOI: 10.1039/d3sm00316g

rsc.li/soft-matter-journal

1 Introduction

Active matter refers to non-equilibrium systems of interacting, self-propelled entities that consume energy from their surrounding in the form of persistent motion and their collective interactions lead to emergent, dynamical patterns, and self-sustained flows.^{1,2} Models of active matter are largely inspired by biological systems from bacterial suspensions^{1,2} and cell monolayers^{3,4} and down to subcellular active systems such as mixtures of cytoskeletal filaments and motor proteins.^{5–8} However, this also pertains to non-living active systems such as layers of vibrated granular matter, microrobots, or synthetic catalytic nanomotors.^{2,9}

Several hydrodynamic models have been proposed to capture the macroscopic dynamics and emergent phenomena corresponding to a collection of active (self-propelled) particles with different symmetries and alignment interactions.^{2,10–12} The prototypical models are based on the analogy to liquid

crystals formed by rod-like particles with polar or apolar symmetries in their alignment interactions. Active rods with only orientational alignment act as headless “shakers” and form apolar phases described by a slowly-varying director field \vec{n} which has head–tail (nematic) symmetry.^{1,2,13,14} By contrast, active rods that align their direction of motion tend to flock into polar systems that are described instead by a slowly-varying polar vector field \vec{p} .^{10–12,15} Active rod-like particles generate persistent flows sustained by the active stress originating from extensile/contractile dipolar forces. On hydrodynamic scales, this active stress is proportional to the nematic \mathbf{Q} tensor order parameter, *i.e.* $\sigma^a = \alpha_0 \mathbf{Q}$ with a proportionality coefficient α_0 as an effective activity parameter.^{2,16} Topological defects, innate to ordered systems with broken continuous symmetries, are also present in active systems. The interplay between active stresses and configurational distortions feeds into self-sustain flows and the proliferation of topological defects to generate chaotic flows also known as active turbulence.^{17–19}

From the rotational symmetry modulo π of the \mathbf{Q} tensor, it follows that the lowest energy orientational defects have a $\pm 1/2$ topological charge corresponding to $\pm \pi$ jump in the orientational phase around them. The $+1/2$ defects acquire a self-propulsion due to the net active flow passing through their cores.^{20,21} The stable, low-energy defects in polar active systems have instead ± 1 topological charges corresponding to a 2π phase jumps around the defects. This is analogous to vortices in the XY-model of 2D ferromagnets.^{15,22}

^a Department of Physics, Njord Centre, University of Oslo, P.O. Box 1048, 0316 Oslo, Norway. E-mail: luizaa@fys.uio.no

^b École Normale Supérieure, PSL Research University, 45 rue d'Ulm, 75005 Paris, France

^c Institute of Science and Technology Austria, Am Campus 1, A-3400 Klosterneuburg, Austria

^d Niels Bohr Institute, University of Copenhagen, Blegdamsvej 17, Copenhagen, Denmark. E-mail: doostmohammadi@nbi.ku.dk

† Electronic supplementary information (ESI) available: https://github.com/jonasron/SM_Flowfield_Polar. See DOI: <https://doi.org/10.1039/d3sm00316g>



The bulk of recent studies have focused on the formation and characterization of half-integer nematic defects (see recent reviews^{23,24}). This is in part due to the ubiquitous emergence of the nematic defects in a wide range of biological systems from subcellular filaments^{8,25} to bacterial colonies^{26,27} and assemblies of eukaryotic cells.^{28,29} This is despite the fact that several biological active entities, such as bacteria or eukaryotic cells, are endowed with a clear head-tail asymmetry and directional self-propulsion, which characterizes a polar order for these systems. Such a polar order at the scale of collective is apparent from flocking domains within bacterial colonies²⁷ and eukaryotic cells.³⁰ Nevertheless, because of the appearance of half-integer defects, at the coarse-grained level, these systems are often modelled as active nematics neglecting the polarity of the self-propelled particles. There have been proposed models that couple the evolution of polar and nematic order parameters^{31–33} to allow for the coexistence of both types of symmetries. Recently, in ref. 34, a hydrodynamic model was proposed for the coexistence of both nematic and polar alignment interactions in the polarization field \vec{p} , and was used to study different active turbulence regimes sustained by both half- and full-integer topological defects. In addition to dipolar (nematic) active forces, the model also includes a polar active force $\vec{f} = \alpha_p \vec{p}$, which describes the self-propulsion direction and is shown to suppress defect-laden active turbulence.³⁵

More recently, theoretical and experimental studies have revealed the importance of full-integer topological defects in cell assemblies. In particular, it is shown that positive full-integer defects formed due to collision of two nematic half-integer defects in fast-moving bacterial colonies can lead to the verticalization of bacteria and escape to the out-of-plane directions.^{27,36} Furthermore, positive full-integer defects induced by confinement of myoblast cells in circular geometries are shown to activate cell differentiation and formation of 3D helical structures.³⁷ Full-integer defects are also observed in cell migrations on curved surfaces^{38,39} and during tissue morphogenesis.⁴⁰ A corresponding theoretical analyses, in the limit of compressible flows inside the core region of defects in small confinements, have revealed the corresponding flow fields and force patterns, and shows how confinement-induced topological defects can be used to probe the material properties of the cell layers.⁴¹

In this paper, we carry out a theoretical analysis that reveals subtle cross-talks between polar and dipolar active forces in generating spontaneous incompressible flows around both ± 1 defects. We theoretically predict spontaneous vortical flows induced by dipolar active forces around $+1$ defects which correspond to isotropic active stress and pressure fields. Interestingly, the competition between dipolar force and viscous force leads to a flow reversal close to the core of the $+1$ defect. This effect is also confirmed by numerical simulations of the full hydrodynamic model including additional passive stresses. However, it turns out the hydrodynamic screening induced by friction lifts up this flow reversal effect. By contrast, the -1 defects which have an innate 4-fold symmetry in the polarity field lead to 8-fold symmetries of the active flows induced by

dipolar active forces. The same 8-fold symmetry is present also in the profile of the pressure field. We demonstrate that polar active force trigger a distinct active flow pattern characterised by uniform flow in the far-field of its source, *i.e.* ± 1 defects. This is very different than the active flows sustained by dipolar forces which decay algebraically with distance. Polar active forces have a drastic effect on the mutual interactions between defects by promoting fast annihilation of defect pairs through non-local and non-reciprocal attraction forces. We show that this distance-independent mechanism of defect pair annihilation is responsible for the suppression of active turbulence by polar forces as recently reported in ref. 35.

The paper is organized as follows: we begin in Section 2 by introducing the flow equations within a minimal polar hydrodynamic model and derive the corresponding defect kinematic equations using Halperin–Mazenko formalism.⁴² The main analytical results on the active flow velocity induced around isolated ± 1 are discussed in Section 3. We also compare the analytical predictions with direct numerical simulations and find very good agreement of the flow profiles around defects and the flow reversal pattern near the $+1$ defect cores. In Section 4, we discuss the polar active force and its effect on the defect kinematics. In particular, we consider the motion of a pair of oppositely charged full-integer defects under the polar active flows induced by each defect and demonstrate that polar active forces enhance the defect annihilation rate. In a recent study ref. 35, it was numerically evidenced that polar active forces suppress defect-laden active turbulence and tend to restore polar order. Here, we demonstrate theoretically that polar active forces have a net effect on the defect kinematics to promote defect pair binding and subsequent annihilation of defects of opposite topological charges. The final section provides a summary of the theoretical insights and concluding remarks.

2 Hydrodynamic model of polar active matter

We consider the hydrodynamic model³⁴ that describes the collective dynamics of self-propelled entities in terms of the evolution of the polar order parameter \vec{p} as given by

$$\partial_t \vec{p} + \vec{u} \cdot \nabla \vec{p} + \lambda \mathbf{E} \cdot \vec{p} + \mathbf{\Omega} \cdot \vec{p} = -\frac{1}{\gamma} \frac{\delta \mathcal{F}}{\delta \vec{p}}, \quad (1)$$

where γ is the rotational viscosity, λ is the flow-aligning parameter⁴³ which aligns the order parameter with the shear rate tensor $2E_{ij} = \partial_i u_j + \partial_j u_i$, while the vorticity tensor is $2\Omega = (\partial_i u_j - \partial_j u_i)$, and the free energy favoring the polar order is described as

$$\mathcal{F} = \int d\vec{r} \left\{ A \left(-\frac{|\vec{p}|^2}{2} + \frac{|\vec{p}|^4}{4} \right) + \frac{K_p}{2} |\nabla \vec{p}|^2 \right\}. \quad (2)$$

Here, K_p is the isotropic elastic constant for distortions in the polarity field and A is the height of local energy barrier. The



polarity is coupled with the flow field u which is described by the incompressible Stokes equations

$$(\Gamma - \eta \nabla^2) \bar{u} = \alpha_0 \nabla \cdot \mathbf{Q} - \nabla P, \quad (3)$$

$$\nabla \cdot \bar{u} = 0, \quad (4)$$

where the active stress is proportional to the nematic tensor $Q_{ij} = \left(p_i p_j - \frac{p^2}{2} \delta_{ij} \right)$ with the proportionality constant given by activity parameter α_0 . The incompressibility constraint determines the fluid pressure P . The viscosity is set by η while the friction with a substrate is introduced by the frictional drag Γ .⁴⁴ Since we focus on theoretical derivations of the active flows induced by polar and dipolar forces, we hereby neglect the additional passive stresses which depend on the polarity and that are typically present in the Stokes equations simulated numerically.

We consider the dimensionless forms of these equations following the appropriate rescalings in units of length $\xi = \sqrt{K_p/A}$ and time $\tau = \gamma/A$. The system is then controlled by two dimensionless parameters: the scale number $\zeta = \ell_d/\xi$ is the ratio between the hydrodynamic dissipation length $\ell_d = \sqrt{\eta/\Gamma}$ and the nematic coherence length ξ , and the rescaled activity $\bar{\alpha}_0 = \alpha_0 \tau / (\xi^2) = \alpha_0 \gamma / (K_p)$. Thus, the dimensionless flow equations read as

$$(1 - \zeta^2 \nabla^2) \bar{u} = \bar{F}_a - \nabla P, \quad (5)$$

$$\nabla^2 P = \nabla \cdot \bar{F}_a \quad (6)$$

where the dipolar active force induced by the active stress is

$$\bar{F}_a = \frac{\bar{\alpha}_0}{\Gamma} \nabla \cdot \mathbf{Q}. \quad (7)$$

For infinite systems, the flow velocity and pressure originated from dipolar active forces can be calculated from convolution integrals of the source terms and the corresponding Green's functions as

$$P(\vec{r}) = \frac{1}{2\pi} \int d\vec{r}' \ln(|\vec{r} - \vec{r}'|) [\nabla' \cdot \bar{F}_a], \quad (8)$$

and

$$\bar{u}(\vec{r}) = \int \frac{d\vec{r}'}{2\pi\zeta^2} K_0 \left(\frac{|\vec{r} - \vec{r}'|}{\zeta} \right) \left(\bar{F}_a(\vec{r}') - \nabla' P(\vec{r}') \right). \quad (9)$$

To derive analytical expressions, we evaluate the source term due to the active stress using the order parameter for an isolated point defect located at the origin and given by

$$\bar{p}(r, \theta) = \chi(r) [\cos(q\theta + \phi) \bar{e}_x + \sin(q\theta + \phi) \bar{e}_y],$$

where $\theta = \arctan(y/x)$ is the polar angle in a coordinate system centered at the defect position and $\chi(r)$ is the core function, where we assume that the core size is much smaller than any other length scales and set $\chi(r) = 1$. The angle of the polar vector order parameter for an ideal defect is given by $\Theta(\theta) = q\theta + \phi$,²² where $q\theta$ is the singular part giving the winding number q

when performing the integral $\oint d\Theta = 2\pi q$ on a contour surrounding the defect and ϕ is a constant, giving a baseline phase to the defect. For defects of charge $q \neq \pm 1$ this constant sets the orientation of the defect and can be ignored since we can always transform to a system with $\phi = 0$ by a change of basis. When $q = +1$ it is impossible to remove a non-zero ϕ by changing the basis.⁴⁵ The $+1$ defects have polar symmetry, *i.e.* 2π rotational invariance. The intrinsic phase ϕ is important for distinguishing different types of positive defects: $\phi = 0$ corresponds to an aster and $\phi = \pi/2$ gives rise to a vortex, and any value in-between corresponds to a spiral defect. For a more intuitive depiction of this, we plot in Fig. 1(a) and (c) the \bar{p} field on the circumference of a circle centered at ± 1 defects to show that ϕ corresponds to the constant angle that \bar{p} makes with the radial direction. For the negative defect one can define a polarisation from the line where \bar{p} is pointing radially outward from the core, the angle of this polarisation is half of ϕ . The different patterns of the \bar{p} field around a ± 1 defect are also illustrated in Fig. 1(b) and (d).

We use the Halperin–Mazenko formalism^{46,47} for tracking topological defects as zeros of the polar order parameter to derive the corresponding equations of motion of defects from the evolution of the \bar{p} field similar the approach from ref. 42 to describe orientational defects in active nematic films. The basic idea is that since the ± 1 defects are associated simultaneously with topological singularities in the orientation field and zero magnitude of the vector order parameter, we can track their position by Dirac delta functions centered at the zeros of the \bar{p} field. Hence, a configuration of well-separated defects punctuating the \bar{p} -field corresponds to a defect charge density field, which can be written equivalently either as a superposition of the delta functions associated with the topological singularities located in the physical space or as the zeros in the order parameter space,

$$\rho(\vec{r}, t) = \sum_n q^{(n)} \delta(\vec{r} - \vec{r}^{(n)}) = D\delta(\vec{p}), \quad (10)$$

where D is the determinant of the polarity distortion tensor $\nabla \bar{p}$, *i.e.* $D = \varepsilon_{ij} \partial_i p_x \partial_j p_y$ which can be expressed equivalently in the complex representation $\psi = p_x + ip_y$ as $2iD = \varepsilon_{ij} \partial_i \bar{\psi} \partial_j \psi$. The D -field is zero in regions of uniform polar order and becomes nonzero where there are distortions in the orientation field. For configurations of well-separated defects punctuating a uniform polar order state, the D field is zero everywhere except at the defect positions labeled by the index n , where the topological charge $q_n = \pm 1$ is determined by the sign of D . Thus, the D field represents a non-singular charge density field.

It can be shown that the D -field follows the conservation law⁴⁶

$$\partial_t D + \partial_j \bar{J}_j = 0, \quad (11)$$

with the current density $J = \varepsilon_{ij} \bar{\psi} (\partial_i \psi \partial_j \bar{\psi})$ determined by the evolution of the polar order. Combining this with the conservation of topological charge density ρ , we can derive a general expression for the defect velocity in terms of the D and its current, $\vec{v}_n = \bar{J}/D|_{\vec{r}_n}$.⁴² In the complex representation, we



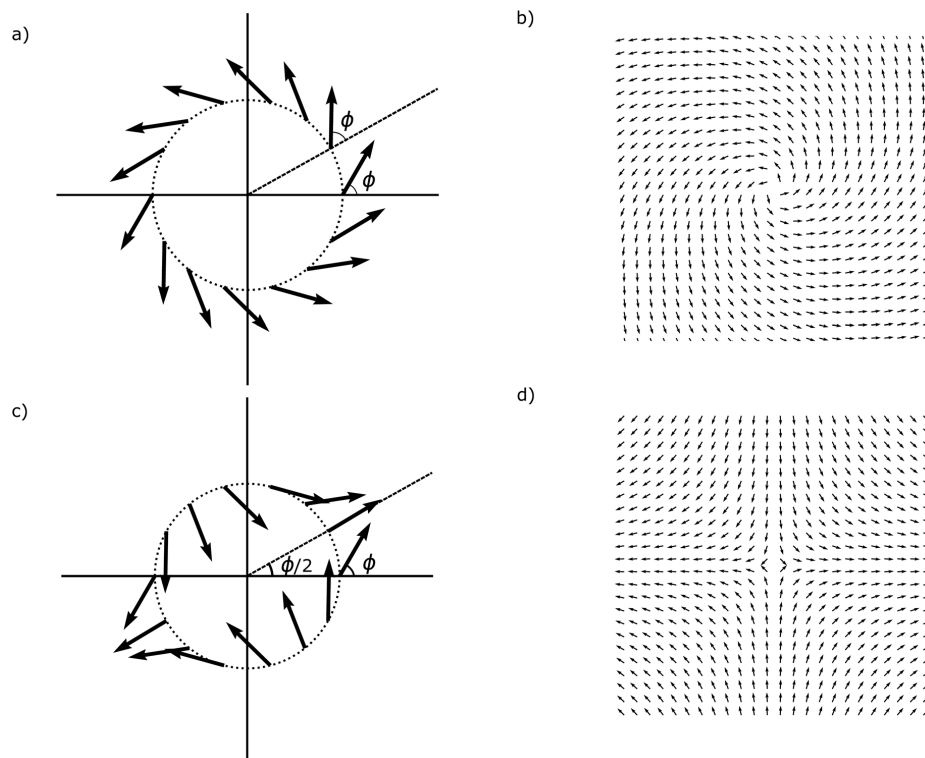


Fig. 1 Polarity field around the ± 1 topological defects. (a) and (b) Show a +1 defect, while (c) and (d) illustrate a -1 defect. The drawings (a) and (c) show the \vec{p} plotted on a circle with the angle ϕ marked. This illustrates why ϕ can be set to zero by a change of basis for the -1 defect and not for the +1 defect. (b) and (d) Show the polarity fields around a +1 defect with $\phi = \pi/3$ (spiral) and a -1 defect with $\phi = 0$ respectively (changing ϕ rotates the negative defect).

parameterise the polarity field centered on the n -th defect as $\psi = \psi_n e^{i\phi_n}$, where ϕ_n is the polarization induced by the n -th defect and ϕ_n is the background phase. Near the defect, the polarization vanishes linearly in magnitude where its phase becomes multivalued. This implies that $\psi_n = |\vec{r} - \vec{r}_n| e^{i\theta_n}$, with $\theta_n = q_n \arctan[(y - y_n)/(x - x_n)]$ being the singular phase.^{42,48} Within this approach, the general expression of the defect current density can be reduced to a closed expression for the defect velocity given by

$$\vec{v}_n = \vec{u}(\vec{r}_n) + 2q_n \nabla^\perp \phi_n |_{\vec{r}=\vec{r}_n}. \quad (12)$$

Using the stationary phase approximation, *i.e.* that the constant (equilibrium) phase remains stationary when it is punctuated by moving defect singularities, we can further simplify the defect velocity and express it in terms of the net spontaneous flow and the forces induced by the other defects as^{42,49}

$$\vec{v}_n = \vec{u}(\vec{r}_n) + 2 \sum_{k \neq n} q_n q_k \frac{\vec{r}_n - \vec{r}_k}{|\vec{r}_n - \vec{r}_k|^2}. \quad (13)$$

The topological defects interact through Coulomb-like forces, where like-signed defects repel, and opposite-signed defects attract each other. However, there are additional interactions through the flow field \vec{u} which depends on the dipolar active forces. In the next section, we derive analytic expressions for this flow velocity and discuss its effect on the defect motion.

3 Active flow fields around ± 1 topological defects

From the parameterization of the \vec{p} -field for a pointwise defect, we can evaluate the dipolar active force induced by an isolated defect with charge $q = \pm 1$ in an otherwise homogeneous polarity field with constant background orientation ϕ as

$$\vec{F}_a^+ = \frac{\tilde{z}_0}{\Gamma r^2} [\vec{r} \cos(2\phi) - \vec{r}^\perp \sin(2\phi)], \quad (14)$$

$$\vec{F}_a^- = -\frac{\tilde{z}_0}{\Gamma r} \mathbf{R}_{2\phi} [\cos(3\theta) \vec{e}_x - \sin(3\theta) \vec{e}_y], \quad (15)$$



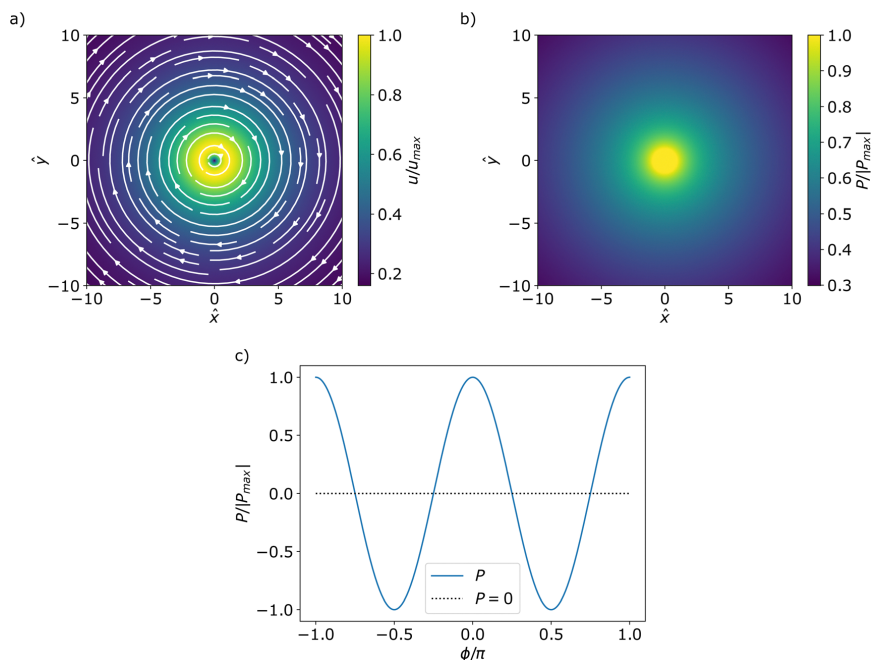


Fig. 2 Incompressible active flow streamlines (a) and corresponding pressure field (b) around an isolated +1 defect with $\sin(2\phi) > 0$ in an extensile ($\tilde{\alpha}_0 < 0$) system. The colormap shows the magnitude of the velocity and pressure normalized by their maximum. Note that the pressure in the far-field diverges with the system size L . Since the pressure diverges at the centre the pressure inside the core $r < 1$ has been set to the value that is used for the normalization. (c) Shows the normalised pressure, for an extensile system, at a fixed radius as a function of ϕ . Notice that for $\phi = \pm\pi/4 + \pi l$ the pressure vanishes.

where $\vec{r}^\perp = (y, -x)$, and $\mathbf{R}_{2\phi}$ is a matrix that rotates the vector by 2ϕ , and can be removed by a change of basis. Notice that the first term in \vec{F}_a^+ is a source of gradient flow, which however is removed by pressure through the incompressibility condition. The second term proportional to $\sin(2\phi)$ is related to a rotated gradient and induces a purely vortical flow.

We insert these forces into the integrals in eqn (8) and (9), and solve them as described in the Supplementary Material.⁵⁰ The resulting expressions for the active flow velocity and pressure for a +1 defect reduce to

$$u_a^+(r, \theta) = \frac{\tilde{\alpha}_0}{\zeta\Gamma\hat{r}}(1 - \hat{r}K_1(\hat{r}))e^{i(\theta+\pi/2)}\sin(2\phi), \quad (16)$$

$$P_a^+ = -\frac{\tilde{\alpha}_0}{\Gamma}\cos(2\phi)\ln\frac{L}{r}. \quad (17)$$

Here L is a cutoff scale set by the system size. We have written the velocity field as a complex field defined as $u = u_x + iu_y$, where r and θ are the polar coordinates centered at the defects position. We define the scaled radial coordinate as $\hat{r} = r/\zeta$, which is the same as changing the length scale to the hydrodynamic dissipation length ℓ_d (see Fig. 2, with the cutoff scale $L = 50$). Notice that the pressure is isotropic and its gradient

force cancels the radial component of the dipolar active force, thus no net pressure flow. Furthermore, the corresponding vorticity is also isotropic

$$\omega_a^+ = \frac{\tilde{\alpha}_0}{\Gamma\zeta^2}K_0(\hat{r})\sin(2\phi), \quad (18)$$

and is non-zero at the centre of the defect as evidenced also in Fig. 2. This has important consequences for the stability of vortex, spiral, or aster shaped positive defects as discussed in detail in ref. 15. The sign of the global circulation is modulated by the character of the +1 defect through ϕ .

Similarly, we find analytical expressions for the active flow velocity, pressure and vorticity related to the -1 defect, which are written in a compact form as

$$u_a^-(r, \theta) = -\frac{\tilde{\alpha}_0}{2\Gamma\zeta}(f_3^a(\hat{r})e^{-3i\theta} + f_5^a(\hat{r})e^{5i\theta}), \quad (19)$$

$$P_a^- = -\frac{\tilde{\alpha}_0}{4\Gamma r^4}(x^4 - 6x^2y^2 + y^4), \quad (20)$$

$$\omega_a^-(r, \theta) = -\frac{\tilde{\alpha}_0}{\Gamma\zeta^2}\sin 4\theta f_\omega^a(\hat{r}). \quad (21)$$



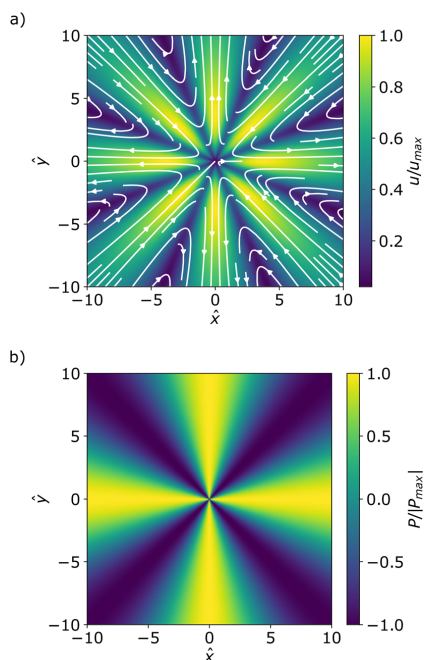


Fig. 3 Incompressible active flow streamlines (a) and corresponding pressure field (b) around an isolated -1 defect with $\phi = 0$ in an extensile ($\tilde{x}_0 < 0$) system. The colormaps show the normalised magnitude of velocity (a) and pressure (b).

The functions f_3^a, f_5^a , and f_ω^a giving the radial dependence of the velocity and vorticity are listed in the Appendix. This velocity and pressure fields are also plotted in Fig. 3 showing that while the positive defect has closed streamlines also in an infinite system, the negative defect has an 8-fold symmetry of the vorticity, underlying a 4-fold symmetry of the polarity field around the defect. The streamlines do not close in an infinite system, but in confinement they might close due to boundary conditions or influence from other defects similarly to the vortices formed around $\pm 1/2$ defects in an active nematic.^{21,51} It is important to note the distinctions of the analytical descriptions provided herein with a recent calculations of compressible flow fields inside circular confinements.⁴¹ In the latter, the analyses is restricted to circular domains with radius smaller than the coherence length $R^2 \ll K_p/A$, *i.e.* the limit where relaxation/penetration length in the free energy is larger than the system size. Those results are therefore in the opposite limit of the calculation performed here.

In addition to the characteristic flow fields, our closed form analytic descriptions provide an insight into the isotropic stress patterns, *i.e.*, half of the trace of the stress tensor, around full-integer topological defects. Such isotropic stresses have been shown to be a determining factor for the biological functionality of nematic defects, where concentration of compressive

stress around $+1/2$ defects was shown to lead to cell death and extrusion,²⁸ while the tensile stresses around $-1/2$ defects has been shown to lead to spontaneous gap opening in epithelial cell layers.⁵² Similarly, we find distinct isotropic stress patterns around positive and negative full-integer defects: while around a negative (-1) defect alternating regions of tension and compression appear in a 4-fold symmetric pattern (Fig. 3b), a strong augmentation of compressive stress is observed at the core of positive $+1$ defects (Fig. 2b). We conjecture that such a concentrated compressive stress at $+1$ defects could contribute to the activation of mechanosensitive signals in cell layer and potentially be linked to the recent observation of the cellular differentiation at $+1$ defect cores in cartilage cells.⁵³

3.1 Vortical flow reversal around $+1$ defect

The results presented above provide closed-form analytical expressions for incompressible flows around full-integer topological defects in polar active matter. Interestingly, in the absence of friction ($\Gamma = 0$), we predict that the vortical active flow around the $+1$ defect changes chirality on a lengthscale comparable with the coherence length outside of the defect core, thus the flow reversal is a near-defect behavior.

Note that that zero friction is a singular limit and the resulting flow equations have no natural lengthscale. Thus the rescaling is done with an appropriate lengthscale coming from the free energy, such as the coherence length. In this limit, the active flow velocity can be derived (details in the ESI[†]) to be on this form

$$u_a^\pm = \frac{i\tilde{x}_0}{4\tilde{\eta}} r(1 - 2\ln(r))e^{i\theta} \sin(2\phi). \quad (22)$$

The corresponding vorticity acquires logarithmic dependence with the distance from the defect

$$\omega_a^\pm = -\frac{\tilde{x}_0}{\tilde{\eta}} \sin(2\phi) \ln(r), \quad (23)$$

where $\tilde{\eta} = \eta/\zeta^2$. We notice that the vorticity changes handedness for $r = \sqrt{e} \approx 1.7$ (in coherence length), giving rise to two concentric, counter-rotating flows, as shown in Fig. 4.

Notice also that the flow diverges at $r \rightarrow \infty$ due to no screening lengthscale and at $r \rightarrow 0$ without adding a core size regularization in the integral solutions. We predict that the flow reversal is a near defect core effect when the far-field boundary conditions generate an opposite torque and disappears in the presence of hydrodynamic screening effects. The Green functions correspond to the homogeneous Dirichlet boundary conditions in an infinite domain. The mathematical reason for this flow reversal is that the logarithmic Greens function changes sign when $r < 1$ in units of the coherence length, unlike the Bessel function K_0 which maintains the same sign on length-scales larger than the hydrodynamic screening length. The flow reversal on a lengthscale comparable with the core size is validated in numerical simulations and this suggests that mutual defect interactions are not important for this near-defect flow changes as long as defects are well-separated.



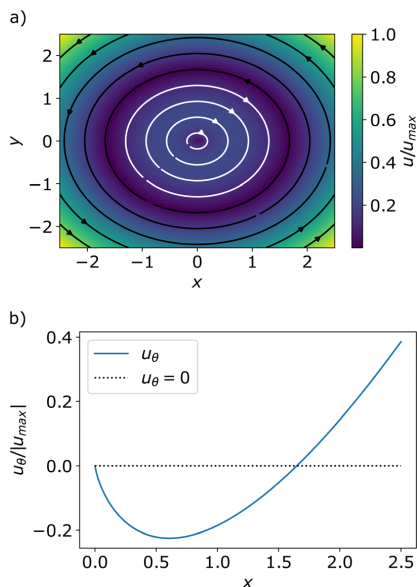


Fig. 4 (a) Streamlines of the theoretical active flow around an isolated +1 defect for $\sin(2\phi) > 0$ for an extensive system and $\Gamma = 0$. The colormap shows the flow magnitude normalized by its largest value in the plotted domain. The change in color of the streamlines from white to black highlight the flow reversal at $r \approx 1.7$. This is more apparent in (b) which is a cross section of the azimuthal velocity component along the positive x axis. The velocity changes sign when it crosses the zero line.

Similar flow reversal is also present in systems confined to circular domains that are small enough such that the energy scale can be treated as linearly dependent on the radial distance from the center of singularity $\chi(r) \sim r$ in the entire domain.⁴¹ For such systems the flow reversal happens inside the core region.

3.2 Comparison with numerical simulations

Here we discuss the comparison of the analytical predictions of active flow induced by ± 1 defects with those obtained from direct numerical simulations of the polarization evolution eqn (1) and (2) coupled with the Navier–Stokes equations

$$\rho(\partial_t \vec{u} + \vec{u} \cdot \nabla \vec{u}) = \alpha_0 \nabla \cdot \mathbf{Q} - \nabla P + \nabla \cdot \mathbf{s}_p, \quad \nabla \cdot \vec{u} = 0 \quad (24)$$

with the additional passive stresses $\sigma_p = \sigma_p^{\text{vis}} + \sigma_p^{\text{el}}$ as defined in ref. 34 and 54, including the viscous stress $\sigma_p^{\text{vis}} = 2\eta\mathbf{E}$, and the elastic stress $\sigma_p^{\text{el}} = \frac{\lambda + 1}{2} \vec{p}\vec{h} + \frac{\lambda - 1}{2} \vec{h}\vec{p} - \frac{\lambda}{2} (\vec{p} \cdot \vec{h}) \mathbf{I}$, where $\vec{h} = \partial F / \partial \vec{p}$ is the molecular field.

For numerical simulations, we use a hybrid lattice-Boltzmann method, combining finite-difference for the evolution of polarity and the lattice-Boltzmann method for that of velocity⁵⁵ (more details in the Appendix). Using the same prescription as in ref. 35 for density and viscosity, *i.e.* $\rho = 40$ and $\eta = 3.6$, we ensure that the Reynolds number in the

simulations remains negligible ($\text{Re} \ll 1$)^{18,56} so that the dynamics of velocity virtually reduces to the incompressible Stokes equations eqn (3) and (4) considered here. We fix the viscosity ratio to $\eta/\gamma = 3.6$, micro to macro length scale to $(\sqrt{K_p/A})/L = 2 \times 10^{-3}$ (assuring that the coherence length $\sqrt{K_p/A}$ is significantly smaller than the domain size L), and the flow alignment parameter to $\lambda = 0.1$. Dimensionless parameters in the simulations are defined similar to the theoretical parameters defined in Section 2.

Simulations were initialized with quiescent velocity field and noisy polar alignments close to the uniformly oriented state $\vec{p} = \vec{e}_x$ under periodic boundary conditions, on square domains of linear dimension $L = 256$. We consider sufficiently large values of the activity parameter $\bar{\alpha}_0 = \pm 1$ such that topological defects to form spontaneously.³⁵ For each simulation, we average the individual flow profiles in the vicinity of each defect over an ensemble of defects (ranging from $\approx 10^2$ to $\approx 10^3$). Because every defect has its own orientation, we have to carefully reorient the defects and the flows as described below.

We define the orientation of -1 defects from the surrounding polarization field \vec{p} . Given the 4-fold symmetry of the -1 defect (see Fig. 1(d)), we search for the two principal axes along which the \vec{p} vector points inwards and outwards, respectively, and rotate the local fields so the principal axes align.

For $+1$ defects, the baseline (intrinsic) phase ϕ plays an important role in distinguishing among vortices, asters and spirals and their orientation (see Fig. 1). We ensemble-average the vortical flow profile for these different types of $+1$ defects. For this, we identify the flow chirality of a $+1$ defect, by computing the sign of the circulation $\oint_C d\vec{l} \cdot \vec{u}$ along a contour C centered on the defect and with a radius smaller than the lengthscale of the flow reversal. For defects with clockwise flow chirality ($\oint_C d\vec{l} \cdot \vec{u} < 0$), the local polarization and velocity profiles are reversed, while for those with counterclockwise flow chirality, the fields are kept with the same orientation, so that all fields are consistently averaged.

The numerical results of the average polarization and flow around aster-like and vortex-like defects are shown in Fig. 5, and around -1 defects are presented in Fig. 6. For both types of defects, the average polarization (right panels in Fig. 5 and 6) has the same rotational symmetries as those corresponding to the polarity director in Fig. 1. However, we also notice that the magnitude of the average polarization \vec{p} varies with the distance to the defect and localises into different patterns, *i.e.* a halo around the $+1$ defect as in Fig. 5 and a “cross”-like pattern for the -1 defect as in Fig. 6. This cross pattern aligns with the principal axes of the 4-fold polarity director for contractile systems ($\bar{\alpha}_0 > 0$) and is rotated by $\pi/4$ for extensile systems ($\bar{\alpha}_0 < 0$) following the inward/outward flow directions. The average flow profile around a -1 defect has the 8-fold rotational symmetry as theoretically predicted for an isolated defect and appears both for extensile and contractile systems as shown in Fig. 6.

We now discuss the numerical results on the average vortical flows generated by aster-like and vortex-like defects in relation



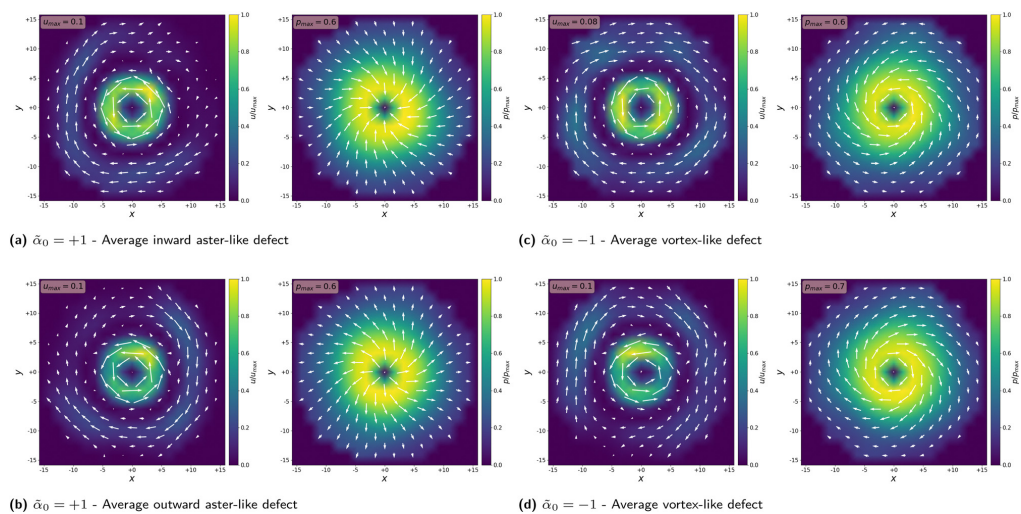


Fig. 5 Numerical average polarization \vec{p} and velocity \vec{v} profile around representative +1 aster-like (a) and (b) and vortex-like defects (c) and (d). Colormaps are scaled by the maximum magnitude in polarization and flow velocity, respectively. Averages are computed for ensembles of ≈ 400 defects as discussed in the Appendix (Fig. 11). Similar average profiles for lower activity are shown in Fig. 12.

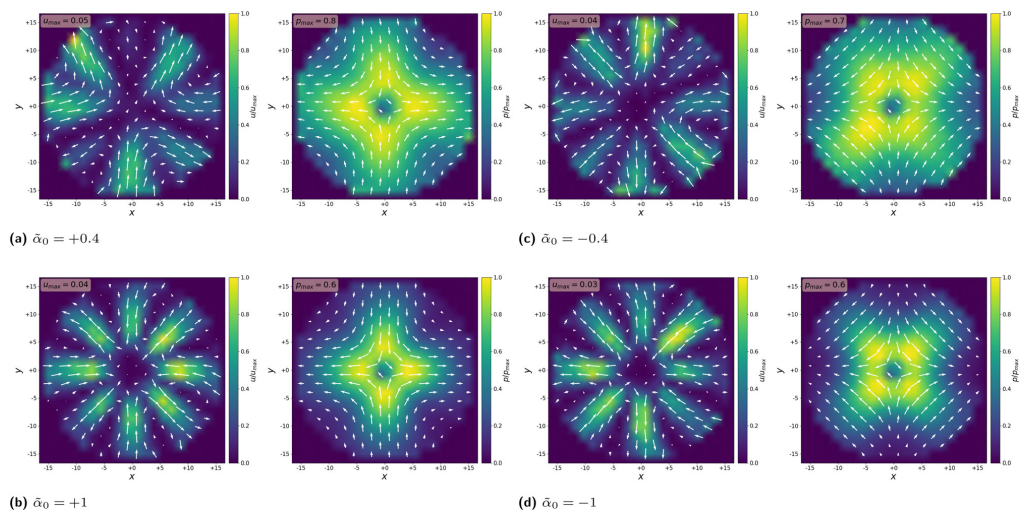


Fig. 6 Numerical average of the polarization \vec{p} and velocity \vec{v} fields around -1 defects, for various activities \bar{x}_0 . Colormaps are scaled by the maximum magnitude in polarization and flow velocity, respectively. For $\bar{x}_0 = \pm 1$, averages are computed from the same simulations as for +1 defects in Fig. 5, but for a larger ensemble of ≈ 1000 defects, since all -1 defects are of the same type. For the lower activity $\bar{x}_0 = \pm 0.4$, averages are computed for smaller ensembles of ≈ 100 defects.

to our theoretical prediction (Fig. 2 and 4). As shown in Fig. 5, we see the predicted flow reversal emerges robustly on the ensemble-average profiles. The counterclockwise flow direction close to the defect is a result of our averaging procedure. Given

that the vortical flow reverses its chirality near the defect cores on a statistical level as theoretically predicted for an isolated defect suggests that collective defect interactions are not crucial for this effect.



3.3 Defect pair interaction modulated by dipolar active forces

As seen in the above section, the dipolar active force does not lead to any defect self-propulsion for isolated ± 1 defects in an infinite domain. We now consider a pair of ± 1 defects and show that the dipolar active force leads to an interaction between them through the active flow. For analytic tractability, we consider the friction-dominated regime $\Gamma \gg \eta$ and set the viscosity to zero, $\ell_d \rightarrow 0$. The defect velocity is calculated using the methods from ref. 42 (see ref. 50 for details) and is given by

$$u_a^+ = \frac{\tilde{z}_0}{\Gamma R} e^{i(3\phi - 2\phi)} \left(\ln\left(\frac{R}{A}\right) - \frac{3}{2} \right), \quad (25)$$

$$u_a^- = \frac{\tilde{z}_0}{\Gamma R} \left(\frac{1}{6} e^{i(3\phi - 2\phi)} + \frac{1}{4} e^{i(2\phi - \phi)} \right), \quad (26)$$

for the +1 defect and -1 defect, respectively. Here A is a regularising lower cut-off corresponding to the finite defect core due to the divergent pressure at the +1 defect. R is the distance between the defects, ϕ is the angle of $\vec{R} = \vec{r}_- - \vec{r}_+$. ϕ is the uniform background orientation field. This effective interaction induced by dipolar active forces decays inversely proportional with the distance between defects similar to the Coulomb-like force induced by the phase gradients alone. However, these interactions are anisotropic since they depend on the orientation of the background polarization as well as the orientation of the defect pair.

4 The effect of polar active forces

Next, we also include the polar active force in the flow equations eqn (5) and study its contribution to the flow velocity u_p and pressure P_p . In dimensionless units, the polar active force is

$$\vec{F}_p = \tilde{\alpha}_p \vec{p}. \quad (27)$$

where $\tilde{\alpha}_p = \alpha_p \tau / (\xi \Gamma)$ is a rescaled parameter that measures the strength of polar active forces relative the frictional drag. We consider $\alpha_p > 0$ corresponding to polar particles moving in the direction of their head. The corresponding flow velocity and pressure fields can now be written compactly as (see details in SM⁵⁰)

$$u_p^+(r, \theta) = i \tilde{\alpha}_p e^{i\theta} \sin(\phi) f_1^p(r), \quad (28)$$

$$P_p^+(r, \theta) = \tilde{\alpha}_p r \cos(\phi), \quad (29)$$

$$u_p^-(r, \theta) = \frac{\tilde{\alpha}_p}{2} (f_1^p(r) e^{-i\theta} + f_3^p(r) e^{3i\theta}), \quad (30)$$

$$P_p^-(r, \theta) = \frac{\tilde{\alpha}_p}{3} \frac{(x^2 - y^2)}{r}. \quad (31)$$

for the positive and the negative defect respectively. The velocity profiles are plotted in the Fig. 7 while the functions f_1 and f_3 are plotted in Fig. 8 together with their asymptotic values. It is straightforward to show that both f_1 and f_3 tend to zero at the defect origin, thus the polar active forces do not contribute to defect self-induced motility. It is important to

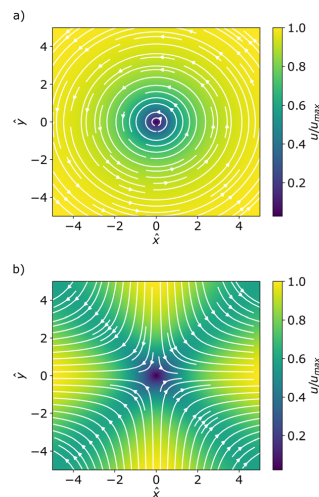


Fig. 7 Velocity streamlines due to polar active forces for (a) the positive defect (vortex flow) and (b) the negative defect (saddle-point flow). Color-map represents the magnitude of the velocity field normalized by its maximum value.

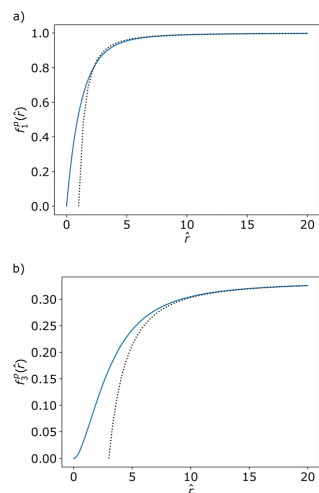


Fig. 8 Plot of the functions (blue, whole lines) f_1^p (a) and f_3^p (b) against their asymptotic limits (black, dotted lines) as given in eqn (32) and (33). Note that the functions asymptotically approach to non-zero values in the far-field.

note that the flow induced by polar active forces around the +1 defect is proportional to $\sin(\phi)$, instead of the $\sin(2\phi)$ dependence that was found for the flow induced by dipolar active forces eqn (16). This means that while the polar active forces do not produce any flow around an ideal aster ($\phi = 0$), there will be



a polar activity-induced flow around an ideal vortex ($\phi = \pi/2$). Furthermore, eqn (29) shows that the pressure is proportional to the radial distance $\sim r$, indicating that, in the absence of any far-field screenings from other defects, the pressure can become quite large. This is related to the flow induced by polar active forces being constant in magnitude in the far-field, as illustrated in Fig. 8, or by explicitly writing the asymptotic limits

$$u_p^-(\hat{r}, \theta) = \frac{\tilde{\alpha}_p}{2} \left[\left(e^{-i\theta} + \frac{1}{3} e^{3i\theta} \right) - \frac{1}{\tilde{r}^2} [e^{-i\theta} + 3e^{3i\theta}] \right], \quad (32)$$

$$u_p^+(\hat{r}, \theta) = i\tilde{\alpha}_p e^{i\theta} \sin\phi \left(1 - \frac{1}{\tilde{r}^2} \right), \quad (33)$$

for the negative and positive defect, respectively. As we will show explicitly for a pair of defects in the next section, eqn (32) and (33), together with eqn (13), indicate that there are strong interactions between defects regardless of the distance between them.

From the closed form formulas of the flow velocity around the defects, the far-field vorticity induced by the +1 defect can be calculated as

$$\omega_p^+ = \frac{\tilde{\alpha}_p}{\zeta} \sin\phi \left(\frac{1}{\tilde{r}} + \frac{1}{\tilde{r}^3} \right), \quad (34)$$

and, for the -1 defect, this is

$$\omega_p^- = \frac{2\tilde{\alpha}_p}{\zeta} \sin 2\theta \left(\frac{1}{\tilde{r}} - \frac{3}{\tilde{r}^3} \right). \quad (35)$$

Interestingly the vorticity of the +1 defect is independent on the baseline/intrinsic angle θ , which is also true in the near-field, because we can write the velocity field in the form $\tilde{u} = \tilde{r}^\perp f(\tilde{r})$. As such, close to the defect center the vorticity of the negative defect vanishes at the center, while the positive defects has a finite vorticity

$$\omega_p^+(r=0) = \frac{\tilde{\alpha}_p \pi}{2\zeta} \sin(\phi), \quad (36)$$

indicating that the +1 defect acquire a rotational motion in addition to their translational motion.

4.1 Defect-pair interaction in friction-dominated system

Taking again the analytically tractable limit of zero viscosity, we can find the velocity induced by polar active forces for a pair of oppositely-charged defects following the approach from Section 3.3. The flow velocities in the centre of the ± 1 defects reduce to

$$\tilde{u}_p^+ = \frac{\tilde{\alpha}_p}{2|\tilde{R}|^2} \tilde{R}^\perp (\tilde{R}^\perp \cdot \hat{p}_0), \quad (37)$$

$$\tilde{u}_p^- = \frac{\tilde{\alpha}_p}{6|\tilde{R}|^2} \tilde{R}^\perp (\tilde{R}^\perp \cdot \hat{p}_0) + \frac{\alpha_p}{3|\tilde{R}|^2} \tilde{R} (\tilde{R} \cdot \hat{p}_0), \quad (38)$$

where $\tilde{R} = \tilde{r}^- - \tilde{r}^+$ is the separation vector between the negative defect and the positive one, and $\hat{p}_0 = \cos(\phi)\tilde{e}_x + \sin(\phi)\tilde{e}_y$ is the uniform background polarity. Interestingly, the polar active forces induce non-reciprocal and non-local mutual interactions

that depend only on the orientation of \tilde{R} relative to ϕ , independent of the separation distance R between the defects. This suggests a truly long-ranged interaction between oppositely-charged defects in the presence of polar active forces.

Furthermore, the -1 defect tends to move towards/away from +1 depending on the orientation angle of \tilde{R} with respect to \hat{p} . Both defects move perpendicular to \tilde{R} but at different rates inducing the pair to rotate. We can see this behavior more clearly by looking at the defect pair velocity under polar active forces alone, $\dot{\tilde{R}} = \tilde{u}_p^- - \tilde{u}_p^+$ given by

$$\frac{d}{dt} \tilde{R} = \frac{\tilde{\alpha}_p}{3R^2} (\tilde{R} \cdot \hat{p}_0) \tilde{R} - \frac{\tilde{\alpha}_p}{3R^2} (\tilde{R}^\perp \cdot \hat{p}_0) \tilde{R}^\perp, \quad (39)$$

where the first term ($\parallel \tilde{R}$) is an attraction/repulsion force between the defects, while the second term ($\perp \tilde{R}$) rotates the defect pair. The rotation is zero, when the defect pair aligns with the background polarization in either directions ($\tilde{R} \parallel \hat{p}_0$). We show in SM⁵⁰ that the defect pair rotates until annihilation, unless \tilde{R} is initially parallel to \hat{p}_0 . For initial orientations where $\tilde{R} \cdot \hat{p}_0 > 1$, the defects first move a part while re-orientating such that they attract each other. Namely, as long as $\tilde{R}^\perp \cdot \hat{p}_0 \neq 0$, the separation vector \tilde{R} will rotate until $\tilde{R} \cdot \hat{p}_0$ becomes negative and the defects move toward each other (see SM⁵⁰ for the derivation). The rate of defect annihilation is thus dependent on the initial orientation. This shows that the polar active force leads to pair annihilation of oppositely-charged defects to promote large-scale polar order.

To check this dynamics numerically, we compare the pair trajectory determined by eqn (13) with that predicted by the full hydrodynamic model from integrating eqn (1), (3) and (4) with the same initial configuration. The initial uniform polarisation $\tilde{p} = \tilde{e}_y$ is seeded with a defect pair in the x -direction, *i.e.* $\tilde{r}_- = -20\tilde{e}_y$ and $\tilde{r}_+ = -20\tilde{e}_x$, such that $\tilde{R} \perp \hat{p}_0$ at $t = 0$. The model parameters are set to $\tilde{\alpha}_p = 0.5$, $\tilde{\alpha}_0 = 0$, $\lambda = 0$ and $\zeta^2 = 0.01$. The hydrodynamic equations are solved with periodic boundary conditions in a domain 256×256 with a spatial discretisation $\Delta = 0.5$, using spectral methods and an exponential time differentiation scheme.⁵⁷ Under the polar active force, the separation vector \tilde{R} rotates relative to \hat{p}_0 , and this changes the shape of the +1 defect from an initial vortex to an aster at the annihilation time. This effect is lost in the absence of polar active forces, *i.e.* at $\tilde{\alpha}_p = 0$ (see animations of the defect pair annihilation in ref. 50).

The two trajectories are shown in Fig. 9(a) and agree very well for large $R = |\tilde{R}|$ in consistency with the pointwise approximation. It also shows that polar active forces increase the annihilation rate. This is further evidenced in Fig. 9(b) where we compare the evolution of the separation distance $R(t)$ when the two defects interact through the Coulomb-like forces with or without the presence of polar active forces. At $\tilde{\alpha}_p = 0$, $R(t)$ decreases in the far-field as $\sqrt{t_0 - t}$ (t_0 being the annihilation time) due to the $1/R$ interaction forces. However, for $\tilde{\alpha}_p \neq 0$, the annihilation timescale is greatly reduced and the deviations from the $\sqrt{t_0 - t}$ behavior arise due the non-local and



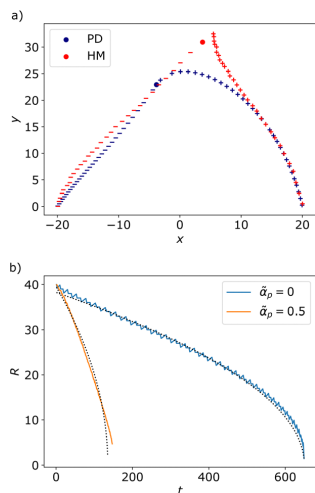


Fig. 9 (a) Phase portraits of the defect pair trajectory obtained from (blue) the kinematics of point defects (PD) from eqn (13), and (red) by direct simulation of the hydrodynamic model (HM) with identical initial condition of the defect pair at $\vec{r}_{\pm} = \pm 20\vec{e}_x$ with the homogeneous background polarization being $\vec{p}_0 = \vec{e}_y$. The +1 defect is marked by +, the -1 by -. $\tilde{\alpha}_p = 0.5$, $\tilde{\alpha}_0 = 0$, $\lambda = 0$ and $\zeta^2 = 0.01$. (b) Distance R between a defect pair as a function of time for Coulomb-like interactions only (blue curve) and in the presence of polar active forces (orange curve). The black dotted lines are fitting curves with the $R(t) = \sqrt{At + B}$ found by linear regression on R^2 .

non-reciprocal attraction force. The rotation rate is also contributing to aligning the defects to increase the attraction between the defects.

5 Discussion/conclusion

In summary, we present theoretical derivations of incompressible flow fields and dynamics of ± 1 defects under dipolar and polar active forces. These active forces do not endow the full-integer defects with any self-propulsion, as expected from the symmetry of the defects. However, the +1 defect acquires a non-zero active torque due to both polar and dipolar active forces. We show that the strength of this spin is dependent on whether the defect is a vortex, aster or spiral. In the absence of hydrodynamic screening due to friction, the vortical active flow around a +1 vortex changes sign on a length scale set by the coherence length as observed in numerical simulations and predicted analytically. For both defects, the dipolar active force contribution to the flow field vanishes with $1/r$ in the defect far-field, whereas the polar active force contribution approach a constant value. Remarkably, polar active forces mediate mutual interaction between oppositely-charged defect pairs in a manner that renders defect-defect interactions independent of the distance between the defect pair. We have shown that, under these polar active forces, a pair of oppositely-charged defects rotates to align with the background polarization field, while

the negative defect chases the positive one until annihilation. The rate of annihilation is greatly enhanced by polar active forces, and this is the main underlying mechanism for the suppression of defect-laden active turbulence in polar active matter as reported numerically in ref. 35. This effect of polar active forces has been studied so far for flat surfaces. It would be interesting to explore this effect further for curved surfaces where additional topological constraints are present.^{24,58}

Author contributions

J. Rø contributed with analytical derivations, numerical simulations, visualisation and data analysis. J. Re contributed with lattice-Boltzmann simulations, visualisation and data analysis. A. D. and L. A. formulated the project and contributed with supervision. A. D. provided computational resources. L. A. checked the analytical calculations. All authors contributed with drafting and writing the manuscript.

Conflicts of interest

There are no conflicts to declare.

Appendices

A1. Analytical expression of the functions defining the active flow fields

Here we write down the radially-dependent functions associated with the flow fields induced by polar and dipolar active forces. Derivation details are found in the SM.⁵⁰ The radial functions for the dipolar active flow velocity are:

$$f_3^d(\hat{r}) = \frac{1}{\hat{r}}[1 - \hat{r}K_1(\hat{r})] - \frac{2}{\hat{r}^3}[4 - \hat{r}^3K_1(\hat{r}) - 2\hat{r}^2K_2(\hat{r})], \quad (40)$$

$$f_3^d(\hat{r}) = \frac{1}{\hat{r}}[1 - \hat{r}K_1(\hat{r})] - \frac{6}{\hat{r}^3}[4 - \hat{r}^3K_1(\hat{r}) - 2\hat{r}^2K_2(\hat{r})] + \frac{6}{\hat{r}^5}[64 - 4\hat{r}^2(8 + \hat{r}^2)K_0(\hat{r}) - \hat{r}(8 + \hat{r}^2)^2K_1(\hat{r})]. \quad (41)$$

The radial function for the corresponding vorticity field

$$f_\omega^d(\hat{r}) = \frac{1}{\hat{r}^4}(-48 + 4\hat{r}^2 + \hat{r}^2(24 + \hat{r}^2)K_0(\hat{r}) + 8\hat{r}(6 + \hat{r}^2)K_1(\hat{r})). \quad (42)$$

The radial functions for the polar active flow velocity are:

$$f_1^p(\hat{r}) = 1 - \hat{r}K_1(\hat{r}) + \frac{\pi}{2}I_1(\hat{r}) + \sum_{k,n=0}^{\infty} \kappa_1(n, k) \frac{\hat{r}^{2k+2}}{((2k)!!)^2} + \sum_{k,n=0}^{\infty} \kappa_2(n, k) \left[\ln\left(\frac{\hat{r}}{2}\right) - \psi^{(0)}(k+1) \right] \frac{\hat{r}^{2k+2}}{((2k)!!)^2}, \quad (43)$$

and

$$f_3^p(\hat{r}) = -\frac{\pi}{2}I_3(\hat{r}) + \sum_{k,n=0}^{\infty} \kappa_3(n, k) \frac{\hat{r}^{2k+2}}{((2k)!!)^2} + \sum_{k,n=0}^{\infty} \kappa_4(n, k) \frac{\hat{r}^{2k+2}}{((2k)!!)^2} \left[\ln\left(\frac{\hat{r}}{2}\right) - \psi^{(0)}(k+1) \right]. \quad (44)$$



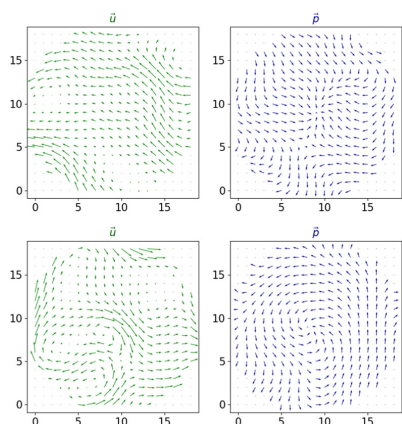


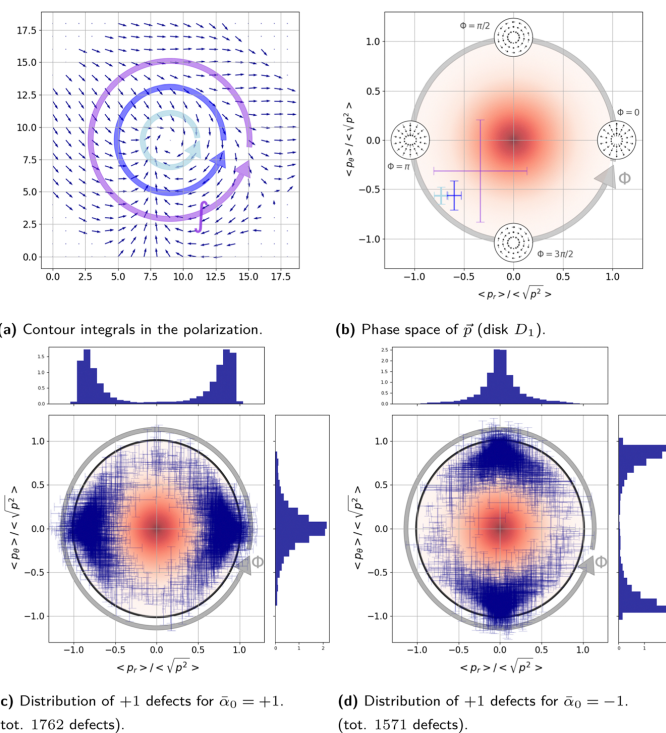
Fig. 10 Velocity and polarisation fields in the vicinity of individual (+1) defects for $\bar{\alpha}_0 = +1$.

Where $\psi^{(0)}$ is the digamma function. The coefficients of the infinite power series are

$$\kappa_1(n, k) = - \left(\frac{(2n-1)!!}{(2n)!!} \right)^2 \frac{1}{2n+2} \times \left(\frac{1}{(2n-1-2k)^2} + \frac{1}{4} \frac{2n+1}{(2n+2)(n+2+k)^2} \right) \quad (45)$$

$$\kappa_2(n, k) = \left(\frac{(2n-1)!!}{(2n)!!} \right)^2 \frac{1}{2n+2} \times \left(\frac{2n+1}{2(2n+2)(n+2+k)} - \frac{1}{2n-1-2k} \right), \quad (46)$$

$$\kappa_3(n, k) = \left(\frac{(2n-1)!!}{(2n)!!} \right)^2 \times \left(\frac{2n+1}{4(3-2n)(1-2n)(n+k+1)^2} + \frac{2n}{(2n+4)(2n+2)(2n-1-2k)^2} \right), \quad (47)$$



(c) Distribution of +1 defects for $\bar{\alpha}_0 = +1$. (tot. 1762 defects).

(d) Distribution of +1 defects for $\bar{\alpha}_0 = -1$. (tot. 1571 defects).

Fig. 11 Distribution of +1 defects in the phase space of polarization \vec{p} given by the D_1 disk.



$$\kappa_4(n, k) = \left(\frac{(2n-1)!!}{(2n)!!} \right)^2 \times \left(\frac{2n}{(2n+4)(2n+2)(2n-1-2k)} - \frac{2n+1}{2(3-2n)(1-2n)(n+k+1)} \right). \quad (48)$$

Note that when summing over n the coefficients $\kappa_4(n, k)$ tends to zero for any k . The infinite series are convergent, but slowly.

A2. Details on the numerical simulations

Numerical and modeling framework. We solve the hydrodynamic model eqn (1) and (2) using a hybrid lattice-Boltzmann and finite difference method^{34,35,55} with periodic boundary conditions on square domains $L \times L$ of size $L = 256$. All simulations are run for model parameters set to $K_p = 0.04$, $A = 0.01$, $\gamma = 1$, $\lambda = 0.1$. This fixes the rescaling units, *i.e.* the nematic coherence length $\zeta = \sqrt{K_p/A} \simeq 0.6$ and a characteristic time $\tau = \gamma/A = 100$. We also fix the shear viscosity such that $\eta/\gamma = 3.6$, and the density to $\rho = 40$, thus ensuring that the Reynolds number in the simulation remains negligible

($Re \ll 1$)^{18,56} and that the dynamics of velocity virtually reduces to the incompressible Stokes equations eqn (3) and (4) considered here. We then run simulations in the frictionless regime ($\Gamma = 0$), for four different values of activity, namely $\alpha_0 \in \{-1, -0.4, +0.4, +1\}$. In the discretisation scheme, we use the space unit $\Delta x = 1$ and time increment $\Delta t = 1$ for the set values of the model parameters.

Simulations were initialized with a quiescent velocity field and noisy, but reproducible polar alignments close to the uniformly oriented state $\vec{p} = \vec{e}_x$, using known random seeds. To collect the individual flow and polarity fields for the ensemble averages, we save a 100 frames with fixed sampling time $n_s = 200$, excluding the first 40 frames to discard early transients from the analysis. In Fig. 10, we illustrate the flow and polarization pattern around individual defects. The pattern of the polarization field (right panels) is aster-like (top) or vortex-like (bottom). We notice that the individual flow profile (left panels) is highly fluctuating while the vortical flow pattern emerges upon averaging out these fluctuations. We identify the type of the topological defect by the circulation of the polarization around the defect as illustrated in Fig. 11(a) and plot them in the phase space of the polarization vector \vec{p}

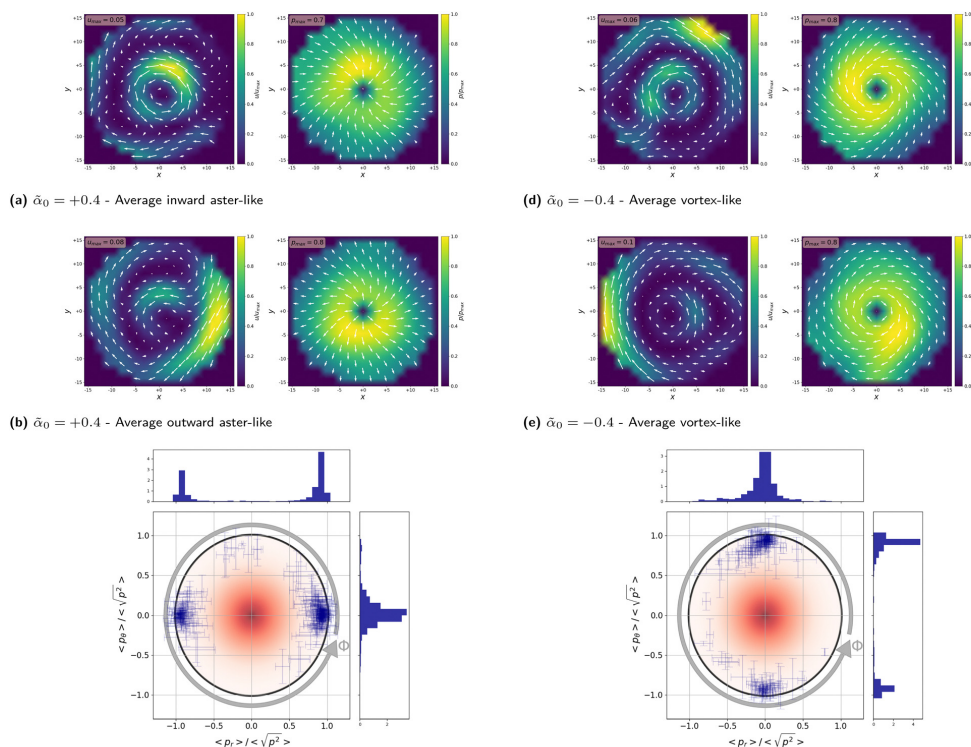


Fig. 12 Analysis of the flow and polarization profile around +1 defects for $\bar{\alpha}_0 = \pm 0.4$.



corresponding to the unit disk D_1 as shown in panel (b). Panels (c) and (d) represent the distributions of the +1 defects from the two of our simulations with $\tilde{z}_0 = \pm 1$ showing that for extensile systems ($\tilde{z}_0 < 0$) most defects are vortex-like, while for contractile ones ($\tilde{z}_0 > 0$) there are mostly aster-like defects. We group the defects accordingly to compute the average fields shown in Fig. 5, after assessing the flow chirality as described in the main text. A similar analysis is carried out for smaller activity $\tilde{z}_0 = \pm 0.4$ and shown in Fig. 12.

Simulation platform. We ran all our simulations on Copenhagen University HPC (High-Performance-Computing) cluster, using the collaborative MASS (Many Active Systems Simulations) program, on which several labs in Europe actively collaborate. This program takes a model definition as an input, under the form of a C++ file, along with a runcard (.dat file) specifying the values to assign to the different parameters.

Acknowledgements

J. Rø and L. A. acknowledge support from the Research Council of Norway through the Center of Excellence funding scheme, Project No. 262644 (PoreLab). A. D. acknowledges funding from the Novo Nordisk Foundation (grant No. NNF18SA0035142 and NERD grant No. NNF21OC0068687), Villum Fonden Grant no. 29476, and the European Union via the ERC-Starting Grant PhysCoMeT. Views and opinions expressed are however those of the authors only and do not necessarily reflect those of the European Union or the European Research Council. Neither the European Union nor the granting authority can be held responsible for them.

Notes and references

- 1 A. Doostmohammadi, J. Ignés-Mullol, J. M. Yeomans and F. Sagués, *Nat. Commun.*, 2018, **9**, 1–13.
- 2 M. C. Marchetti, J.-F. Joanny, S. Ramaswamy, T. B. Liverpool, J. Prost, M. Rao and R. A. Simha, *Rev. Mod. Phys.*, 2013, **85**, 1143.
- 3 C. Blanch-Mercader, V. Yashunsky, S. Garcia, G. Duclos, L. Gioni and P. Silberzan, *Phys. Rev. Lett.*, 2018, **120**, 208101.
- 4 S.-Z. Lin, W.-Y. Zhang, D. Bi, B. Li and X.-Q. Feng, *Commun. Phys.*, 2021, **4**, 1–9.
- 5 T. Sanchez, D. T. Chen, S. J. DeCamp, M. Heymann and Z. Dogic, *Nature*, 2012, **491**, 431–434.
- 6 P. Guillamat, J. Ignés-Mullol and F. Sagués, *Nat. Commun.*, 2017, **8**, 1–8.
- 7 D. Needleman and Z. Dogic, *Nat. Rev. Mater.*, 2017, **2**, 17048.
- 8 N. Kumar, R. Zhang, J. J. de Pablo and M. L. Gardel, *Sci. Adv.*, 2018, **4**, eaat7779.
- 9 A. Kudrolli, G. Lumay, D. Volfson and L. S. Tsimring, *Phys. Rev. Lett.*, 2008, **100**, 058001.
- 10 K. Kruse, J.-F. Joanny, F. Jülicher, J. Prost and K. Sekimoto, *Eur. Phys. J. E: Soft Matter Biol. Phys.*, 2005, **16**, 5–16.
- 11 J. Toner and Y. Tu, *Phys. Rev. Lett.*, 1995, **75**, 4326.
- 12 F. Jülicher, K. Kruse, J. Prost and J.-F. Joanny, *Phys. Rep.*, 2007, **449**, 3–28.
- 13 L. Gioni, M. J. Bowick, X. Ma and M. C. Marchetti, *Phys. Rev. Lett.*, 2013, **110**, 228101.
- 14 S. Ramaswamy, R. A. Simha and J. Toner, *Europhys. Lett.*, 2003, **62**, 196.
- 15 K. Kruse, J.-F. Joanny, F. Jülicher, J. Prost and K. Sekimoto, *Phys. Rev. Lett.*, 2004, **92**, 078101.
- 16 R. A. Simha and S. Ramaswamy, *Phys. Rev. Lett.*, 2002, **89**, 058101.
- 17 S. P. Thampi, R. Golestanian and J. M. Yeomans, *Philos. Trans. R. Soc., A*, 2014, **372**, 20130366.
- 18 A. Doostmohammadi, T. N. Shendruk, K. Thijsen and J. M. Yeomans, *Nat. Commun.*, 2017, **8**, 1–7.
- 19 S. Chandragiri, A. Doostmohammadi, J. M. Yeomans and S. P. Thampi, *Phys. Rev. Lett.*, 2020, **125**, 148002.
- 20 L. Gioni, M. J. Bowick, X. Ma and M. C. Marchetti, *Phys. Rev. Lett.*, 2013, **110**, 228101.
- 21 J. Rønning, C. M. Marchetti, M. J. Bowick and L. Angheluta, *Proc. R. Soc., A*, 2022, **478**, 20210879.
- 22 P. M. Chaikin and T. C. Lubensky, *Frontmatter*, Cambridge University Press, 1995, pp. i–vi.
- 23 A. Doostmohammadi and B. Ladoux, *Trends Cell Biol.*, 2021, **32**(2), 140–150.
- 24 S. Shankar, A. Souslov, M. J. Bowick, M. C. Marchetti and V. Vitelli, *Nat. Rev. Phys.*, 2022, **4**, 380–398.
- 25 S. J. DeCamp, G. S. Redner, A. Baskaran, M. F. Hagan and Z. Dogic, *Nat. Mater.*, 2015, **14**, 1110–1115.
- 26 G. Duclos, C. Blanch-Mercader, V. Yashunsky, G. Salbreux, J.-F. Joanny, J. Prost and P. Silberzan, *Nat. Phys.*, 2018, **14**, 728–732.
- 27 O. J. Meacock, A. Doostmohammadi, K. R. Foster, J. M. Yeomans and W. M. Durham, *Nat. Phys.*, 2021, **17**, 205–210.
- 28 T. B. Saw, A. Doostmohammadi, V. Nier, L. Kocgozlu, S. Thampi, Y. Toyama, P. Marcq, C. T. Lim, J. M. Yeomans and B. Ladoux, *Nature*, 2017, **544**, 212–216.
- 29 G. Duclos, C. Erlenkämper, J.-F. Joanny and P. Silberzan, *Nat. Phys.*, 2017, **13**, 58–62.
- 30 C. Malinverno, S. Corallino, F. Giavazzi, M. Bergert, Q. Li, M. Leoni, A. Disanza, E. Frittoli, A. Oldani and E. Martini, *et al.*, *Nat. Mater.*, 2017, **16**, 587–596.
- 31 A. Baskaran and M. C. Marchetti, *Phys. Rev. E*, 2008, **77**, 011920.
- 32 A. Baskaran and M. C. Marchetti, *J. Stat. Mech.: Theory Exp.*, 2010, **2010**, P04019.
- 33 A. Baskaran and M. C. Marchetti, *Eur. Phys. J. E: Soft Matter Biol. Phys.*, 2012, **35**, 1–8.
- 34 A. Amiri, R. Mueller and A. Doostmohammadi, *J. Phys. A: Math. Theor.*, 2022, **55**, 094002.
- 35 B. H. Andersen, J. Renaud, J. Rønning, L. Angheluta and A. Doostmohammadi, *Phys. Rev. Fluids*, 2023, **8**, 063101.
- 36 A. Ardaševa and A. Doostmohammadi, *Nat. Rev. Phys.*, 2022, **4**, 354–356.
- 37 P. Guillamat, C. Blanch-Mercader, G. Pernollet, K. Kruse and A. Roux, *Nat. Mater.*, 2022, **21**, 588–597.



- 38 T. Brandstätter, D. B. Brückner, Y. L. Han, R. Alert, M. Guo and C. P. Broedersz, *Nat. Commun.*, 2023, **14**, 1643.
- 39 T. H. Tan, A. Amiri, I. Seijo-Barandiarán, M. F. Staddon, A. Materne, S. Tomas, C. Duclut, M. Popovic, A. Grapin-Botton and F. Jülicher, *bioRxiv*, 2022, preprint, DOI: [10.1101/2022.09.29.510101](https://doi.org/10.1101/2022.09.29.510101).
- 40 Y. Maroudas-Sacks, L. Garion, L. Shani-Zeribib, A. Livshits, E. Braun and K. Keren, *Nat. Phys.*, 2021, **17**, 251–259.
- 41 C. Blanch-Mercader, P. Guillamat, A. Roux and K. Kruse, *Phys. Rev. E*, 2021, **103**, 012405.
- 42 L. Angheluta, Z. Chen, M. C. Marchetti and M. J. Bowick, *New J. Phys.*, 2021, **23**, 033009.
- 43 S. Chandragiri, A. Doostmohammadi, J. M. Yeomans and S. P. Thampi, *Soft Matter*, 2019, **15**, 1597–1604.
- 44 A. Doostmohammadi, M. F. Adamer, S. P. Thampi and J. M. Yeomans, *Nat. Commun.*, 2016, **7**, 1–9.
- 45 X. Tang and J. V. Selinger, *Soft Matter*, 2017, **13**, 5481–5490.
- 46 G. F. Mazenko, *Phys. Rev. Lett.*, 1997, **78**, 401.
- 47 B. Halperin, *proceedings of Les Houches, Session XXXV 1980* NATO ASI, ed. R. Balian, M. Kléman and J.-P. Poirier, published in *Physics of Defects*, 1981.
- 48 L. M. Pismen *et al.*, *Vortices in nonlinear fields: From liquid crystals to superfluids, from non-equilibrium patterns to cosmic strings*, Oxford University Press, 1999, vol. 100.
- 49 F. Vafa, M. J. Bowick, M. C. Marchetti and B. I. Shraiman, 2020, arXiv:2007.02947.
- 50 ESI, https://github.com/jonasron/SM_Flowfield_Polar.
- 51 L. Giomi, M. J. Bowick, P. Mishra, R. Sknepnek and M. Cristina Marchetti, *Philos. Trans. R. Soc., A*, 2014, **372**, 20130365.
- 52 S. Sonam, L. Balasubramaniam, S.-Z. Lin, Y. M. Y. Ivan, I. Pi-Jaumà, C. Jebane, M. Karnat, Y. Toyama, P. Marcq and J. Prost, *et al.*, *Nat. Phys.*, 2022, 1–10.
- 53 E. Makhija, Y. Zheng, J. Wang, H. R. Leong, R. B. Othman, E. X. Ng, E. H. Lee, L. Tucker-Kellogg, Y. H. Lee and H. Yu *et al.*, *bioRxiv*, 2022.
- 54 J. Prost, F. Jülicher and J. F. Joanny, *Nat. Phys.*, 2015, **11**, 111–117.
- 55 D. Marenduzzo, E. Orlandini, M. E. Cates and J. M. Yeomans, *Phys. Rev. E: Stat., Nonlinear, Soft Matter Phys.*, 2007, **76**, 031921.
- 56 S. P. Thampi, R. Golestanian and J. M. Yeomans, *EPL*, 2014, **105**, 18001.
- 57 S. M. Cox and P. C. Matthews, *J. Comput. Phys.*, 2002, **176**, 430–455.
- 58 F. C. Keber, E. Loiseau, T. Sanchez, S. J. DeCamp, L. Giomi, M. J. Bowick, M. C. Marchetti, Z. Dogic and A. R. Bausch, *Science*, 2014, **345**, 1135–1139.



Appendices

Appendix A

**Supplementary information for
Paper (IV)**

A unified field theory of topological defects and non-linear local excitations

Supplementary Information

Vidar Skogvoll, Jonas Rønning, Marco Salvalaglio, and Luiza Angheluta

SUPPLEMENTARY NOTES

For the proofs in this section, we follow the notation conventions of Ref. [1]. We consider topological defects for \mathcal{S}^k order parameters, which is the space consisting of $(k + 1)$ -dimensional unit vectors. It is known that the i -th homotopy group of \mathcal{S}^k is trivial for $i < k$. In particular, every loop ($i = 1$) on the two-sphere ($k = 2$) can be reduced to a point by a continuous deformation. Thus, to get a description of the topological defects for \mathcal{S}^k order parameters, we need to consider the k -th homotopy groups $\pi_k(\mathcal{S}^k) \simeq \mathbb{Z}$ corresponding to topological defects with integer charges. The dimension of the defect is given by $d_{\text{top}} = d - (k + 1)$, where d is the physical space dimension. The homotopy classification of loops in \mathcal{S}^k is useful beyond the direct application to models from this group because, in many systems, their order parameter space can be mapped or decomposed into products of \mathcal{S}^k spaces. We define an order parameter $\Psi = (\Psi_1, \dots, \Psi_n)$ which resides in the order parameter space \mathcal{D}^n . The subvolume of \mathcal{D}^n swept by Ψ and $n - 1$ independent variations $\{d\Psi^{(k)}\}_{k=2}^n$ is given by the (signed) volume of the n -dimensional cone

$$\frac{1}{n} \tilde{\epsilon}^{\nu_1 \dots \nu_n} \Psi_{\nu_1} d\Psi_{\nu_2}^{(2)} \dots d\Psi_{\nu_n}^{(n)}, \quad (1)$$

where $\tilde{\epsilon}^{\nu_1 \dots \nu_n}$ are the components of the Levi-Civita tensor in order parameter space. See Supplementary Figure 1 for an example of $n = d = 3$. The charge s is then given as the natural generalization of Equation (4) of the main article, i.e.,

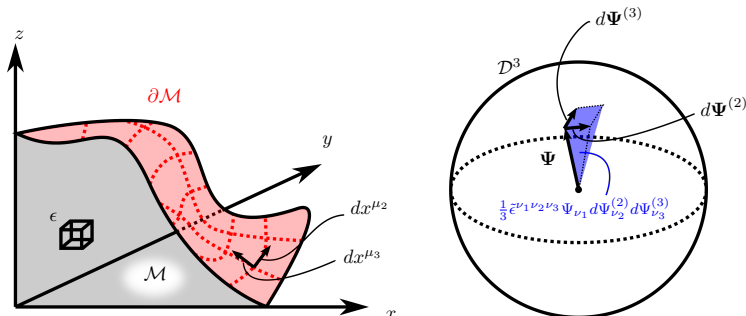
$$s = \frac{1}{V_n \Psi_0^n} \oint_{\partial \mathcal{M}} \frac{1}{n} \tilde{\epsilon}^{\nu_1 \dots \nu_n} \Psi_{\nu_1} d\Psi_{\nu_2}^{(2)} \dots d\Psi_{\nu_n}^{(n)}. \quad (2)$$

Here, $\partial \mathcal{M}$ is a $(n - 1)$ -dimensional submanifold of \mathbb{R}^d , the boundary of some n -dimensional submanifold \mathcal{M} , and $\{d\Psi^{(k)}\}_{k=2}^n$ are changes in Ψ due to displacements dx^μ on $\partial \mathcal{M}$. Formally, we write the integrand in terms of the coordinates $\{x^\mu\}_{\mu=1}^d$ of \mathbb{R}^d as follows

$$\omega = \frac{1}{n} \tilde{\epsilon}^{\nu_1 \dots \nu_n} \Psi_{\nu_1} (\partial_{\mu_2} \Psi_{\nu_2}) \dots (\partial_{\mu_n} \Psi_{\nu_n}) dx^{\mu_2} \otimes \dots \otimes dx^{\mu_n}, \quad (3)$$

Since $\omega_{\mu_2 \dots \mu_n}$ is completely anti-symmetric under interchange of indices, ω is a $(n - 1)$ -form and we can apply Stokes' generalized theorem

$$\oint_{\partial \mathcal{M}} \omega = \int_{\mathcal{M}} d\omega \quad (4)$$



Supplementary Figure 1. Real 3D space and order parameter space for a \mathcal{D}^3 order parameter. $\partial \mathcal{M}$ is the boundary of a 3D subvolume \mathcal{M} , on which variations along the surface (dx^{μ_2}, dx^{μ_3}) lead to variations of the order parameter ($d\Psi^{(2)}, d\Psi^{(3)}$).

where $d\omega$ is the exterior derivative of ω , whose components are given by

$$(d\omega)_{\mu_1 \dots \mu_n} = n \partial_{[\mu_1} \omega_{\mu_2 \dots \mu_n]} = \partial_{[\mu_1} (\tilde{\epsilon}^{\nu_1 \dots \nu_n} \Psi_{\nu_1} (\partial_{\mu_2} \Psi_{\nu_2}) \dots (\partial_{\mu_n}] \Psi_{\nu_n})) = \tilde{\epsilon}^{\nu_1 \dots \nu_n} (\partial_{\mu_1} \Psi_{\nu_1}) \dots (\partial_{\mu_n} \Psi_{\nu_n}), \quad (5)$$

where the notation $[\dots]$ is the antisymmetrization over free indices $(\mu_1 \dots \mu_n)$. Thus, we get

$$s = \frac{1}{V_n \Psi_0^n} \int_{\mathcal{M}} \tilde{\epsilon}^{\nu_1 \dots \nu_n} (\partial_{\mu_1} \Psi_{\nu_1}) \dots (\partial_{\mu_n} \Psi_{\nu_n}) dx^{\mu_1} \otimes \dots \otimes dx^{\mu_n}. \quad (6)$$

In the case of $n = 1$, for which $V_1 = 2$, integrals over \mathcal{M} are typically evaluated in this way, i.e., as line integrals over the one-dimensional manifold \mathcal{M} . We then immediately recover the defect density for $n = 1$, given by

$$\rho_\mu = \frac{\partial_\mu \Psi}{2\Psi_0} \quad (n = 1). \quad (7)$$

For higher values of n , however, one evaluates the integral in coordinates on the manifold \mathcal{M} . Thus, at each point, we choose $d - n$ orthogonal unit vectors $\{\mathbf{n}_{(k)}\}_{k=1}^{d-n}$ normal to the manifold \mathcal{M} and introduce local coordinates $\{y^i\}_{i=1}^n$ on \mathcal{M} . Expressed in these coordinates, we have

$$\begin{aligned} s &= \frac{1}{V_n \Psi_0^n} \int_{\mathcal{M}} \tilde{\epsilon}^{\nu_1 \dots \nu_n} (\partial_{\tau_1} \Psi_{\nu_1}) \dots (\partial_{\tau_n} \Psi_{\nu_n}) dy^{\tau_1} \otimes \dots \otimes dy^{\tau_n} \\ &= \frac{1}{V_n \Psi_0^n} \int_{\mathcal{M}} \tilde{\epsilon}^{\nu_1 \dots \nu_n} (\partial_{\tau_1} \Psi_{\nu_1}) \dots (\partial_{\tau_n} \Psi_{\nu_n}) \delta_{\kappa_1}^{\tau_1} \dots \delta_{\kappa_n}^{\tau_n} dy^{\kappa_1} \otimes \dots \otimes dy^{\kappa_n}, \end{aligned} \quad (8)$$

where τ -indices iterate from 1 to n . Now, we invoke the identity

$$n! \delta_{\kappa_1}^{[\tau_1} \dots \delta_{\kappa_n}^{\tau_n]} = \tilde{\epsilon}^{\tau_1 \dots \tau_n} \hat{\epsilon}_{\kappa_1 \dots \kappa_n} \quad (9)$$

where $\hat{\epsilon}$ is the Levi-Civita tensor on \mathcal{M} , i.e., the induced volume element from \mathbb{R}^d . Using the fact that the integrand is already anti-symmetric in τ -indices, we can replace $\delta_{\kappa_1}^{\tau_1} \dots \delta_{\kappa_n}^{\tau_n} \rightarrow \delta_{\kappa_1}^{[\tau_1} \dots \delta_{\kappa_n}^{\tau_n]}$ and get

$$\begin{aligned} s &= \frac{1}{V_n \Psi_0^n} \int_{\mathcal{M}} \tilde{\epsilon}^{\nu_1 \dots \nu_n} (\partial_{\tau_1} \Psi_{\nu_1}) \dots (\partial_{\tau_n} \Psi_{\nu_n}) \frac{1}{n!} \tilde{\epsilon}^{\tau_1 \dots \tau_n} \hat{\epsilon}_{\kappa_1 \dots \kappa_n} dy^{\kappa_1} \otimes \dots \otimes dy^{\kappa_n} \\ &= \frac{1}{V_n \Psi_0^n} \int_{\mathcal{M}} \frac{1}{n!} \tilde{\epsilon}^{\tau_1 \dots \tau_n} \tilde{\epsilon}^{\nu_1 \dots \nu_n} (\partial_{\tau_1} \Psi_{\nu_1}) \dots (\partial_{\tau_n} \Psi_{\nu_n}) \hat{\epsilon} \end{aligned} \quad (10)$$

Finally, we want to express the integrand in terms of coordinates of \mathbb{R}^d . Using that $\hat{\epsilon}$ expressed in these coordinates is

$$\hat{\epsilon}^{\mu_1 \dots \mu_n} = N^{i_1 \dots i_{d-n}} \epsilon_{i_1 \dots i_{d-n}}^{\mu_1 \dots \mu_n} \quad (11)$$

where $N^{i_1 \dots i_{d-n}} \equiv n_{(1)}^{i_1} \dots n_{(d-n)}^{i_{d-n}}$, we get

$$s = \frac{1}{V_n \Psi_0^n} \int_{\mathcal{M}} \frac{1}{n!} \epsilon^{\mu_1 \dots \mu_n}_{i_1 \dots i_{d-n}} \tilde{\epsilon}^{\nu_1 \dots \nu_n} (\partial_{\mu_1} \Psi_{\nu_1}) \dots (\partial_{\mu_n} \Psi_{\nu_n}) N^{i_1 \dots i_{d-n}} \hat{\epsilon} \quad (12)$$

Identifying $N^{i_1 \dots i_{d-n}} \hat{\epsilon}$ as the oriented volume element of \mathcal{M} , we identify the defect density as

$$\rho_{i_1 \dots i_{d-n}} = \frac{D_{i_1 \dots i_{d-n}}}{V_n \Psi_0^n} \quad (n \geq 2) \quad (13)$$

where

$$D_{i_1 \dots i_{d-n}} = \frac{1}{n!} \epsilon^{\mu_1 \dots \mu_n}_{i_1 \dots i_{d-n}} \tilde{\epsilon}^{\nu_1 \dots \nu_n} (\partial_{\mu_1} \Psi_{\nu_1}) \dots (\partial_{\mu_n} \Psi_{\nu_n}). \quad (14)$$

We now turn to finding the general equation for the velocity of the defect density. To differentiate Equation (13) with respect to time, consider

$$\begin{aligned}
\partial_t D_{i_1 \dots i_{d-n}} &= \partial_t \left(\frac{1}{n!} \epsilon^{\mu_1 \dots \mu_n}{}_{i_1 \dots i_{d-n}} \tilde{\epsilon}^{\nu_1 \dots \nu_n} (\partial_{\mu_1} \Psi_{\nu_1}) \dots (\partial_{\mu_n} \Psi_{\nu_n}) \right) \\
&= \frac{1}{n!} \epsilon^{\mu_1 \dots \mu_n}{}_{i_1 \dots i_{d-n}} \tilde{\epsilon}^{\nu_1 \dots \nu_n} \left((\partial_{\mu_1} \partial_t \Psi_{\nu_1}) \dots (\partial_{\mu_n} \Psi_{\nu_n}) + \dots + (\partial_{\mu_1} \Psi_{\nu_1}) \dots (\partial_{\mu_n} \partial_t \Psi_{\nu_n}) \right) \\
&= \frac{1}{n!} \epsilon^{\mu_1 \dots \mu_n}{}_{i_1 \dots i_{d-n}} \tilde{\epsilon}^{\nu_1 \dots \nu_n} \left((\partial_{\mu_1} \partial_t \Psi_{\nu_1}) \dots (\partial_{\mu_n} \Psi_{\nu_n}) + \dots (\partial_{\mu_n} \Psi_{\nu_n}) + \dots + (\partial_{\mu_1} \Psi_{\nu_1}) \dots (\partial_{\mu_1} \partial_t \Psi_{\nu_1}) \right) \\
&= \frac{1}{(n-1)!} \epsilon^{\mu_1 \dots \mu_n}{}_{i_1 \dots i_{d-n}} \tilde{\epsilon}^{\nu_1 \dots \nu_n} (\partial_{\mu_1} \partial_t \Psi_{\nu_1}) \dots (\partial_{\mu_n} \Psi_{\nu_n}) \\
&= \partial_{\mu_1} \left(\frac{1}{(n-1)!} \epsilon^{\mu_1 \dots \mu_n}{}_{i_1 \dots i_{d-n}} \tilde{\epsilon}^{\nu_1 \dots \nu_n} (\partial_t \Psi_{\nu_1}) \dots (\partial_{\mu_n} \Psi_{\nu_n}) \right), \quad (15)
\end{aligned}$$

where, in going from line 2 to 3, we have used that due to the contraction with both the anti-symmetric Levi-Civitas, the terms are invariant under simultaneously interchanging $\mu_k \leftrightarrow \mu_{k'}$ and $\nu_k \leftrightarrow \nu_{k'}$, so that we can write every term in the parenthesis like the first. In going from line 4 to 5, we have used that the contraction with $\epsilon^{\mu_1 \dots \mu_n}{}_{i_1 \dots i_{d-n}}$ ensures that only the first term survives when applying the product rule. Thus, we find $\partial_t \rho_{i_1 \dots i_{d-n}} + \partial_{\mu_1} J^{\mu_1}{}_{i_1 \dots i_{d-n}} = 0$, where

$$J^{\mu_1}{}_{i_1 \dots i_{d-n}} = \frac{-1}{V_n \Psi_0^n (n-1)!} \epsilon^{\mu_1 \mu_2 \dots \mu_n}{}_{i_1 \dots i_{d-n}} \tilde{\epsilon}^{\nu_1 \dots \nu_n} (\partial_t \Psi_{\nu_1}) (\partial_{\mu_2} \Psi_{\nu_2}) \dots (\partial_{\mu_n} \Psi_{\nu_n}). \quad (16)$$

Like for the $d = n = 2$ case, we want to identify this expression with the density current $v^{\mu_1} \rho_{i_1 \dots i_{d-n}}$. They are related up to a divergence free contribution $\partial_{\mu_1} K^{\mu_1}{}_{i_1 \dots i_{d-n}} = 0$, so

$$v^m \rho_{i_1 \dots i_{d-n}} = J^{\mu_1}{}_{i_1 \dots i_{d-n}} + K^{\mu_1}{}_{i_1 \dots i_{d-n}}. \quad (17)$$

In the $d = n = 2$ case, the charge density on the left-hand side had no free indices and so we could simply divide by the charge density to solve for \mathbf{v} . In the general case, however, we project the equation by contracting with $\frac{\rho^{i_1 \dots i_{d-n}}}{|\rho|^2}$, where $|\rho| = \sqrt{\rho^{i_1 \dots i_{d-n}} \rho_{i_1 \dots i_{d-n}}}$ is the Frobenius norm, and get

$$v_1^\mu = \frac{\rho^{i_1 \dots i_{d-n}} J^{\mu_1}{}_{i_1 \dots i_{d-n}}}{|\rho|^2} + \frac{\rho_{i_1 \dots i_{d-n}} K^{\mu_1}{}_{i_1 \dots i_{d-n}}}{|\rho|^2}. \quad (18)$$

In order to fix the gauge $K^{\mu_1}{}_{i_1 \dots i_{d-n}}$, we look at the evolution of the order parameter Ψ as advected by a velocity field $\mathbf{v}(\Psi)$

$$\partial_t \Psi_n + v_{(\Psi)}^{\mu_1} \partial_{\mu_1} \Psi_n = 0. \quad (19)$$

These are n linearly independent linear equations to determine d components of the velocity $\mathbf{v}(\Psi)$. If $n < d$, it is under-determined and therefore $d - n$ additional equations are needed to determine v^{μ_1} uniquely. We define

$$\begin{aligned}
v_{\text{candidate}}^{\mu_1} &\equiv \frac{\rho^{i_1 \dots i_{d-n}} J^{\mu_1}{}_{i_1 \dots i_{d-n}}}{|\rho|^2} \\
&= \frac{\frac{1}{n!} \epsilon_{\mu'_1 \dots \mu'_n}{}^{i_1 \dots i_{d-n}} \tilde{\epsilon}_{\nu'_1 \dots \nu'_n}{}^{\mu_1 \dots \mu_n} (\partial_{\mu'_1} \Psi^{\nu'_1}) \dots (\partial_{\mu'_n} \Psi^{\nu'_n}) \frac{-1}{(n-1)!} \epsilon^{\mu_1 \mu_2 \dots \mu_n}{}_{i_1 \dots i_{d-n}} \tilde{\epsilon}^{\nu_1 \dots \nu_n} (\partial_t \Psi_{\nu_1}) (\partial_{\mu_2} \Psi_{\nu_2}) \dots (\partial_{\mu_n} \Psi_{\nu_n})}{|D|^2} \\
&= - \frac{(d-n)! \delta_{[\mu'_1}^{\mu_1} \delta_{\mu'_2}^{\mu_2} \dots \delta_{\mu'_n]}^{\mu_n} \tilde{\epsilon}_{\nu'_1 \dots \nu'_n}{}^{\mu_1 \dots \mu_n} (\partial_{\mu'_1} \Psi^{\nu'_1}) \dots (\partial_{\mu'_n} \Psi^{\nu'_n}) \tilde{\epsilon}^{\nu_1 \dots \nu_n} (\partial_t \Psi_{\nu_1}) (\partial_{\mu_2} \Psi_{\nu_2}) \dots (\partial_{\mu_n} \Psi_{\nu_n})}{(n-1)! |D|^2} \\
&= - \frac{(d-n)! n! \delta_{\nu'_1}^{[\nu_1} \dots \delta_{\nu'_n]}^{\nu_n]} (\partial^{\mu_1} \Psi^{\nu'_1}) \dots (\partial^{\mu_n} \Psi^{\nu'_n}) (\partial_t \Psi_{\nu_1}) (\partial_{\mu_2} \Psi_{\nu_2}) \dots (\partial_{\mu_n} \Psi_{\nu_n})}{(n-1)! |D|^2} \\
&= - \frac{(d-n)! n! \delta_{\nu'_1}^{[\nu_1} \dots \delta_{\nu'_n]}^{\nu_n]} (\partial_t \Psi_{\nu_1}) (\partial^{\mu_1} \Psi^{\nu'_1}) \prod_{l=2}^n (\partial_{\mu_l} \Psi_{\nu_l}) (\partial^{\mu_l} \Psi^{\nu'_l})}{|D|^2} \quad (20)
\end{aligned}$$

Calculating $|D|^2$ gives

$$\begin{aligned}
|D|^2 &= \frac{1}{n!} \epsilon^{\mu_1 \dots \mu_n} \tilde{\epsilon}^{\nu_1 \dots \nu_n} (\partial_{\mu_1} \Psi_{\nu_1}) \dots (\partial_{\mu_n} \Psi_{\nu_n}) \frac{1}{n!} \epsilon_{\mu'_1 \dots \mu'_n} \tilde{\epsilon}_{\nu'_1 \dots \nu'_n} (\partial^{\mu_1} \Psi_{\nu'_1}) \dots (\partial^{\mu_n} \Psi_{\nu'_n}) \\
&= \frac{1}{(n!)^2} n! (d-n)! \delta_{\mu'_1}^{[\mu_1} \dots \delta_{\mu'_n}^{\mu_n]} \tilde{\epsilon}^{\nu_1 \dots \nu_n} (\partial_{\mu_1} \Psi_{\nu_1}) \dots (\partial_{\mu_n} \Psi_{\nu_n}) \tilde{\epsilon}_{\nu'_1 \dots \nu'_n} (\partial^{\mu'_1} \Psi_{\nu'_1}) \dots (\partial^{\mu'_n} \Psi_{\nu'_n}) \\
&= (d-n) \delta_{\nu'_1}^{[\nu_1} \dots \delta_{\nu'_n}^{\nu_n]} \prod_{l=1}^n (\partial_{\mu_l} \Psi_{\nu_l}) (\partial^{\mu_l} \Psi_{\nu'_l}). \quad (21)
\end{aligned}$$

which gives

$$v_{\text{candidate}}^{\mu_1} = -n \frac{\delta_{\nu'_1}^{[\nu_1} \dots \delta_{\nu'_n}^{\nu_n]} (\partial_t \Psi_{\nu_1}) (\partial^{\mu_1} \Psi_{\nu'_1}) \prod_{l=2}^n (\partial_{\mu_l} \Psi_{\nu_l}) (\partial^{\mu_l} \Psi_{\nu'_l})}{\delta_{\nu'_1}^{[\nu_1} \dots \delta_{\nu'_n}^{\nu_n]} \prod_{l=1}^n (\partial_{\mu_l} \Psi_{\nu_l}) (\partial^{\mu_l} \Psi_{\nu'_l})} \quad (22)$$

where it is understood that the repeated indices are summed over independently in the numerator and denominator. By inserting this expression in the LHS of Equation (19) after multiplying by the denominator, we get

$$\underbrace{\delta_{\nu'_1}^{[\nu_1} \dots \delta_{\nu'_n}^{\nu_n]} \left(\prod_{l=1}^n (\partial_{\mu_l} \Psi_{\nu_l}) (\partial^{\mu_l} \Psi_{\nu'_l}) \right)}_{\text{(Mercury)}} \partial_t \Psi_k - \underbrace{n \delta_{\nu'_1}^{[\nu_1} \dots \delta_{\nu'_n}^{\nu_n]} (\partial_t \Psi_{\nu_1}) (\partial^{\mu_1} \Psi_{\nu'_1}) \left(\prod_{l=2}^n (\partial_{\mu_l} \Psi_{\nu_l}) (\partial^{\mu_l} \Psi_{\nu'_l}) \right)}_{\text{(Venus)}} \partial_{\mu_1} \Psi_k. \quad (23)$$

We split the term (Venus) into $\nu_1 = k$ and $\nu_1 \neq k$ as follows

$$\begin{aligned}
\text{(Venus)} &= \underbrace{n \delta_{\nu'_1}^{[k} \delta_{\nu'_2}^{\nu_2} \dots \delta_{\nu'_n}^{\nu_n]} (\partial_t \Psi_k) (\partial^{\mu_1} \Psi_{\nu'_1}) \left(\prod_{l=2}^n (\partial_{\mu_l} \Psi_{\nu_l}) (\partial^{\mu_l} \Psi_{\nu'_l}) \right)}_{\text{(Tellus)}} \partial_{\mu_1} \Psi_k \\
&\quad + n \underbrace{\sum_{\nu_1 \neq k} \delta_{\nu'_1}^{[\nu_1} \dots \delta_{\nu'_n}^{\nu_n]} (\partial_t \Psi_{\nu_1}) (\partial^{\mu_1} \Psi_{\nu'_1}) \left(\prod_{l=2}^n (\partial_{\mu_l} \Psi_{\nu_l}) (\partial^{\mu_l} \Psi_{\nu'_l}) \right)}_{\text{(Mars)}} \partial_{\mu_1} \Psi_k. \quad (24)
\end{aligned}$$

(Mars) is identically zero, which the following argument shows: Because of the antisymmetrization over $\nu_1 \dots \nu_n$, in every term in (Mars) ν_1, \dots, ν_n will take every value $1, \dots, n$. Since $\nu_1 \neq k$, it means that there is some $m > 1$ such that $\nu_m = k$. Isolating the corresponding factor from the product, we get

$$\text{(Mars)} = n \sum_{\nu_1 \neq k} \delta_{\nu'_1}^{[\nu_1} \dots \delta_{\nu'_n}^{\nu_n]} (\partial_t \Psi_{\nu_1}) (\partial^{\mu_1} \Psi_{\nu'_1}) (\partial_{\mu_1} \Psi_k) (\partial_{\mu_m} \Psi_k) (\partial^{\mu_m} \Psi_{\nu'_m}) \left(\prod_{l=2, l \neq m}^n (\partial_{\mu_l} \Psi_{\nu_l}) (\partial^{\mu_l} \Psi_{\nu'_l}) \right) = 0 \quad (25)$$

because the factor $(\partial^{\mu_1} \Psi_{\nu'_1}) (\partial_{\mu_1} \Psi_k) (\partial_{\mu_m} \Psi_k) (\partial^{\mu_m} \Psi_{\nu'_m})$, this is symmetric under the interchange $\nu'_1 \leftrightarrow \nu'_m$, but the Kronecker-delta product is antisymmetric. Now consider (Mercury). As before, in every term, ν_1, \dots, ν_n will take every value $1, \dots, n$. Thus, in each term of (Mercury), there will be an m such that $\nu_m = k$, so we write

$$\begin{aligned}
\text{(Mercury)} &= \sum_{m=1}^n \delta_{\nu'_1}^{[\nu_1} \dots \delta_{\nu'_m}^k \dots \delta_{\nu'_n}^{\nu_n]} (\partial_{\mu_m} \Psi_k) (\partial^{\mu_m} \Psi_{\nu'_m}) \left(\prod_{l=1, l \neq m}^n (\partial_{\mu_l} \Psi_{\nu_l}) (\partial^{\mu_l} \Psi_{\nu'_l}) \right) (\partial_t \Psi_k) \\
&= \sum_{m=1}^n \delta_{\nu'_m}^{[k} \delta_{\nu'_1}^{\nu_1} \dots \delta_{\nu'_{m-1}}^{\nu_{m-1}} \delta_{\nu'_{m+1}}^{\nu_{m+1}} \dots \delta_{\nu'_n}^{\nu_n]} (\partial_{\mu_m} \Psi_k) (\partial^{\mu_m} \Psi_{\nu'_m}) \left(\prod_{l=1, l \neq m}^n (\partial_{\mu_l} \Psi_{\nu_l}) (\partial^{\mu_l} \Psi_{\nu'_l}) \right) (\partial_t \Psi_k). \quad (26)
\end{aligned}$$

Now, renaming $\nu'_m \rightarrow \nu'_1$, $\nu_1 \rightarrow \nu_2$, $\nu'_1 \rightarrow \nu'_2$, and so on up to $\nu'_{m-1} \rightarrow \nu'_m$, and $\mu_m \rightarrow \mu_1$, $\mu_1 \rightarrow \mu_2$, and so on up to $\mu_{m-1} \rightarrow \mu_m$, we get

$$\begin{aligned} (\text{Mercury}) &= \sum_{m=1}^n \delta_{\nu'_1}^{[k} \delta_{\nu'_2}^{\nu_2} \dots \delta_{\nu'_n}^{\nu_n]} (\partial_{\mu_1} \Psi_k) (\partial^{\mu_1} \Psi^{\nu'_1}) \left(\prod_{l=2}^n (\partial_{\mu_l} \Psi_{\nu_l}) (\partial^{\mu_l} \Psi^{\nu'_l}) \right) (\partial_t \Psi_k) \\ &= n \delta_{\nu'_1}^{[k} \delta_{\nu'_2}^{\nu_2} \dots \delta_{\nu'_n}^{\nu_n]} (\partial_{\mu_1} \Psi_k) (\partial^{\mu_1} \Psi^{\nu'_1}) \left(\prod_{l=2}^n (\partial_{\mu_l} \Psi_{\nu_l}) (\partial^{\mu_l} \Psi^{\nu'_l}) \right) (\partial_t \Psi_k) = (\text{Tellus}). \end{aligned} \quad (27)$$

This, in turn, means $(\text{Mercury}) = (\text{Venus})$, which shows that $v_{\text{candidate}}^{\mu_1}$ is a solution to Equation (19). We have verified this calculation explicitly up to $n = d = 5$, using symbolic mathematical software. In addition, it is straight-forward to show that $v_{\text{candidate}}^{\mu_1}$ is orthogonal to $\rho_{i_1 \dots i_{d-n}}$ in the sense that $v_{\text{candidate}}^{\mu_1} \rho_{i_1 \dots i_{d-n}} = 0$ for all k . Identifying these as the $(d - n)$ necessary conditions to determine $\mathbf{v}^{(\Psi)}$, we get $\mathbf{v}_{(\Psi)} = \mathbf{v}_{\text{candidate}}$, and fix the gauge on \mathbf{v} by $\mathbf{v} = \mathbf{v}_{(\Psi)}$, which gives, finally, the closed expression for the velocity

$$v^\mu = -n \frac{\delta_{\nu'_1}^{[\nu_1} \dots \delta_{\nu'_n}^{\nu_n]} (\partial_t \Psi_{\nu_1}) (\partial^{\mu_1} \Psi^{\nu'_1}) \prod_{l=2}^n (\partial_{\mu_l} \Psi_{\nu_l}) (\partial^{\mu_l} \Psi^{\nu'_l})}{\delta_{\nu'_1}^{[\nu_1} \dots \delta_{\nu'_n}^{\nu_n]} \prod_{l=1}^n (\partial_{\mu_l} \Psi_{\nu_l}) (\partial^{\mu_l} \Psi^{\nu'_l})} \quad (28)$$

While this derivation holds in general, we note that in the case of $n = d$, there is no contraction in getting to Equation (18), so the velocity can be equivalently written as

$$\text{Special case } n = d: \quad v^\mu = \frac{J^\mu}{\rho} = -n \frac{\epsilon^{\mu_1 \dots \mu_n} \tilde{\epsilon}^{\nu_1 \dots \nu_n} (\partial_t \Psi_{\nu_1}) \prod_{l=2}^n (\partial_{\mu_l} \Psi_{\nu_l})}{\epsilon^{\mu_1 \dots \mu_n} \tilde{\epsilon}^{\nu_1 \dots \nu_n} \prod_{l=1}^n \partial_{\mu_l} \Psi_{\nu_l}}, \quad (29)$$

which together give the expressions of the velocities in Equations (14-15) of the main article. For the physically most interesting cases of $n \leq d \leq 3$, see Supplementary Figure 2.

SUPPLEMENTARY REFERENCES

- [1] S. Carroll, *Spacetime and Geometry: Pearson New International Edition* (Pearson Education Limited, 2014).
- [2] S. Nguyen, R. Folch, V. K. Verma, H. Henry, and M. Plapp, Phase-field simulations of viscous fingering in shear-thinning fluids, *Phys. Fluids* **22**, 103102 (2010).
- [3] N. Kanazawa *et al.*, Direct Observation of the Statics and Dynamics of Emergent Magnetic Monopoles in a Chiral Magnet, *Phys. Rev. Lett* **125**, 137202 (2020).

Case	Order parameter	Charge density	Formulae
$d = 1, n = 1$ Point defects			$\rho = \frac{\partial_x \Psi}{2\Psi_0}$ $v_x = -\frac{\partial_x \Psi}{\partial_x \Psi}$
$d = 2, n = 1$ Line defects			$\rho_i = \frac{\partial_i \Psi}{2\Psi_0}$ $v_i = -\frac{\partial_i \Psi \partial_i \Psi}{ \nabla \Psi ^2}$
$d = 2, n = 2$ Point defects			$\rho = \frac{\epsilon^{ij} \bar{\epsilon}^{mn} (\partial_i \Psi_m) (\partial_j \Psi_n)}{2\pi \Psi_0^2}$ $v_i = -2 \frac{\epsilon^{ij} \bar{\epsilon}^{mn} (\partial_i \Psi_m) (\partial_j \Psi_n)}{\epsilon^{ij} \bar{\epsilon}^{mn} (\partial_i \Psi_m) (\partial_j \Psi_n)}$
$d = 3, n = 1$ Wall defects			$\rho_i = \frac{\partial_i \Psi}{2\Psi_0}$ $v_i = -\frac{\partial_i \Psi \partial_i \Psi}{ \nabla \Psi ^2}$
$d = 3, n = 2$ Line defects			$\rho_i = \frac{\epsilon^{ijk} \bar{\epsilon}^{mno} (\partial_j \Psi_m) (\partial_k \Psi_n)}{2\pi \Psi_0^2}$ $v_i = -2 \frac{\delta_{m'}^{[m} \delta_n^{k]} (\partial_i \Psi_m) (\partial^i \Psi_{m'}) (\partial_j \Psi_n) (\partial^j \Psi_{n'})}{\delta_{m'}^{[m} \delta_n^{k]} (\partial_i \Psi_m) (\partial^i \Psi_{m'}) (\partial_j \Psi_n) (\partial^j \Psi_{n'})}$
$d = 3, n = 3$ Point defects			$\rho = \frac{\epsilon^{ijk} \bar{\epsilon}^{mno} (\partial_i \Psi_m) (\partial_j \Psi_n) (\partial_k \Psi_o)}{8\pi \Psi_0^3}$ $v^i = -3 \frac{\epsilon^{ijk} \bar{\epsilon}^{mno} \partial_i \Psi_m \partial_j \Psi_n \partial_k \Psi_o}{\epsilon^{ijk} \bar{\epsilon}^{mno} \partial_i \Psi_m \partial_j \Psi_n \partial_k \Psi_o}$

Supplementary Figure 2. Examples of reduced defect field corresponding to stable topological defects in $O(n)$ models for $n = 1, 2, 3$ in $d = 1, 2, 3$. While the manuscript has centered on systems where $n = 2$, the methodology can be applied to other cases, such as interfacial systems with $n = 1$ with wall defects [2] or systems with $n = 3$ such as the 3D Heisenberg model which features emergent magnetic monopoles as topological defects [3].

Appendix B

**Supplementary information for
Paper (V)**

Spontaneous flows and dynamics of full-integer topological defects in polar active matter

Supplementary Information

Jonas Rønning,¹ Julian Renaud,² Amin Doostmohammadi,³ and Luiza Angheluta¹

¹*Njord Centre, Department of Physics, University of Oslo, P. O. Box 1048, 0316 Oslo, Norway*

²*École Normale Supérieure, PSL Research University, 45 rue d'Ulm, 75005 Paris, France*

³*Niels Bohr Institute, University of Copenhagen, Blegdamsvej 17, Copenhagen, Denmark*

In this supplementary material, we provide theoretical details for solving for Stokes flows with sources given by isolated polar defects. The dimensionless forms of the momentum equations are

$$(1 - \zeta^2 \nabla^2) \vec{u} = \vec{F}_p + \vec{F}_a - \nabla P, \quad (1)$$

$$\nabla^2 P = \nabla \cdot \vec{F}_p + \nabla \cdot \vec{F}_a, \quad (2)$$

where we denote as \vec{F}_a the active dipolar force and \vec{F}_p the active polar force. From the linearity of this Stokesian flow, we can use the superposition principle to write the solutions of the pressure and velocity as a sum of their polar and the dipolar force contribution, namely $\vec{u} = \vec{u}_a + \vec{u}_p$ and similar for pressure. Each contribution is an integral solution given by

$$P_{a,p}(\vec{r}) = \frac{1}{2\pi} \int d\vec{r}' \ln(|\vec{r} - \vec{r}'|) \nabla' \cdot \vec{F}_{a,p}, \quad (3)$$

$$\vec{u}_{a,p}(\vec{r}) = \frac{1}{2\pi\zeta^2} \int d\vec{r}' K_0 \left(\frac{|\vec{r} - \vec{r}'|}{\zeta} \right) \left(\vec{F}_{a,p}(\vec{r}') - \nabla' P_{a,p}(\vec{r}') \right). \quad (4)$$

Using complex analysis, we solve these integrals analytically for active forces induced by isolated polar defects as in Ref. [1, 2]. For this we use the parameterization of the polarization field for an isolated topological defect given by [3]

$$\vec{p}(r, \theta) = \chi(r) [\cos(q\theta + \phi) \vec{e}_x + \sin(q\theta + \phi) \vec{e}_y], \quad (5)$$

where (r, θ) are polar coordinates centered at the defect position (origin), $\chi(r)$ is a core function, $q = \pm 1$ is topological charge and ϕ is a constant background phase. For most parts, we assume that the defects are pointwise, i.e. $\chi(r) = 1$. The exception is when we evaluate the flow field at the defect position in the friction dominated limit, where we use that $\chi(r) \sim r$ to avoid getting a multi-valued velocity.

I. DIPOLAR FORCES

In this section, we derive analytical expressions of the flow fields induced by the active dipolar force $\vec{F}^a = (\tilde{\alpha}_0/\Gamma) \nabla \cdot (\vec{p}\vec{p}^T - \frac{p^2}{2} \mathbf{I})$ [4-6].

A. The negative defect

We start our calculations by considering the dipolar force generated by a $q = -1$ defect. As mentioned in the main document, the effect of the uniform background polarisation on the negative defect is to rotate it, thus for simplicity we can fix $\phi = 0$ and write the force components as:

$$F_{ax}^- = \frac{\tilde{\alpha}_0}{2\Gamma} [\partial_x \cos(2\theta) - \partial_y \sin(2\theta)], \quad (6)$$

$$F_{ay}^- = -\frac{\tilde{\alpha}_0}{2\Gamma} [\partial_x \sin(2\theta) + \partial_y \cos(2\theta)]. \quad (7)$$

Using that $\theta = \arctan(y/x)$, we express the force as

$$\vec{F}_a^- = -\frac{\tilde{\alpha}_0}{\Gamma r} \cos(-3\theta) \vec{e}_x - \frac{\tilde{\alpha}_0}{\Gamma r} \sin(-3\theta) \vec{e}_y. \quad (8)$$

where $\vec{e}_x = [1, 0]$ and $\vec{e}_y = [0, 1]$.

a. Flow pressure: By an integration by parts in Eq. (3), we find that the pressure field induced by the negative defect can be rewritten as

$$P_a^- = -\frac{1}{2\pi} \int dr' \vec{r} \left(\vec{F}_x^a \frac{(x' - x)}{|\vec{r}' - \vec{r}|^2} + \vec{F}_y^a \frac{(y' - y)}{|\vec{r}' - \vec{r}|^2} \right). \quad (9)$$

To evaluate it, we first do a change of variables to the complex coordinates $z' = x' + iy'$ and its conjugate $\bar{z}' = x' - iy'$, and similar for z and \bar{z} . To further isolate singularities in the complex plane, we do a second variable change to complex polar forms $z' = r'\hat{w}$ with $\hat{w} = e^{i\theta'}$. The integrals then can be expressed as

$$P_a^- = \frac{i\tilde{\alpha}_0}{2\pi\Gamma} \int_0^\infty dr' r' \oint_{|\hat{w}|=1} \frac{d\hat{w}}{\hat{w}} \left(-\frac{1}{4r'} (\hat{w}^3 + \hat{w}^{-3}) \frac{(r'\hat{w} - z) + (r'\hat{w}^{-1} - \bar{z})}{(r'\hat{w} - z)(r'\hat{w}^{-1} - \bar{z})} - \frac{1}{4r'} (\hat{w}^3 - \hat{w}^{-3}) \frac{(r'\hat{w} - z) - (r'\hat{w}^{-1} - \bar{z})}{(r'\hat{w} - z)(r'\hat{w}^{-1} - \bar{z})} \right). \quad (10)$$

After some algebraic manipulations to simplify the integrand expression, we can reduce it to

$$P_a^- = \frac{\tilde{\alpha}_0}{4\pi i\Gamma} \int_0^\infty dr' \oint_{|\hat{w}|=1} d\hat{w} \left(\frac{1}{r'\hat{w}^4(\hat{w} - z/r')} - \frac{\hat{w}^3}{\bar{z}(\hat{w} - r'/\bar{z})} \right). \quad (11)$$

The contour integral over \hat{w} can be evaluated by using the residue theorem. Note that the poles at $\hat{w} = z/r'$ and $\hat{w} = r'/\bar{z}$ are only inside the unit circle $|\hat{w}| = 1$ when $|z| = r < r'$ and $r > r'$ respectively. Thus,

$$\begin{aligned} P_a^- &= \frac{\tilde{\alpha}_0}{4\pi i\Gamma} \int_0^\infty dr' 2\pi i \left(\frac{(r')^3}{z^4} \Big|_{r < r'} - \frac{(r')^3}{z^4} - \frac{(r')^3}{\bar{z}^4} \Big|_{r > r'} \right) \\ &= -\frac{\tilde{\alpha}_0}{4\Gamma} \frac{x^4 - 6x^2y^2 + y^4}{r^4}. \end{aligned} \quad (12)$$

The pressure gradient follow straightforwardly as

$$\partial_x P_a^- = \frac{\tilde{\alpha}_0}{2r\Gamma} (\cos 5\theta - \cos 3\theta), \quad (13)$$

$$\partial_y P_a^- = \frac{\tilde{\alpha}_0}{2r\Gamma} (\sin 5\theta + \sin 3\theta), \quad (14)$$

and is subtracted from the dipolar force for incompressible flows.

b. Flow velocity: The total flow source term can be written in the complex form as:

$$F_a^- - 2\partial_z P_a^- = -\frac{\tilde{\alpha}_0}{2\Gamma} \left(\frac{\bar{z}}{z^2} + \frac{z^2}{\bar{z}^3} \right), \quad (15)$$

where we have used that the gradient in complex coordinates is $2\partial_z = \partial_x + i\partial_y$. By a change of variables to complex coordinates in Eq. (4), we rewrite the integral form of the complex velocity field $u_a^- = u_{a,x}^- + iu_{a,y}^-$ as

$$u_a^- = -\frac{\tilde{\alpha}_0 i}{8\pi\Gamma\zeta^2} \int dz' d\bar{z}' K_0 \left(\frac{|z' - z|}{\zeta} \right) \left(\frac{\bar{z}'}{(z')^2} + \frac{z'^2}{\bar{z}'^3} \right), \quad (16)$$

which can be transformed into

$$u_a^- = -\frac{\tilde{\alpha}_0}{4i\pi\Gamma\zeta^2} \int_0^\infty dr' r' K_0 \left(\frac{r'}{\zeta} \right) \oint_{|\hat{w}|=1} d\hat{w} \left(\frac{r' + \bar{z}\hat{w}}{\hat{w}^2 r'^2 (\hat{w} + z/r')^2} + \frac{(\hat{w}^2 (r'\hat{w} + z)^2)}{\bar{z}^3 (r'/\bar{z} + \hat{w})^3} \right) \quad (17)$$

The integral over \hat{w} can be evaluated by the residual theorem, such that the velocity can be expressed as

$$u_a^- = -\frac{\tilde{\alpha}_0}{2\Gamma\zeta^2} \left(\zeta^2 \int_0^{r/\zeta} dt t K_0(t) \left(\frac{\bar{z}z}{z^3} + \frac{\bar{z}^2 z^2}{\bar{z}^5} \right) - \zeta^4 \int_0^{r/\zeta} dt t^3 K_0(t) \left(\frac{2}{z^3} + \frac{6\bar{z}z}{\bar{z}^5} \right) + \frac{6\zeta^6}{\bar{z}^5} \int_0^{r/\zeta} dt t^5 K_0(t) \right), \quad (18)$$

leading to

$$\begin{aligned} u_a^-(r, \theta) &= -\frac{\tilde{\alpha}_0}{2\Gamma\zeta} \left([1 - \hat{r}K_1(\hat{r})] \left(\frac{1}{\hat{r}} e^{-3i\theta} + \frac{1}{\hat{r}} e^{5i\theta} \right) - [4 - \hat{r}^3 K_1(\hat{r}) - 2\hat{r}^2 K_2(\hat{r})] \left(\frac{2}{\hat{r}^3} e^{-3i\theta} + \frac{6}{\hat{r}^3} e^{5i\theta} \right) \right. \\ &\quad \left. + \frac{6}{\hat{r}^5} e^{5i\theta} [64 - 4\hat{r}^2(8 + \hat{r}^2)K_0(\hat{r}) - \hat{r}(8 + \hat{r}^2)^2 K_1(\hat{r})] \right). \end{aligned} \quad (19)$$

Where we have scaled the radial variable to $\hat{r} = r/\zeta$. The corresponding vorticity, $\omega = \partial_y u_x - \partial_x u_y$, reduces to

$$\omega_a^-(r, \theta) = -\frac{\tilde{\alpha}_0}{\hat{r}^4 \zeta^2 \Gamma} \sin 4\theta \left(-48 + 4\hat{r}^2 + \hat{r}^2(24 + \hat{r}^2)K_0(\hat{r}) + 8\hat{r}(6 + \hat{r}^2)K_1(\hat{r}) \right). \quad (20)$$

B. The positive defect

The +1 defect is more special in that an additional constant phase to the complex field $\psi = \chi(r)e^{i\theta+i\phi}$ changes the defect structure from vortex to spiral or aster. In the general case ($\phi \neq 0$), the dipolar force induced by +1 defect is

$$\vec{F}_a^+ = \frac{\tilde{\alpha}_0}{\Gamma r^2} \vec{r} \cos(2\phi) - \frac{\tilde{\alpha}_0}{\Gamma r^2} \vec{r}^\perp \sin(2\phi) = \vec{F}_a^+ + \hat{F}_a^+, \quad (21)$$

where $\vec{r}^\perp = (y, -x)$. We notice that \vec{F}_a^+ is a source/sink which gets removed by pressure for incompressible flows, \hat{F}_a^+ contributes to vorticity as seen below.

First, from the linearity of the main equations, we can decompose the pressure as superposition of different contributions

$$P_a^+ = \tilde{P}_a^+ \cos(2\phi) + \hat{P}_a^+ \sin(2\phi). \quad (22)$$

We will start by looking at the \tilde{P}_a^+ term, which reduces to the integral form

$$\tilde{P}_a^+ = \frac{\tilde{\alpha}_0 i}{8\pi\Gamma} \int_0^\infty dr' \oint_{|\hat{w}|=1} \frac{d\hat{w}}{\hat{w}} \left((\hat{w} + \hat{w}^{-1}) \left(\frac{1}{(r'\hat{w} - z)} + \frac{1}{(r'\hat{w}^{-1} - \bar{z})} \right) + (\hat{w} - \hat{w}^{-1}) \left(\frac{1}{(r'\hat{w} - z)} - \frac{1}{(r'\hat{w}^{-1} - \bar{z})} \right) \right). \quad (23)$$

which can be simplified to

$$\tilde{P}_a^+ = \frac{\tilde{\alpha}_0 i}{4\pi\Gamma} \int_0^\infty dr' \oint_{|\hat{w}|=1} d\hat{w} \left(\frac{1}{r'(\hat{w} - z/r')} - \frac{1}{\bar{z}\hat{w}(\hat{w} - r'/\bar{z})} \right) = -\alpha_0 \ln \frac{L}{r}. \quad (24)$$

where the core size L is introduced to remove the small-scale divergence in the limit of pointwise defects. Notice that the gradient of this pressure cancel out \vec{F}_a^+ as expected from the incompressibility constraint. Similarly, we find that the other pressure contribution and show that it actually vanishes

$$\begin{aligned} \hat{P}_a^+ &= \frac{i\tilde{\alpha}_0}{2\pi\Gamma} \int_0^\infty dr' r' \oint_{|\hat{w}|=1} \frac{d\hat{w}}{\hat{w}} \left(-\frac{1}{2ir'^2} r' (\hat{w} - \hat{w}^{-1}) \frac{\Re(r'\hat{w} - z)}{(r'\hat{w} - z)(r'\hat{w}^{-1} - \bar{z})} + \frac{1}{2r'^2} r' (\hat{w} + \hat{w}^{-1}) \frac{\Im(r'\hat{w} - z)}{(r'\hat{w} - z)(r'\hat{w}^{-1} - \bar{z})} \right) \\ &= -\frac{\tilde{\alpha}_0}{4\pi\Gamma} \int_0^\infty dr' \oint_{|\hat{w}|=1} d\hat{w} \left(\frac{1}{r'(\hat{w} - z/r')} + \frac{1}{\bar{z}\hat{w}(\hat{w} - r'/\bar{z})} \right) = 0, \end{aligned} \quad (25)$$

which implies that this rotational part of the force \hat{F}_a^+ does not induce any pressure. Writing this force in a complex form

$$\hat{F}_a^+ = \frac{i\tilde{\alpha}_0}{\bar{z}\Gamma}, \quad (26)$$

we express the complex velocity field as

$$\begin{aligned} u_a^+ &= \frac{i\tilde{\alpha}_0 \sin(2\phi)}{4\pi\zeta^2\Gamma} \int dz' dz' K_0 \left(\frac{|z' - z|}{\zeta} \right) \frac{i}{\bar{z}'} \\ &= \frac{\tilde{\alpha}_0 \sin(2\phi)}{2\pi\zeta^2\Gamma} \int_0^\infty dr' r' K_0 \left(\frac{r'}{\zeta} \right) \oint_{|\hat{w}|=1} \frac{d\hat{w}}{\bar{z}(r'/\bar{z} + \hat{w})} \\ &= \frac{\tilde{\alpha}_0 \sin(2\phi)}{\Gamma\zeta\hat{r}} (1 - \hat{r}K_1(\hat{r})) e^{i(\theta+\pi/2)}. \end{aligned} \quad (27)$$

where $\hat{r} = r/\zeta$. The corresponding vorticity field is then

$$\omega_a^+ = \frac{\tilde{\alpha}_0}{\Gamma\zeta^2} K_0(\hat{r}) \sin(2\phi), \quad (28)$$

which diverges logarithmically as $r \rightarrow 0$ since we have not included core size effects.

a. Zero friction limit: We notice that the absence of friction has an interesting implication. In this limit, the flow equations reduce to

$$-\tilde{\eta}\nabla^2 \vec{u}_a^+ = -\nabla \hat{P}_a^+ + \vec{F}_a, \quad (29)$$

$$\nabla \cdot \vec{u}_a^+ = 0, \quad (30)$$

with $\tilde{\eta} = \eta/\xi^2$, and the corresponding integral solution for the velocity is modified to

$$\vec{u}_a^+ = -\frac{1}{2\pi\tilde{\eta}} \int d\vec{r}' \ln(|\vec{r} - \vec{r}'|) \left(\vec{F}_a(\vec{r}') - \nabla P_a^+(\vec{r}') \right), \quad (31)$$

Since the pressure is the same as before, we have that

$$u_a^+ = -\frac{i\tilde{\alpha}_0}{\tilde{\eta}\bar{z}} \sin(2\phi) \int_0^r dt t \ln(t) = \frac{i\tilde{\alpha}_0 \sin(2\phi)}{4\tilde{\eta}} r(1 - 2\ln(r))e^{i\theta} \quad (32)$$

and its corresponding vorticity is

$$\omega_a^+ = -\frac{\tilde{\alpha}_0 \sin(2\phi)}{\tilde{\eta}} \ln r. \quad (33)$$

This changes sign for $r = \sqrt{e} \approx 1.7$ giving the two counter rotating regions and it is divergent for $r \rightarrow \infty$. The reason is because the Greens function changes sign. Note that in this case there is no intrinsic hydrodynamic lengthscale. Numerical simulations shows that the change of rotation is happening on the lengthscale of the defects core, $\sim \xi$, which comes from the free energy of the polar order parameter.

C. Defect pair: zero-viscosity limit

We consider a pair of oppositely charged defects in the analytically solvable limit of zero viscosity, i.e. $\zeta \rightarrow 0$, where the incompressible flow equations reduce to

$$\Gamma \vec{u}_a = \vec{F}_a - \nabla P_a, \quad (34)$$

$$\nabla \cdot \vec{u}_a = 0. \quad (35)$$

Making use of the complex representation and evaluating the dipolar force in terms of the complex order parameter $\psi = p_x + ip_y$, we can map the flow equations into

$$u_a = -2\partial_{\bar{z}} P_a + \frac{\tilde{\alpha}_0}{\Gamma} \partial_z \psi^2, \quad (36)$$

$$4\partial_z \partial_{\bar{z}} P_a = \frac{2\tilde{\alpha}_0}{\Gamma} \Re(\partial_{\bar{z}}^2 \psi^2). \quad (37)$$

The integral solution of the pressure reads as

$$2P_a = \frac{i\tilde{\alpha}_0}{4\pi\Gamma} \int dz' d\bar{z}' \ln[(\bar{z} - \bar{z}') (z - z')] \Re(\partial_{\bar{z}}^2 \psi^2). \quad (38)$$

We are interested in the derivative of the pressure and to ease the notation we define the factor $(\tilde{\alpha}_0/\Gamma)\mathcal{I}_a(z, \bar{z}) = -\partial_{\bar{z}} P_a$, which is given by the integral

$$\mathcal{I}_a(z, \bar{z}) = -\frac{i}{4\pi} \int dz' d\bar{z}' \frac{1}{\bar{z} - \bar{z}'} \Re(\partial_{\bar{z}}^2 \psi^2). \quad (39)$$

Furthermore, we are only interested in its value at the defect position, we introduce

$$\mathcal{I}_a \equiv \mathcal{I}_a(0, 0) = \frac{i}{4\pi} \int dz' d\bar{z}' \frac{1}{\bar{z}'} \Re(\partial_{\bar{z}}^2 \psi^2). \quad (40)$$

The equation for the velocity at the defect position can now be written as

$$u_a = \frac{\tilde{\alpha}_0}{\Gamma} \partial_{\bar{z}}^2 \psi^2|_{|z|=0} + \frac{\tilde{\alpha}_0}{\Gamma} \mathcal{I}_a. \quad (41)$$

a. At +1 defect position: Let us place the +1 defect at the center $z = 0$ and the -1 defect at the position $w_n = R_1 + iR_2$, with \vec{R} being the position vector, such that we can parameterise the order parameter as

$$\psi = \chi(z, \bar{z}) \sqrt{\frac{\bar{z}}{z}} \sqrt{\frac{\bar{z} - \bar{w}_n}{z - w_n}} e^{i\phi}, \quad (42)$$

with ϕ being a homogeneous background orientation. We have neglected the core function for the negative defect, while keeping it for the positive defect so that we can evaluate the active force at its position. Near the defect position $\chi(z, \bar{z}) = a\sqrt{z\bar{z}}$ and

$$\partial_z \psi^2 = a^2 \partial_z \left(z^2 \frac{\bar{z} - \bar{w}_n}{z - w_n} \right) e^{2i\phi} = a^2 (\bar{z} - \bar{w}_n) \frac{z^2 - 2zw_n}{(z - w_n)^2} e^{2i\phi}, \quad (43)$$

which vanishes at $z = 0$. Thus, there is no contribution from the active force to the defect velocity. However, the pressure has a net effect given by

$$\mathcal{I}_a^+ = \frac{i}{4\pi} \int dz d\bar{z} \frac{1}{\bar{z}} \left(\frac{w_n(\bar{z} - \bar{w}_n)}{\bar{z}(z - w_n)^3} e^{2i\phi} + \frac{\bar{w}_n(z - w_n)}{z(\bar{z} - \bar{w}_n)^3} e^{-2i\phi} \right). \quad (44)$$

This can be solved by a similar technique of complex integration and leads to

$$\mathcal{I}_a^+ = - \int_{\Lambda}^{|w_n|} dr \frac{1}{2r\bar{w}_n^2} \left(\frac{6r^2}{\bar{w}_n} - 2w_n \right) e^{-2i\phi} = \frac{w_n}{\bar{w}_n^2} \ln \left(\frac{|w_n|}{\Lambda} \right) e^{-2i\phi} - \frac{3}{2} \left(\frac{|w_n|^2}{\bar{w}_n^3} - \frac{\Lambda^2}{\bar{w}_n^2} \right) e^{-2i\phi} \quad (45)$$

The term containing Λ^2/\bar{w}_n^2 can be neglected since it is assumed that the defects are well separated. It is straightforward to show that core contributions with the ansatz $\chi = a\sqrt{z\bar{z}}$ are of the same order $O(\Lambda^2)$. The positive defect velocity induced by this pressure is

$$u_a^+ = \frac{\tilde{\alpha}_0}{\Gamma} \frac{w_n}{\bar{w}_n^2} e^{-2i\phi} \left(\ln \left(\frac{|w_n|}{\Lambda} \right) - \frac{3}{2} \right) \quad (46)$$

which tends to zero when separation between defects diverges, i.e. $|w_n| \rightarrow \infty$.

b. At the -1 defect position: Now, we place the negative defect at the origin and the positive defect at the position w_p , such that the order parameter takes the form

$$\psi = \chi(r) \sqrt{\frac{\bar{z}}{z}} \sqrt{\frac{z - w_p}{\bar{z} - \bar{w}_p}} e^{i\phi}, \quad (47)$$

from which we see that the active force at the defect position vanishes since

$$\partial_z \psi_{in}^2 = \frac{a^2 \bar{z}^2}{(\bar{z} - \bar{w}_p)} e^{2i\phi}. \quad (48)$$

However, the pressure contribution is given by

$$\mathcal{I}_a^- = - \frac{1}{2\pi i} \int dr \oint d\hat{z} \left(\frac{\hat{z}^4 \bar{w}_p}{r^3(\hat{z} - w_p/r)} e^{-2i\phi} - \frac{w_p}{r^2 \bar{w}_p \hat{z}^3 (\hat{z} - r/\bar{w}_p)} e^{2i\phi} \right). \quad (49)$$

which is solved to

$$\mathcal{I}_a^- = - \frac{w_p^4 \bar{w}_p}{6|w_p|^6} e^{-2i\phi} - \frac{w_p \bar{w}_p^2}{4|w_p|^4} e^{2i\phi}. \quad (50)$$

Therefore, the velocity of the negative defect induced by this pressure is

$$u_a^- = - \frac{\tilde{\alpha}_0}{\Gamma} \left(\frac{w_p}{6\bar{w}_p^2} e^{-2i\phi} + \frac{1}{4w_p} e^{2i\phi} \right), \quad (51)$$

Which also decrease inversely proportional with the distance between the defects, similarly to that of the positive defect.

II. POLAR FORCE

We are now studying the effect of the polar force, $\vec{F}_p = \tilde{\alpha}_p \vec{p}$ [6] on the ± 1 defects. The order parameter is then given by

$$\vec{p} = \cos(q\theta + \phi)\vec{e}_x + \sin(q\theta + \phi)\vec{e}_y. \quad (52)$$

A. Positive defect

Using the parameterization of the order parameter for an isolated +1 defect, we evaluate the polar force as

$$\vec{F}_p^+ = \frac{\tilde{\alpha}_p}{r} [r\vec{r} \cos \phi - r^\perp \sin \phi], \quad (53)$$

the first term is a source eliminated by the incompressibility constraint through the pressure contribution $P_p^+ = r \cos \theta$, while the second term is a rotational contribution. The flow velocity induced by this polar force is given by the integral

$$\vec{u}_p^+ = -\frac{\tilde{\alpha}_p}{2\pi\zeta^2} \int d\vec{r}' K_0 \left(\frac{|\vec{r} - \vec{r}'|}{\zeta} \right) \frac{r'^\perp}{r'} \sin \phi, \quad (54)$$

which in the complex form reads as

$$u_p^+ = -\frac{\tilde{\alpha}_p}{4\pi\zeta} \sin \phi \int dwd\bar{w} K_0 \left(\frac{|w|}{\zeta} \right) \sqrt{\frac{w+z}{\bar{w}+\bar{z}}}, \quad (55)$$

and the complex coordinates r' and $\hat{w} = e^{i\theta'}$,

$$u_p^+ = \frac{\tilde{\alpha}_p}{2\pi\zeta} \sin \phi \int_{|\hat{w}|=1} dr' r' K_0(r'/\zeta) \oint \frac{d\hat{w}}{\hat{w}} \sqrt{\frac{r'\hat{w}+z}{r'\hat{w}^{-1}+\bar{z}}}. \quad (56)$$

a. Contour integral: The contour integral over \hat{w}

$$I = \oint_{|\hat{w}|=1} \frac{d\hat{w}}{\hat{w}} \sqrt{\frac{r'\hat{w}+z}{r'\hat{w}^{-1}+\bar{z}}}, \quad (57)$$

has branch cuts which can be isolated by the keyhole contour. Using that z/r' and r'/\bar{z} have the same argument $e^{i\theta}$ and changing variables to $u = e^{-i\theta}\hat{w}$, i.e rotating the system so that the branch cuts are on the real axis, we rewrite the above integral as

$$I = \sqrt{\frac{r'}{\bar{z}}} e^{i\theta/2} \oint_{|u|=1} du \frac{\sqrt{u+r/r'}}{\sqrt{u}\sqrt{u+r'/r}}. \quad (58)$$

There are three branch points that we have to consider: $u = 0$, $u = -r/r'$ and $u = -r'/r$ as shown in Fig. 1. The two branch points inside unit disk are isolated by the two keyhole contour. Therefore, the contour integral equals the keyhole integral

$$I = \lim_{\epsilon \rightarrow 0} \left(\int_{-a-i\epsilon}^{-i\epsilon} + \int_{i\epsilon}^{-a+i\epsilon} + \int_{C_1} + \int_{C_2} \right) \sqrt{\frac{r'}{\bar{z}}} e^{i\theta/2} du \frac{\sqrt{u+r/r'}}{\sqrt{u}\sqrt{u+r'/r}}. \quad (59)$$

The integrals over C_1 and C_2 vanishes regardless whether a is r'/r or r/r' , thus

$$I = -2\sqrt{\frac{r'}{\bar{z}}} e^{i\theta/2} \int_{-a}^0 du \frac{\sqrt{u+r/r'}}{\sqrt{u}\sqrt{u+r'/r}}. \quad (60)$$

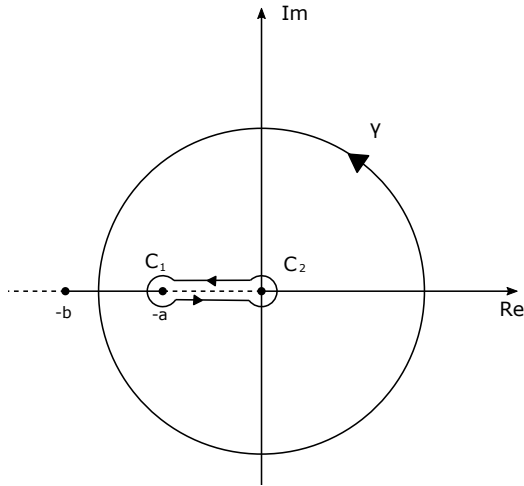


FIG. 1: Contour and branch points.

We can now perform the integral. For $r < r'$, we have that $a = r/r'$ is inside the contour. Therefore

$$I_{r < r'} = 4ie^{i\theta} \left(\left[\frac{r}{r'} - \frac{r'}{r} \right] K \left(\frac{r^2}{r'^2} \right) + \frac{r'}{r} E \left(\frac{r^2}{r'^2} \right) \right), \quad (61)$$

where K and E are the complete elliptic integrals of the first and second kind, respectively, and their infinite power series representations are

$$K(x) = \frac{\pi}{2} \sum_{n=0}^{\infty} \left(\frac{(2n-1)!!}{(2n)!!} \right)^2 x^n, \quad (62)$$

$$E(x) = \frac{\pi}{2} \left(1 - \sum_{n=1}^{\infty} \left(\frac{(2n-1)!!}{(2n)!!} \right)^2 \frac{x^n}{2n-1} \right). \quad (63)$$

Similarly, for $r > r'$, then $a = r'/r$ and $b = r/r'$, so that the integral becomes

$$I_{r > r'} = 4ie^{i\theta} E \left(\frac{r'^2}{r^2} \right). \quad (64)$$

The expression for the complex velocity is then:

$$u_p^+ = \frac{2i\tilde{\alpha}_p}{\pi\zeta^2} e^{i\theta} \left(\int_0^r dr' r' K_0(r'/\zeta) E \left(\frac{r'^2}{r^2} \right) + \int_r^\infty dr' r' K_0(r'/\zeta) \left(\left[\frac{r}{r'} - \frac{r'}{r} \right] K \left(\frac{r^2}{r'^2} \right) + \frac{r'}{r} E \left(\frac{r^2}{r'^2} \right) \right) \right) \quad (65)$$

Inserting the series expansions, the velocity field is a series expansions in moments of the Bessel function

$$u_p^+ = i\tilde{\alpha}_p e^{i\theta} \sin \phi \left(1 - \hat{r} K_1(\hat{r}) - \left(\int_0^{\hat{r}} dt t K_0(t) \left(\sum_{n=1}^{\infty} \left(\frac{(2n-1)!!}{(2n)!!} \right)^2 \frac{1}{2n-1} \left(\frac{t}{\hat{r}} \right)^{2n} \right) + \int_{\hat{r}}^\infty dt t K_0(t) \left(\sum_{n=0}^{\infty} \left(\frac{(2n-1)!!}{(2n)!!} \right)^2 \frac{1}{2n+2} \left(\frac{\hat{r}}{t} \right)^{2n+1} \right) \right). \quad (66)$$

using that $t = r'/\zeta$, and $\hat{r} = r/\zeta$.

b. Far-field asymptotic: In the limit of $\hat{r} \rightarrow \infty$, since the Bessel function decays exponential, we can ignore the factor $\hat{r}K_1(\hat{r})$ and second integral in Eq. (66). We replace the upper bound with ∞ and perform the integration up to second order in $1/\hat{r}$

$$u_p^+ = i\tilde{\alpha}_p e^{i\theta} \sin \phi \left(1 - \frac{1}{\hat{r}^2}\right) \quad (67)$$

There are two things to note. Firstly, the length of u becomes constant in the far-field as expected. Secondly, this is the flow field of a vortex centered at the defect position.

c. Series expansion: The integrals over the Bessel functions from Eq. (66) were evaluated in Ref. [1] and given by

$$\int_0^r dt K_0(t) t^{2n+1} = \frac{1}{4} \hat{r}^{2n+2} F_1(\hat{r}, n) \quad (68)$$

$$\int_r^\infty dt K_0(t) t^{-2n} = \frac{1}{4} \hat{r}^{-2n+1} F_2(\hat{r}, n) \quad (69)$$

with the functions given as

$$F_1(n, \hat{r}) = \sum_{k=0}^{\infty} \left[\frac{1}{(n+k+1)} - 2 \ln \left(\frac{\hat{r}}{2}\right) + 2\psi^{(0)}(k+1) \right] \frac{1}{(n+k+1)(k!)^2} \left(\frac{\hat{r}}{2}\right)^{2k} \quad (70)$$

and

$$F_2(n, \hat{r}) = 4 \sum_{k=0}^{\infty} \left[\psi^{(0)}(k+1) - \ln \left(\frac{\hat{r}}{2}\right) - \frac{1}{2n-1-2k} \right] \frac{1}{(2n-1-2k)(k!)^2} \left(\frac{\hat{r}}{2}\right)^{2k} + \frac{2\pi}{((2n-1)!!)^2} (\hat{r})^{2n-1}. \quad (71)$$

Inserting these expressions into Eq. (66) and after some algebra, we express the velocity field as

$$u_p^+ = i\tilde{\alpha}_p e^{i\theta} \sin \phi \left(1 - \hat{r}K_1(\hat{r}) + \frac{\pi}{2} I_1(\hat{r}) + \sum_{k,n=0}^{\infty} \kappa_1(n, k) \frac{\hat{r}^{2k+2}}{((2k)!!)^2} + \sum_{k,n=0}^{\infty} \kappa_2(n, k) \left[\ln \left(\frac{\hat{r}}{2}\right) - \psi^{(0)}(k+1) \right] \frac{\hat{r}^{2k+2}}{((2k)!!)^2} \right) \quad (72)$$

with the coefficients

$$\kappa_1(n, k) = - \left(\frac{(2n-1)!!}{(2n)!!} \right)^2 \frac{1}{2n+2} \left(\frac{1}{(2n-1-2k)^2} + \frac{2n+1}{4(2n+2)(n+2+k)^2} \right) \quad (73)$$

$$\kappa_2(n, k) = \left(\frac{(2n-1)!!}{(2n)!!} \right)^2 \frac{1}{2n+2} \left(\frac{2n+1}{2(2n+2)(n+2+k)} - \frac{1}{2n-1-2k} \right). \quad (74)$$

B. The negative defect

The polar force for the negative defect is

$$\vec{F}_p^- = \tilde{\alpha}_p [\vec{e}_x (\cos \theta \cos \phi + \sin \theta \sin \phi) + \vec{e}_y (\cos \theta \sin \phi - \sin \theta \cos \phi)]. \quad (75)$$

or equivalently

$$\vec{F}_p^- = \tilde{\alpha}_p \mathcal{R} [\vec{e}_x \cos \theta - \vec{e}_y \sin \theta] \quad (76)$$

where the rotation matrix \mathcal{R} is given as

$$\mathcal{R} = \begin{pmatrix} \cos \phi & -\sin \phi \\ \sin \phi & \cos \phi \end{pmatrix}. \quad (77)$$

Therefore, we can rotate the basis so that the phase is $\phi = 0$.

a. **Pressure:** The integral solution of the pressure can be written as

$$P_p^- = \frac{i}{2\pi} \int dr' r' \oint_{|\hat{w}|=1} \frac{d\hat{w}}{\hat{w}} \left(\mathbf{F}_x^p(r', \hat{w}) \frac{\Re(r' \hat{w} - z)}{(r' \hat{w} - z)(r' \hat{w}^{-1} - \bar{z})} + \mathbf{F}_y^p(r', \hat{w}) \frac{\Im(r' \hat{w} - z)}{(r' \hat{w} - z)(r' \hat{w}^{-1} - \bar{z})} \right), \quad (78)$$

with the polar force is given as

$$\vec{F}_p^-(r', \hat{w}) = \tilde{\alpha}_p [\vec{e}_x \Re(\hat{w}) - \vec{e}_y \Im(\hat{w})]. \quad (79)$$

Inserting this into the pressure and doing some manipulations we find

$$\begin{aligned} P_p^- &= \frac{\tilde{\alpha}_p i}{4\pi} \int_0^\infty dr' r' \oint_{|\hat{w}|=1} d\hat{w} \left(\frac{1}{r' \hat{w}^2 (\hat{w} - z/r')} - \frac{\hat{w}}{\bar{z} (\hat{w} - r'/\bar{z})} \right) \\ &= \frac{\tilde{\alpha}_p}{3} \frac{(x^2 - y^2)}{r}. \end{aligned}$$

Hence, the velocity field induced by the polar force becomes

$$u_p^- = -\frac{i\tilde{\alpha}_p}{12\pi\zeta^2} \int dr' r' K_0 \left(\frac{r'}{\zeta} \right) \oint_{|\hat{w}|=1} \frac{d\hat{w}}{\hat{w}} \left(3\sqrt{\frac{r' \hat{w}^{-1} + \bar{z}}{r' \hat{w} + z}} + \left(\frac{r' \hat{w} + z}{r' \hat{w}^{-1} + \bar{z}} \right)^{3/2} \right). \quad (80)$$

b. **The contour:** The contour integral has the same type of branch points as for discussed before, thus we use the contour drawn in Fig. 1. We start by looking at the component

$$3 \oint_\gamma \frac{d\hat{w}}{\hat{w}} \sqrt{\frac{r' \hat{w}^{-1} + \bar{z}}{r' \hat{w} + z}}. \quad (81)$$

This one is more straightforward to solve. By changing variables to $t = 1/\hat{w}$ with $dt = -d\hat{w}/\hat{w}^2$, and inserting an extra negative sign since we have to reverse the contour

$$3 \oint_\gamma \frac{dt}{t} \sqrt{\frac{r't + \bar{z}}{r't^{-1} + z}}, \quad (82)$$

which is the contour integral we solved for the positive defect in section II A 0 a with z and \bar{z} switched. We can then use the solution we found replacing $\theta \rightarrow -\theta$.

For the other integral

$$I = \oint \frac{d\hat{w}}{\hat{w}} \left(\frac{r' \hat{w} + z}{r' \hat{w}^{-1} + \bar{z}} \right)^{3/2} = \left(\frac{r'}{\bar{z}} \right)^{3/2} \oint d\hat{w} \sqrt{\hat{w}} \frac{(\hat{w} + e^{i\theta} r/r')^{3/2}}{(\hat{w} + e^{i\theta} r'/r)^{3/2}}. \quad (83)$$

As for the positive defect we rotate the integral domain so that the branch points falls on the real axis. That is we change variables to $u = e^{-i\theta} \hat{w}$ and get

$$I = \left(\frac{r'}{r} \right)^{3/2} e^{3i\theta} \oint du \sqrt{u} \frac{(u + r/r')^{3/2}}{(u + r'/r)^{3/2}}. \quad (84)$$

It have three branch points, but we can only use the keyhole integration that we did for the positive defect when $r < r'$. This is because we need the integrand to approach zero when we approach the branch cut. In the other limit, we need to take a binomial expansion. We first do the $r < r'$ case. Then we have

$$I_{r < r'} = -2 \left(\frac{r'}{r} \right)^{3/2} e^{3i\theta} \int_{-r/r'}^0 du \sqrt{u} \frac{(u + r/r')^{3/2}}{(u + r'/r)^{3/2}} \quad (85)$$

$$= -2 \frac{4i}{3} \frac{r'}{r} e^{3i\theta} \left(\left[3 \left(\frac{r}{r'} \right)^2 - 11 + 8 \left(\frac{r'}{r} \right)^2 \right] K \left(\left(\frac{r}{r'} \right)^2 \right) + \left[7 - 8 \left(\frac{r'}{r} \right)^2 \right] E \left(\left(\frac{r}{r'} \right)^2 \right) \right). \quad (86)$$

In the other case, $r > r'$, it is the r'/r pole that is inside the contour. We need to change variables to $h = \sqrt{u}$ so that the integral reads:

$$I_{r > r'} = b^{3/2} a^{3/2} e^{3i\theta} \oint_\gamma dh \frac{(1 + h^2/a)^{3/2}}{h(1 + b/h^2)^{3/2}}. \quad (87)$$

We can expand the exponents as

$$e^{3i\theta} \oint_{\gamma} dh \frac{1}{h} \left(\sum_{k=0}^{\infty} \binom{3/2}{k} \left(\frac{h^2}{a} \right)^k \right) \left(\sum_{n=0}^{\infty} \binom{-3/2}{n} \left(\frac{b}{h^2} \right)^n \right). \quad (88)$$

We use the residue theorem to solve the integral term by term. Conveniently, only the terms where $n = k$ contribute to the integral. We therefore have

$$2\pi i e^{3i\theta} \sum_{n=0}^{\infty} \binom{3/2}{n} \binom{-3/2}{n} \left(\frac{r'}{r} \right)^{2n} = 6\pi i e^{3i\theta} \sum_{n=0}^{\infty} \frac{2n+1}{(3-2n)(1-2n)} \left(\frac{(2n-1)!!}{(2n)!!} \right)^2 \left(\frac{r'}{r} \right)^{2n}. \quad (89)$$

Where in the last relation we have used the definition of the generalized binomial coefficient.

c. **Velocity field** The corresponding velocity field is

$$u_p^- = -\frac{i\tilde{\alpha}_p}{12\pi\zeta^2} \int_0^{\infty} dr' r' K_0 \left(\frac{r'}{\zeta} \right) \oint_{\gamma} \frac{d\hat{w}}{\hat{w}} \left(3\sqrt{\frac{r'\hat{w}^{-1} + \bar{z}}{r'\hat{w} + z}} + \left(\frac{r'\hat{w} + z}{r'\hat{w}^{-1} + \bar{z}} \right)^{3/2} \right), \quad (90)$$

which becomes

$$\begin{aligned} u_p^- = & -\frac{i\tilde{\alpha}_p}{12\pi\zeta^2} \int_0^{\infty} dr' r' K_0 \left(\frac{r'}{\zeta} \right) \left(3 \left[4ie^{-i\theta} \left(\left[\frac{r}{r'} - \frac{r'}{r} \right] K \left(\frac{r^2}{r'^2} \right) + \frac{r'}{r} E \left(\frac{r^2}{r'^2} \right) \right) \Big|_{r < r'} + 4ie^{-i\theta} E \left(\frac{r'^2}{r^2} \right) \Big|_{r > r'} \right] \right. \\ & + \left. \left[\frac{4i}{3} \frac{r'}{r} e^{3i\theta} \left(\left[3 \left(\frac{r'}{r'} \right)^2 - 11 + 8 \left(\frac{r'}{r} \right)^2 \right] K \left(\left(\frac{r}{r'} \right)^2 \right) + \left[7 - 8 \left(\frac{r'}{r} \right)^2 \right] E \left(\left(\frac{r}{r'} \right)^2 \right) \right] \Big|_{r < r'} \right. \right. \\ & \left. \left. + \left[6\pi i e^{3i\theta} \sum_{n=0}^{\infty} \frac{2n+1}{(3-2n)(1-2n)} \left(\frac{(2n-1)!!}{(2n)!!} \right)^2 \left(\frac{r'}{r} \right)^{2n} \right] \Big|_{r > r'} \right). \quad (91) \end{aligned}$$

The $e^{-i\theta}$ is strait forward because it is the same as the $e^{i\theta}$ term for the positive defect, but with factors $2i\tilde{\alpha}_p/(\pi\zeta^2)$ in stead of $\tilde{\alpha}_p/(\pi\zeta^2)$. Inserting the expressions for E and K given in eq. (62) and (63) one can find the relation

$$\begin{aligned} & \left[3 \left(\frac{r}{r'} \right)^2 - 11 + 8 \left(\frac{r'}{r} \right)^2 \right] K \left(\left(\frac{r}{r'} \right)^2 \right) + \left[7 - 8 \left(\frac{r'}{r} \right)^2 \right] E \left(\left(\frac{r}{r'} \right)^2 \right) \\ & = -\frac{18}{8} \pi \sum_{n=0}^{\infty} \left(\frac{(2n-1)!!}{(2n)!!} \right)^2 \frac{n}{(n+2)(n+1)} \left(\frac{r}{r'} \right)^{2n+2}, \quad (92) \end{aligned}$$

so that the velocity become

$$\begin{aligned} u_p^- = & \frac{\tilde{\alpha}_p}{2} \left(e^{-i\theta} \left[\sum_{n=0}^{\infty} \left(\frac{(2n-1)!!}{(2n)!!} \right)^2 \frac{1}{2n+2} \int_{\hat{r}}^{\infty} dt t K_0(t) \left(\frac{\hat{r}}{t} \right)^{2n+1} + \right. \right. \\ & \left. \left(\int_0^{\hat{r}} dt t K_0(t) - \sum_{n=1}^{\infty} \left(\frac{(2n-1)!!}{(2n)!!} \right)^2 \frac{1}{2n-1} \int_0^{\hat{r}} dt t K_0(t) \left(\frac{t}{\hat{r}} \right)^{2n} \right) \right] \\ & + e^{3i\theta} \left[\sum_{n=0}^{\infty} \frac{2n+1}{(3-2n)(1-2n)} \left(\frac{(2n-1)!!}{(2n)!!} \right)^2 \int_0^{\hat{r}} dt t K_0(t) \left(\frac{t}{\hat{r}} \right)^{2n} \right. \\ & \left. \left. - \sum_{n=0}^{\infty} \left(\frac{(2n-1)!!}{(2n)!!} \right)^2 \frac{2n}{(2n+4)(2n+2)} \int_{\hat{r}}^{\infty} dt t K_0(t) \left(\frac{\hat{r}}{t} \right)^{2n+1} \right] \right) \quad (93) \end{aligned}$$

Here we have changed variables to $t = r'/\zeta$ and introduced $\hat{r} = r/\zeta$. The integrals over the Bessel functions are the same as we considered in section II A 0 c. Inserting their expression and doing some work we can write the velocity as:

$$u_p^- = \frac{\tilde{\alpha}_p}{2} (f_1^p(\hat{r})e^{-i\theta} + f_3^p(\hat{r})e^{3i\theta}). \quad (94)$$

Where the function f_1^p is given as

$$f_1^p(\hat{r}) = 1 - \hat{r}K_1(\hat{r}) + \frac{\pi}{2}I_1(\hat{r}) + \sum_{k,n=0}^{\infty} \kappa_1(n, k) \frac{\hat{r}^{2k+2}}{((2k)!!)^2} + \sum_{k,n=0}^{\infty} \kappa_2(n, k) \left[\ln\left(\frac{\hat{r}}{2}\right) - \psi^{(0)}(k+1) \right] \frac{\hat{r}^{2k+2}}{((2k)!!)^2}, \quad (95)$$

with the coefficients defined in eq. (73) and (74). The other function f_3^p is given as

$$f_3^p(r) = -\frac{\pi}{2}I_3(\hat{r}) + \sum_{k,n=0}^{\infty} \kappa_3(n, k) \frac{r^{2k+2}}{((2k)!!)^2} + \sum_{k,n=0}^{\infty} \kappa_4(n, k) \frac{r^{2k+2}}{((2k)!!)^2} \left[\ln\left(\frac{\hat{r}}{2}\right) - \psi^{(0)}(k+1) \right], \quad (96)$$

and the new coefficients are defined as

$$\kappa_3(n, k) = \left(\frac{(2n-1)!!}{(2n)!!} \right)^2 \left(\frac{2n+1}{4(3-2n)(1-2n)(n+k+1)^2} + \frac{2n}{(2n+4)(2n+2)(2n-1-2k)^2} \right), \quad (97)$$

$$\kappa_4(n, k) = \left(\frac{(2n-1)!!}{(2n)!!} \right)^2 \left(\frac{2n}{(2n+4)(2n+2)(2n-1-2k)} - \frac{2n+1}{2(3-2n)(1-2n)(n+k+1)} \right). \quad (98)$$

The asymptotic velocity from Eq. (93) is obtained by the same procedure as used for positive defect in Eq. (67) and given by

$$u_p^-(\hat{r}, \theta) = \frac{\tilde{\alpha}_p}{2} \left[\left(e^{-i\theta} + \frac{1}{3}e^{3i\theta} \right) - \frac{1}{\hat{r}^2} [e^{-i\theta} + 3e^{3i\theta}] \right]. \quad (99)$$

As for the positive defect we see that the velocity tends to a constant non-zero value fare away from the defect core.

C. Defect pair: zero-viscosity limit

Similar to the flow equation in the frictionless limit for the dipolar force, we can find the equation for the polar flow,

$$u_p = \tilde{\alpha}_p \psi + \tilde{\alpha}_p \mathcal{I}_p, \quad (100)$$

where $\psi = p_x + ip_y$ is the complex order parameter and the integral factor at the origin is given as

$$\mathcal{I}_p = \frac{i}{4\pi} \int dz' d\bar{z}' \frac{1}{\bar{z}'} \Re(\partial_{z'} \psi). \quad (101)$$

We are now going to use this to find the flow at the centre of the defects for a dipole configuration.

a. At the positive defect position: We consider first a positive defect placed at the origin with a negative defect placed at w_n for which complex order parameter is

$$\psi = \chi(r) \sqrt{\frac{z}{\bar{z}}} \sqrt{\frac{\bar{z} - \bar{w}_n}{z - w_n}} e^{i\phi}, \quad (102)$$

Where χ is the core function given as $\chi(r) = 1$ for $r \gg a$ and $\chi(r \ll a) = a\sqrt{z\bar{z}}$. It is straightforward to show that the polar force at the centre of the positive defect $\tilde{\alpha}_p \psi(z=0) = 0$, so the only contribution to the flow at the defects center comes from the pressure gradient given by the integral factor eq. (101). To find it we start by finding the derivative of the order parameter

$$\partial_z \psi = \frac{1}{2} \frac{w_n}{z(w_n - z)} \sqrt{\frac{z}{\bar{z}}} \sqrt{\frac{\bar{z} - \bar{w}_n}{z - w_n}} e^{i\phi} \quad (103)$$

So that the integral we need to solve is

$$\mathcal{I}_p^+ = \frac{i}{16\pi} \int dz d\bar{z} \frac{1}{\bar{z}} \left(\frac{w_n}{z(w_n - z)} \sqrt{\frac{z}{\bar{z}}} \sqrt{\frac{\bar{z} - \bar{w}_n}{z - w_n}} e^{i\phi} + \frac{\bar{w}_n}{\bar{z}(\bar{w}_n - \bar{z})} \sqrt{\frac{\bar{z}}{z}} \sqrt{\frac{z - w_n}{\bar{z} - \bar{w}_n}} e^{-i\phi} \right). \quad (104)$$

We now scale the integral variable so that we use $z' = z/w_n$ and $\bar{z}' = \bar{z}/\bar{w}_n$ and rewrite the integral to

$$\mathcal{I}_p^+ = \frac{i}{16\pi} \int dz' d\bar{z}' \frac{1}{\bar{z}'} \frac{1}{z'(1-z')} \sqrt{\frac{z'}{\bar{z}'}} \sqrt{\frac{\bar{z}'-1}{z'-1}} e^{i\phi} + \frac{iw_n}{16\pi\bar{w}_n} \int dz' d\bar{z}' \frac{1}{\bar{z}'} \frac{1}{z'(1-\bar{z}')} \sqrt{\frac{z'}{\bar{z}'}} \sqrt{\frac{\bar{z}'-1}{z'-1}} e^{-i\phi}. \quad (105)$$

To get rid of the square roots we change variables to $\hat{u}^2 = z'/(z'-1)$ and $\hat{u}^2 = \bar{z}'/(\bar{z}'-1)$,

$$\mathcal{I}_p^+ = -\frac{i}{8\pi} \int dud\bar{u} \frac{1}{\hat{u}^2(\hat{u}^2-1)} e^{i\phi} - \frac{iw_n}{8\pi\bar{w}_n} \int dud\bar{u} \frac{(\hat{u}^2-1)}{\hat{u}^2(\hat{u}^2-1)^2} e^{-i\phi}. \quad (106)$$

We now change variables to complex polar form,

$$\mathcal{I}_p^+ = -\frac{1}{4i\pi} \int dr r \oint \frac{d\hat{u}}{\hat{u}} \frac{1}{r^2 \hat{u}^{-2} (r^2 \hat{u}^{-2} - 1)} e^{i\phi} - \frac{w_n}{4i\pi\bar{w}_n} \int dr r \oint \frac{d\hat{u}}{\hat{u}} \frac{(r^2 \hat{u}^{-2} - 1)}{r^2 \hat{u}^{-2} (r^2 \hat{u}^{-2} - 1)^2} e^{-i\phi}. \quad (107)$$

and apply the residue theorem to evaluate it. Thus,

$$u_p^+ = \frac{\tilde{\alpha}_p}{4} e^{i\phi} \left(1 - e^{2i(\varphi-\phi)}\right). \quad (108)$$

This is independent on the distance between the defects, which is not surprising since the velocity field of individual defects are also independent on the distance in the far-field. φ is here the angle of the position vector for the negative defect. The motion of one defect is therefore dependent on the uniform orientation field and its relative position with respect to the other defect. In real coordinates, this becomes

$$\vec{u}_p^+ = \frac{\tilde{\alpha}_p}{2R^2} \vec{R}^\perp (\vec{R}^\perp \cdot \hat{p}_0), \quad (109)$$

where $\vec{R} = \vec{r}_- - \vec{r}_+$ with \vec{r}_- and \vec{r}_+ is the position vector for the negative and positive defect respectively, and $\hat{p}_0 = \cos(\phi)\vec{e}_x + \sin(\phi)\vec{e}_y$ which we will assume is a constant vector. Notice that the velocity of the positive defect is always perpendicular to the relative position vector \vec{R} .

b. At negative position: We now place the negative defect at the origin and the positive defect at w_p so that the order parameter can be represented as

$$\psi = \chi(r) \sqrt{\frac{\bar{z}}{z}} \sqrt{\frac{z-w_p}{\bar{z}-w_p}} e^{i\phi}, \quad (110)$$

with

$$\psi(0) = 0. \quad (111)$$

In the far-field the derivative is given as

$$\partial_z \psi = -\frac{1}{2} \frac{w}{z(w-z)} \sqrt{\frac{\bar{z}}{z}} \sqrt{\frac{z-w}{\bar{z}-w}} e^{i\phi}, \quad (112)$$

so that the integral is

$$\begin{aligned} \mathcal{I}_p^- &= -\frac{i}{8\pi} \int dz d\bar{z} \frac{1}{\bar{z}} \Re \left(\frac{w_p}{z(w_p-z)} \sqrt{\frac{\bar{z}}{z}} \sqrt{\frac{z-w_p}{\bar{z}-w_p}} e^{i\phi} \right) \\ &= \frac{i}{8\pi} \int dud\bar{u} \frac{1}{u^2(\bar{u}^2-1)} e^{i\phi} + \frac{iw_p}{8\pi\bar{w}_p} \int dud\bar{u} \frac{u^2(\bar{u}^2-1)}{\bar{u}^4(\bar{u}^2-1)^2} e^{-i\phi} \\ &= -\frac{1}{4\pi i} \int dr r \oint \frac{d\hat{u}}{\hat{u}} \frac{1}{r^2(\hat{u}-r)(\hat{u}+r)} e^{i\phi} + \frac{w_p}{4\pi i\bar{w}_p} \int dr r \oint \frac{d\hat{u}}{\hat{u}} \frac{\hat{u}^3(r^2-\hat{u}^2)}{r^6(\hat{u}-1/r)^2(\hat{u}+1/r)^2} e^{-i\phi}. \end{aligned}$$

using the same kind of variable transformations: $z' = z/w_p$ and $\bar{z}' = \bar{z}/\bar{w}_p$, $u^2 = z'/(z'-1)$ and $\bar{u}^2 = \bar{z}'/(\bar{z}'-1)$ and complex polar form. Solving these using the residual theorem we end up with a velocity of

$$u_p^- = \frac{\tilde{\alpha}_p}{4} e^{i\phi} \left(1 + \frac{1}{3} e^{2i(\varphi_p-\phi)}\right), \quad (113)$$

Where $\varphi_p = \pi + \varphi$ is the angle of the position vector of the positive defect $-\vec{R}$. In real coordinates this is

$$\vec{u}_p = \frac{\tilde{\alpha}_p}{6R^2} \vec{R}^\perp (\vec{R}^\perp \cdot \vec{p}_0) + \frac{\tilde{\alpha}_p}{3R^2} \vec{R} (\vec{R} \cdot \vec{p}_0). \quad (114)$$

This has a component that is perpendicular to the relative position vector \vec{R} and one that is parallel to it. Note that the perpendicular velocity is in the same direction as the one for the positive defect, but it is always smaller in magnitude. This means that the vector is rotating. This rotation has two zeros. To see this easier we consider the evolution of the relative position due to these velocities. The evolution of the relative position of the defects is

$$\dot{\vec{R}} = \frac{\tilde{\alpha}_p}{3R^2} (\vec{R} \cdot \vec{p}_0) \vec{R} - \frac{\tilde{\alpha}_p}{3R^2} (\vec{R}^\perp \cdot \vec{p}_0) \vec{R}^\perp. \quad (115)$$

We notice that one component is parallel and the other is perpendicular to \vec{R} , so that their effect is to stretch and rotate the relative position. The rotation has two zeros, when \vec{R} is parallel or antiparallel to \vec{p}_0 . To check whether these are attractive or repulsive we write $\vec{R} = R(\cos \Omega, \sin \Omega)$, with Ω being the angle of \vec{R} relative to \vec{p}_0 . Assuming that they are almost pointing in the same direction, $\Omega \ll 1$, we have the equations

$$\dot{R} = \frac{\tilde{\alpha}_p}{3}, \quad (116)$$

$$\dot{\Omega} = \frac{\tilde{\alpha}_p}{3R} \Omega, \quad (117)$$

The equation for Ω shows that $\Omega = 0$ is an unstable zero, meaning that \vec{R} tends to rotate away from this direction. The other zero is when \vec{R} is close to antiparallel with \vec{p}_0 . Then we can write the angle as $\Omega = \pi - \Omega_a$, where Ω_a a small angle. The equations are in this configuration approximately

$$\dot{R} = -\frac{\tilde{\alpha}_p}{3}, \quad (118)$$

$$\dot{\Omega}_a = -\frac{\tilde{\alpha}_p}{3R} \Omega_a \quad (119)$$

Meaning that we have a stable zero at $\Omega = \pi$. Notice that the unstable zero corresponds to repulsion force and the stable one corresponds to attraction. This means that, as long as \vec{R} and \vec{p} are not pointing in the same direction, the defects will eventually annihilate.

- [1] Jonas Rønning, Cristina M Marchetti, Mark J Bowick, and Luiza Angheluta. Flow around topological defects in active nematic films. *Proceedings of the Royal Society A*, 478(2257):20210879, 2022.
- [2] Luiza Angheluta, Zhitao Chen, M Cristina Marchetti, and Mark J Bowick. The role of fluid flow in the dynamics of active nematic defects. *New Journal of Physics*, 23(3):033009, 2021.
- [3] Len M Pismen et al. *Vortices in nonlinear fields: From liquid crystals to superfluids, from non-equilibrium patterns to cosmic strings*, volume 100. Oxford University Press, 1999.
- [4] M Cristina Marchetti, Jean-François Joanny, Sriram Ramaswamy, Tanniemola B Liverpool, Jacques Prost, Madan Rao, and R Aditi Simha. Hydrodynamics of soft active matter. *Rev. Mod. Phys.*, 85(3):1143, 2013.
- [5] R Aditi Simha and Sriram Ramaswamy. Hydrodynamic fluctuations and instabilities in ordered suspensions of self-propelled particles. *Physical review letters*, 89(5):058101, 2002.
- [6] Aboutaleb Amiri, Romain Mueller, and Amin Doostmohammadi. Unifying polar and nematic active matter: emergence and co-existence of half-integer and full-integer topological defects. *Journal of Physics A: Mathematical and Theoretical*, 55(9):094002, feb 2022.